
TAILORING LONG-RANGE ENERGY TRANSPORT IN
SUPRAMOLECULAR ARCHITECTURES

Von der Universität Bayreuth
zur Erlangung des Grades eines
Doktors der Naturwissenschaften (Dr. rer. nat.)
genehmigte Abhandlung

von

Bernd Wittmann

aus Weiden i.d.OPf.

1. Gutachter: Prof. Dr. Richard Hildner
2. Gutachter: Prof. Dr. Anna Köhler

Tag der Einreichung: 05.08.2020

Tag des Kolloquiums: 11.11.2020

CONTENTS

1	ABSTRACT	1
2	INTRODUCTION	7
2.1	Motivation	7
2.2	Electronic structure and optical properties of molecules	9
2.2.1	Radiative and non-radiative transitions	11
2.2.2	Jablonski diagram	17
2.2.3	Photophysical parameters	19
2.3	Collective excited states	20
2.3.1	Supramolecular systems	21
2.3.2	Frenkel excitons	23
2.3.3	Frenkel polarons: Expanded theory of H- and J-aggregates	27
2.4	Energy transport	36
2.5	Exciton-exciton annihilation	43
2.6	Wave guiding in self-assembled material	46
2.7	Experimental methods for measuring energy transport	48
	BIBLIOGRAPHY	52
3	OVERVIEW OF THE THESIS	69
3.1	Key results	73
3.2	Individual contribution	83
4	PUBLICATIONS	85
4.1	Energy transport and light propagation mechanisms in organic single crystals	85
4.2	Enhancing long-range energy transport in supramolecular archi- tectures by tailoring coherence properties	128
4.3	All-optical control of singlet exciton transport in individual supramolecular nanostructures by triplet gating	161

1 | ABSTRACT

Organic electronics, such as organic solar cells, light-emitting diodes, and field-effect transistors, are based on tailored conjugated small molecules or polymers. In virtually all organic optoelectronic devices, the material's ability to transport excitation energy plays an important role and is a constraint for device design. For instance, the distance over which energy can be transported is of great importance for organic solar cell performance, as an excitation has to reach an interface to form a charge-separated state.

Artificial nanostructures with tailored properties are important model systems to investigate and understand energy transport phenomena. In this context, supramolecular chemistry offers a powerful tool for the construction of functional materials. Non-covalent interactions between molecular building blocks and advanced processing pathways are exploited to adapt the molecules' spatial arrangement within the supramolecular architecture and thus to tune the (overall) electronic properties.

So far, studies on supramolecular assemblies have demonstrated that energy transport is closely related to the precise arrangement of interacting molecules and that the function typically results from the collective properties of many interacting molecules. However, reports on nanostructures that support long-range or directed transport of excitons are still rare. This might be related to the lack of model systems, since their construction is a challenge. In particular, subtle changes in the molecular framework and the processing can have a huge impact on the material properties. Moreover, numerous fundamental questions about the mechanisms of exciton transport remain unanswered. For instance, the precise role of quantum coherence (delocalization), the influence of electronic and structural disorder, the local environment, the dimensionality and morphology of the structures, and the mutual interplay of these factors are still not fully understood.

In order to further advance in this direction, disentangling the different contributions of energy transport is essential. This requires methods for the direct resolution and unambiguous quantification of energy transport at the level of single objects to avoid ensemble averaging over the intrinsic structural and electronic disorder of supramolecular assemblies. To uncover the role of coherence in energy transport, supramolecular systems that allow disorder and electronic coupling to be adjusted separately are indispensable. In addition, concepts to control exciton transport, preferably externally, are needed to increase the range of possible applications.

This thesis contributes to the points raised above and is thus concerned with the issue of tailoring long-range energy transport in supramolecular assemblies.

The first part of this thesis (4.1) contributes to obtaining unambiguous information about spatio-temporal exciton dynamics in self-assembled materials. We use state-of-the-art spatio-temporal imaging of energy transport via detection-beam scanning of the transient photoluminescence of individual crystals based on thiophene-benzene-thiophene oligomers. In combination with numerical simulations, we address and resolve ambiguities in direct measurements of spatio-temporal exciton dynamics and are able to quantify the influence of exciton-exciton annihilation, photon recycling, and leaky mode waveguiding as sources of 'error' in such experiments. We demonstrate how these mechanisms can be discriminated by a careful design of experiments, data evaluation, and numerical simulations. Furthermore, our single crystals, in which the oligomers are stacked in an H-type arrangement, exhibit singlet exciton transport distances of up to 210 nm with a diffusivity of up to $0.2 \text{ cm}^2/\text{s}$. Surprisingly, we observe a variation in the exciton transport lengths and exciton dynamics from crystal to crystal, which we relate to varying degrees of electronic disorder.

The second part (4.2) deals with the construction and characterization of suitable supramolecular architectures that allow for tailoring coherence characteristics. Depending on the solvent, we can prepare either single supramolecular nanofibers or bundles of supramolecular nanofibers based on a carbonyl-bridged triarylamine-based (CBT) building block. We found that the excited state energy landscape, i.e., the correlation between transition energies of the building blocks, is tuned by bundling-induced electronic disorder. Consequently, excitons in single nanofibers are delocalized over more molecules than in bundles. Using optical microscopy with detection-beam scanning capability, we visualize long-range singlet exciton transport in both architectures. Due to the high degree of exciton delocalization, single nanofibers feature superior energy transport characteristics with the largest exciton diffusion coefficients of $1 \text{ cm}^2/\text{s}$ reported for H-aggregates so far. The unique combination of these supramolecular model systems and advanced optical microscopy methods thus enables us to reveal the role of morphology and coherence, i.e., exciton delocalization in energy transport.

The last part of this thesis (4.3) is concerned with the demonstration of an all-optical approach to control singlet exciton transport pathways via singlet-triplet annihilation in supramolecular CBT-based bundles of nanofibers. We use two temporally and spatially separated laser pulses to generate a triplet and a subsequent singlet exciton population. The laser-generated, freely positionable triplet exciton population acts as a barrier for the mobile singlet exciton population since singlet-triplet annihilation suppresses singlet exciton transport in the direction of the triplet barrier. Our new approach paves the way towards new design principles for functional photonic nanodevices and ultimately to complete control over singlet exciton motion.

ZUSAMMENFASSUNG

Organische Elektronik, wie z.B. organische Solarzellen, Leuchtdioden und Feldeffekttransistoren, basiert auf maßgeschneiderten konjugierten Molekülen oder Polymeren. In praktisch allen organischen optoelektronischen Bauelementen spielt die Fähigkeit des verwendeten Materials, Anregungsenergie zu transportieren, eine wichtige Rolle und kann daher das Bauteildesign einschränken. Zum Beispiel ist die Entfernung, über die Energie transportiert werden kann, von großer Bedeutung für die Leistungsfähigkeit organischer Solarzellen, da eine Anregung eine Grenzfläche erreichen muss, um einen ladungsgetrennten Zustand zu bilden.

Künstliche Nanostrukturen mit maßgeschneiderten Eigenschaften sind wichtige Modellsysteme zur Untersuchung von Energietransportphänomenen. Hierbei ist die supramolekulare Chemie ein leistungsfähiger Ansatz zur Konstruktion funktioneller Materialien. Nicht-kovalente Wechselwirkungen zwischen molekularen Bausteinen werden in Kombination mit ausgeklügelten Verarbeitungswegen ausgenutzt, um die räumliche Anordnung der Moleküle innerhalb der supramolekularen Architektur anzupassen und so die elektronischen Eigenschaften abzustimmen.

Bisherige Studien über supramolekulare Architekturen haben gezeigt, dass der Energietransport eng mit der genauen Anordnung der interagierenden Moleküle zusammenhängt und dass die Funktion typischerweise aus den kollektiven Eigenschaften vieler Moleküle resultiert. Jedoch sind Berichte über Nanostrukturen, die einen weit reichenden oder gerichteten Transport von Exzitonen zulassen, noch selten. Dies hängt zum Teil mit dem Fehlen von Modellsystemen zusammen, denn selbst subtile Veränderungen des molekularen Gerüsts und der Verarbeitung können enorme Auswirkungen auf die Materialeigenschaften haben. Darüber hinaus sind zahlreiche grundlegende Fragen zu den Mechanismen des Exzitonentransports unbeantwortet. So sind zum Beispiel die genaue Rolle der Quantenkohärenz (Exziton-Delokalisation), der Einfluss der elektronischen und strukturellen Unordnung, der lokalen Umgebung, der Dimensionalität und Morphologie der Strukturen und das gegenseitige Zusammenspiel dieser Faktoren noch nicht vollständig verstanden.

Um weitere Fortschritte in diese Richtung zu erzielen, ist eine Entflechtung der verschiedenen Beiträge zum Energietransport unerlässlich. Dies erfordert Methoden zur direkten Auflösung und eindeutigen Quantifizierung des Energietransports auf der Ebene einzelner Objekte, um eine Ensemble-Mittelung über die intrinsische strukturelle und elektronische Unordnung in supramolekularen Aggregaten zu vermeiden. Nur so kann ein allumfassendes Bild der Mechanismen erworben werden, die den Energietransport diktieren. Um die Rolle der

Kohärenz beim Energietransport aufzudecken, werden supramolekulare Systeme benötigt, die es erlauben Unordnung und elektronische Kopplung getrennt voneinander einzustellen. Darüber hinaus sind Konzepte zur Steuerung des Exzitonentransports (vorzugsweise durch externe Einflussnahme) erforderlich, um die Bandbreite möglicher Anwendungen zu erweitern.

Diese Arbeit leistet einen Beitrag zu den oben aufgeworfenen Aufgaben und Fragestellungen und beschäftigt sich mit der Frage, wie der Energietransport in supramolekularen Anordnungen verbessert und kontrolliert werden kann.

Der erste Teil dieser Arbeit (4.1) trägt dazu bei, eindeutige Informationen über die raumzeitliche Exzitudynamik in selbst-assemblierten Materialien zu erhalten. Wir verwenden modernste raumzeitliche Bildgebungsmethoden des Energietransports mittels Detektionsstrahlabtastung der transienten Photolumineszenz. Als Modellsystem wurden Thiophen-Benzol-Thiophen-Oligomer Einkristalle verwendet. In Kombination mit numerischen Simulationen konnten wir Mehrdeutigkeiten bei direkten Messungen der raumzeitlichen Exzitudynamik aufdecken und waren in der Lage, den Einfluss von Exziton-Exziton-Annihilation, Photonen-Recycling und Leaky-Mode-Wellenleitung als „Fehlerquellen“ in solchen Experimenten zu quantifizieren. Wir zeigen, wie diese Mechanismen durch eine sorgfältige Versuchsplanung, Datenauswertung und numerische Simulationen unterschieden werden können. Unsere Einkristalle, in denen die Oligomere in einer H-Typ-Anordnung gestapelt sind, weisen eindeutig zugeordnete Singulett-Exziton-Transportstrecken von bis zu 210 nm und Diffusivitäten von bis zu $0,2 \text{ cm}^2/\text{s}$ auf. Überraschenderweise beobachten wir eine Variation der Exzitonentransportlängen und der Exzitudynamik von Kristall zu Kristall, die wir mit unterschiedlichen Graden elektronischer Unordnung in Verbindung bringen.

Der zweite Teil (4.2) dieser Arbeit befasst sich mit der Konstruktion und Charakterisierung geeigneter supramolekularer Architekturen, die eine Anpassung der Kohärenzeigenschaften ermöglichen. Je nach Lösungsmittel sind wir in der Lage, entweder einzelne supramolekulare Nanofasern oder Bündel von supramolekularen Nanofasern auf der Basis eines Carbonyl-verbrückten Triarylamin (CBT) Bausteins herzustellen. Wir fanden heraus, dass die Energielandschaft des angeregten Zustands, genauer gesagt die Korrelation zwischen den Übergangsenergien der Bausteine, durch Bündelung induzierte elektronische Unordnung abgestimmt wird. Folglich sind Exzitonen in einzelnen Nanofasern über mehr Moleküle als in Bündeln delokalisiert. Mit Hilfe der optischen Mikroskopie und der Detektionsstrahlabtastung der transienten Photolumineszenz visualisieren wir den langreichweitigen Transport von Singulett-Exzitonen in beiden Architekturen. Aufgrund des hohen Grades der Exziton-Delokalisierung besitzen einzelne Nanofasern überlegene Energietransporteigenschaften gegenüber Bündeln. Insbesondere stellen wir fest, dass einzelne supramolekulare Nanofasern die höchsten Diffusivitäten von bis zu $1 \text{ cm}^2/\text{s}$ aufweisen, die bisher für H-Aggregate berichtet wurden. Die einzigartige Kombination dieser supramolekularen Modellsysteme mit fortschrittlichen Methoden der optischen Mikroskopie ermöglicht

es uns somit, die Rolle der Morphologie und Kohärenz (Delokalisierung der Exzitonen) beim Energietransport aufzuzeigen.

Der letzte Teil dieser Arbeit (4.3) befasst sich mit der Demonstration eines rein optischen Ansatzes zur Kontrolle von Singulett-Exziton-Transportwegen durch Singulett-Triplett-Annihilation in supramolekularen CBT-basierten Nanofaserbündeln. Wir verwenden zwei zeitlich und räumlich getrennte Laserpulse, um eine Triplett- und eine nachfolgende Singulett-Exzitonenpopulation zu erzeugen. Die mit dem Laser erzeugte, frei positionierbare Triplett-Exzitonenpopulation wirkt als Barriere für die mobile Singulett-Exzitonenpopulation, da durch die Singulett-Triplett-Annihilation der Transport von Singulett-Exzitonen in Richtung der Triplett-Barriere unterdrückt wird. Unser neuer Ansatz ebnet den Weg zu neuen Designprinzipien für funktionelle photonische Nanobaulemente und letztlich zur vollständigen Kontrolle über die Bewegung von Singulett-Exzitonen.

2 | INTRODUCTION

2.1 MOTIVATION

The steadily increasing demand for energy is one of the greatest challenges of modern age [1–3]. In this context, sunlight is both the largest and the most widely available energy source on our planet [1, 3, 4]. Within one hour, more solar energy reaches the earth than humans consume within a whole year [3]. However, to make a significant contribution to primary energy supply, we have to gain a deeper understanding of how to improve solar energy harvesting, energy transport, and storage of energy [1, 3–6].

Research in this field is inspired by the manner how nature has mastered and optimized this challenging task [4, 7–13]. In natural photosynthetic systems, the elementary steps are photon capture (absorption) by a dense network of pigment-protein complexes, subsequent energy transport through the network to a reaction center, and utilization of energy to drive a desired reaction. Specifically, excitation energy from absorbing molecules is funneled with near-unity efficiency to a target molecule due to an outstanding spatial control of densely packed molecules with precisely tuned interactions [4, 11, 14, 15]. Since efficient transport of excitation energy is a key process in photosynthesis, as well as in the development of renewable and clean energy technology [9, 10, 16, 17], many scientists are working to extract and mimic natural mechanisms to be exploited for artificial systems. Synthetic molecular chemistry has been successful in optimizing photon absorption by creating extended π -conjugated molecules with highly tunable optical properties [12, 18, 19]. However, an important lesson learned from nature as well as from many studies on organic materials is that function arises from the collective behavior of many interaction molecules [4, 6, 7, 9, 14, 20–22]. Thus, design principles beyond the molecular formula must be developed to gain an in-depth understanding of energy transport [6, 9, 17, 23].

In this context, self-assembly offers bioinspired strategies to develop nanoscale functional materials for energy transport, storage and conversion [10]. In this bottom-up approach, directed non-covalent interactions between molecules are exploited for the construction of well-defined model systems that provide functionalities beyond the molecular framework [10, 24–27]. However, the construction of suitable model systems is challenging. In addition to the molecular design, which inherits the capability of forming non-covalent interactions, processing conditions, such as solvent, concentration, temperature window, and rate are important. Moreover, to meet the desired functionality of the self-assembled material, a development feedback loop between the molecular design, the processing conditions, and the material properties is needed. Thus, creating

functional self-assembled systems is not yet fully understood and often remains unpredictable [10, 24].

A large number of studies have been performed to explain and characterize energy transport in various self-assembled model systems, e.g., molecular crystals [28, 29], 1-dimensional nanofibers [26, 30] and nanotubes [31–34]. It turns out that excitation energy transport is highly dependent on the interaction between the building blocks and their respective alignment [5, 7, 22, 35]. In these model systems, the molecules are tightly packed and thus feature reasonably strong electronic coupling, facilitating the formation of delocalized excited states (exciton states), i.e., excitations are coherently shared by many molecules. These delocalized exciton states are widely considered to play a key role in the enhancement of energy transport [4, 7, 8, 20, 26, 31, 34]. Electronic and structural disorder competes with the coupling between the molecules and impedes the delocalization of the exciton states. Reducing disorder typically facilitates exciton delocalization, which is considered to be highly beneficial for long-range energy transport [7, 16, 17, 20, 26, 36]. In this regard, molecular H-type nanofibers based on carbonyl-bridged triarylamine trisamides, featuring a suppressed radiative decay channel in addition to high order and coupling, have attracted considerable interest, as they are able to transport excitation energy over more than 4 μm [26]. Since the interplay between intermolecular interactions, electronic and structural disorder, and the interactions with the surrounding environment is complex, a full understanding and control of energy transport remains elusive [6, 7, 9, 16, 20, 23]. This challenging task requires model systems that make it possible to disentangle the complex interplay of parameters. In addition, the achievement of a directed exciton transport remains a major challenge [6, 11, 37]. Directed, controllable energy transport would not only lead to increased efficiency of solar cells but also represents a key function in optical communication and information processing [6, 11, 27, 37, 38]. To date, the available concepts are either limited in their transport lengths [11, 39] or are not reversible [40] or flexible [38] in their use, inhibiting full control over transport.

Moreover, to achieve a full picture of exciton dynamics, experimental methods are required to resolve energy transport much more directly on the level of single nanostructures [41, 42]. Widely used bulk approaches suffer from sample heterogeneities and thus are unable to detect structural defects or (local) changes in the environment [41]. These insights remain hidden but are highly relevant to understand the underlying mechanisms that dictate energy transport. The latest optical imaging techniques allow spatio-temporal detection of energy transport in individual nanostructures [41]. These new methods facilitate the development of new theoretical descriptions of energy transport beyond the standard diffusion models and ultimately lead to a microscopic picture of material properties that determine energy transport [41]. However, such direct measurements are also sensitive to several additional effects, such as photon recycling [28] and exciton-

exciton annihilation [41]. Thus, a differentiation between these effects is required to extract the material characteristics of interest.

This thesis focuses on finding concepts to influence exciton energy transport in supramolecular systems. For this purpose, spatio-temporal detection of energy transport on pico- to nanosecond time scales was implemented experimentally and applied to self-assembled H-type model systems. On the experimental side, this work contributes to an unambiguous identification of exciton dynamics using direct imaging techniques of exciton transport in single nanostructures. Moreover, it adds new dimensions to a fundamental understanding of the interplay of morphology, electronic coupling and disorder, and their influence on the energy transport properties in self-assembled materials. Finally, a new all-optical approach to control singlet exciton transport is introduced and implemented experimentally.

This thesis is organized as follows: Chapter 2 aims to provide the theoretical background necessary to understand the results of this work. In section 2.2 the basic photophysical properties of organic molecules are discussed. Since the focus of this work are the photophysical and energy transport properties of self-assembled structures, in section 2.3 the interaction between molecules is considered and the associated spectral changes are discussed. In this context, collective excited states of aggregates and their spectroscopic signatures are discussed in the framework introduced by Spano and co-workers. In section 2.4, the transport of excitation energy in such systems is explained and section 2.5 deals with the associated mechanism of exciton-exciton annihilation. The last two sections in the introduction deal with the possible waveguiding effects within self-assembled structures (section 2.6) and experimental methods to resolve excitation energy transport in space and time (section 2.7). Chapter 3 shows the connections between the publications and summarizes their content. The publications can be found in chapter 4.

2.2 ELECTRONIC STRUCTURE AND OPTICAL PROPERTIES OF MOLECULES

Most molecular spectroscopy experiments probe quantum mechanical properties [43]. In particular, in electronic molecular spectra, in principle any combination of energy levels $\{E_i, E_f\}$ of a molecule can be assigned to a frequency f_{fi} according to $hf_{fi} = |E_i - E_f|$, with the Planck constant h . However, whether this frequency is observed in the spectrum and the intensity of this spectral line can be explained by so-called selection rules [44]. The observed absorption and emission spectra can be rather complex and can consist of line sequences, bands, or band systems, covering the spectral range between ultraviolet and far-infrared. Moreover, spectra provide information about several basic molecular properties,

such as the energy level structure, the frequencies of rotations and vibrations, relaxation mechanisms, and much more [44–46].

An understanding of molecular properties and the analysis of molecular spectra is provided by the framework of quantum mechanics [47]. As a starting point, it is assumed that molecules can be described as a many-body system composed of electrons and nuclei with the electronic and nuclear coordinates \mathbf{r} and \mathbf{R} , respectively. All quantum mechanical information about the stationary properties of the molecule is contained in wave functions $|\Psi\rangle$ that obey the stationary Schrödinger equation

$$\hat{H} |\psi\rangle = E |\psi\rangle. \quad (2.1)$$

The solution of equation (2.1) provides an energy spectrum E and the corresponding eigenfunctions $|\Psi\rangle$ [47]. The non-relativistic many-body Hamiltonian \hat{H} of the molecule consists of five terms:

$$\hat{H} = \hat{T}_{el}(\mathbf{r}) + \hat{T}_{nuc}(\mathbf{R}) + \hat{U}_{el,el}(\mathbf{r}) + \hat{U}_{nuc,nuc}(\mathbf{R}) + \hat{V}_{el,nuc}(\mathbf{r}, \mathbf{R}). \quad (2.2)$$

Here, \hat{T}_{el} and \hat{T}_{nuc} describe the kinetic energy of the electrons and the nuclei. The terms $\hat{U}_{el,el}$ and $\hat{U}_{nuc,nuc}$ contain the repulsive Coulomb interaction between electrons and nuclei, respectively, and $\hat{V}_{el,nuc}$ describes the attractive interaction between electrons and nuclei. Interactions due to electron and nuclear spins were neglected. However, the Schrödinger equation (2.1) cannot be solved exactly for molecules, not even for the simplest one, H_2^+ . Therefore, equation (2.1) is solved numerically or simplifications have to be introduced [44].

One fundamental approximation in molecular physics is the adiabatic approximation. It is based on the large mass difference between electrons and nuclei, i.e., the mass of electrons is negligible compared to the nuclear mass. Consequently, the nuclei of a molecule move much slower compared to their electrons. Hence, the electrons can follow the oscillations of the nuclei adiabatically and adjust to the respective nuclear configuration. As a result, each nuclear configuration \mathbf{R} has a defined electron distribution [43, 44, 47–49]. Treating the kinetic energy of the nuclei as a small perturbation and neglecting the coupling terms between electronic and nuclear wave functions during a perturbation theoretical calculation, one arrives at the Born-Oppenheimer approximation [44, 50]. In the Born-Oppenheimer approximation, the Schrödinger equation splits into two separate, decoupled equations for the electronic $|\Phi_n^{el}(\mathbf{r})\rangle$ and nuclear wave functions $|\chi_{n,\nu}(\mathbf{R})\rangle$. The total wave function of the molecule in the n -th electronic state and ν -th nuclear state can then be written as a product of the corresponding wave functions (leaving aside the electrons' spin)

$$|\Psi_{n,\nu}(\mathbf{r}, \mathbf{R})\rangle = |\Phi_n^{el}(\mathbf{r}; \mathbf{R})\rangle |\chi_{n,\nu}(\mathbf{R})\rangle. \quad (2.3)$$

Note, that the electronic wave functions depend parametrically on the nuclear coordinates \mathbf{R} . The solution of the electronic part of the Schrödinger equation as a function of the nuclear coordinates \mathbf{R} yields the eigenvalues $V_n(\mathbf{R})$ of

the molecule in the n -th electronic state. These eigenvalues are known as potential energy surfaces (see Fig. 2.1) and describe effective potentials for the nuclei, in which the nuclear framework can perform quantized oscillations. For each electronic state $|\Phi_n^{el}\rangle$ with energy $V_n(\mathbf{R})$ there is a set of vibrational wave functions $|\chi_{n,\nu}\rangle$ of the nuclei with the corresponding vibrational quantum number ν .

The quantized oscillations of the nuclear framework can be described in terms of several normal modes, which can be approximated as harmonic oscillations around an equilibrium position \mathbf{R}_0 in the minima of the corresponding potential energy surface. Then, the total vibrational energy of the molecule is the sum of the vibrational energies of all excited normal modes. Consequently, the total energy of the system is [43, 44, 50, 51]

$$E_{n\nu} = V_n(\mathbf{R}_0) + \sum_i \omega_{n,i}(\nu_i + \frac{1}{2}), \quad (2.4)$$

where $\omega_{n,i}$ is the energy of the i -th vibrational mode in the n -th electronic state. The total energy is the sum of the kinetic energy of the nuclei and the electronic energy. Hence, the Born-Oppenheimer approximation allows to assign transitions as primarily electronic or vibrational in nature and is therefore of fundamental importance in spectroscopy [49].

In the context of this work, energetically close vibrational modes cannot be resolved. Therefore, an effective vibrational mode of energy $\omega_{n,0}$ is considered [35, 51] and equation (2.4) reduces to

$$E_{n\nu} = V_n(\mathbf{R}_0) + \omega_{n,0}(\nu + \frac{1}{2}), \quad (2.5)$$

where $\omega_{n,0}(\nu + \frac{1}{2})$ is the quantized vibrational energy of the effective oscillation around the equilibrium position in the n -th electronic state.

2.2.1 Radiative and non-radiative transitions

Absorption and emission spectra are results of optical transitions between different energy states in molecules. The different spectral shapes of molecular spectra are based on the fact that certain transitions are more likely than others. The starting point of the quantum mechanical description is an unperturbed system, described with the Hamiltonian \hat{H}_0 . If, for example, the molecule is exposed to an external electromagnetic field or experiences an additional intramolecular interaction that was not considered in \hat{H}_0 , transitions between states can occur [43]. As long as these interactions are small compared to those already present in the absence of the interaction, it is appropriate to treat them as a perturbation \hat{H}' . Consequently, the total Hamiltonian is the sum of the original Hamiltonian and the perturbation $\hat{H} = \hat{H}_0 + \hat{H}'$ [43, 48, 51] and in general, the new wave functions of the system can be described in good approximation as a linear combination of the eigenstates of \hat{H}_0 .

From time-dependent perturbation theory, an expression can be obtained that describes how a perturbation affects an initially unperturbed system in an eigenstate $|\Psi_i\rangle$ of the unperturbed Hamiltonian \hat{H}_0 . The transition rate from an initial state $|\Psi_i\rangle$ to a final state $|\Psi_f\rangle$, with energies E_i and E_f , respectively, driven by an oscillatory, time-dependent perturbation of frequency f , can be expressed as

$$k_{if} = \frac{2\pi}{\hbar} |\langle \Psi_f | \hat{H}' | \Psi_i \rangle|^2 \delta(|E_f - E_i| - hf). \quad (2.6)$$

Here, $\langle \Psi_f | \hat{H}' | \Psi_i \rangle$ is the matrix element of the perturbation between the final and the initial state. The delta function $\delta(|E_f - E_i| - hf)$ ensures energy conservation during the transition, i.e., the transition rate between states is only significant if the energy difference between initial and final state matches hf [43, 48, 49]. For a constant, time-independent perturbation, this delta function reduces to $\delta(E_f - E_i)$ and hence, only transitions between states with the same energy are possible [43]. Equation (2.6) is called Fermi's golden rule. An alternative form of Fermi's Golden rule can be derived for the transition from one initial state to a quasi-continuum of final states. In this case, the delta function must be replaced by the density of energy-conserving final states ρ_F and the matrix element by an averaged matrix element [43, 48, 49, 51–53].

To completely describe electrons and the basic electronic transitions between states, the spin degree of freedom must also be considered [47, 54]. Since the non-relativistic Hamiltonian in equation (2.2) makes no references to spin, a spin wave function has to be introduced. Importantly, owing to the Pauli principle, the wave function of a system of electrons has to be anti-symmetric with respect to the interchange of any two electronic indices (spin and space) [47, 54]. Therefore, within the Born-Oppenheimer approximation, the total wave function can be approximated as the product of the electronic ($|\Phi_{el}\rangle$), nuclear ($|\chi\rangle$) and spin wave function ($|\Phi_{spin}(\alpha_i, \beta_i)\rangle$). The latter describes the spins of the electrons. α_i and β_i are the spin wave functions of the individual electrons, which describe electrons whose spin is parallel (spin up) or anti-parallel (spin down) with respect to some direction in space [47]. The spins are coupled to a total spin quantum number S and states with distinct spins are orthogonal [43, 49, 54, 55]. For example, in electronic singlet states, $S = 0$ and all electron spins are paired and anti-parallel with respect to each other. In triplet states $S = 1$ due to two unpaired (parallel) spins.

RADIATIVE TRANSITIONS Radiative transitions are accompanied by the absorption or emission of a photon. In spectroscopy, the most common perturbation is a time-dependent oscillatory perturbation of frequency f , originating from electromagnetic radiation [43]. In the simplest approach, the perturbation is assumed as the interaction of a classical electric field $\mathbf{E}(t)$ with an electrically neutral molecule. The leading term of this interaction, writing the molecular charge distribution in a multipole expansion and assuming that the electromagnetic field strength hardly varies over the extensions of the molecule, is the

dipole interaction, i.e., $\hat{H}' = \mathbf{E}(t)\hat{\mathbf{p}}$ [43]. The so-called transition dipole operator $\hat{\mathbf{p}} = \hat{\mathbf{p}}_{el} + \hat{\mathbf{p}}_{nuc}$ consists of an electronic and nuclei part and is determined by the charges e and the coordinates of electrons \mathbf{r}_i as well as the charges $Z_j e$ and coordinates \mathbf{R}_j of the nuclei $\hat{\mathbf{p}} = \hat{\mathbf{p}}_{el} + \hat{\mathbf{p}}_{nuc} = -\sum_i e\mathbf{r}_i + \sum_j Z_j e\mathbf{R}_j$ [48, 49, 56]. In the case of spontaneous emission, the perturbation is caused by the zero-point radiation field [43, 49].

According to Fermi's golden rule (Eq. (2.6)), transitions occur between states whose energy difference corresponds to hf , where f is the frequency of the electromagnetic field [43, 48, 49]. Moreover, for electric dipole transitions, such as absorption and emission of light (radiative transitions), the matrix element in equation (2.6) is proportional to the transition dipole moment

$$\boldsymbol{\mu}_{if} = \langle \Psi_f | \hat{\mathbf{p}} | \Psi_i \rangle. \quad (2.7)$$

The squared magnitude of the transition dipole moment is called the dipole strength D_{if} , which is a measure for the intensity of the transition [48, 49, 56].

Inserting the total wave function $|\Psi\rangle = |\Phi_{el}\rangle |\Phi_{spin}\rangle |\chi\rangle$ into the expression for the dipole strength yields

$$D_{if} = |\boldsymbol{\mu}_{if}|^2 \approx |\langle \Phi_{el,f} | \hat{\mathbf{p}}_{el} | \Phi_{el,i} \rangle|^2 |\langle \Phi_{spin,f} | \Phi_{spin,i} \rangle|^2 |\langle \chi_f | \chi_i \rangle|^2. \quad (2.8)$$

The separation into three factors is rigorously not correct because of the parametric dependence of the electronic wave functions on \mathbf{R} . This so-called Condon approximation is only possible, if the dependence of the nuclear degrees of freedom on the electronic transition moment is sufficiently weak or averaged over the nuclear configurations [43, 48, 49, 51].

To make statements about transition probabilities, the integrals in equation (2.8) must be evaluated. This can be complicated since one must know the wave functions of the initial and final state and these are usually only available as approximations. However, using symmetry consideration it can be determined whether one of the three terms is nonzero, i.e., whether the transition is optically allowed (for this section see Ref. [51]).

If the integral $|\langle \Phi_{el,f} | \hat{\mathbf{p}}_{el} | \Phi_{el,i} \rangle|^2$ is not equal to zero, the transition is dipole allowed. Since the electronic dipole operator is of odd symmetry, the integral disappears if the parities of initial and final wave functions are equal.

The second factor $|\langle \Phi_{spin,f} | \Phi_{spin,i} \rangle|^2$ specifies that the spin state must be maintained during a transition. Since spin wave functions with different spin quantum numbers are orthogonal by definition [43, 49, 54, 55], this integral is nonzero (spin-allowed) for transitions between states with the same spin quantum number. In particular, the spin-allowed emission of a photon is called fluorescence. Concerning the non-relativistic Hamiltonian (2.2), there is no term coupling spatial coordinates and spin, resulting in a product type wave function. One can speak of having pure singlet and pure triplet states [57]. However, due to a relativistic effect called spin-orbit coupling, states of different spin quantum numbers are mixed, i.e., singlet states ($S = 0$) are mixed with a small triplet

character ($S = 1$) and vice-versa. Therefore, quantum mechanically, radiative transitions between states of different spins become possible, treating spin-orbit coupling in the framework of a perturbation theory approach [51, 57, 58]. Here, the so-called spin-forbidden emission of a photon is termed phosphorescence. In particular, it can be shown that spin-orbit coupling Hamiltonians depend on the nuclear charge [43, 51, 57, 58]. For example, in atoms, one can show that spin-orbit coupling is proportional to the fourth power of the atomic charge. Therefore, spin-orbit coupling is expected to increase with the atomic number [43, 51, 58]. Simplified, an electron in the immediate vicinity of a nucleus with positive charge Z is accelerated to relativistic velocities, and hence the coupling of spin and orbital magnetic momentum is large [59]. As a result, phosphorescence is often observed, when atoms with high masses are incorporated (so-called heavy atom effect) [51, 57, 58].

The third term of equation (2.8) is called Franck-Condon factor. The integral $f_{\tilde{\nu},\nu} = \langle \chi_{f,\tilde{\nu}} | \chi_{i,\nu} \rangle$ describes the overlap of the vibrational wave functions involved in the transition and is called the Franck-Condon overlap integral. The corresponding Franck-Condon factor is the squared magnitude of this integral, i.e., $f_{\tilde{\nu},\nu}^2$. This factor describes the probability of a transition from the vibrational state $\nu = \nu_1 \dots \nu_n$ of the electronic state Ψ_i to an vibrational state $\tilde{\nu} = \tilde{\nu}_1 \dots \tilde{\nu}_m$ of the final electronic state Ψ_f . Since the other two factors of equation (2.8) are constant for transitions between two potential energy surfaces, the Franck-Condon factor is responsible for the relative intensities of the vibronic transitions and hence is responsible for the spectral shape [48, 51]. An analytical form of Franck-Condon factors for vibronic transitions can be obtained using the wave functions of the harmonic oscillator with equal vibrational energies but different equilibrium positions \mathbf{R}_0 (shifted harmonic wells or displaced oscillators) [35, 43, 51]. Then, the Franck-Condon factors for the transition from the lowest vibrational level of the ground state to level $\tilde{\nu}$ of the excited state can be written as a Poisson distribution [43, 49, 51]:

$$f_{\tilde{\nu},0}^2 = \frac{\lambda^{2\tilde{\nu}}}{\tilde{\nu}!} e^{-\lambda^2}. \quad (2.9)$$

Here, λ^2 is the Huang-Rhys parameter, which specifies the relaxation energy in units of the vibrational energy, i.e., $E_{rel} = \lambda^2 \omega_0 \propto \Delta \mathbf{R}$. It serves as a measure for the coupling of the vibrations to the electronic transition (electron-phonon coupling) [49], or is a measure for the displacement $\Delta \mathbf{R}$ of the excited state potential curve along the configuration coordinate of the associated oscillation with respect to the ground state potential curve [43, 51]. The general case, $f_{\tilde{\nu},\nu}$ can be calculated numerically as an overlap integral between the eigenfunctions of the harmonic oscillator.

Figure 2.1 summarizes the basic concepts of dipole- and spin-allowed optical transitions ($D_{if} \neq 0$, see Eq. (2.8)) and illustrates the resulting spectra. The transitions between electronic states take place on a femtosecond time scale [49, 51, 60, 61] and can be considered to be fast compared to the movement of the

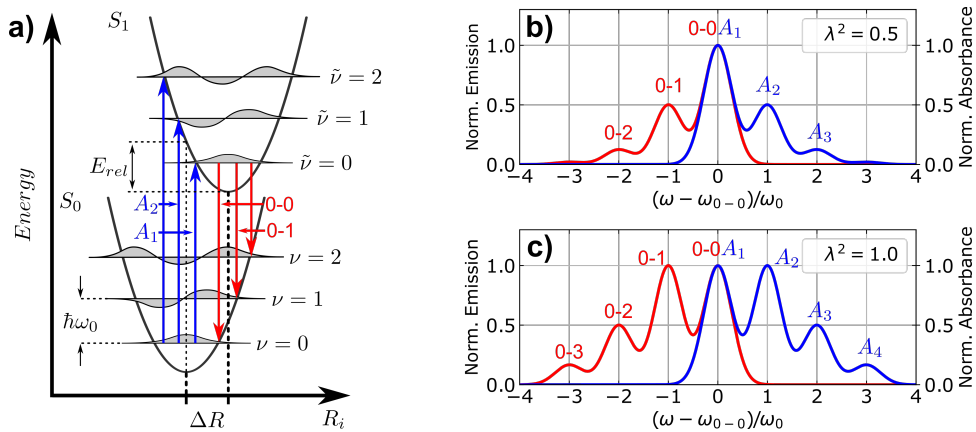


Figure 2.1: Radiative transitions. a) Ground state S_0 and first excited state S_1 potential energy surfaces are shifted by ΔR with respect to each other along the configurational coordinate R_i of an effective vibrational mode. Selected wave function amplitudes of the vibrational wave functions are sketched in grey, ν and $\tilde{\nu}$ denote the vibrational quantum numbers in S_0 and S_1 , respectively. Optical transitions are shown as vertical blue (absorption) and red (emission) arrows. b) Franck-Condon progression in absorption (blue) and emission (red) for a Huang-Rhys parameter $\lambda^2 = 0.5$ according to equations (2.11) and (2.10). c) Franck-Condon progression for $\lambda^2 = 1$. With increasing λ^2 , the probability of transitions into higher vibrational states increases. For further details, see text. Adapted from [35].

nuclei. Hence, the nuclear configuration can be considered as stationary during the transition [47, 62]. Therefore, radiative transitions are drawn as vertical arrows in the picture of potential energy surfaces, which is called Franck-Condon principle. Due to changed charge densities upon excitation, the potential energy surfaces of the ground and excited state (here denoted as S_0 and S_1) are shifted with respect to each other and because of relaxation processes, emission occurs at a different nuclear configuration compared to absorption [49–51, 61]. The energy released upon this relaxation to the minimum of the excited state potential is called relaxation energy E_{rel} [35, 51]. As explained above, the probability of radiative transitions occurs with a higher likelihood between states whose nuclear wave functions show a high overlap. Depending on the shift between the potential energy surfaces against each other, this results in distinct transition probabilities between the involved vibrational states. Typically, the resulting vibronic transitions are labeled by the initial and final vibrational quantum number [48], i.e., $\nu - \tilde{\nu}$. For absorption, which normally takes place from the so-called vibrationless ground states (electronic and vibrational ground state with $\nu = 0$), only the final quantum number is used and labeled as $0 - \tilde{\nu} = A_{\tilde{\nu}+1}$ [35].

The observed spectra consist of lines separated by the corresponding vibrational energy ω_0 . For one dominant vibrational mode whose vibrational energy is

large compared to the thermal energy ($kT \ll \omega_0$), the emission and absorption spectrum is given by

$$\frac{I_{PL}(\omega)}{[n(\omega)\omega]^3} = \sum_m \frac{\lambda^{2m}}{m!} e^{-\lambda^2} \Gamma \delta(\omega - (\omega_{0-0} - m\omega_0)) \quad (2.10)$$

$$\frac{I_{Abs}(\omega)}{[n(\omega)\omega]} = \sum_m \frac{\lambda^{2m}}{m!} e^{-\lambda^2} \Gamma \delta(\omega - (\omega_{0-0} + m\omega_0)). \quad (2.11)$$

The factor $[n(\omega)\omega]^3$ and $[n(\omega)\omega]$, respectively, stems from the density of photon states of the surrounding medium with refractive index $n(\omega)$ at the photon energy ω . $m = 0, 1, 2, \dots$ count the number of the vibrational level of energy ω_0 . ω_{0-0} is the energy of the 0-0 transition, corresponding to the energetic distance of the vibrationless electronic ground state and excited state. $\Gamma(w) = \exp(-(\omega/2\sigma)^2)$ is the lineshape function, which is usually assumed to be a Gaussian function with variance σ^2 . This function is necessary because transitions are not observed as sharp lines, but are homogeneously and inhomogeneously broadened (see also sections 2.3 and 2.4). The δ -function describes the conservation of energy and ω is the energy of the absorbed or emitted photon. These expressions are known as Franck-Condon progressions. It should also be mentioned that for an adequate description of molecular spectra several vibrational modes might be involved. If the inhomogeneous broadening of the individual lines is large compared to the energetic separation between two modes, they can no longer be distinguished. Therefore, instead of several vibrational modes, an effective mode is used in equations (2.10) and (2.11) [35, 51].

According to equations (2.10) and (2.11), the intensities of the vibronic peaks depend strongly on the Huang-Rhys parameter, since the overlap between the vibrational wave functions of the excited and ground states is determined by the displacement of the corresponding potential energy surfaces, e.g., for $\lambda^2 = 0$ only purely electronic (0-0) transitions are allowed. With increasing Huang-Rhys parameter, transitions to energetically higher vibrational states become more and more likely (see Fig. 2.1).

The Huang-Rhys parameter can be determined from the line strength ratio, $I_{A_2}/I_{A_1} = I_{0-1}/I_{0-0} = \lambda^2$, where $I_{A_{\bar{\nu}+1}}$ and $I_{\nu-\bar{\nu}}$ correspond to the intensities of the transitions in absorption and emission, respectively. In the later course of this work, special attention will be paid to these ratios, since they change upon aggregation and contain information on, e.g., the interaction between molecules and the coherence of exciton wave functions [35].

NON-RADIATIVE TRANSITIONS Non-radiative transitions are isoenergetic transitions that take place from the 0-th vibrational level of the initial electronic state (or thermally populated vibrational levels) to the k-th isoenergetic vibrational state of the final electronic state and therefore are shown as horizontal arrows in energy diagrams. Usually, this transition is followed by the rapid irreversible dissipation of vibrational energy to the environment within

one electronic state (thermal relaxation, vibrational relaxation). These non-radiative transitions are shown as vertical arrows in energy diagrams [51], but are not discussed further here. The non-radiative transition rate can be approximately described using Fermi's golden rule (Eq. (2.6)) and is given, according to Robinson and Frosch [57, 58, 63, 64], by

$$k_{if} = \frac{2\pi}{\hbar} f_{\nu,\nu}^2 \langle \Phi_{el,f} | \hat{H}' | \Phi_{el,i} \rangle \delta(E_f - E_i). \quad (2.12)$$

Here, $f_{\nu,\nu}^2$ is the Franck-Condon factor and $\langle \Phi_{el,f} | \hat{H}' | \Phi_{el,i} \rangle$ is the matrix element of the perturbation between the initial and the isoenergetic final state $|f\rangle$, with energies E_i and $E_f = E_i$, respectively. The delta function $\delta(E_f - E_i)$ ensures energy conservation [43, 57, 65].

If the involved states have both the same spin quantum number, then \hat{H}' is the nuclear kinetic energy operator and the transition is called internal conversion [51, 57]. The coupling terms between electronic and nuclear wave functions are no longer negligible, i.e., electronic and nuclear motion can no longer be separated. This means, the wave functions given in equation (2.3) are not actually stationary states of the system and transition between them can occur induced by nuclear motion. Consequently, different electronic states are mixed by the nuclear movement [43, 44].

Another reason for the deviation from the Born-Oppenheimer approximation is the spin-orbit coupling. If the involved states have different spin quantum numbers and \hat{H}' is a spin-orbit coupling operator the transition is called intersystem crossing [43, 51, 57, 58]. Additionally, the matrix element, and consequently the rate of intersystem crossing, depends also on the involved states, as outlined qualitatively by El-Sayed [43, 57, 58, 66–68]. Hence, to achieve an efficient intersystem crossing, changes in spin must be compensated by a corresponding change in angular momentum to guarantee the conservation of the total angular momentum. [43, 57, 58, 67].

As a limitation to this discussion, it should be noted that for almost all molecules the wave function of a state is usually a superposition consisting of odd and even parity and different spin states. Thus, practically every transition is possible, even with partly very low probabilities.

2.2.2 Jablonski diagram

In summary, the basic transitions can be discussed in an energy level scheme known as Jablonski diagram (see Fig. 2.2) [51, 61]. In this diagram, states are arranged vertically in ascending energetic order and horizontally according to their total spin quantum number. For most organic molecules, the energetically lowest state is a singlet state denoted by S_0 with an overall spin quantum number of $S = 0$. The energetically higher excited singlet states are denoted by S_1, S_2, \dots . In triplet states, denoted by T_1, T_2, \dots , the overall spin quantum number is $S = 1$. These electronic states are accompanied by vibrational states

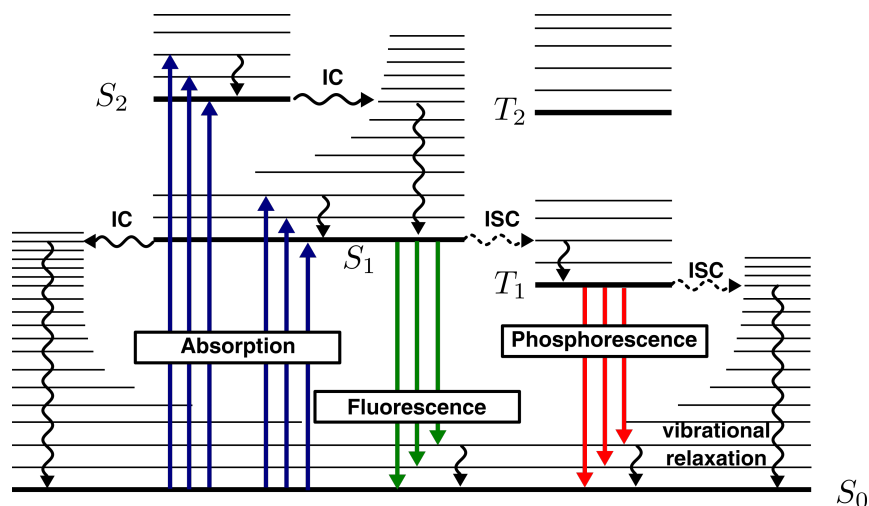


Figure 2.2: Jablonski diagram for a typical organic molecule. Radiative transitions are drawn as solid lines and non-radiative transitions are illustrated as curved lines. IC stands for internal conversion (solid curved horizontal lines) and ISC for intersystem crossing (dashed curved horizontal lines). Vibrational relaxation is depicted with curved vertical lines. For reasons of clarity, vibrational levels are not labeled. For further details, see text. Adapted from [61].

(ν_i). Typical vibrational energies are in the range of 100–300 meV, and hence at room temperature mainly the lowest vibrational level of the electronic ground state is occupied [43, 51], since the thermal energy ($\approx 26\text{meV}$) is not sufficient to occupy energetically higher states. As explained above, transitions between states can only occur if the transition rates are not zero. Typically, by absorbing a photon (on a time scale of 10^{-15} s), the molecule is excited to an vibrational state of S_1 , S_2 , Then, it usually relaxes non-radiatively within $10^{-13} - 10^{-11}$ s (so-called vibrational relaxation) into the energetically lowest vibrational state of S_1 .

From this state a radiative transition to a vibrational state of the electronic ground state S_0 can take place, which is approximately determined by the Franck-Condon factor. This spin-allowed process is called fluorescence. Typical fluorescence lifetimes are in the order of nanoseconds. Subsequently, a vibrational relaxation into the energetically lowest vibrational state ($\nu = 0$) of the electronic ground state S_0 takes place. Due to relaxation processes (mainly due to solvent relaxation) and interaction of the molecule with its environment, the 0-0 transition in emission is red-shifted with respect to the A_1 transition in absorption. This shift is called Stokes-shift.

Another possible process is the non-radiative internal conversion from S_1 to S_0 , which is accompanied by subsequent vibrational relaxation.

Furthermore, a non-radiative transition from the S_1 to the T_1 level can take place by means of intersystem crossing. The subsequent spin-forbidden relaxation from the triplet state to the ground state takes place either via emission of

a photon (so-called phosphorescence) or non-radiatively by intersystem crossing and subsequent vibrational relaxation. Due to the low transition probabilities between singlet and triplet states, the excited state lifetimes of triplet states are significantly longer compared to those of singlet states, ranging from microseconds to a few minutes. Because of their long lifetime, triplet states are very efficiently deactivated non-radiatively, e.g., by collision with solvent molecules, due to molecular motion, and thermal perturbations [61, 69].

2.2.3 Photophysical parameters

Molecular properties, such as the excited state lifetime and the quantum yield of a process, are determined by the rates explained above. In the following, the radiative deactivation of an excited state is described by the rate constant k_r and the non-radiative deactivation by the rate k_{nr} . Here, k_{nr} includes all non-radiative processes, i.e., is a sum over internal conversion k_{ic} , intersystem crossing k_{isc} , and energy transport processes k_{ET} in more complex systems [49, 51, 61]. The depopulation of an excited state is governed by the sum of all decay rates. The inverse of the total decay rate is defined as the excited state lifetime

$$\tau = \frac{1}{k_r + k_{nr}}, \quad (2.13)$$

which is the average time a molecule remains in its excited state before it returns into lower energy states, e.g., the electronic ground state.

The quantum yield of a process indicates the probability how often a certain event out of several possible processes occurs, i.e., it is defined by the ratio of the rate constant of the process of interest to the total rate constant [51, 60, 61]. Concerning radiative quantum yields, a distinction is made between fluorescence and phosphorescence. The fluorescence quantum yield (Θ_F) is a measure of the fraction of excited molecules that typically return from an singlet excited state S_1 to the ground state S_0 via emission of a fluorescence photon (see above and Fig. 2.2), i.e,

$$\Theta_F = \frac{k_{r,S_1}}{k_{r,S_1} + k_{nr,S_1}} = k_{r,S_1} \tau_{S_1}. \quad (2.14)$$

Here, τ_S is the lifetime of the excited singlet state S_1 . Since ordinarily, the triplet excited state T_1 is generated via intersystem crossing from initially excited singlet states, for the phosphorescence quantum yield the intersystem crossing yield has to be taken into account [51, 61, 70]. The quantum yield of intersystem crossing (Θ_{isc}) describes the conversion efficiency from a singlet excited state into a triplet state [51, 61] and is given by

$$\Theta_{isc} = \frac{k_{isc}}{k_{r,S_1} + k_{nr,S_1}}. \quad (2.15)$$

The quantum yield of phosphorescence (Θ_P) is thus given by

$$\Theta_P = \frac{k_{r,T_1}}{k_{r,T_1} + k_{nr,T_1}} \Theta_{isc}. \quad (2.16)$$

Typical values for these quantum yields can be found elsewhere [51, 61].

Since transitions are stochastic processes, the depopulation of an excited state can be described using a rate equation. In the simplest case one gets

$$\frac{\partial n(t)}{\partial t} = -\frac{1}{\tau}n. \quad (2.17)$$

Here, $n(t)$ is the time-dependent density of excited molecules. In particular, the fluorescence intensity $I(t)$, which is proportional to the number of excited molecules in S_1 , follows a simple exponential decay according to equation (2.17) [51]

$$I(t) \propto \exp(-t/\tau_{S_1}). \quad (2.18)$$

The experimentally measured intensity decay is an average over a large number of excitation-emission cycles, that can be recorded for example using the method of time-correlated single photon counting. If one averages over a distribution of lifetimes, which is the case, e.g., when measuring multiple molecular species or a sample that shows inhomogeneities in the structure or the environment, more complex expressions are required. Therefore, the decay of the intensity is often described with a multiexponential approach [60].

2.3 COLLECTIVE EXCITED STATES

Organic electronics and their applications in displays, renewable, clean energy, and wearable technology are based on electronic excitation in organic aggregates, films, and crystals [10, 18, 19, 35]. Intermolecular interactions, which are strongly correlated to the mutual arrangement of the densely packed molecules in these materials, lead to the formation of collective excited states, i.e., the excitation energy is coherently shared by many molecules [22, 35, 71]. Moreover, intermolecular interactions and the collective excited states give rise to changed optical properties and play an important role in energy transport processes within multi-chromophoric systems [35, 71–74]. Generally, the nature of electronically excited states and their dynamics are governed by a complex interplay of parameters, such as the intermolecular interactions, electronic and structural disorder, and the coupling between the system and the environment [7, 22, 72].

In this context, Jelley [75] and Scheibe [76] were the first who realized, that aggregation influences the optical properties of a molecular system. Here, the term aggregate is used to characterize a system that consists of non-covalently bound molecules [47]. Upon increasing the concentration of pseudo-isocyanine (PIC), they observed that the absorption spectrum of PIC-molecules disappears and is replaced by a narrower, red-shifted absorption band. These changes were attributed to the aggregation of PIC molecules and the formation of collective excited states.

The basic concepts for understanding the relationship between morphology and photophysical properties were developed by the photochemist Michael Kasha

[22, 35, 71, 77, 78]. Kasha showed that for molecular side-by-side stacked dimers the absorption maximum is blue-shifted and the radiative decay is suppressed, while dimers stacked in a head-to-tail fashion exhibit a red-shifted absorption and an enhanced radiative decay compared to the isolated molecule. Extensions of the theory of Kasha, for example, the integration of charge-transfer states and electron-phonon coupling, are part of current research and summarized in the review of Hestand and Spano [35].

2.3.1 Supramolecular systems

To investigate and understand the properties of collective excited states, artificial supramolecular nanostructures with tailored properties can be important model systems. In this context, supramolecular chemistry offers the opportunity to control the arrangement of molecules within aggregates using non-covalent interactions [18, 22, 24, 25, 79–81], which can result in polymer-like chains termed as supramolecular polymers [82]. Thus, in principle, one can manipulate the interaction between molecules and influence the properties of the collective excited states [22, 83].

The building blocks, i.e., the individual molecules, are designed to inherit the capability of forming non-covalent interactions, such as hydrogen-bonding, $\pi - \pi$ -stacking, Van-der-Waals, and hydrophilic/-phobic interactions. These non-covalent interactions are the driving forces in self-assembly and determine the thermodynamically stable structure [25, 81, 84–86]. Even small changes in the molecular structure can have a major impact on the associated intermolecular interactions and therefore ultimately on the supramolecular architecture and the optical properties of the system. Since the involved non-covalent interactions are significantly weaker compared to covalent bonds, self-assembly is usually a dynamic process and the formed bonds can be easily created and released. Due to this reversibility of non-covalent interactions, supramolecular polymers often display self-healing effects [24, 25, 82, 87].

In addition to the molecular design, processing conditions, such as changes in temperature (T), concentration or solvent, are equally important and can drive the aggregation in certain directions [24, 25, 80, 87]. Thermodynamically, self-assembly is an interplay between enthalpy and entropy. The increase in enthalpy (ΔH), associated with the intermolecular forces, must compensate for the entropic losses ($-T\Delta S$) associated with higher order within an aggregate, i.e., the changes in the Gibbs free energy should be negative upon aggregation $\Delta G = \Delta H - T\Delta S < 0$. For spontaneous self-assembly, the decrease in entropy, $\Delta S < 0$, due to the higher organization, must be compensated by the enthalpy term that holds the structures together. This highly dynamic organization process is not completed until the energetically most stable state is reached. Depending on the kinetics, the system may fall into thermodynamic traps and may even not reach the state of the global energy minimum, i.e., the final state depends strongly on the processing conditions [25, 87–91].

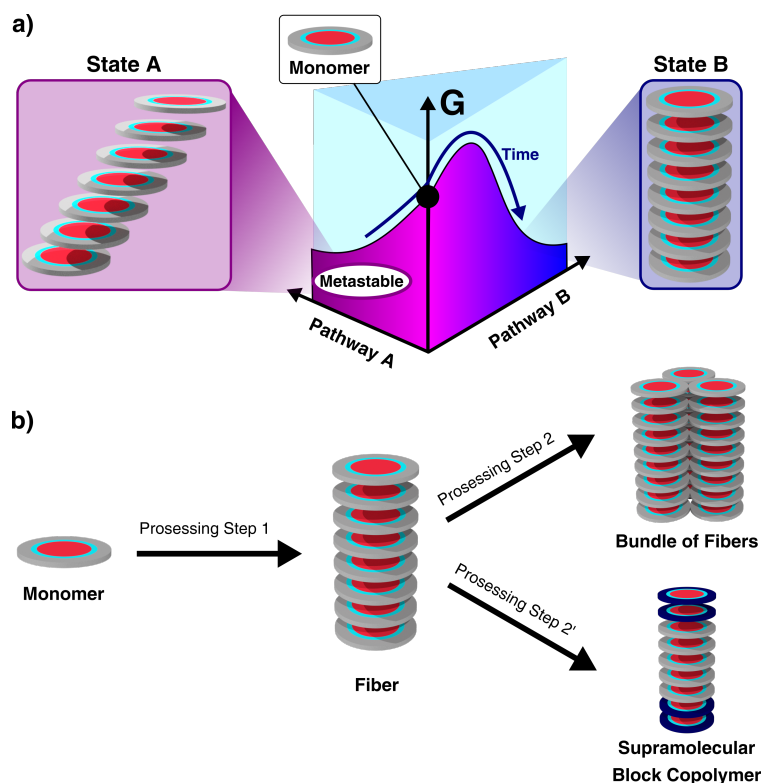


Figure 2.3: Self-assembly of a building-block. a) Pathway complexity: Self-assembly free energy landscape of a monomer with different pathways, resulting in nanostructures with different morphologies and optical properties. A metastable state A is kinetically formed, but over time this states transforms into the stable state B. Adapted from [91]. b) Multistep approach. Multiple processing steps can lead to the formation of hierarchical architectures or multi-component assemblies. For example, starting from the monomer, fibers can be produced, which in turn can be further processed into bundles or in supramolecular block copolymers via admixing of a second building-block.

Therefore, because of kinetic and thermodynamic considerations, different pathways for self-assembly may be accessible. This phenomenon, referred to as pathway complexity, results in thermodynamically and kinetically stable supramolecular aggregates with different molecular packings and thus significantly different photophysical properties [25, 81, 86, 90–92]. For example, Fukui et al. have demonstrated that self-assembly of the same building-block can follow different pathways leading either to kinetically trapped nanoparticles or thermodynamically stable nanofibers [91] (see Fig. 2.3a).

In addition, multiple steps of processing (multistep approach) can be advantageous for the construction of model systems [29, 85, 93], since ,e.g., each hierarchical structure [31, 33, 94, 95] can be examined and understood individually [10, 24]. This can, on the one hand, simplify the identification of the architectures and, on the other hand, make an understanding of the involved

interactions easier [24]. For instance, Wagner et al. [85] have recently demonstrated, that mixing aggregates formed from two distinct building blocks can lead to the formation of supramolecular block copolymers (see Fig. 2.3b).

In summary, the desired material properties depend not only on the molecule itself (information stored in the covalent framework) but also on the kinetics and thermodynamic reactions, i.e., the experimental processing protocols [24, 25].

To study self-assembly and the changed optical signatures due to the formation of collective excited states upon aggregation, spectroscopic techniques are important tools [7, 22, 35, 96]. The following sections focus on the description of collective excited states, their optical signatures, and energy transport mechanisms in molecular aggregates.

2.3.2 Frenkel excitons

As a starting point to explain the concept of collective excited states, a molecular aggregate is assumed to consist of N equidistantly arranged identical molecules (for this section see [22, 47]). Although a molecule usually exhibits many excited states, its energy level structure is approximated as a two-level system with a ground state $|g\rangle$ and an excited state $|e\rangle$, energetically separated by the energy E_0 . Neglecting the nuclei degree of freedom, i.e., a rigid molecular framework is assumed, these two states correspond to the ground S_0 and first electronically excited state S_1 of the molecules (see section 2.2). Furthermore, the exchange of electrons between monomers is neglected (tight-binding approximation), the Born-Oppenheimer approximation is used to factorize the wave functions and a rigid lattice is assumed [97]. In other words, the electronic structure of the individual molecules stays approximately unchanged, i.e., the molecules keep their identity, and their positions are fixed [7]. The Hamiltonian for N non-interacting molecules is represented by

$$\hat{H}_0 = \sum_{n=1}^N E_0 |n\rangle \langle n|, \quad (2.19)$$

where $|n\rangle$ describes a wave function in which only molecule n is excited while all other $N - 1$ molecules remain in their ground state. Since the probability of being in the excited state is the same for all molecules, this wave function is N -fold degenerate.

However, due to intermolecular interactions this degeneracy is cancelled and the optical properties are significantly changed with respect to the individual, non-interacting molecules due to the formation of collective excited states. The Hamiltonian for a linear aggregate with N -coupled identical molecules is [22, 35, 51]

$$\hat{H} = \sum_{n=1}^N (E_0 + D) |n\rangle \langle n| + \sum_{n=1}^N \sum_{m \neq n}^N J_{nm} |n\rangle \langle m|. \quad (2.20)$$

Here, the first term describes the excitation energies, i.e., E_0 is the transition energy of the monomer's $S_0 \rightarrow S_1$ transition and D is the gas-to-crystal shift caused by London dispersion forces, such as Van-der-Waals interactions, between the molecule and its environment [5, 35, 98].

The second term accounts for the interaction energies between the molecules. $J_{mn} = \langle n|V(nm)|m \rangle$ is the matrix element that describes the interaction between the molecules n and m . This matrix element is also known as the transfer integral or coupling between the molecules. In particular, the interaction and the exchanges of electronic excitations between two molecules n and m is mediated by the Coulomb interaction [7, 50]

$$V(nm) = \frac{1}{4\pi\epsilon_0\epsilon} \int \int \frac{\rho_n(\mathbf{r}')\rho_m(\mathbf{r}'')}{|\mathbf{r}' - \mathbf{r}''|} d\mathbf{r}' d\mathbf{r}'' \quad (2.21)$$

ρ_n and ρ_m are the charge distributions of molecules n and m , respectively, which depend on the electronic coordinates \mathbf{r} and $\epsilon_0\epsilon$ reflects the electric permittivity of the surrounding environment. If the extension of the charge distributions of the individual molecules is much smaller than the intermolecular distances $|\mathbf{R}_{nm}| = |\mathbf{r}_m - \mathbf{r}_n|$ between the centers of masses of the molecules (\mathbf{r}_n and \mathbf{r}_m), the leading term of $V(nm)$ for an electronically neutral molecule can be specified in the dipole-dipole approximation [22, 47, 50]. Under this approximation, the coupling J_{nm} reads as

$$J_{mn} = \frac{\kappa_{nm}}{4\pi\epsilon_0\epsilon} \frac{|\boldsymbol{\mu}_n||\boldsymbol{\mu}_m|}{|\mathbf{R}_{nm}|^3}, \quad (2.22)$$

where $\boldsymbol{\mu}_n = \langle g_n|\hat{\mathbf{p}}|e_n \rangle$ is the transition dipole moment of the i -th molecule and κ_{nm} is the so-called orientation factor defined as

$$\kappa_{nm} = \mathbf{e}_n \mathbf{e}_m - 3(\mathbf{e}_{nm} \mathbf{e}_n)(\mathbf{e}_{nm} \mathbf{e}_m). \quad (2.23)$$

The unit vector \mathbf{e}_n (\mathbf{e}_m) points in the direction of the transition dipole moment $\boldsymbol{\mu}_n$ ($\boldsymbol{\mu}_m$) and \mathbf{e}_{nm} along the distance vector \mathbf{R}_{nm} . Thus, excited molecules interact with each other via a Coulomb interaction between their transition dipole moments [7]. Moreover, according to equation (2.22), the coupling between molecules strongly depends on the mutual arrangement of the building blocks, i.e., the distance and the orientation between the molecules. Hence, for different orientations of the transition dipole moments, the values of κ_{nm} range between -2 and 1 . For example, for a collinear head-to-tail arrangement $\kappa_{nm} = -2$ and the sign of the interaction energy is negative, defining a J-aggregate. Instead, for parallel stacked transition dipole moments, a so-called cofacial arrangement, $\kappa_{nm} = 1$ and the interaction energy is positive, defining an H-aggregate (see Fig. 2.4). Note that in this section and in the following a dominant Coulomb coupling is assumed, which is only mediated through space. However, for closely spaced molecules, as it is common for molecular π -stacks, the intermolecular distances are often smaller than the intramolecular distances and so-called short-range, charge-transfer-mediated couplings due to overlap of the wave functions can occur [35, 71].

As a consequence of the interaction between the molecules, the wave functions $|n\rangle$ are no longer eigenstates of the total Hamiltonian \hat{H} . Considering only nearest neighbor interactions J_0 and assuming periodic boundary conditions, the new eigenstates and eigenenergies of the coupled system are obtained via diagonalizing the Hamiltonian and are given by [22, 35, 47, 50, 51]

$$|k\rangle = \frac{1}{\sqrt{N}} \sum_{n=1}^N e^{ikn} |n\rangle, \quad k = 0, \pm 2\pi/N, \pm 4\pi/N, \dots, \pi \quad (2.24)$$

with the eigenenergies

$$E_k = E_0 + D + 2J_0 \cos(k). \quad (2.25)$$

The new eigenstates are superpositions of the locally excited states $|n\rangle$ and hence the excitation is delocalized over all N spatially separated molecules, i.e., the excitation is shared coherently with all molecules. Generally, delocalization can lead to profound changes in optical as well as energy transport properties (see also section 2.4) and serves as a signature of quantum coherence in aggregates [7]. The new eigenstates are called *Frenkel excitons* [47] and according to equation (2.25) the N -fold energy degeneracy is cancelled. Note that also for open boundary conditions and finite sizes of the aggregates, the general conclusions are not affected [22]. Figure 2.4 shows the splitting of the energy levels caused by the coupling and the resulting exciton band of width $W = 4|J_0|$. This width is defined as the energy difference between the energetically highest and lowest exciton state and is called free exciton bandwidth.

To understand the optical properties of an aggregate, the transition dipole moments between the ground- and exciton states (Eq. (2.24)) must be considered

$$\boldsymbol{\mu}(k) = \langle G | \hat{\mathbf{M}} | k \rangle = \frac{1}{\sqrt{N}} \sum_{n=1}^N \exp(ikn) \boldsymbol{\mu}_n. \quad (2.26)$$

Here, $\hat{\mathbf{M}} = \sum_n \hat{\mathbf{p}}_n$ is the total transition dipole operator, given by the sum of the molecular dipole operators $\hat{\mathbf{p}}$ and $|G\rangle$ is the overall ground state wave function, which is approximated as the product of the individual ground state wave functions of the molecules $|G\rangle = \prod_n |g_n\rangle$ [5, 35, 49, 51]. The transition dipole moments $\boldsymbol{\mu}(k)$ of the aggregate are proportional to the vector sum of the transition dipole moments of the individual molecules. In particular, due to the electronic coupling, the dipole moments are redistributed to only a few states, e.g., from equation (2.26) it follows, that $k = 0$ inherits the maximal dipole moment $\boldsymbol{\mu}(k = 0) = \sqrt{N} \boldsymbol{\mu}$, since the phase of the wave function coefficients does not change along the entire aggregate (see Eq. (2.24)). The transition dipole moment is enhanced by \sqrt{N} relative to the monomer [35], meaning the transition dipole moments of the coupled monomers interfere constructively. In the $|k = \pi\rangle$ state, the phase alternates from molecule to molecule, resulting in a cancelled transition dipole moment $\boldsymbol{\mu}(k = \pi) = 0$ [35]. Depending on the sign

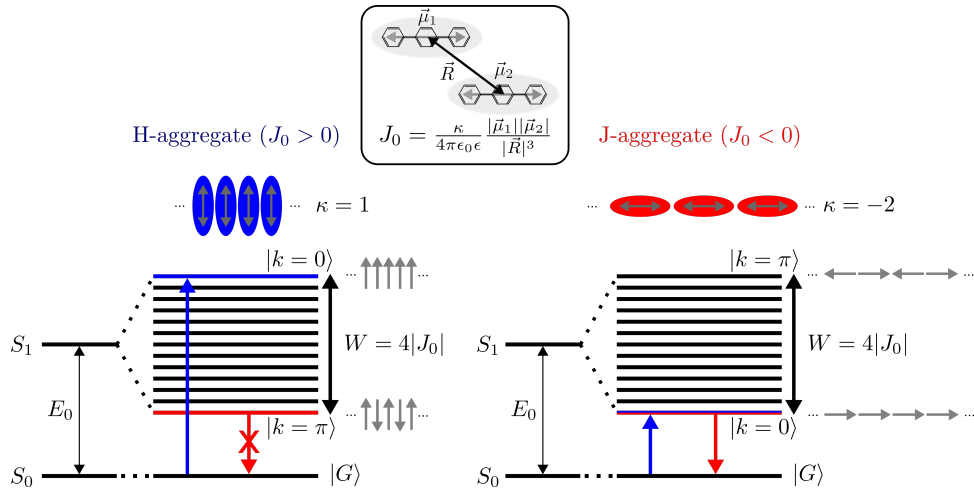


Figure 2.4: Energy diagram for linear aggregates with periodic boundary conditions and next-neighbor interaction J_0 . The free exciton bandwidth is $W = 4|J_0|$. For H-aggregates, the $|k = 0\rangle$ state is at the top of the band and the $|k = \pi\rangle$ state is at the bottom. For J-aggregates the opposite is the case. Only transitions to the $|k = 0\rangle$ state are accessible from the ground state $|G\rangle$. Emission takes place from the lowest energy exciton state. This transition is forbidden for H-aggregates. The grey arrows illustrate the phase relationship of the transition dipole moments from molecule to molecule for the $|k = 0\rangle$ and $|k = \pi\rangle$ states. The ellipses above show the morphological arrangement of the molecules with the orientation of their transition dipole moments with respect to each other. The gas-to-crystal shift D is set to zero. The inset illustrates the dependence of the dipole-dipole interaction on the mutual arrangement of the molecules.

of the coupling, i.e., whether J- or H-aggregates are formed, these states are located at the bottom or at the top of the exciton band.

Figure 2.4 shows the energy diagram for ideal H- and J-aggregates and the possible optical transitions. Absorption occurs in the $|k = 0\rangle$ state since this state exhibits the combined dipole moment. For J-aggregates, the sign of the coupling is negative ($J_0 < 0$) and states with a dipole moment (i.e. $|k = 0\rangle$) to the ground state $|G\rangle$ are located at the bottom of the exciton band. The opposite is true for H-aggregates ($J_0 > 0$). For J-aggregates this results in a redshift of the main absorption peak compared to the monomer spectrum, while for H-aggregates a blueshift of the absorption peak is observed [22, 35]. Note that these shifts are no reliable criteria for the identification of whether the aggregate is of H- or J-type, since the energy shift D can be larger than the exciton bandwidth [5, 98].

According to Kasha's rule, emission takes place from the energetically lowest excited state for low temperatures. For J-aggregates, emission occurs from the $|k = 0\rangle$ state, which features a N-fold increased radiative rate with respect to the decay rate of the monomer. Therefore, this state is referred to as a superradiant state with lifetimes as short as a few picoseconds. Ideally, there is no Stokes shift

[22, 35]. In H-aggregates, rapid relaxation from the highest energy exciton state $|k = 0\rangle$ populates the $|k = \pi\rangle$ state, and hence the transition to the ground state is optically prohibited [22, 35, 78]. Therefore, perfectly ordered H-aggregates are non-emissive and emission is only possible in the presence of symmetry breaking disorder or vibronic coupling [22, 35].

2.3.3 Frenkel polarons: Expanded theory of H- and J-aggregates

As already mentioned in section 2.2, both absorption and emission spectra of organic molecules show a vibronic progression due to electron-phonon coupling to vibrational modes (e.g., a carbon-bond stretching modes with energy ω_0 between 0.15-0.2 eV (1200-1600 cm^{-1})), characterized by the Huang-Rhys parameter. Since molecules are the building blocks of aggregates, these vibrational modes can also be found in the aggregate spectra. Hence, the simple two-level approximation of molecules, as used above, is not sufficient and the influence of electron-phonon coupling on the aggregate spectra has to be included.

The theory of Spano and co-workers considers the coupling of exciton states to an effective molecular vibration for H- and J-aggregates. Thus, a quantitative understanding of the vibrational structures of aggregate spectra is obtained. Furthermore, the theory explains how the Franck-Condon progression is modified as a function of the interaction between the molecules and how information about the structural arrangement, exciton bandwidth, disorder, and coherence length can be obtained [5, 35, 51]. The following section summarizes the results of [74, 98–101]. A more detailed summary can be found in the review by Hestand and Spano [35].

THEORETICAL DESCRIPTION Each molecule is described as a two-level system (S_0, S_1), which couples to one (effective) intramolecular vibration with the vibrational energy ω_0 . The ground and excited state potential energy surfaces are displaced harmonic potentials (see Fig. 2.5 and Fig. 2.1). This shift is quantified by the Huang-Rhys parameter λ^2 . Furthermore, each aggregate consists of N equally spaced identical monomer units.

The key element of this theory is the expansion of the exciton wave functions based on one- and two-particle basis states (see Fig. 2.5). A one-particle state $|n, \tilde{\nu}\rangle$ consists of one vibronically excited molecule n , i.e., molecule n is in its electronically excited state with $\tilde{\nu}$ vibrational quanta while all other molecules of the aggregate remain in their vibrationless electronic ground state. For two-particle states $|n, \tilde{\nu}; n', \nu'\rangle$, in addition to the vibronic excitation of molecule n , molecule $n' (\neq n)$ is in a vibrationally excited state $\nu' \geq 1$ of its electronic ground state. These states are necessary to describe the spatial impact of the vibronically excited molecule on its environment and thus a collective excitation, i.e., the deformation of the aggregate with respect to the central excitation.

Without electronic coupling, the states shown in Fig. 2.5 are eigenstates of \hat{H}_0 , describing a system of N non-interacting molecules. Hence, in the one- and

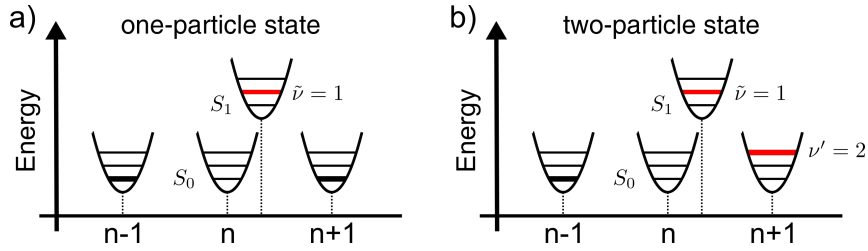


Figure 2.5: Examples of two basic excitations in organic aggregates within the Spano model. a) One-particle state: Here only molecule n is vibronically excited ($|n, \tilde{\nu} = 1\rangle$), while all other molecules remain in the vibrationless ground state. b) Two-particle state: In addition to the vibronic excitation of the molecule n , one molecule $n' \neq n$ is in its vibrationally excited ground state ($|n, \tilde{\nu} = 1; n + 1, \nu' = 2\rangle$). The excitations are indicated in red. Adapted from [35, 74, 98].

two-particle basis set, \hat{H}_0 is diagonal. The eigenenergies of one-particle ($E_{n,\tilde{\nu}}$) and two-particle states ($E_{n,\tilde{\nu};n',\nu'}$) are given by

$$E_{n,\tilde{\nu}} = \omega_{0-0} + D + \Delta_n + \tilde{\nu}\omega_0, \quad (2.27)$$

and

$$E_{n,\tilde{\nu};n',\nu'} = \omega_{0-0} + D + \Delta_n + (\tilde{\nu} + \nu')\omega_0. \quad (2.28)$$

In this equations ω_{0-0} is the molecular 0-0 ($S_0 \rightarrow S_1$) transition energy, D is the gas-to-crystal shift due to Van-der-Waals interactions between the molecules and their environment, Δ_n accounts for a shift in the transition energies of the monomers, which allows the simulation of energetic disorder within the aggregate, and ω_0 is the vibrational energy. In analogy to the concepts of Frenkel excitons, the Coulomb interactions between the molecules have a delocalizing effect on the excitations and the above mentioned one- and two-particle states are no longer eigenstates of the system. The Hamiltonian \hat{H} for the coupled system can be written as

$$\hat{H} = \hat{H}_0 + \hat{H}_{ex}, \quad (2.29)$$

with

$$\hat{H}_{ex} = \sum_{n,m} J_{nm} |n\rangle \langle m|. \quad (2.30)$$

Here again, \hat{H}_0 is the diagonal part of \hat{H} containing the above defined eigenenergies of the basis set (Eq. (2.27) and Eq. (2.28)). The off-diagonal elements are determined by \hat{H}_{ex} , represented in the basis of pure electronic states $|n\rangle$ (see Frenkel excitons). Further, J_{nm} is the electronic coupling between the n -th and m -th molecule. In the following, the calculations are simplified by assuming only next-neighbor interaction J_0 . Due to the coupling \hat{H}_{ex} , one- and two-particle states are mixed. Therefore, within the two particle basis set approximation,

the α -th eigenstate of the aggregate can be approximated as a superposition of one- and two-particle states,

$$|\Psi^\alpha\rangle = \sum_{n,\tilde{\nu}} c_{n,\tilde{\nu}}^\alpha |n, \tilde{\nu}\rangle + \sum_{n,\tilde{\nu}} \sum_{n',\nu'} c_{n,\tilde{\nu};n',\nu'}^\alpha |n, \tilde{\nu}; n', \nu'\rangle, \quad (2.31)$$

where the wave function coefficients c_j^α are obtained via diagonalization of the Hamiltonian \hat{H} . Note that higher order contributions (e.g., the three-particle approximation) have negligible effect on absorption and emission within the weak-to-intermediate exciton coupling regime (see below) [35, 98].

In what follows, the reduced absorption and emission spectra are derived. That is, the pure dipole strengths are shown, as conveniently used in the literature [35]. Therefore, the respective photon density of states are neglected via suppressing the $n(\omega)\omega$ dependence in equation (2.32) and by suppressing the $n(\omega)^3\omega^3$ dependence in equation (2.33) [35] (see also section 2.2).

The absorption spectrum $A(\omega)$ derives from the sum over all allowed transitions from the vibrationless ground states $|G\rangle$ to all eigenstates $|\Psi^{(\alpha)}\rangle$ with the energies $\omega^{(\alpha)}$, i.e.,

$$A(\omega) = \frac{1}{N\mu^2} \sum_{\alpha} |\langle G | \hat{M} | \Psi^{(\alpha)} \rangle|^2 \Gamma(\omega - \omega^{(\alpha)}). \quad (2.32)$$

Here, \hat{M} is the total transition dipole operator of the aggregate, μ is the magnitude of the transition dipole moment of a monomer and the dividing with N normalizes the spectrum to the number of molecules [35]. $\Gamma(\omega)$ is the homogeneous line shape function, taken to be Gaussian $\Gamma(\omega) = \exp(-(\omega/\sigma_{hom})^2)$ [35, 98]. Since the spectral widths at room temperature are often dominated by static, inhomogeneous broadening, the details of homogeneous broadening are not that important [35]. Rather, an average over a distribution of transition energies, chosen randomly from a distribution function (usually taken to be Gaussian), is needed [35]. The detectable bands in the absorption spectrum are referred to as $A_{\tilde{\nu}+1}$ ($\tilde{\nu}=0,1,\dots$) (see Fig. 2.6 and Fig. 2.7), analogous to the optically accessible states $|A_{\tilde{\nu}+1}\rangle$ of the monomer (see Fig. 2.1). Thermally populated vibrational states of the electronic ground state are neglected since the considered vibrational energy exceeds the thermal energy at room temperature ($\omega_0 > k_b T$, i.e., $\approx 170\text{meV} > 26\text{meV}$).

At zero temperature ($T = 0\text{K}$), according to Kasha's rule, emission originates only from the energetically lowest excited state $|em\rangle$ with energy ω_{em} . The spectral shape is determined by

$$S(\omega) = \sum_{v_t=0,1,2,\dots} I^{0-v_t} \Gamma(\omega - \omega_{em} + v_t\omega_0) \quad (2.33)$$

and I^{0-v_t} are dimensionless line strengths, given by

$$I^{0-v_t} = \mu^{-2} \sum_{T(v_t)} |\langle em | \hat{M} | T(v_t) \rangle|^2. \quad (2.34)$$

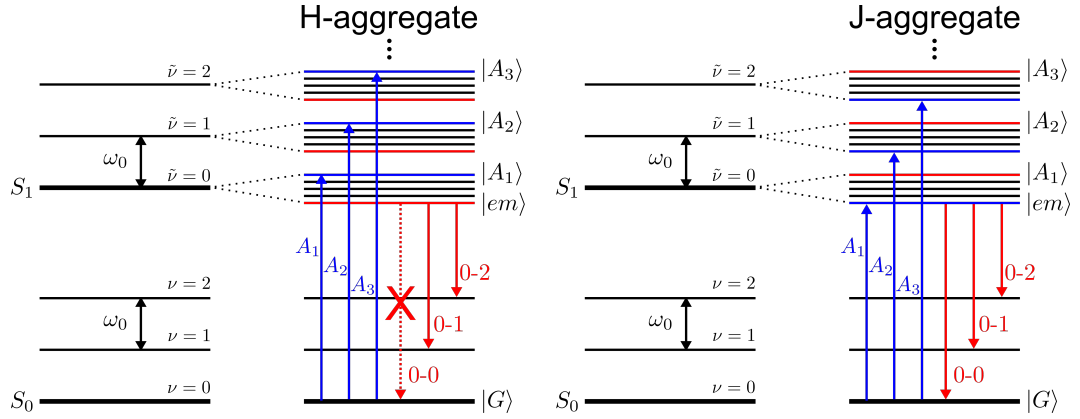


Figure 2.6: Simplified energy level scheme in the Spano picture for the weak coupling regime in ideal H- and J-aggregates. The corresponding energy diagram of the monomer is shown on the left side. In the aggregate, $|k=0\rangle$ states are shown in blue, while red drawn levels represent $|k=\pi\rangle$ states. Only transitions into $|k=0\rangle$ states are optically accessible from the vibrationless ground state $|G\rangle$ (absorption, blue arrows). For H-(J)-aggregates, these states are located at the upper (lower) edge of the bands. For $T=0K$, emission takes place from the energetically lowest exciton state $|em\rangle$ (red arrows). In H-aggregates, the transition from $|em\rangle$ to the vibrationless ground state is optically forbidden. Adapted from [98]. For details, see text.

The terminal states, $|T(\nu_t)\rangle$, are vibrational excited electronic ground states with a total of $\nu_t = \sum_n \nu_n$ vibrational quanta and importantly these vibrational quanta can be distributed over all N molecules [98]. At higher temperatures $T \neq 0K$, emission stems no longer exclusively from the lowest-energy exciton state $|em\rangle$, since the electronic coupling gives rise to energetically densely packed exciton bands (see Fig. 2.6). This means, energetically higher exciton states can be thermally excited and participate in the emission. Therefore, the emission spectrum is obtained by averaging over a Boltzmann distribution of the emitting, thermally accessible states $|\Psi^\alpha\rangle$.

Figure 2.6 shows the schematic energy diagram with allowed and forbidden transitions for ideal (disorder-free) aggregates at temperature $T=0K$. Compared to the Frenkel exciton picture, each vibronic state of the molecule splits into a band, which is characterized by its vibrational quantum number. Due to electron-phonon coupling, the energetic widths W' of the bands are reduced by approximately the respective Franck-Condon factor compared to the free exciton bandwidth $W = 4|J_0|$, i.e., $W' \approx W \frac{\lambda^{2\tilde{\nu}}}{\tilde{\nu}!} e^{-\lambda^2}$.

Depending on the coupling strength, these bands may overlap. According to Spano's notation, the coupling strength is defined via the free exciton bandwidth $W = 4|J_0|$ and the relaxation energy $E_{rel} = \lambda^2 \omega_0$. $W > \lambda^2 \omega_0$, indicates the strong coupling limit, in which bands overlap and a cumulative band is formed. Otherwise, in the weakly coupled limit ($W < \lambda^2 \omega_0$), the bands are separated

(approximately by ω_0 , see Fig. 2.6), making this regime ideal to illustrate the underlying physics of electron-phonon coupling in H- and J-aggregates. Note that in the Frenkel exciton picture the coupling strength is defined differently. The coupling is regarded as strong as long as the interaction is much larger than the difference in site energies of the molecules, i.e., $|J_0| \gg \Delta_n$, whereas $|J_0| \ll \Delta_n$ indicates the weak-coupling limit [22] (see also section 2.4).

For H-(J-)aggregates only transitions from the ground state to the highest-energy (lowest-energy) exciton states of each band are allowed. These optically accessible states are labeled $|A_{\tilde{\nu}+1}\rangle$ ($\tilde{\nu}=0,1,\dots$) and correlate to the $0 - \tilde{\nu}$ transitions of the isolated molecule and in cases where periodic boundary conditions apply these states are $|k=0\rangle$ states in analogy to the Frenkel exciton picture. Consequently, in the absorption spectrum, the optically accessible exciton states show up as a progression of peaks, which are energetically separated by the vibrational energy ω_0 . According to Kasha's rule (for $T = 0K$), emission takes place from the energetically lowest exciton state $|em\rangle$. For ideal H-aggregates (without disorder at temperature $T = 0K$) this state is a $|k = \pi\rangle$ state, but in contrast to the Frenkel exciton picture only the 0-0 transition is symmetry forbidden.

Figure 2.7 shows the calculated spectra for increasing exciton bandwidths W (left for H-aggregates, right for J-aggregates). The absorption spectrum of the isolated monomer is shown in grey, while the theoretically calculated absorption spectrum for aggregates is shown in blue and the emission in red. Here $\lambda^2 = 1$, because for this value the 0-0 and 0-1 transitions of the monomer spectrum are equally intense and hence the influence of the coupling on the aggregate spectra can be demonstrated ideally. As the magnitude of the coupling $|J_0|$ or rather the exciton bandwidth $W = 4|J_0|$ rises, the oscillator strength is increasingly redistributed towards higher (lower) energy bands, i.e., from $|A_1\rangle$ ($|A_2\rangle$) to $|A_2\rangle$ ($|A_1\rangle$), Consequently, in H-(J-)aggregates, the ratio $R_{abs} = \frac{I_{A_1}}{I_{A_2}}$ of the line strength of the first two vibronic peaks A_1 and A_2 decreases (increases) as the coupling $|J_0|$ rises. Hence, a comparison of R_{abs} between the isolated molecule and the aggregate provides a reliable test for H- or J-type aggregation and a direct measure for the magnitude of the electronic coupling.

In addition, for weak coupling a blueshift (redshift) in the H-(J-)aggregate absorption spectrum is observable. This results from the fact that in H-(J-)aggregates mainly the transition to the energetically highest (lowest) exciton state of the bands ($|A_{\tilde{\nu}+1}\rangle$ see Fig. 2.6) is allowed. When W reaches the regime of strong coupling ($W > \lambda^2\omega_0$), only statements about spectral centroids are possible, since the energetic separation between the $|A_{\tilde{\nu}+1}\rangle$ states exceed the vibrational energy ω_0 (cf. $W' \approx W \frac{\lambda^{2\tilde{\nu}}}{\tilde{\nu}!} e^{-\lambda^2}$ and Fig. 2.6). With increasing W , the spectral centroids shift to higher energies for H-aggregates and to lower energies for J-aggregates, due to the redistribution of the dipole strengths mediated by the electronic coupling.

Emission takes place from the lowest-energy exciton state $|em\rangle$ of the lowest-energy vibronic exciton band (for $T = 0K$). In the case of non-rigid molecules

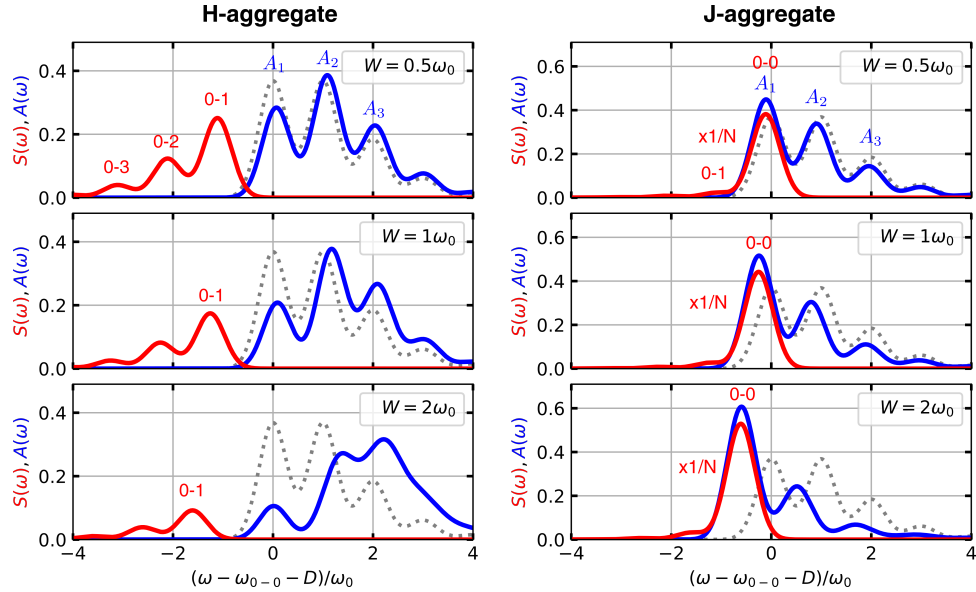


Figure 2.7: Calculated absorption (blue) and emission spectra (red) for ideal H- and J-aggregates (at $T = 0K$) together with the absorption spectrum of the monomer (grey) to illustrate the changed optical properties in aggregates. Linear aggregates of $N=20$ monomers and only next-neighbor interaction are assumed. Further, $\omega_0 = 0.17eV$, $\sigma_{hom} = 0.4\omega_0$, $D = 0$ and $(\Delta_n = 0, \text{ for all } n)$. The exciton bandwidth W (the coupling $|J_0|$) increases from the top to the bottom. The emission spectra of J-aggregates were reduced by the factor N . For details, see text. Adapted from [35].

($\lambda^2 > 0$), only the 0-0 transition ($|em\rangle \rightarrow |G\rangle$) is optically forbidden for H-aggregates (see also Fig. 2.6). This is, in the absence of disorder, $|em\rangle$ possesses a highly symmetric exciton wave function with an alternating sign of wave function coefficients between consecutive monomers, leading to destructive interference of the 0-0 transition dipole moments. Hence, in ideal H-aggregates the 0-0-peak in emission is completely suppressed, while the remaining progression (0-1, 0-2, etc.) is still visible because such a destructive interference cannot occur for the sidebands. As W increases, the emission spectrum shifts towards lower energies, since the width of the exciton bands increases, leading to a reduction of the emitting state's ($|em\rangle$) energy. In addition, sideband emissions strongly decrease, resulting in a diminished fluorescence of H-aggregates. Consequently, the radiative rate $k_r \propto \int \omega^3 S(\omega)$ decreases.

For J-aggregates, the energetically lowest state $|em\rangle$ corresponds to the state $|A_1\rangle$ (see Fig. 2.6). In contrast to H-aggregates, the wave function coefficients between the monomers are in phase and nodeless, leading to constructive interference of the 0-0 transition dipole moments and hence the emitting exciton ($|em\rangle = |k=0\rangle$) exhibits the greatest dipole strength. Therefore, the 0-0 transition is allowed and the transition rate is amplified by the factor N , compared to the isolated monomer. Additionally, since the emitting state corresponds to the

state $|A_1\rangle$, the Stokes shift is negligible. Analogous to the H-aggregates, as W increases (see Fig. 2.7), the emission spectra shift towards lower energies.

DISORDER AND THERMAL EFFECTS Until now, disorder-free aggregates, with excitons being delocalized over the entire aggregate, are considered, i.e., the number of coherently coupled monomers equals N ($N_{coh} = N$). However, in real H- and J-aggregates structural and electronic disorder is unavoidably present and breaks the perfect symmetry, leading to a localization of the exciton wave functions on a smaller part of the aggregate ($N_{coh} < N$). Disorder in the structural arrangement of the assembly gives rise to a variation of the electronic interaction around a mean value [35]. However, within this work, only electronic disorder is considered. The electronic disorder is caused by a variation in the interaction between the building blocks and their immediate environment. Consequently, the transition energies of the individual molecules are shifted by $[\Delta_1, \dots, \Delta_N]$ and distributed around an average transition energy w_{0-0} , where Δ_n is the transition energy offset of the n -th molecule (see Eq. (2.27) and Eq. (2.28)). For a description of this distribution, the transition energy offsets Δ_n are chosen from a joint Gaussian distribution

$$P(\Delta_1, \dots, \Delta_N) = \frac{1}{(2\pi)^{N/2} \sqrt{\det(A)}} \exp\left(-\sum_{m,n=1}^N \frac{1}{2} (A^{-1})_{mn} \Delta_m \Delta_n\right), \quad (2.35)$$

where $(A^{-1})_{mn}$ are elements of the inverse covariance matrix A . The matrix elements are given by

$$A_{mn} = \langle \Delta_n \Delta_m \rangle_C = \sigma_{inhom}^2 \exp(-|m - n|/l_0), \quad (2.36)$$

where σ_{inhom} is a measure for the disorder strength, i.e., the standard deviation of the site-energy distribution. $\langle \dots \rangle_C$ denotes the average over different aggregate energy configurations $C = [\Delta_1, \dots, \Delta_N]$, which specifies the energy disorder of one aggregate in an ensemble. According to the work of Knapp [102], the intersite correlation depends exponentially on the spatial distance between the molecules and here l_0 describes the spatial correlation of transition energies in units of monomers. Figure 2.8 shows two different energy configurations of the monomers in an aggregate for four different correlation lengths. For $l_0 = 0$ each transition energy offset Δ_n is chosen independently from a Gaussian distribution. With increasing l_0 the distribution of the transition energies within one realization becomes smoother until, in the opposite limit of infinite spatial correlation ($l_0 = \infty$), each monomer within one aggregate exhibits the same energy and disorder is entirely inter-aggregate. By means of spatially correlated transition energies, inter-aggregate (disorder between aggregates, parameter σ_{inhom}) as well as intra-aggregate electronic disorder (within one aggregate, parameter l_0) is taken into account.

Note that besides most standard models, which consider a Gaussian distribution for the molecule's energies, these distributions may not always be

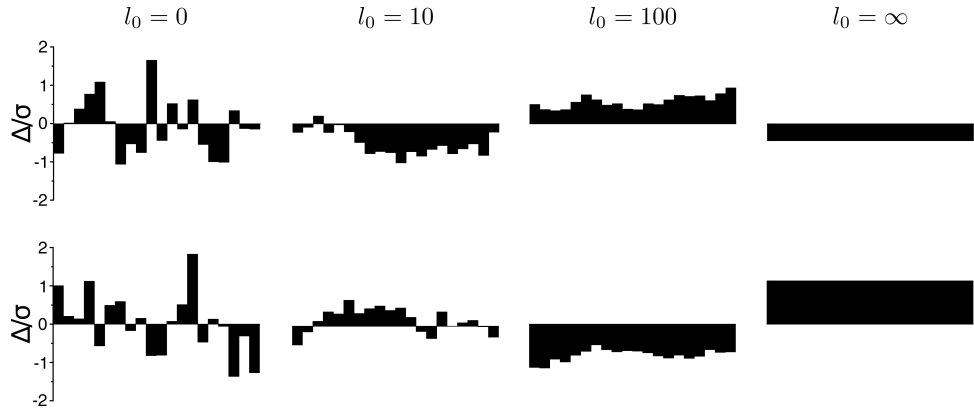


Figure 2.8: Two representations of energy configurations $C = [\Delta_1, \dots, \Delta_N]$ along an aggregate consisting of $N = 20$ monomers for four different correlation lengths l_0 . The correlation length l_0 increases from left to right. For $l_0 = 0$ there is no correlation, whereas for $l_0 \rightarrow \infty$ each monomer within one aggregate shows the same site-energy offset. Adapted from [74].

appropriate [35, 103, 104]. For example, energy funneling in one-dimensional J-aggregates was explained using Levy distributions [104], which are non-Gaussian distributions that increases the likelihood of local, low energy states, termed traps. These traps can act as a barrier in energy transport and can also be populated more efficiently [103, 104].

In the following, special attention is paid to the intensity ratio $R_{em} = \frac{I_{0-0}}{I_{0-1}}$, which increases (decreases) with increasing disorder in H-(J-)aggregates [98]. The changes in this ratio derive from the fact, that the 0-0 peak in aggregates depends entirely on the coherence of the emitting exciton, in contrast to the sideband emissions 0-1, 0-2,... [74]. Therefore, ultimately the 0-0 photoluminescence (PL) intensity reports not only about the disorder but also on the degree of coherence of the emitting exciton. Exciton delocalization is of considerable interest, since delocalization can be beneficial for energy transport dynamics (see section 2.4) [7, 16, 20, 35, 74]. In particular, as a measure for the spatially collective emission the number of coherently coupled molecules N_{coh} can be determined from

$$N_{coh} = \frac{1}{\langle C^{em}(0) \rangle} \sum_{s=-(N-1)}^{N-1} |\langle C^{em}(s) \rangle|. \quad (2.37)$$

Here, the coherence function for the emitting exciton $|em\rangle$, i.e., the delocalization of the vibronically excited center of mass of the exciton, is defined as

$$C^{em}(s) := \sum_n \sum_{\tilde{\nu}, \tilde{\nu}'} f_{\tilde{\nu}, 0} f_{\tilde{\nu}', 0} c_{n, \tilde{\nu}}^{em} c_{n+s, \tilde{\nu}'}^{em}, \quad (2.38)$$

where $f_{\tilde{\nu}, \nu}$ are the Franck-Condon overlap integrals, $c_{n, \tilde{\nu}}^{em}$ are the one-particle coefficients, and s counts the monomers along the aggregate.

For example, for aggregates without disorder ($\sigma_{inhom} = 0$ and/or $l_0 = \infty$) and periodic boundary conditions, the coherence number equals the total number

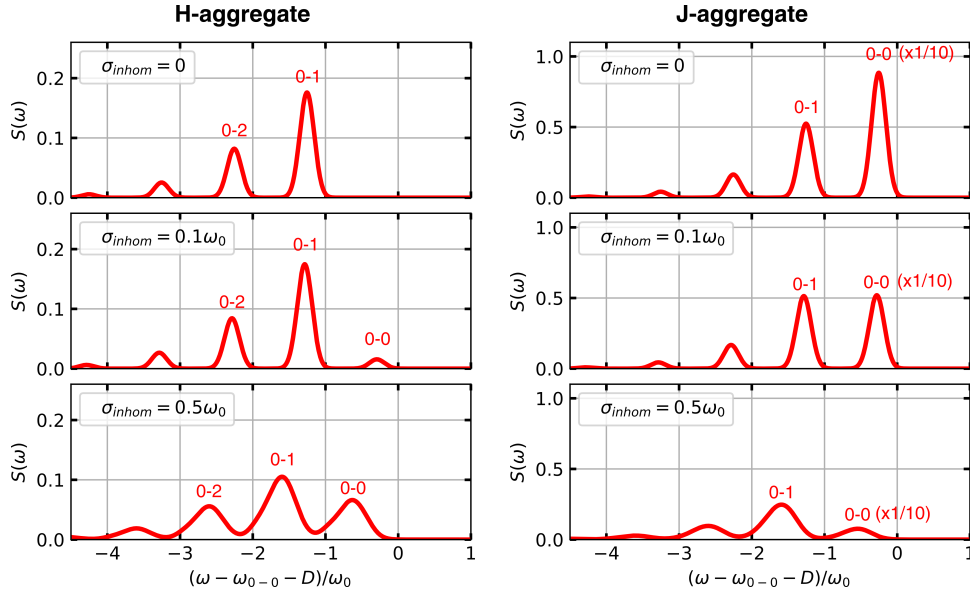


Figure 2.9: Calculated emission spectra for H- and J-aggregates as a function of increasing disorder σ_{inhom} at $T = 0K$ for linear aggregates with $N=20$ monomers averaged over 10^3 configurations of energetic disorder C . Further, for all graphs $D = 0$, $W = \lambda^2\omega_0$, $\lambda^2 = 1$, $\omega_0 = 0.17eV$, $l_0 = 0$ and $\sigma_{hom} = 0.4\omega_0$ were used. For J-aggregates, the 0-0 transition has been reduced by a factor of 10. For details, see text. Adapted from [98].

of molecules within the aggregate $N_{coh} = N$. For completely localized exciton states, in the presence of huge disorder, N_{coh} reduces to one [35]. Generally, in H-(J)-aggregates the ratio $R_{em} = \frac{I_{0-0}}{I_{0-1}}$ decreases (increases) as the coherence number N_{coh} increases.

Figure 2.9 shows the effects of increasing inter-aggregate electronic disorder (σ_{inhom}) on the emission spectra. The variation of l_0 represents a change in the intra-aggregate disorder and leads to similar effects as shown in the following. Qualitatively, at $T = 0K$ and for increasing disorder (increasing σ_{inhom} and/or decreasing l_0) the 0-0 PL intensity in H-(J)-aggregates increases (decreases), due to the broken symmetry in the exciton wave function. Additionally, rising disorder σ_{inhom} increases the probability of low-energy states of the monomers within the aggregates (see also Fig. 2.8), which increases the probability of low-energy exciton states. This leads to a redshift of the aggregate emission spectrum. In addition, the lines broaden with increasing disorder. As mentioned above, with growing disorder $R_{em} = \frac{I_{0-0}}{I_{0-1}}$ increases (decreases) in H-(J)-aggregates [98].

If emission spectra are recorded at temperatures $T \neq 0K$, states above the lowest-energy exciton state become thermally accessible (thermally activated emission), i.e., emission stems no longer exclusively from the lowest-energy exciton state $|em\rangle$. For ideal H-(J)-aggregates, increasing temperature leads to an enhanced (decreased) 0-0 PL intensity (see Fig. 2.10). In H-aggregates, this can be explained by thermally activated emission from the dipole allowed $|k = 0\rangle$ state ($|A_1\rangle$), which is $e^{-\lambda^2 W}$ above the lower edge of the band. In J-aggregates,

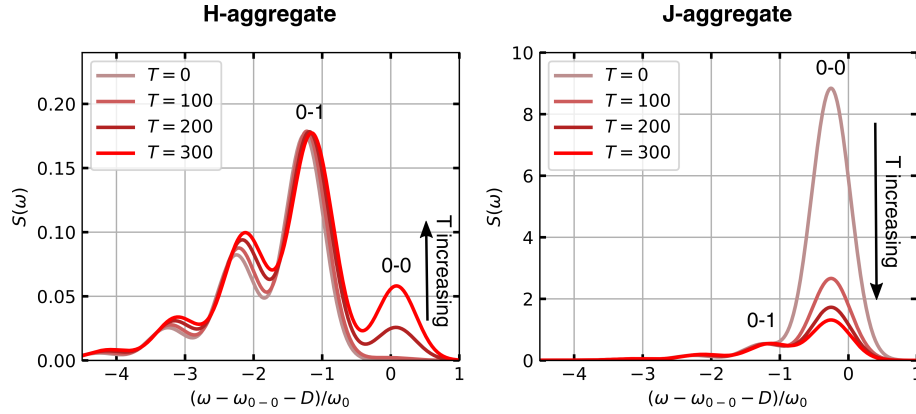


Figure 2.10: Calculated emission spectra for ideal ($\Delta_n = 0$) H- and J-aggregates as a function of temperature T , averaged over a Boltzmann distribution of the emitting states. Linear aggregates of $N=20$ monomers and only next-neighbor interaction are assumed. The parameters $D = 0$, $W = \lambda^2\omega_0$, $\lambda^2 = 1$, $\omega_0 = 0.17\text{eV}$ and $\sigma_{hom} = 0.4\omega_0$ were used. For details, see text. Adapted from [98].

these thermally activated states with $k \neq 0$ have a smaller dipole strength, leading to the reduction of the 0-0 transition. As the bandwidth W' of the lowest-energy exciton band rises, thermal occupation of higher-energy exciton states becomes less likely, i.e., the 0-0 PL intensity is determined by the ratio between the thermal energy and the exciton bandwidth W' . Importantly, the peak ratio $R_{em} = \frac{I_{0-0}}{I_{0-1}}$ remains an accurate measure of exciton coherence, even when disorder and thermal effects are present [35].

2.4 ENERGY TRANSPORT

In perfectly ordered and isolated aggregates, excitons are delocalized over the entire aggregate [35, 47]. However, as mentioned above, aggregates are surrounded by an environment, for example, a solvent or they are embedded in a film, and hence aggregates perceive an environment that can change spatially and temporally [7, 9]. The interaction of the aggregate with the environment induces disorder in the aggregate, causing heterogeneities and fluctuations in the electronic parameters [7, 16, 47]. Therefore, energy transport occurs across a disordered energy landscape that is modulated by the surrounding environment and is an interplay between intermolecular interactions, causing exciton delocalization, and the interaction with an environment, leading to localization and relaxation of excitons [7, 9, 16, 103]. Hence, the degree of delocalization and the type of exciton motion strongly depends on the interaction of the aggregates with the environment [7, 47, 105]. Note that in the following, the considerations are limited to the Frenkel exciton picture, but the presented concepts are generally valid and can also be transferred to the Spano theory.

Mainly, there are two effects depending on the timescale in which the environment changes the aggregate properties [47, 103]: Static and dynamic disorder. Changes that are slow compared to the exciton dynamics are often modeled as static disorder. Here, the local environment can be interpreted as a time independent stochastic potential in which the excitons move in [7, 47, 103]. Essentially each molecule sees its own local environment, leading to a statistic distribution of transition energies $E = E_0 + \Delta_n$ (so-called diagonal static disorder). Here, E_0 is the mean transition energy and Δ_n accounts for the environmentally changed transition energies, which are taken from a distribution with a standard deviation of σ_{inhom} , serving as a measure for the amount of induced disorder [35, 106]. Energetic disorder breaks wave function's symmetry and localizes excitons on parts of the aggregates (see above) [7, 22, 103]. As long as $\sigma_{inhom} \gg |J_{nm}|$, electronic excitations are localized on individual molecules (see Fig. 2.11a). In the opposite situation ($|J_{nm}| \geq \sigma_{inhom}$), the description of electronic excitations in terms of largely delocalized excitons is a good approximation (see Fig. 2.11b) [7, 22]. Since, due to static disorder, the transition energies of each molecule differ, averaging over an ensemble of molecules leads to broadening of spectral lines. Usually, this is referred to as inhomogeneous line broadening [47]. Note, as stated above, there is also the possibility of disorder due to structural inhomogeneities, which leads to a variation in the interaction between the molecules around a mean value (so-called off-diagonal static disorder) [22, 35, 106].

In contrast, for dynamic disorder, the modulation of the molecules' transition energies by the environment is fast or comparable to the time scale of exciton dynamics. This leads to dynamic localization of initially delocalized excitons [7, 47, 103]. Generally, the environment tends to destroy phase relations between the excited states of different molecules, ultimately yielding an excited state to be more localized compared to an isolated aggregate, i.e., an aggregate in a vacuum. This can be described with a rate γ_{ij} [7, 8], which measures the environmentally induced dephasing of coherence. Experimentally, this rate can be obtained from non-linear pump-probe spectroscopy [7, 8, 105]. The decay of the phase relation between the ground and excited state wave function, which is manifested in the homogeneous line broadening σ_{hom} , also reflects an estimation of the aggregate environment interaction [7, 17]. This dynamic effects of the environment on the aggregate is often modeled as a dynamical, time-dependent (t) modulation of the transition energy $E = E_0 + \Delta_n(t)$ [7, 106].

Since energy transport is closely related to the coupling of the aggregate to the environment (here denoted with σ_{hom}) and the magnitude of the intermolecular interactions $|J_{nm}|$, transport mechanisms can be classified with respect to these two parameters [7, 47, 107]. In the following, two limits of energy transport mechanisms are presented, in which the excitation energy is transported from one molecule to the next in a completely incoherent or coherent manner.

The first mentioned limit offers a good description, if the homogeneous line width is much larger than the electronic interaction ($\sigma_{hom} \gg |J_{nm}|$), i.e., if the electronic coupling is weak compared to the aggregate environment coupling. In

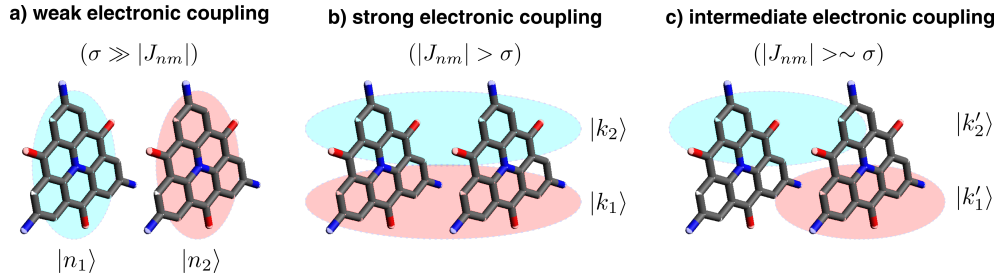


Figure 2.11: Localization of excitons in an electronic dimer. a) In the weak electronic coupling regime, the environment fully localizes the excited states $|n\rangle$. b) In the strong coupling regime, the aggregate is in a mixture of the fully delocalized Frenkel exciton states $|k\rangle$. c) In the intermediate electronic coupling regime, the environment localizes the exciton states to some degree. Depending on whether static or dynamic disorder should be considered, σ must be replaced accordingly. In the case of dynamic disorder, the interaction leads to relaxation and time-dependent localization of excitons. For more details, see text. Adapted from [7].

the so-called Förster regime, the intermolecular interactions can be treated as a small perturbation and the energy transport can be understood as hopping of the completely localized excitations, since the environment rapidly destroys the coherence between the molecules (see Fig. 2.11a) [7, 9, 107]. Within Förster theory, all coherence between consecutive molecules is neglected and energy transport is described with rate equations for the populations

$$\frac{\partial p_i(t)}{\partial t} = - \sum_j k_{ij} p_i + \sum_i k_{ji} p_j, \quad (2.39)$$

where p_i describes the probability of finding molecule i in the excited state and k_{ij} is the transport rate from site i to site j , which can be obtained via Fermi's golden rule [47]

$$k_{ij} = \frac{2\pi}{\hbar} |J_{ij}| \rho. \quad (2.40)$$

Here, ρ denotes the density of the energy conserving terminal states, which can be interpreted as the overlap of the emission spectrum of the energy donor and the absorption spectrum of the energy acceptor. The first term in equation (2.39) describes the depopulation and the second term the population of molecule i , which is possible between all molecules as long as $k_{ij} \neq 0$. To account for thermally activated transport, these rates have to be weighted by a Boltzmann factor such that in thermal equilibrium the molecules are populated according to a Boltzmann distribution [7, 47, 103, 108–110].

In the very strong electronic coupling limit $|J_{nm}| \gg \sigma_{hom}$, excitation energy can move through the aggregate as a quantum mechanical wave packet [7, 47, 107]. This type of motion is described by the time-dependent Schrödinger equation

$$i\hbar \frac{\partial |\Psi(t)\rangle}{\partial t} = \hat{H} |\Psi(t)\rangle \quad (2.41)$$

and requires fixed phase relations between the excited state wave functions of different molecules. Therefore, it is called the coherent transport limit in which the excited state is delocalized and the wave function forms a pattern of amplitudes across the molecules [7, 8]. Phenomena of this kind were found in individual, highly ordered polydiacetylene chains at cryogenic temperatures [111]. However, this type of motion is characteristic for an isolated quantum system without interaction to an environment or only valid for very small time scales and perturbations from the environment have to be included [47]. If the electronic interaction is still stronger than the aggregate environment coupling ($|J_{nm}| > \sigma_{hom}$), relaxation between the eigenstates of the Frenkel Hamiltonian takes place. In thermal equilibrium, the system is a statistical mixture of the eigenstates (see Fig. 2.11b).

In the intermediate regime ($|J_{nm}| \sim \sigma_{hom}$), coupling to the temporally changing environment effectively renormalizes the exciton basis and hence dynamical localization and relaxation take place. However, the excitation can remain to some degree delocalized (see Fig. 2.11c) [7].

In reality, in self-assembled materials, energy transport is likely a mixture of coherent and incoherent transport [16, 17, 26, 74, 103, 107]. On very short time scales, it is possible to enter a regime in which the environmental interaction is too slow and the coherence is not completely destroyed. Quantum mechanical processes lead to a coherent wave packet that is delocalized across several molecules. On longer time scales unavoidable interaction with the environment becomes dominant and destroys the phase coherence and the transport becomes quasi-classical [47, 112].

INCOHERENT TRANSPORT DYNAMICS: PAULI MASTER EQUATION In this work, the focus is on the regime of incoherent energy transport. In this case, initial femtosecond coherent population oscillations between molecules are damped quickly on the time scale of energy transport processes due to interaction with the environment and energy transport can be described through incoherent rate equations [7–9]. In order to illustrate how energy transport occurs within a disordered energy landscape (see Fig. 2.12a), the limit of weak aggregate environment coupling is ideal and offers a straightforward approach to understand the underlying processes. Under the Born-Markov approximation, which assumes the environment to equilibrate infinitely fast after an electronic transition and its interaction with the aggregate can be treated as a small perturbation [7, 16, 110, 113], the interaction of the aggregate with the environment makes incoherent hopping between the eigenstates of the aggregate Hamiltonian possible [16, 114]. Thus, on the one hand, excitons can relax within their exciton band, and on the other hand, it enables excitons to spatially diffuse [103, 115]. Here, the environment represents the vibrations of the outer part of the molecules [114], including, e.g., molecular side groups and the surrounding matrix. The considered time scales are long compared to the typical times for coherent oscillations of populations between individual molecule sites and hence the time evolution

of the population $P_k(t)$ of the exciton state $|k\rangle$ can be written in terms of a Pauli master equation [103, 110]

$$\frac{\partial P_k(t)}{\partial t} = \sum_{k'} [W_{kk'} P_{k'}(t) - W_{k'k} P_k(t)]. \quad (2.42)$$

Note that all decay channels are neglected since the focus is on the transport. The first term on the right side describes all population that enters state $|k\rangle$ from all other states $|k'\rangle$, while the second term describes the depopulation of state $|k\rangle$ to all other states $|k'\rangle$. The exciton eigenstates $|k\rangle$, with energies E_k and wave function coefficients (site amplitudes) c_{kn} , follow from diagonalizing the exciton Hamiltonian. The model includes on-site scattering of excitons on a phonon bath. $W_{kk'}$ are transition rates (scattering rates) from state $|k\rangle$ to $|k'\rangle$, which are given using Fermi's golden rule, with the exciton-vibration interaction as the perturbation. In the limit of one-phonon processes, the transition rates are [72, 103, 113]

$$W_{kk'} = W_0 S(|E_k - E_{k'}|) \sum_{n=1}^N |c_{kn}|^2 |c_{k'n}|^2 B(E_k - E_{k'}). \quad (2.43)$$

Here, W_0 denotes the magnitude of the exciton scattering. The spectral factor $S(|E_k - E_{k'}|)$ depends on the details of the environment and how it couples to the aggregate, i.e., this factor covers the phonon spectral density of states as well as the coupling to the excitons [72]. For example this factor has been modeled with a linear as well as a cubic dependency of $|E_k - E_{k'}|$ [72, 114, 115]. The term $\sum_{n=1}^N |c_{kn}|^2 |c_{k'n}|^2$ represents the overlap integral of the exciton probabilities between the state $|k\rangle$ and $|k'\rangle$. Due to this term, only hops between neighboring localized states are efficient. The last term,

$$B(E_k - E_{k'}) = \begin{cases} [\exp(\frac{E_k - E_{k'}}{k_B T}) - 1]^{-1} & E_k > E_{k'} \\ 1 + [\exp(\frac{E_{k'} - E_k}{k_B T}) - 1]^{-1} & E_k < E_{k'} \end{cases}, \quad (2.44)$$

ensures that the scattering rates obey the detailed balance condition:

$$W_{k'k} = W_{kk'} \exp\left(\frac{E_k - E_{k'}}{k_B T}\right), \quad (2.45)$$

thermalizing the population distribution, in absence of decay channels, to a Boltzmann distribution [103, 110, 113]. Essentially, the transition probability depends on the temperature, the energy spacing between the involved states, and their wave function overlap [115].

The resulting energy transport within this model can be best understood for a one-dimensional Frenkel exciton chain of N coupled molecules with transition energies randomly taken from a Gaussian distribution. The energy structure of disordered excitons is shown in Fig. 2.12a. Disorder tends to localize exciton wave functions at segments of the aggregate of typical size $N' < N$ (localization

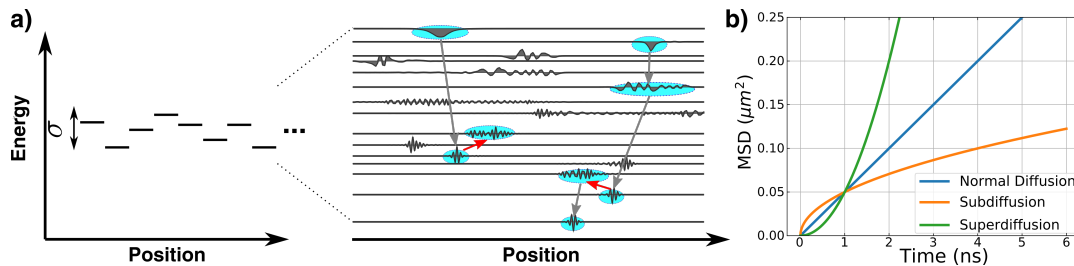


Figure 2.12: Energy transport in a disordered aggregate. a) Left: Schematic picture of the transition energies of individual molecules along an aggregate (energy landscape), randomly taken from a Gaussian distribution with a standard deviation of σ . Right: Typical realization of exciton wave functions for a disordered aggregate. Intraband relaxation processes are shown with gray arrows and thermally activated transport processes are shown with red arrows. The ellipses indicate the delocalization of the exciton states. Adapted from [103, 115]. b) Mean squared displacement for normal, sub- and superdiffusion. Adapted from [41]. For details, see text.

length). In detail, molecules with transition energies in the tails of the Gaussian energy distribution will coherently share their excitation with their neighbors to a small extent, effectively acting as segment boundaries, separating the system into weakly coupled subchains of variable length [103, 115]. Typically, energetically higher states are more delocalized and hence provide a higher overlap with other (energetically lower) exciton states. Generally, transitions between states localized on the same part of the aggregate are allowed due to wave function overlap and hence localization will reduce the transport. Starting at an exciton state $|k\rangle$, transitions to higher states are only possible by absorbing thermally available phonons with the appropriate energy. Transitions to lower states are possible via emitting a phonon or stimulated emission of phonons. At low temperatures (compared to the exciton bandwidth), localized, low-energy states will tend to trap excitations and exciton motion is inhibited for two reasons: First, traps have a small overlap with wave functions localized in their neighborhood and second, they are lying energetically too deep. Both effects make transitions out of traps unlikely. At higher temperatures, scattering to a more delocalized, higher-energy state enables the exciton to escape from low-energy traps [103, 110]. Once the time evolution has been calculated according to equation (2.42), the mean squared displacement (MSD) is considered to characterize the spatial diffusion of excitons. The MSD of the exciton populations are given by

$$MSD(t) = \sum_n p_n(t)(n - n_0)^2, \quad (2.46)$$

where p_n is the population of monomer n in the site basis and n_0 the mean value of the starting position [103].

The temporal evolution of the MSD due to exciton transport is modeled as [28, 33, 103, 116–118]

$$MSD(t) = 2D(t)t. \quad (2.47)$$

In a general situation, the diffusivity is given by $D(t) = 0.5A_\alpha t^{\alpha-1}$, where A is the exciton hopping coefficient with fractional time units. For normal diffusion $\alpha = 1$ and the MSD evolves linearly in time. The diffusivity $D = 0.5A$ is time independent with units of cm^2s^{-1} . For subdiffusion, $0 < \alpha < 1$, the MSD increases slower, due to the inhibited exciton motion in a disordered excited state energy landscape [103, 119]. In the limit of so-called ballistic or superdiffusivity, $1 < \alpha \leq 2$ and the temporal increase of the MSDs is larger compared to normal diffusion. This limit is characteristic of coherent motion of delocalized states that are frequently interrupted by scattering effects [41] (see Fig. 2.12b).

While a microscopic picture of exciton diffusion has been described above, the exciton dynamics are often modeled in a macroscopic picture using a classical diffusion equation [28, 41, 119–123]

$$\frac{\partial n(x, t)}{\partial t} = D(t) \frac{\partial^2 n(x, t)}{\partial^2 x} - \frac{n(x, t)}{\tau}, \quad (2.48)$$

where D is the time-dependent diffusivity (see above), τ the exciton lifetime and $n(x, t)$ the exciton density as a function of time t and space x (for details, see supporting information of sections 4.1 and 4.2). In this picture, the diffusivity D depends on the exciton delocalization. In a simple random walk, the diffusion constant D scales quadratically with the step size or in this case with the delocalization, i.e., $D = kN'^2/2$, where N' is the exciton's localization length and k is the exciton transport rate [20]. Simplified, excitons with larger delocalization can move farther within one hopping step of size N' [20, 124]. However, with increasing delocalization, the transport rate k decreases as the wavefunction amplitude at each molecular site diminishes (for example see Eq. (2.43)). In the ideal case, k scales with $1/N'$ [20], meaning that the diffusion constant could increase proportionally to exciton delocalization [16, 20]. The MSD of the exciton density also evolves in time according to equation (2.47).

To conclude this discussion, it should be mentioned that there are plenty of models treating exciton dynamics. For example, the Haken-Strobl-Reineker (HSR) model treats the aggregate-environment interaction as classical fluctuations of transition energies. Here, an initial ballistic period is followed by a diffusive transport, and hence the HSR-model covers coherent and incoherent transport in a high-temperature limit [9, 16, 120]. Standard versions of Redfield theory assume a Markovian environment and also allow the treatment of coherent and incoherent motion in the limit of weak aggregate environment coupling [7]. Similarly to Redfield theory, an intuitive picture for coherent-incoherent transport is provided considering the exciton as a quantum walker moving through the sites [17, 124]. The walker propagates coherently with the speed of $2J_0$. Either the walker reaches its delocalization length on the time scale t_l and subsequently gets stuck or the number of steps is limited by the interaction with

the environment on the time scale t_H . The subsequent interaction with the environment frees the walker and enables him to propagate further. Consequently, the total number of steps is determined by the exciton lifetime [17, 124]. The hierarchical equation of motion approach (HEOM) accounts for non-Markovian aggregate environment interactions and thus captures time-dependent reorganization of the environment [7, 9]. However, HEOM is computationally expensive [9].

As key parameters for optimized energy transport, many studies on organic materials have shown that energy transport properties are closely related to highly defined arrangements of the building blocks, reasonable electronic coupling, and the associated formation of collective excited states. For example, Caram et al. [17] have demonstrated transport distances of $1.6 \mu m$ in a J-type aggregate of double-walled tubular nanostructures. It was suggested that the high energetic order within the structures and resulting long delocalization length of excitons are key factors for long-range energy transport in J-aggregates. Hence, simplified transport is enhanced due to the increased step size during exciton hopping achieved by delocalization [20]. However, in J-aggregates, the lowest exciton state is a superradiant state and transport competes with radiative deactivation. In H-type aggregates, a step further was gone and besides the delocalization of the wave functions also their non-radiative character, i.e., the optically forbidden lowest-energy transition, was exploited to minimize radiative losses and thus distances up to $4.4 \mu m$ were demonstrated [26]. However, many key parameters that determine efficient energy transport and their interplay are not fully understood and are the subject of current research [6, 20, 23, 73]. These issues will be addressed in section 4.2 of this thesis, which adds new aspects for a theoretical understanding of energy transport and design principles for supramolecular architectures that enable long-range energy transport.

2.5 EXCITON-EXCITON ANNIHILATION

The above explained single exciton limit is only appropriate for weak laser excitation intensities, resulting in the formation of single Frenkel excitons [47, 125]. However, upon increasing the excitation intensity, several excitons localized at different positions within the aggregate are excited. When these mobile excitons interact, they annihilate, and thus excitons can act as (mobile) quenching centers for other excitons [17, 70]. This opens up a new relaxation channel for excitons, known as exciton-exciton annihilation (EEA) [17, 47, 70, 125]. In particular, at high excitation densities, EEA can represent a large part of the possible relaxation mechanisms and hence becomes an important dimension in the context of energy transport processes [47, 70, 125] and in the design of optoelectronic devices [42, 73, 123].

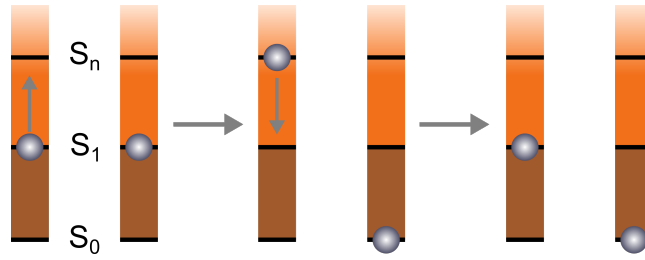


Figure 2.13: Energy level scheme visualizing singlet-exciton singlet-exciton annihilation. Shown are the ground state S_0 , the first excited state S_1 , and a higher excited state S_n of two excitons (the spheres indicate the degree of excitation). Left part: Both excitons are in the first excited state. Central part: The left exciton is excited to a higher state while the right exciton returns to its ground state (exciton fusion). Right part: Internal conversion leads the left exciton to reach its first excited state. For details, see text. Adapted from [125].

Figure 2.13 shows a scheme of the EEA process in the simplest case for completely localized excitons on single molecules [47, 125], but the mechanisms shown are generally valid for any kind of interacting excitons (delocalized or localized). Here, the molecular building blocks are approximated as three-level systems with a ground state S_0 , a first excited state S_1 , and a higher excited state S_n . The prerequisite for EEA are neighboring excitons, both in their first excited state. In this picture, EEA is represented as a two-step process. First, both excitons have to approach each other by means of energy transport. If the excitons interact, their excitation energies can be used to excite one of the excitons to a higher excited state S_n ($n > 1$). This step, called exciton-fusion, leaves behind the other exciton in its ground state S_0 . In the second step, probably internal conversion returns the exciton in S_n back to S_1 [47, 125]. If the energy loss due to relaxation is large, the generation of two S_1 excitons is prohibited [42] and hence of the initial two excitons, only one is available for the cycle $S_1 \rightarrow S_0$. Therefore, the fluorescence quantum yield decreases and the excited state lifetime of S_1 is reduced [17, 125].

EEA is commonly regarded as an incoherent, stochastic process described with a rate equation for the exciton density $n(\mathbf{r}, t)$ at the spatial position \mathbf{r} and a delay time t after laser excitation. In this description, a term $-\gamma n(\mathbf{r}, t)^2$ was introduced phenomenologically to describe annihilation with an annihilation rate γ [42, 47, 70, 125]. Especially, the rate equation describing the singlet exciton decay for exciton self-quenching in a homogeneous system is given by [17, 70, 126, 127]

$$\frac{\partial n(t)}{\partial t} = -\frac{n(t)}{\tau} - \frac{1}{2}\gamma(t)n(t)^2, \quad (2.49)$$

where τ is the intrinsic exciton lifetime due to radiative and non-radiative decay of excitons and the non-linear term $-\frac{1}{2}\gamma(t)n(t)^2$ describes the depopulation of excitons by annihilation. The factor $\frac{1}{2}$ indicates, that only one exciton remains

after an EEA process ($S_1 + S_1 \rightarrow S_n + S_0 \rightarrow S_1 + S_0 + \text{heat}$). The formal solution to this equation is

$$n(t) = \frac{n_0 \exp(-t/\tau)}{1 + \frac{1}{2} n_0 \int_0^t \gamma(t') \exp(-t'/\tau) dt'}. \quad (2.50)$$

Since EEA is usually a diffusion-limited process, the annihilation rate $\gamma(t)$ depends on a diffusion coefficient D . For example, for diffusion in three dimensions (3D) $\gamma(t)$ is given by

$$\gamma_{3D}(t) = 8\pi DR \left(1 + \frac{R}{\sqrt{2\pi Dt}}\right), \quad (2.51)$$

where R is the interaction radius of the excitons. For longer times $t \gg R^2/(2\pi D)$ the annihilation rate becomes time independent $\gamma_{3D} = 8\pi DR$. For diffusion in one dimension (1D) the annihilation rate is given by

$$\gamma_{1D}(t) = 4\pi DR \frac{R}{\sqrt{2\pi Dt}}. \quad (2.52)$$

Due to the different time dependencies of the annihilation rate, EEA probes the dimensionality and the diffusion length, which is given by $L_D = \sqrt{D\tau}$ [17, 121, 127].

If singlet excitons can be converted into triplet excitons via intersystem crossing, singlet-triplet annihilation creates an additional decay channel for excitons, e.g., for singlet excitons, [70]

$$\frac{\partial n(t)}{\partial t} = -\frac{n(t)}{\tau} - \frac{1}{2} \gamma(t) n(t)^2 - \gamma_{ST} n_T(t) n(t), \quad (2.53)$$

where γ_{ST} is the rate of singlet-triplet annihilation and n_T is the density of triplet states. These rate equations (Eq. (2.49) and (2.53)) can be easily extended since other products of energy transport and annihilation are possible [121]. For example, diffusion equations comparable to Eq. (2.48) with a time- and position-dependent exciton density have been extended for the diffusion of singlet as well as triplet excitons and there are also variants that include singlet fission, triplet fusion, and many more [121, 123, 128].

Also, EEA is described using Monte-Carlo simulations. Here, excitons move to neighboring molecules with a transport rate until they can interact with each other within their interaction radius [17, 73].

Note that these descriptions using rate equations are macroscopic pictures valid for large aggregates and excitons propagating in a diffusive manner [47, 70]. As illustrated in figure 2.13, a microscopic picture has to account for at least a three-level model for every molecular building block, at least two-exciton states, and internal conversion. Further, to consider any type of spatial exciton delocalization, delocalized single- and two-exciton states have to be used, and

hence EEA can take place between delocalized, localized, and between localized and delocalized states. A detailed description can be found in [47, 125]. Doing so, Roel Tempelaar et. al [42] have demonstrated a strong dependence of the annihilation rate on the sign of the dipole-dipole coupling, i.e., whether H- or J-aggregates are considered. Because of the destructive interference in the annihilation properties, due to the phase relations of the two-exciton wave function in H-aggregates, annihilation rates of H-aggregates are reduced by a factor of three compared to J-aggregates at room temperature. This reduction is even more pronounced at lower temperatures, where annihilation rates differ up to one order of magnitude.

In summary, with increasing excitation densities the probability of introducing several excitons into the system increases and according to the equation (2.49) EEA becomes more likely. Similarly, high laser pulse repetition frequencies f_{pulse} can lead to accumulated populations, since exciton populations may not have decayed completely between subsequent laser pulses ($\tau > \frac{1}{f_{pulse}}$). Thus, effectively a higher density of excitons is available, leading to an increased annihilation probability [70, 129, 130]. On the one hand, EEA can be exploited to study the structure-function relationship of materials [17, 42, 73, 131], e.g., EEA can be used to determine the exciton diffusion length through its characteristic signatures on fluence-dependent time-resolved spectroscopy measurements. On the other hand, EEA can complicate the interpretation of experimental measurements [41, 42], and hence a careful design of experiments and knowledge about the signatures characteristic of the process are required.

In section 4.1 of this thesis, EEA becomes relevant as it leads to an apparent enhancement of exciton transport in direct measurements of spatio-temporal exciton dynamics. Moreover, in section 4.3 singlet-triplet annihilation is exploited to manipulate the direction of mobile singlet excitons.

2.6 WAVE GUIDING IN SELF-ASSEMBLED MATERIAL

Besides their spectroscopic signatures and their ability to transport excitation energy, self-assembled organic materials such as micro- or nanocrystals can show optical microcavity behavior, optically pumped lasing and waveguiding [18, 19, 132]. The ability to confine and guide light results from the fact that these crystals show a higher refractive index than their environment [18, 133].

For example, in an asymmetric planar waveguide, the middle layer with refractive index n_2 is surrounded by media with smaller refractive indices $n_{1,3} < n_2$ (see Fig. 2.14). This three-layer geometry allows light to be confined and guided in the middle layer. In a ray optic description, guided transport of light through the material is achieved by multiple total internal reflections of the light at the boundaries, i.e., light is transported through the waveguide without radiating into the surrounding media [133]. Total internal reflection at the

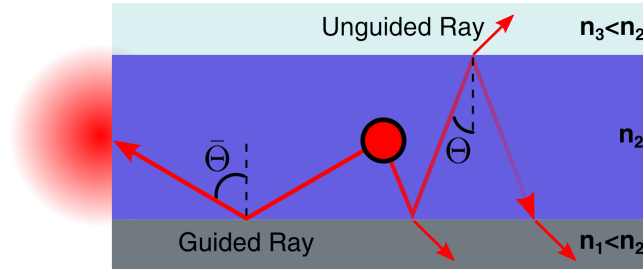


Figure 2.14: Active waveguiding in the picture of ray optics. The waveguide with refractive index n_2 is surrounded by media with lower refractive indices (n_2, n_3). Emitted light making an angle $\Theta > \Theta_C = \arcsin(\frac{n_{1,3}}{n_2})$ are guided by total internal reflection towards the edges of the waveguide. For smaller angles $\Theta < \Theta_C$ the emitted light is not completely confined and can escape into the surrounding media. For details, see text. Adapted from [133].

boundaries occurs if the angle of incidence is greater than the critical angle Θ_C . For light waves incident from a medium with refractive index n_2 to a medium with refractive index $n_{1,3} < n_2$ the critical angle for total internal reflection is determined by Snell's law

$$\Theta_C = \arcsin\left(\frac{n_{1,3}}{n_2}\right). \quad (2.54)$$

Rays propagating under larger angles can be reflected multiple times within the material by bouncing between the surfaces. Rays making smaller incident angles are not completely confined and leak into the adjacent medium (see Fig. 2.14) [133, 134]. They are partly reflected and refracted according to Fresnel's equations and thus lose a portion of their power to the environment at each reflection (see Fig. 2.14) [133]. More precisely, for waves to be guided in the waveguide, a self-consistency condition must be fulfilled, i.e., for a planar dielectric waveguide, this means that rays must reproduce themselves in phase and amplitude after reflection at both boundary layers. Thus, only discrete bounce angles $\Theta_m > \Theta_C$ fulfill the condition for constructive interference [133]. Fields that satisfy the self-consistency condition are called modes of the waveguide. Since in this example, the discrete mode angles are limited by the critical angle and the surface ($\Theta_C < \Theta_m \leq \frac{\pi}{2}$), the waveguide can support a certain number of modes only. For a sufficiently thin layer or sufficiently long wavelength, a single-mode operation can be achieved, where exactly one propagation angle is allowed [133]. Note that the principle of operation explained above is also similar for channel waveguides, but the mathematical treatment is more complex [133].

In self-assembled dielectric waveguides, a distinction is made between passive and active waveguiding. Passive waveguiding refers to the ability to guide light which is coupled into the material externally [133]. In the case of active waveguiding, the transported light is generated by the excitation of the material itself, i.e., the guided light results from photoluminescence (PL) of the waveguide

[18]. Only emission fulfilling the self-consistency condition is guided and the other part of the emission leaves the waveguide [132]. Therefore, if the waveguide is excited at one position, emission can be detected directly at the excitation position or the emission can be guided to the output point, which is usually an edge of the waveguide (see Fig. 2.14) [134].

Notably, since the absorption and emission spectrum in organic materials often overlap strongly, photon recycling, which refers to the re-absorption and delayed re-emission of PL-photons by other molecules within the waveguide, can occur. In combination with waveguiding, photon recycling can take place more frequently. This effect can be significant if the PL quantum yield of the material is high and/or the absorption and PL spectra strongly overlap and hence, photon recycling can have an influence on the spectral as well as temporal signatures of organic materials [135–137].

In summary, a variety of effects, such as waveguiding, exciton transport, exciton-exciton annihilation, and many other effects can occur in self-assembled materials. Therefore, in order to design experiments correctly and to draw the right conclusions, all these mechanisms have to be considered, as demonstrated in section 4.1.

2.7 EXPERIMENTAL METHODS FOR MEASURING ENERGY TRANSPORT

To study energy transport in molecular assemblies, various indirect methods have been applied to date [121, 131]. For example, emission quenching at sensitizers or surfaces [29, 30, 116, 121, 138, 139] have been used to extract exciton dynamics in organic materials. These methods are based on knowing the distance to the surface or the average distance between sensitizer. If these distances approach the exciton diffusion length, a fraction of the excitons will be quenched and consequently, the PL lifetime will be shortened compared to a non-modified sample. The changes in the PL signal can then be fitted to model assumptions, yielding the exciton diffusion length and diffusion constant [121, 140, 141]. However, quencher molecules perturb the system and can introduce structural defects. Exciton-exciton annihilation is also frequently used [17, 73, 141] to obtain information about the exciton dynamics (see section 2.5). However, these methods are usually applied to ensembles in films or solutions and thus the extracted transport parameters represent averaged values. Ordinarily, the investigated materials are not perfectly homogeneous and can suffer from structural defects or other forms of disorder [41]. These insights remain hidden but are highly desirable to understand the underlying mechanisms that dictate the transport properties, i.e., as shown in sections 2.3 and 2.4, the energy landscape of an aggregate has a huge influence on the spectroscopic signatures and energy transport properties. The main disadvantage of these methods is

that they do not directly measure the time-resolved transport distance. Rather, they are based on translating an indirect measurement quantity, such as the lifetime of annihilation measurements, into a diffusion constant or diffusion length via theoretical considerations.

Only recently, a few direct measurements of transport distances have been reported. In analogy to single-molecule spectroscopy, the spectroscopic properties are measured locally in space, allowing to characterize distributions of properties in addition to mean parameters [41]. These techniques are based on detecting the broadening of an exciton population that is initially created in a defined spatial region. A simple approach uses static microscopy to create an initial exciton population with a diffraction-limited excitation spot. The spatial broadening of the detected steady state PL is compared to the excitation profile and broadenings are attributed to exciton diffusion [26, 31, 33].

This technique has been extended for time-resolution using locally focused pulsed laser excitation and follows the exciton dynamics in space and time (see Fig. 2.15). Common to all these spatio-temporal methods is that they are based on repeated excitation and time-delayed imaging cycles of the exciton dynamics. In a transient absorption approach, the exciton population can be followed via raster scanning a focused probe pulse [122] or using a wide-field probe pulse in combination with widefield detection [142]. Recently, a time-resolved transient scattering method has been used to characterize how the spatio-temporal exciton population alters the local dielectric constant [143]. Finally, detection-beam scanning of the transient photoluminescence signal can probe the exciton dynamics via the radiative recombination as excitons return to the ground state [28, 119]. Since all these methods are based on measuring absolute changes in the spatial exciton distributions over time, there is in principle no limit to the minimum diffusion length that can be measured [41]. In this context, Ginsberg and Tisdale presented a detailed review of spatio-temporal techniques, the evaluation of the measurement results, and selected experimental results [41]. The advantage of these methods is to determine the exciton dynamics in time and space and to apply and develop theoretical concepts beyond standard diffusion models [41].

In this work, self-assembled materials showing long-range energy transport in the order of 200 nm with partly small absorption cross-sections are used. To avoid non-linear effects like annihilation (see section 4.1), and thus to be able to detect exciton dynamics at low excitation densities, the detection-scanning method of the PL-signal is particularly suitable, because it has the highest sensitivity and requires the lowest excitation powers [41]. The experimental realization is shown in Fig. 2.15. The pulsed laser excitation is directed via a dichroic mirror into a high-numerical aperture objective and focused on the sample. The PL of the focal plane is collected by the same objective and separated from the excitation light by the dichroic mirror. The following detection path consists of two telecentrically arranged lenses (L1 and L2), a scanning mirror, and a detection lens (L3), which images the PL onto a photodiode (detector).

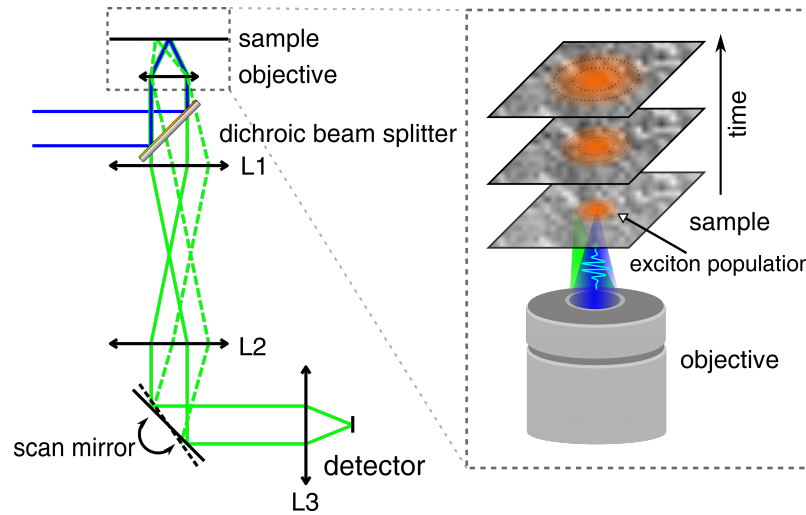


Figure 2.15: Experimental implementation of detection scanning. Left: The solid blue lines show the excitation path, the green lines represent the emission beam path with the undeflected mirror, and the green dashed lines correspond to the emission beam path with the mirror tilted. During the entire detection-beam scan, the confocal excitation spot remains at the same position in the sample, while the detection position imaged onto the detector is independently moved with the scan mirror. Right: Schematic representation of the initially generated exciton population with a focused laser pulse and three snapshots showing how the population evolves in space and time due to the energy transport. For details, see text. Adapted from [41] and [144].

The telecentric lens system is designed for ensuring that all PL collected by the objective reaches the detector regardless of the scanning angle of the mirror. For this purpose, the scanning mirror must be imaged into the objective rear aperture to prevent signal fall-off at the scan extremes. Therefore, the front focal point of L1 is centered in the objective rear aperture and the distance between the telecentric lenses corresponds to the sum of the two focal lengths of L1 and L2. Hence, parallel PL light remains parallel after passing through the telecentric lens system. Importantly, the pivot point of the mirror and the rear focal point of L2 must coincide. Then, a change of the mirror's pivot angle leads to a linear shift of the detected position in the sample plane, and hence scanning of the detection point over the sample is enabled independently of the excitation position [145, 146].

The electrical signal of the photodiode is fed into a time-correlated single-photon-counting module, allowing the measurement of the time-resolved PL. With this method, the PL of the sample can be recorded at different positions and at different times after laser excitation and thus information about the exciton kinetics can be obtained.

A detailed characterization of this microscope was worked out in the context of a master thesis by Stephan Wiesneth [144]. Further details, concerning the

experimental setup and the analyses of the obtained signals, can be found in this master thesis and the additional information of sections 4.1 and 4.2.

BIBLIOGRAPHY

- [1] Wooseok Yang, Rajiv Ramanujam Prabhakar, Jeiwan Tan, S. David Tilley, and Jooho Moon. “Strategies for enhancing the photocurrent, photovoltage, and stability of photoelectrodes for photoelectrochemical water splitting.” In: *Chem. Soc. Rev.* 48.19 (2019), pp. 4979–5015. DOI: 10.1039/C8CS00997J. URL: <http://dx.doi.org/10.1039/C8CS00997J>.
- [2] Timothy R. Cook, Dilek K. Dogutan, Steven Y. Reece, Yogesh Surendranath, Thomas S. Teets, and Daniel G. Nocera. “Solar Energy Supply and Storage for the Legacy and Nonlegacy Worlds.” In: *Chem. Rev.* 110.11 (2010), pp. 6474–6502. DOI: 10.1021/cr100246c. URL: <https://doi.org/10.1021/cr100246c>.
- [3] Nathan S. Lewis and Daniel G. Nocera. “Powering the planet: Chemical challenges in solar energy utilization.” In: *Proceedings of the National Academy of Sciences* 103.43 (2006), pp. 15729–15735. DOI: 10.1073/pnas.0603395103. URL: <https://www.pnas.org/content/103/43/15729>.
- [4] Gregory D. Scholes, Graham R. Fleming, Alexandra Olaya-Castro, and Rienk van Grondelle. “Lessons from nature about solar light harvesting.” In: *Nature chemistry* 3.10 (2011), pp. 763–774. DOI: 10.1038/nchem.1145. URL: <https://doi.org/10.1038/nchem.1145>.
- [5] Richard Hildner, Anna Köhler, Peter Müller-Buschbaum, Fabian Panzer, and Mukundan Thelakkat. “ π -Conjugated Donor Polymers: Structure Formation and Morphology in Solution, Bulk and Photovoltaic Blends.” In: *Advanced Energy Materials* 7.16 (2017), p. 1700314. DOI: 10.1002/aenm.201700314.
- [6] Johannes Gierschner. “Directional exciton transport in supramolecular nanostructured assemblies.” In: *Physical chemistry chemical physics : PCCP* 14.38 (2012), pp. 13146–13153. DOI: 10.1039/c2cp42057k.
- [7] Francesca Fassioli, Raymond Dinshaw, Paul C. Arpin, and Gregory D. Scholes. “Photosynthetic light harvesting: excitons and coherence.” In: *Journal of the Royal Society, Interface* 11.92 (2014), p. 20130901. DOI: 10.1098/rsif.2013.0901.
- [8] Gregory D. Scholes, Graham R. Fleming, Lin X. Chen, Alán Aspuru-Guzik, Andreas Buchleitner, David F. Coker, Gregory S. Engel, Rienk van Grondelle, Akihito Ishizaki, David M. Jonas, Jeff S. Lundeen, James K. McCusker, Shaul Mukamel, Jennifer P. Ogilvie, Alexandra Olaya-Castro, Mark A. Ratner, Frank C. Spano, K. Birgitta Whaley, and Xiaoyang Zhu. “Using coherence to enhance function in chemical and

- biophysical systems.” In: *Nature* 543.7647 (2017), pp. 647–656. DOI: 10.1038/nature21425.
- [9] Anna S. Bondarenko, Jasper Knoester, and Thomas L.C. Jansen. “Comparison of methods to study excitation energy transfer in molecular multichromophoric systems.” In: *Chemical Physics* 529 (2020), p. 110478. DOI: 10.1016/j.chemphys.2019.110478.
- [10] Oliver Dumele, Jiahao Chen, James V. Passarelli, and Samuel I. Stupp. “Supramolecular Energy Materials.” In: *Advanced Materials* 32.17 (2020), p. 1907247. DOI: 10.1002/adma.201907247. URL: <https://doi.org/10.1002/adma.201907247>.
- [11] Étienne Boulais, Nicolas P. D. Sawaya, Rémi Veneziano, Alessio Andreoni, James L. Banal, Toru Kondo, Sarthak Mandal, Su Lin, Gabriela S. Schlau-Cohen, Neal W. Woodbury, Hao Yan, Alán Aspuru-Guzik, and Mark Bathe. “Programmed coherent coupling in a synthetic DNA-based excitonic circuit.” In: *Nature materials* 17.2 (2018), pp. 159–166. DOI: 10.1038/nmat5033. URL: <https://doi.org/10.1038/nmat5033>.
- [12] Ritesh Haldar, Marius Jakoby, Antoine Mazel, Qiang Zhang, Alexander Welle, Tawheed Mohamed, Peter Krolla, Wolfgang Wenzel, Stéphane Diring, Fabrice Odobel, Bryce S. Richards, Ian A. Howard, and Christof Wöll. “Anisotropic energy transfer in crystalline chromophore assemblies.” In: *Nature communications* 9.1 (2018), p. 4332. DOI: 10.1038/s41467-018-06829-3. URL: <https://doi.org/10.1038/s41467-018-06829-3>.
- [13] Dong Xiang, Xiaolong Wang, Chuancheng Jia, Takhee Lee, and Xuefeng Guo. “Molecular-Scale Electronics: From Concept to Function.” In: *Chem. Rev.* 116.7 (2016), pp. 4318–4440. DOI: 10.1021/acs.chemrev.5b00680. URL: <https://doi.org/10.1021/acs.chemrev.5b00680>.
- [14] Richard J. Cogdell, Andrew Gall, and Jürgen Köhler. “The architecture and function of the light-harvesting apparatus of purple bacteria: from single molecules to in vivo membranes.” In: *Quarterly reviews of biophysics* 39.3 (2006), pp. 227–324. DOI: 10.1017/S0033583506004434.
- [15] Tihana Mirkovic, Evgeny E. Ostroumov, Jessica M. Anna, Rienk van Grondelle, Govindjee, and Gregory D. Scholes. “Light Absorption and Energy Transfer in the Antenna Complexes of Photosynthetic Organisms.” In: *Chem. Rev.* 117.2 (2017), pp. 249–293. DOI: 10.1021/acs.chemrev.6b00002. URL: <https://doi.org/10.1021/acs.chemrev.6b00002>.
- [16] Jeremy M. Moix, Michael Khasin, and Jianshu Cao. “Coherent quantum transport in disordered systems: I. The influence of dephasing on the transport properties and absorption spectra on one-dimensional systems.” In: *New Journal of Physics* 15.8 (2013), p. 085010. DOI: 10.1088/1367-2630/15/8/085010.

- [17] Justin R. Caram, Sandra Doria, Dörthe M. Eisele, Francesca S. Freyria, Timothy S. Sinclair, Patrick Rebstroff, Seth Lloyd, and Mounqi G. Bawendi. “Room-Temperature Micron-Scale Exciton Migration in a Stabilized Emissive Molecular Aggregate.” In: *Nano letters* 16.11 (2016), pp. 6808–6815. DOI: [10.1021/acs.nanolett.6b02529](https://doi.org/10.1021/acs.nanolett.6b02529).
- [18] Chuang Zhang, Yongli Yan, Yong Sheng Zhao, and Jiannian Yao. “From molecular design and materials construction to organic nanophotonic devices.” In: *Accounts of chemical research* 47.12 (2014), pp. 3448–3458. DOI: [10.1021/ar500192v](https://doi.org/10.1021/ar500192v).
- [19] Johannes Gierschner, Larry Lüer, Begoña Milián-Medina, Dieter Oelkrug, and Hans-Joachim Egelhaaf. “Highly Emissive H-Aggregates or Aggregation-Induced Emission Quenching? The Photophysics of All-Trans para-Distyrylbenzene.” In: *The Journal of Physical Chemistry Letters* 4.16 (2013), pp. 2686–2697. DOI: [10.1021/jz400985t](https://doi.org/10.1021/jz400985t).
- [20] Jean-Luc Brédas, Edward H. Sargent, and Gregory D. Scholes. “Photovoltaic concepts inspired by coherence effects in photosynthetic systems.” In: *Nature materials* 16.1 (2016), pp. 35–44. DOI: [10.1038/nmat4767](https://doi.org/10.1038/nmat4767).
- [21] Gregory D. Scholes. “Quantum-Coherent Electronic Energy Transfer: Did Nature Think of It First?” In: *J. Phys. Chem. Lett.* 1.1 (2010), pp. 2–8. DOI: [10.1021/jz900062f](https://doi.org/10.1021/jz900062f). URL: <https://doi.org/10.1021/jz900062f>.
- [22] Tobias Brixner, Richard Hildner, Jürgen Köhler, Christoph Lambert, and Frank Würthner. “Exciton Transport in Molecular Aggregates - From Natural Antennas to Synthetic Chromophore Systems.” In: *Advanced Energy Materials* 7.16 (2017), p. 1700236. DOI: [10.1002/aenm.201700236](https://doi.org/10.1002/aenm.201700236).
- [23] Zachary B. Henson, Klaus Müllen, and Guillermo C. Bazan. “Design strategies for organic semiconductors beyond the molecular formula.” In: *Nature chemistry* 4.9 (2012), pp. 699–704. DOI: [10.1038/nchem.1422](https://doi.org/10.1038/nchem.1422). URL: <https://doi.org/10.1038/nchem.1422>.
- [24] Ghislaine Vantomme and E. W. Meijer. “The construction of supramolecular systems.” In: *Science* 363.6434 (2019), pp. 1396–1397. DOI: [10.1126/science.aav4677](https://doi.org/10.1126/science.aav4677).
- [25] Hans-Werner Schmidt and Frank Würthner. “A Periodic System of Supramolecular Elements.” In: *Angewandte Chemie (International ed. in English)* 59.23 (2020), pp. 8766–8775. DOI: [10.1002/anie.201915643](https://doi.org/10.1002/anie.201915643).
- [26] Andreas T. Haedler, Klaus Kreger, Abey Issac, Bernd Wittmann, Milan Kivala, Natalie Hammer, Jürgen Köhler, Hans-Werner Schmidt, and Richard Hildner. “Long-range energy transport in single supramolecular nanofibres at room temperature.” In: *Nature* 523.7559 (2015), pp. 196–199. DOI: [10.1038/nature14570](https://doi.org/10.1038/nature14570).

- [27] Morgan Stefik, Stefan Guldin, Silvia Vignolini, Ulrich Wiesner, and Ullrich Steiner. “Block copolymer self-assembly for nanophotonics.” In: *Chem. Soc. Rev.* 44.15 (2015), pp. 5076–5091. DOI: 10.1039/C4CS00517A. URL: <http://dx.doi.org/10.1039/C4CS00517A>.
- [28] Gleb M. Akselrod, Parag B. Deotare, Nicholas J. Thompson, Jiye Lee, William A. Tisdale, Marc A. Baldo, Vinod M. Menon, and Vladimir Bulović. “Visualization of exciton transport in ordered and disordered molecular solids.” In: *Nature communications* 5 (2014), p. 3646. DOI: 10.1038/ncomms4646.
- [29] Xu-Hui Jin, Michael B. Price, John R. Finnegan, Charlotte E. Boott, Johannes M. Richter, Akshay Rao, S. Matthew Menke, Richard H. Friend, George R. Whittell, and Ian Manners. “Long-range exciton transport in conjugated polymer nanofibers prepared by seeded growth.” In: *Science* 360.6391 (2018), pp. 897–900. DOI: 10.1126/science.aar8104. URL: <https://science.sciencemag.org/content/360/6391/897>.
- [30] Christian B. Winiger, Shaoguang Li, Ganesh R. Kumar, Simon M. Langenegger, and Robert Häner. “Long-distance electronic energy transfer in light-harvesting supramolecular polymers.” In: *Angewandte Chemie (International ed. in English)* 53.49 (2014), pp. 13609–13613. DOI: 10.1002/anie.201407968.
- [31] Taehee Kim, Sujin Ham, Sang Hyeon Lee, Yongseok Hong, and Dongho Kim. “Enhancement of exciton transport in porphyrin aggregate nanostructures by controlling the hierarchical self-assembly.” In: *Nanoscale* 10.35 (2018), pp. 16438–16446. DOI: 10.1039/C8NR05016C. URL: <http://dx.doi.org/10.1039/C8NR05016C>.
- [32] Dorte M. Eisele, Jasper Knoester, Stefan Kirstein, Jurgen P. Rabe, and David A. Vanden Bout. “Uniform exciton fluorescence from individual molecular nanotubes immobilized on solid substrates.” In: *Nature nanotechnology* 4.10 (2009), pp. 658–663. DOI: 10.1038/nnano.2009.227.
- [33] Katie A. Clark, Emma L. Krueger, and David A. Vanden Bout. “Direct Measurement of Energy Migration in Supramolecular Carbocyanine Dye Nanotubes.” In: *The journal of physical chemistry letters* 5.13 (2014), pp. 2274–2282. DOI: 10.1021/jz500634f.
- [34] Yan Wan, Anna Stradomska, Jasper Knoester, and Libai Huang. “Direct Imaging of Exciton Transport in Tubular Porphyrin Aggregates by Ultrafast Microscopy.” In: *J. Am. Chem. Soc.* 139.21 (2017), pp. 7287–7293. DOI: 10.1021/jacs.7b01550. URL: <https://doi.org/10.1021/jacs.7b01550>.
- [35] Nicholas J. Hestand and Frank C. Spano. “Expanded Theory of H- and J-Molecular Aggregates: The Effects of Vibronic Coupling and Intermolecular Charge Transfer.” In: *Chemical reviews* 118.15 (2018), pp. 7069–7163. DOI: 10.1021/acs.chemrev.7b00581.

- [36] Gregory D. Scholes. “Designing light-harvesting antenna systems based on superradiant molecular aggregates.” In: *Chemical Physics* 275.1 (2002), pp. 373–386. DOI: 10.1016/S0301-0104(01)00533-X. URL: <http://www.sciencedirect.com/science/article/pii/S030101040100533X>.
- [37] Nicolas P. D. Sawaya, Dmitriy Rappoport, Daniel P. Tabor, and Alán Aspuru-Guzik. “Excitonics: A Set of Gates for Molecular Exciton Processing and Signaling.” In: *ACS Nano* 12.7 (2018), pp. 6410–6420. DOI: 10.1021/acsnano.8b00584. URL: <https://doi.org/10.1021/acsnano.8b00584>.
- [38] Qiu Hong Cui, Qian Peng, Yi Luo, Yuqian Jiang, Yongli Yan, Cong Wei, Zhigang Shuai, Cheng Sun, Jiannian Yao, and Yong Sheng Zhao. “Asymmetric photon transport in organic semiconductor nanowires through electrically controlled exciton diffusion.” In: *Sci Adv* 4.3 (2018), eaap9861. DOI: 10.1126/sciadv.aap9861.
- [39] Mike Heilemann, Philip Tinnefeld, Gabriel Sanchez Mosteiro, Maria Garcia Parajo, Niek F. van Hulst, and Markus Sauer. “Multistep Energy Transfer in Single Molecular Photonic Wires.” In: *J. Am. Chem. Soc.* 126.21 (2004), pp. 6514–6515. DOI: 10.1021/ja049351u. URL: <https://doi.org/10.1021/ja049351u>.
- [40] Debangshu Chaudhuri, Dongbo Li, Yanke Che, Eyal Shafran, Jordan M. Gerton, Ling Zang, and John M. Lupton. “Enhancing Long-Range Exciton Guiding in Molecular Nanowires by H-Aggregation Lifetime Engineering.” In: *Nano Lett* 11.2 (2011), pp. 488–492. DOI: 10.1021/nl1033039. URL: <https://doi.org/10.1021/nl1033039>.
- [41] Naomi S. Ginsberg and William A. Tisdale. “Spatially Resolved Photogenerated Exciton and Charge Transport in Emerging Semiconductors.” In: *Annual review of physical chemistry* 71 (2020), pp. 1–30. DOI: 10.1146/annurev-physchem-052516-050703.
- [42] Roel Tempelaar, Thomas L. C. Jansen, and Jasper Knoester. “Exciton-Exciton Annihilation Is Coherently Suppressed in H-Aggregates, but Not in J-Aggregates.” In: *The journal of physical chemistry letters* 8.24 (2017), pp. 6113–6117. DOI: 10.1021/acs.jpcllett.7b02745.
- [43] Anne Myers Kelley. *Condensed-Phase Molecular Spectroscopy and Photophysics*. New York: John Wiley & Sons, 2012.
- [44] Wolfgang Demtröder. *Molekülphysik - Theoretische Grundlagen und experimentelle Methoden*. Berlin: Walter de Gruyter, 2013.
- [45] Wolfgang Demtröder. *Laserspektroskopie: Grundlagen und Techniken*. Berlin, Heidelberg: Springer-Verlag Berlin Heidelberg, 2007.
- [46] Hermann Haken and Hans C. Wolf. *Molekülphysik und Quantenchemie - Einführung in die experimentellen und theoretischen Grundlagen*. Berlin Heidelberg New York: Springer-Verlag, 2013.

- [47] Volkhard May and Oliver Kühn. *Charge and Energy Transfer Dynamics in Molecular Systems*. New York: John Wiley & Sons, 2011.
- [48] Jeanne L. McHale. *Molecular Spectroscopy*. Boca Raton, Fla: CRC Press, 2017.
- [49] William W. Parson. *Modern Optical Spectroscopy - With Exercises and Examples from Biophysics and Biochemistry*. Berlin, Heidelberg: Springer, 2007.
- [50] Leonas Valkunas, Darius Abramavicius, and Tomás Mancal. *Molecular Excitation Dynamics and Relaxation - Quantum Theory and Spectroscopy*. New York: John Wiley & Sons, 2013.
- [51] Anna Köhler and Heinz Bässler. *Electronic Processes in Organic Semiconductors - An Introduction*. New York: John Wiley & Sons, 2015.
- [52] Wikipedia contributors. *Fermi's golden rule* — *Wikipedia, The Free Encyclopedia*. [Online; accessed 13-May-2020]. 2020. URL: https://en.wikipedia.org/w/index.php?title=Fermi%27s_golden_rule&oldid=954331572.
- [53] Rodney Loudon. *The Quantum Theory of Light*. New York, London: OUP Oxford, 2000.
- [54] Attila Szabo and Neil S. Ostlund. *Modern Quantum Chemistry - Introduction to Advanced Electronic Structure Theory*. New York: Dover Publications, 2012.
- [55] Wolfgang Demtröder. *Atoms, Molecules and Photons - An Introduction to Atomic-, Molecular- and Quantum Physics*. Berlin Heidelberg: Springer Science & Business Media, 2010.
- [56] Wikipedia contributors. *Franck–Condon principle* — *Wikipedia, The Free Encyclopedia*. [Online; accessed 14-May-2020]. 2020. URL: https://en.wikipedia.org/w/index.php?title=Franck%E2%80%93Condon_principle&oldid=943817290.
- [57] S. K. Lower and M. A. El-Sayed. “The Triplet State and Molecular Electronic Processes in Organic Molecules.” In: *Chem. Rev.* 66.2 (1966), pp. 199–241. DOI: [10.1021/cr60240a004](https://doi.org/10.1021/cr60240a004).
- [58] Thomas J. Penfold, Etienne Gindensperger, Chantal Daniel, and Christel M. Marian. “Spin-Vibronic Mechanism for Intersystem Crossing.” In: *Chemical reviews* 118.15 (2018), pp. 6975–7025. DOI: [10.1021/acs.chemrev.7b00617](https://doi.org/10.1021/acs.chemrev.7b00617).
- [59] Jianzhang Zhao, Wanhua Wu, Jifu Sun, and Song Guo. “Triplet photosensitizers: from molecular design to applications.” In: *Chemical Society reviews* 42.12 (2013), pp. 5323–5351. DOI: [10.1039/c3cs35531d](https://doi.org/10.1039/c3cs35531d).
- [60] Joseph R. Lakowicz. *Principles of Fluorescence Spectroscopy*. Berlin Heidelberg: Springer Science & Business Media, 2007.

- [61] Bernard Valeur and Mário Nuno Berberan-Santos. *Molecular Fluorescence - Principles and Applications*. New York: John Wiley & Sons, 2013.
- [62] David Willock. *Molecular Symmetry*. New York: John Wiley & Sons, 2009.
- [63] G. W. Robinson and R. P. Frosch. “Theory of Electronic Energy Relaxation in the Solid Phase.” In: *The Journal of Chemical Physics* 37.9 (1962), pp. 1962–1973. DOI: 10.1063/1.1733413.
- [64] G. W. Robinson and R. P. Frosch. “Electronic Excitation Transfer and Relaxation.” In: *The Journal of Chemical Physics* 38.5 (1963), pp. 1187–1203. DOI: 10.1063/1.1733823.
- [65] W. Siebrand. “Radiationless Transitions in Polyatomic Molecules. I. Calculation of Franck—Condon Factors.” In: *The Journal of Chemical Physics* 46.2 (1967), p. 440. DOI: 10.1063/1.1840685.
- [66] Zhongfu An, Chao Zheng, Ye Tao, Runfeng Chen, Huifang Shi, Ting Chen, Zhixiang Wang, Huanhuan Li, Renren Deng, Xiaogang Liu, and Wei Huang. “Stabilizing triplet excited states for ultralong organic phosphorescence.” In: *Nature materials* 14.7 (2015), pp. 685–690. DOI: 10.1038/nmat4259.
- [67] Kenry, Chengjian Chen, and Bin Liu. “Enhancing the performance of pure organic room-temperature phosphorescent luminophores.” In: *Nature communications* 10.1 (2019), p. 2111. DOI: 10.1038/s41467-019-10033-2.
- [68] Hisahiro Sasabe, Yuki Kato, Yuichiro Watanabe, Tatsuya Ohsawa, Naoya Aizawa, Wataru Fujiwara, Yong-Jin Pu, Hiroshi Katagiri, and Junji Kido. “Room-Temperature Phosphorescence from a Series of 3-Pyridylcarbazole Derivatives.” In: *Chemistry – A European Journal* 25.71 (2019), pp. 16294–16300. DOI: 10.1002/chem.201903100. URL: <https://doi.org/10.1002/chem.201903100>.
- [69] Suzhi Cai, Huifang Shi, Dan Tian, Huili Ma, Zhichao Cheng, Qi Wu, Mingxing Gu, Ling Huang, Zhongfu An, Qian Peng, and Wei Huang. “Enhancing Ultralong Organic Phosphorescence by Effective π -Type Halogen Bonding.” In: *Advanced Functional Materials* 28.9 (2018), p. 1705045. DOI: 10.1002/adfm.201705045.
- [70] Leonas Valkunas, Herbert Van Amerongen, and Rienk Van Grondelle. *Photosynthetic Excitons*. Singapur: World Scientific, 2000.
- [71] Nicholas J. Hestand and Frank C. Spano. “Molecular Aggregate Photo-physics beyond the Kasha Model: Novel Design Principles for Organic Materials.” In: *Accounts of chemical research* 50.2 (2017), pp. 341–350. DOI: 10.1021/acs.accounts.6b00576.

- [72] D. J. Heijs, V. A. Malyshev, and J. Knoester. “Decoherence of excitons in multichromophore systems: thermal line broadening and destruction of superradiant emission.” In: *Physical review letters* 95.17 (2005), p. 177402. DOI: [10.1103/PhysRevLett.95.177402](https://doi.org/10.1103/PhysRevLett.95.177402).
- [73] Björn Kriete, Julian Lüttig, Tenzin Kunsel, Pavel Malý, Thomas L. C. Jansen, Jasper Knoester, Tobias Brixner, and Maxim S. Pshenichnikov. “Interplay between structural hierarchy and exciton diffusion in artificial light harvesting.” In: *Nature communications* 10.1 (2019), p. 4615. DOI: [10.1038/s41467-019-12345-9](https://doi.org/10.1038/s41467-019-12345-9).
- [74] Frank C. Spano, Jenny Clark, Carlos Silva, and Richard H. Friend. “Determining exciton coherence from the photoluminescence spectral line shape in poly(3-hexylthiophene) thin films.” In: *The Journal of Chemical Physics* 130.7 (2009), p. 074904. DOI: [10.1063/1.3076079](https://doi.org/10.1063/1.3076079).
- [75] Jelley E.E. In: *Nature* 138 (1936), p. 1009.
- [76] Scheibe G. In: *Angew. Chem.* 49 (1936), p. 563.
- [77] M. Kasha, H. R. Rawls, and M. Ashraf El-Bayoumi. “The exciton model in molecular spectroscopy.” In: *Pure and Applied Chemistry* 11.3-4 (1965), pp. 371–392. DOI: [10.1351/pac196511030371](https://doi.org/10.1351/pac196511030371).
- [78] Frank C. Spano and Carlos Silva. “H- and J-aggregate behavior in polymeric semiconductors.” In: *Annual review of physical chemistry* 65 (2014), pp. 477–500. DOI: [10.1146/annurev-physchem-040513-103639](https://doi.org/10.1146/annurev-physchem-040513-103639).
- [79] De Greef, Tom F A, Maarten M. J. Smulders, Martin Wolfs, Schenning, Albert P H J, Rint P. Sijbesma, and E. W. Meijer. “Supramolecular polymerization.” In: *Chemical reviews* 109.11 (2009), pp. 5687–5754. DOI: [10.1021/cr900181u](https://doi.org/10.1021/cr900181u).
- [80] Mathijs F. J. Mabesoone and E. W. Meijer. “Counterintuitive consequences of competitive pathways in supramolecular polymerizations.” In: *Journal of Polymer Science* 58.1 (2019), pp. 25–29. DOI: [10.1002/pola.29456](https://doi.org/10.1002/pola.29456).
- [81] Peter A. Korevaar, Subi J. George, Albert J. Markvoort, Maarten M. J. Smulders, Peter A. J. Hilbers, Schenning, Albert P H J, De Greef, Tom F A, and E. W. Meijer. “Pathway complexity in supramolecular polymerization.” In: *Nature* 481.7382 (2012), pp. 492–496. DOI: [10.1038/nature10720](https://doi.org/10.1038/nature10720).
- [82] Chidambar Kulkarni, E. W. Meijer, and Anja R. A. Palmans. “Cooperativity Scale: A Structure-Mechanism Correlation in the Self-Assembly of Benzene-1,3,5-tricarboxamides.” In: *Accounts of chemical research* 50.8 (2017), pp. 1928–1936. DOI: [10.1021/acs.accounts.7b00176](https://doi.org/10.1021/acs.accounts.7b00176).

- [83] April Oleson, Tong Zhu, Ian S. Dunn, David Bialas, Yu Bai, Wenqing Zhang, Mingji Dai, David R. Reichman, Roel Tempelaar, Libai Huang, and Frank C. Spano. “Perylene Diimide-Based H_j- and h_J-Aggregates: The Prospect of Exciton Band Shape Engineering in Organic Materials.” In: *The Journal of Physical Chemistry C* 123.33 (2019), pp. 20567–20578. DOI: 10.1021/acs.jpcc.9b04429.
- [84] Juan Wang, Kai Liu, Ruirui Xing, and Xuehai Yan. “Peptide self-assembly: thermodynamics and kinetics.” In: *Chemical Society reviews* 45.20 (2016), pp. 5589–5604. DOI: 10.1039/c6cs00176a.
- [85] Wolfgang Wagner, Marius Wehner, Vladimir Stepanenko, and Frank Würthner. “Supramolecular Block Copolymers by Seeded Living Polymerization of Perylene Bisimides.” In: *Journal of the American Chemical Society* 141.30 (2019), pp. 12044–12054. DOI: 10.1021/jacs.9b04935.
- [86] Marius Wehner, Merle Insa Silja Röhr, Michael Bühler, Vladimir Stepanenko, Wolfgang Wagner, and Frank Würthner. “Supramolecular Polymorphism in One-Dimensional Self-Assembly by Kinetic Pathway Control.” In: *Journal of the American Chemical Society* 141.14 (2019), pp. 6092–6107. DOI: 10.1021/jacs.9b02046.
- [87] Andreas Haedler. “Synthesis, Self-Assembly and Photophysical Properties of Multichromophoric Systems.” In: *Doctoral thesis, 2015, University of Bayreuth, Interdisciplinary Institutions* (2015).
- [88] Yoon S. Lee. *Self-Assembly and Nanotechnology - A Force Balance Approach*. New York: John Wiley & Sons, 2008.
- [89] G. M. Whitesides, J. P. Mathias, and C. T. Seto. “Molecular self-assembly and nanochemistry: a chemical strategy for the synthesis of nanostructures.” In: *Science* 254.5036 (1991), pp. 1312–1319. DOI: 10.1126/science.1962191.
- [90] Andreas T. Haedler, Stefan C. J. Meskers, R. Helen Zha, Milan Kivala, Hans-Werner Schmidt, and E. W. Meijer. “Pathway Complexity in the Enantioselective Self-Assembly of Functional Carbonyl-Bridged Triarylamine Trisamides.” In: *Journal of the American Chemical Society* 138.33 (2016), pp. 10539–10545. DOI: 10.1021/jacs.6b05184.
- [91] Tomoya Fukui, Shinnosuke Kawai, Satoko Fujinuma, Yoshitaka Matsushita, Takeshi Yasuda, Tsuneaki Sakurai, Shu Seki, Masayuki Takeuchi, and Kazunori Sugiyasu. “Control over differentiation of a metastable supramolecular assembly in one and two dimensions.” In: *Nature chemistry* 9.5 (2017), pp. 493–499. DOI: 10.1038/nchem.2684. URL: <https://doi.org/10.1038/nchem.2684>.

- [92] Wolfgang Wagner, Marius Wehner, Vladimir Stepanenko, Soichiro Ogi, and Frank Würthner. “Living Supramolecular Polymerization of a Perylene Bisimide Dye into Fluorescent J-Aggregates.” In: *Angewandte Chemie* 129.50 (2017), pp. 16224–16228. DOI: 10.1002/ange.201709307.
- [93] Aritra Sarkar, Tejmani Behera, Ranjan Sasmal, Riccardo Capelli, Charly Empereur-mot, Jaladhar Mahato, Sarit S. Agasti, Giovanni M. Pavan, Arindam Chowdhury, and Subi J. George. “Cooperative Supramolecular Block Copolymerization for the Synthesis of Functional Axial Organic Heterostructures.” In: *J. Am. Chem. Soc.* 142.26 (2020), pp. 11528–11539. DOI: 10.1021/jacs.0c04404.
- [94] Dörthe M. Eisele, Dylan H. Arias, Xiaofeng Fu, Erik A. Bloemsma, Colby P. Steiner, Russell A. Jensen, Patrick Rebentrost, Holger Eisele, Andrei Tokmakoff, Seth Lloyd, Keith A. Nelson, Daniela Nicastro, Jasper Knoester, and Mounji G. Bawendi. “Robust excitons inhabit soft supramolecular nanotubes.” In: *Proceedings of the National Academy of Sciences* 111.33 (2014), E3367–E3375. DOI: 10.1073/pnas.1408342111. URL: <https://www.pnas.org/content/111/33/E3367>.
- [95] Bernd Wittmann, Felix A. Wenzel, Stephan Wiesneth, Andreas T. Haedler, Markus Drechsler, Klaus Kreger, Jürgen Köhler, E. W. Meijer, Hans-Werner Schmidt, and Richard Hildner. “Enhancing Long-Range Energy Transport in Supramolecular Architectures by Tailoring Coherence Properties.” In: *J. Am. Chem. Soc.* 142.18 (2020), pp. 8323–8330. DOI: 10.1021/jacs.0c01392. URL: <https://doi.org/10.1021/jacs.0c01392>.
- [96] Leon van Dijk, Peter A. Bobbert, and Frank C. Spano. “Extreme Sensitivity of Circular Dichroism to Long-Range Excitonic Couplings in Helical Supramolecular Assemblies.” In: *J. Phys. Chem. B* 114.2 (2010), pp. 817–825. DOI: 10.1021/jp911081b. URL: <https://doi.org/10.1021/jp911081b>.
- [97] Michael R. Philpott. “Theory of the Coupling of Electronic and Vibrational Excitations in Molecular Crystals and Helical Polymers.” In: *The Journal of Chemical Physics* 55.5 (1971), p. 2039. DOI: 10.1063/1.1676371.
- [98] Frank C. Spano. “The spectral signatures of Frenkel polarons in H- and J-aggregates.” In: *Accounts of chemical research* 43.3 (2010), pp. 429–439. DOI: 10.1021/ar900233v.
- [99] Frank C. Spano, Stefan C. J. Meskers, Emanuelle Hennebicq, and David Beljonne. “Probing excitation delocalization in supramolecular chiral stacks by means of circularly polarized light: experiment and modeling.” In: *Journal of the American Chemical Society* 129.22 (2007), pp. 7044–7054. DOI: 10.1021/ja067321g.

- [100] Frank C. Spano. "Absorption and emission in oligo-phenylene vinylene nanoaggregates: The role of disorder and structural defects." In: *The Journal of Chemical Physics* 116.13 (2002), p. 5877. DOI: 10.1063/1.1446034.
- [101] Frank C. Spano. "Modeling disorder in polymer aggregates: the optical spectroscopy of regioregular poly(3-hexylthiophene) thin films." In: *The Journal of chemical physics* 122.23 (2005), p. 234701. DOI: 10.1063/1.1914768.
- [102] E.W. Knapp. "Lineshapes of molecular aggregates, exchange narrowing and intersite correlation." In: *Chemical Physics* 85.1 (1984), pp. 73–82. DOI: 10.1016/S0301-0104(84)85174-5. URL: <http://www.sciencedirect.com/science/article/pii/S0301010484851745>.
- [103] S. M. Vlaming, V. A. Malyshev, A. Eisfeld, and J. Knoester. "Subdiffusive exciton motion in systems with heavy-tailed disorder." In: *The Journal of Chemical Physics* 138.21 (2013), p. 214316. DOI: 10.1063/1.4808155.
- [104] Aboma Merdasa, Ángel J. Jiménez, Rafael Camacho, Matthias Meyer, Frank Würthner, and Ivan G. Scheblykin. "Single Lévy states-disorder induced energy funnels in molecular aggregates." In: *Nano letters* 14.12 (2014), pp. 6774–6781. DOI: 10.1021/nl5021188.
- [105] Semion K. Saikin, Mars A. Shakirov, Christoph Kreisbeck, Uri Peskin, Yurii N. Proshin, and Alán Aspuru-Guzik. "On the Long-Range Exciton Transport in Molecular Systems: The Application to H-Aggregated Heterotriangulene Chains." In: *The Journal of Physical Chemistry C* 121.45 (2017), pp. 24994–25002. DOI: 10.1021/acs.jpcc.7b08933.
- [106] Anna Bondarenko. "Modeling of excitonic properties in tubular molecular aggregates." PhD thesis. University of Groningen, 2019. DOI: 10.33612/diss.98528598.
- [107] J. A. Leegwater. "Coherent Versus Incoherent Energy Transfer and Trapping in Photosynthetic Antenna Complexes." In: *J. Phys. Chem.* 100.7 (1996). DOI: 10.1109/EQEC.1996.561788.
- [108] Philip D. Laible, Robert S. Knox, and Thomas G. Owens. "Detailed Balance in Förster–Dexter Excitation Transfer and Its Application to Photosynthesis." In: *The Journal of Physical Chemistry B* 102.9 (1998), pp. 1641–1648. DOI: 10.1021/jp9730104. URL: <https://doi.org/10.1021/jp9730104>.
- [109] Ranko Richert and Alexander Blumen. *Disorder Effects on Relaxational Processes - Glasses, Polymers, Proteins*. Berlin Heidelberg: Springer Science & Business Media, 2012.
- [110] Sebastiaan Maarten Vlaming. "Localization and transport of excitation energy in inhomogeneous supramolecular arrays." PhD thesis. University of Groningen, 2010.

- [111] François Dubin, Romain Melet, Thierry Barisien, Roger Grousson, Laurent Legrand, Michel Schott, and Valia Voliotis. “Macroscopic coherence of a single exciton state in an organic quantum wire.” In: *Nature Physics* 2.1 (2006), pp. 32–35. DOI: 10.1038/nphys196. URL: <https://doi.org/10.1038/nphys196>.
- [112] William Barford and Christopher D. P. Duffy. “Role of quantum coherence and energetic disorder in exciton transport in polymer films.” In: *Physical Review B* 74.7 (2006). DOI: 10.1103/PhysRevB.74.075207.
- [113] S. M. Vlaming, V. A. Malyshev, and J. Knoester. “Nonmonotonic energy harvesting efficiency in biased exciton chains.” In: *The Journal of Chemical Physics* 127.15 (2007), p. 154719. DOI: 10.1063/1.2784556.
- [114] M. Bednarz, V. A. Malyshev, and J. Knoester. “Temperature dependent fluorescence in disordered Frenkel chains: interplay of equilibration and local band-edge level structure.” In: *Physical review letters* 91.21 (2003), p. 217401. DOI: 10.1103/PhysRevLett.91.217401.
- [115] A. V. Malyshev, V. A. Malyshev, and F. Domínguez-Adame. “On the Low-Temperature Diffusion of Localized Frenkel Excitons in Linear Molecular Aggregates.” In: *The Journal of Physical Chemistry B* 107.18 (2003), pp. 4418–4425. DOI: 10.1021/jp0341218.
- [116] S. Matthew Menke and Russell J. Holmes. “Exciton diffusion in organic photovoltaic cells.” In: *Energy Environ. Sci.* 7.2 (2014), pp. 499–512. DOI: 10.1039/C3EE42444H.
- [117] Shlomo Havlin and Daniel Ben-Avraham. “Diffusion in disordered media.” In: *Advances in Physics* 36.6 (1987), pp. 695–798. DOI: 10.1080/00018738700101072.
- [118] Jianrong Wu and Keith M. Berland. “Propagators and time-dependent diffusion coefficients for anomalous diffusion.” In: *Biophysical journal* 95.4 (2008), pp. 2049–2052. DOI: 10.1529/biophysj.107.121608. URL: <https://pubmed.ncbi.nlm.nih.gov/18487294>.
- [119] Gleb M. Akselrod, Ferry Prins, Lisa V. Poulidakos, Elizabeth M. Y. Lee, Mark C. Weidman, A. Jolene Mork, Adam P. Willard, Vladimir Bulović, and William A. Tisdale. “Subdiffusive exciton transport in quantum dot solids.” In: *Nano letters* 14.6 (2014), pp. 3556–3562. DOI: 10.1021/nl501190s.
- [120] P. Reineker V.M. Kenkre. *Exciton Dynamics in Molecular Crystals and Aggregates*. Berlin: Springer, 1982.
- [121] Oleksandr V. Mikhnenko, Paul W. M. Blom, and Thuc-Quyen Nguyen. “Exciton diffusion in organic semiconductors.” In: *Energy & Environmental Science* 8.7 (2015), pp. 1867–1888. DOI: 10.1039/C5EE00925A.

- [122] Tong Zhu, Yan Wan, and Libai Huang. “Direct Imaging of Frenkel Exciton Transport by Ultrafast Microscopy.” In: *Accounts of chemical research* 50.7 (2017), pp. 1725–1733. DOI: 10.1021/acs.accounts.7b00155.
- [123] Yan Wan, Zhi Guo, Tong Zhu, Suxia Yan, Justin Johnson, and Libai Huang. “Cooperative singlet and triplet exciton transport in tetracene crystals visualized by ultrafast microscopy.” In: *Nature chemistry* 7.10 (2015), pp. 785–792. DOI: 10.1038/nchem.2348.
- [124] Seth Lloyd, Masoud Mohseni, Alireza Shabani, and Herschel Rabitz. *The quantum Goldilocks effect: on the convergence of timescales in quantum transport*. 2011. arXiv: 1111.4982.
- [125] Volkhard May. “Kinetic theory of exciton-exciton annihilation.” In: *The Journal of chemical physics* 140.5 (2014), p. 054103. DOI: 10.1063/1.4863259.
- [126] Daniel ben Avraham, Martin A. Burschka, and Charles R. Doering. “Statics and dynamics of a diffusion-limited reaction: Anomalous kinetics, nonequilibrium self-ordering, and a dynamic transition.” In: *Journal of Statistical Physics* 60.5 (1990), pp. 695–728. DOI: 10.1007/BF01025990. URL: <https://doi.org/10.1007/BF01025990>.
- [127] Yasunari Tamai, Hideo Ohkita, Hiroaki Bente, and Shinzaburo Ito. “Exciton Diffusion in Conjugated Polymers: From Fundamental Understanding to Improvement in Photovoltaic Conversion Efficiency.” In: *The journal of physical chemistry letters* 6.17 (2015), pp. 3417–3428. DOI: 10.1021/acs.jpcllett.5b01147.
- [128] Shibin Deng, Enzheng Shi, Long Yuan, Linrui Jin, Letian Dou, and Libai Huang. “Long-range exciton transport and slow annihilation in two-dimensional hybrid perovskites.” In: *Nature communications* 11.1 (2020), p. 664. DOI: 10.1038/s41467-020-14403-z.
- [129] G. Lanzani C. Gadermaier. “Photophysics of conjugated polymers: the contribution of ultrafast spectroscopy.” In: *Journal of Physics: Condensed Matter* 14.9785 (2002).
- [130] Clement Daniel, Laura M. Herz, and Carlos Silva. “Exciton bimolecular annihilation dynamics in supramolecular nanostructures of conjugated oligomers.” In: *Physical review. B, Condensed matter* 68 (2003).
- [131] Jason D. A. Lin, Oleksandr V. Mikhnenko, Jingrun Chen, Zarifi Masri, Arvydas Ruseckas, Alexander Mikhailovsky, Reilly P. Raab, Jianhua Liu, Paul W. M. Blom, Maria Antonietta Loi, Carlos J. García-Cervera, Ifor D. W. Samuel, and Thuc-Quyen Nguyen. “Systematic study of exciton diffusion length in organic semiconductors by six experimental methods.” In: *Mater. Horiz.* 1.2 (2014), pp. 280–285. DOI: 10.1039/C3MH00089C.

- [132] Deirdre O’Carroll, Ingo Lieberwirth, and Gareth Redmond. “Microcavity effects and optically pumped lasing in single conjugated polymer nanowires.” In: *Nature nanotechnology* 2.3 (2007), pp. 180–184. DOI: 10.1038/nnano.2007.35.
- [133] Bahaa E. A. Saleh and Malvin Carl Teich. *Fundamentals of Photonics*. New York: John Wiley & Sons, 2019.
- [134] Christian Schörner, Sajedeh Motamen, Laurent Simon, Günter Reiter, and Richard Hildner. “Self-Interference of Exciton Emission in Organic Single Crystals Visualized by Energy-Momentum Spectroscopy.” In: *ACS omega* 3.6 (2018), pp. 6728–6736. DOI: 10.1021/acsomega.8b00811.
- [135] Ibrahim Dursun, Yangzi Zheng, Tianle Guo, Michele de Bastiani, Bekir Turedi, Lutfan Sinatra, Md Azimul Haque, Bin Sun, Ayan A. Zhumeckenov, Makhsud I. Saidaminov, García de Arquer, F. Pelayo, Edward H. Sargent, Tom Wu, Yuri N. Gartstein, Osman M. Bakr, Omar F. Mohammed, and Anton V. Malko. “Efficient Photon Recycling and Radiation Trapping in Cesium Lead Halide Perovskite Waveguides.” In: *ACS Energy Letters* 3.7 (2018), pp. 1492–1498. DOI: 10.1021/acsenergylett.8b00758.
- [136] Yanjun Fang, Haotong Wei, Qingfeng Dong, and Jinsong Huang. “Quantification of re-absorption and re-emission processes to determine photon recycling efficiency in perovskite single crystals.” In: *Nature communications* 8 (2017), p. 14417. DOI: 10.1038/ncomms14417.
- [137] Luis M. Pazos-Outón, Monika Szumilo, Robin Lamboll, Johannes M. Richter, Micaela Crespo-Quesada, Mojtaba Abdi-Jalebi, Harry J. Beeson, Milan Vrućinić, Mejd Alsari, Henry J. Snaith, Bruno Ehrler, Richard H. Friend, and Felix Deschler. “Photon recycling in lead iodide perovskite solar cells.” In: *Science* 351.6280 (2016), pp. 1430–1433. DOI: 10.1126/science.aaf1168. URL: <https://science.sciencemag.org/content/351/6280/1430>.
- [138] Anna K. Topczak, Tobias Roller, Bernd Engels, Wolfgang Brütting, and Jens Pflaum. “Nonthermally activated exciton transport in crystalline organic semiconductor thin films.” In: *Physical Review B* 89.20 (2014). DOI: 10.1103/PhysRevB.89.201203.
- [139] Jovana Jevric, Simon M. Langenegger, and Robert Häner. “Light-Harvesting Supramolecular Polymers: Energy Transfer to Various Polyaromatic Acceptors.” In: *European Journal of Organic Chemistry* 30 (2020), p. 31. DOI: 10.1002/ejoc.202000441.
- [140] O. V. Mikhnenko, F. Cordella, A. B. Sieval, J. C. Hummelen, P. W. M. Blom, and M. A. Loi. “Temperature dependence of exciton diffusion in conjugated polymers.” In: *The journal of physical chemistry. B* 112.37 (2008), pp. 11601–11604. DOI: 10.1021/jp8042363.

-
- [141] Björn Kriete. “Exciton dynamics in self-assembled molecular nanotubes.” English. PhD thesis. University of Groningen, 2020. DOI: 10.33612/diss.123832795.
- [142] Raj Pandya, Richard Y. S. Chen, Qifei Gu, Jeffrey Gorman, Florian Auras, Jooyoung Sung, Richard Friend, Philipp Kukura, Christoph Schneidermann, and Akshay Rao. “Femtosecond Transient Absorption Microscopy of Singlet Exciton Motion in Side-Chain Engineered Perylene-Diimide Thin Films.” In: *The journal of physical chemistry. A* 124.13 (2020), pp. 2721–2730. DOI: 10.1021/acs.jpca.0c00346.
- [143] Milan Delor, Hannah L. Weaver, QinQin Yu, and Naomi S. Ginsberg. “Imaging material functionality through three-dimensional nanoscale tracking of energy flow.” In: *Nature materials* 19.1 (2020), pp. 56–62. DOI: 10.1038/s41563-019-0498-x.
- [144] Stephan Wiesneth. “Visualisierung von Exzitondynamik in supramolekularen Strukturen und organischen Kristallen.” MA thesis. University of Bayreuth, 2018.
- [145] James Pawley. *Handbook of Biological Confocal Microscopy*. Berlin Heidelberg: Springer Science & Business Media, 2013.
- [146] Spring , Kenneth R. and Fellers , Thomas J. and Davidson , Michael W. *Confocal Microscope Scanning Systems*. [Online; accessed 16-June-2020]. 2020. URL: <https://www.olympus-lifescience.com/fr/microscope-resource/primer/techniques/confocal/confocalscanningsystems>.

3 | OVERVIEW OF THE THESIS

This thesis focuses on tailoring long-range energy transport in supramolecular assemblies based on functional organic molecules. It contributes to a fundamental understanding of the interplay between morphology, electronic coupling, and disorder as well as their influence on the optical and energy transport characteristics in self-assembled materials. One key insight of this thesis is the superior energy transport properties in isolated supramolecular nanofibers compared to those in bundles, which is in contrast to the common notion. In consequence, these results suggest that individual nanofibers should be preferred over fiber bundles when implementing them in devices. Another highlight is the developed all-optical approach to control singlet exciton transport pathways via singlet-triplet annihilation in bundles of supramolecular nanofibers. The most impactful results that were obtained in the course of this thesis are condensed in 3 publications. One is published in the *Journal of the American Chemical Society*, one is submitted to *The Journal of Chemical Physics* and one is intended for submission to *Nano Letters*. An outline of the conducted research is presented in Figure 3.1.

The transport of excitation energy is a key process in natural and artificial light-harvesting as well as in the operation of organic electronics. In order to exploit the full potential of new materials and to tune their properties, a complete understanding of the properties of collective excited states, as well as energy transport, is necessary. For example, the interplay between electronic and structural disorder as well as the electronic coupling between densely packed molecules, and its impact on optical spectra and energy transport properties have been widely studied but not fully understood. Disentangling the contributions of the different factors to energy transport becomes difficult, both on the theoretical and experimental side since electronic Coulomb coupling and (structural and electronic) disorder in organic assemblies are typically of the same order of magnitude. Sophisticated experimental techniques are required to analyze such systems on the level of single objects to avoid ensemble averaging over the intrinsic structural and electronic disorder of supramolecular assemblies. Moreover, progress in this field is hampered by the lack of suitable supramolecular architectures and concepts that allow for tailoring energy transport characteristics.

For these reasons, this thesis was divided into three parts:

1. The characterization and differentiation of energy transport and light propagation mechanisms in self-assembled material, using a spatio-temporal detection scanning approach of the transient photoluminescence.

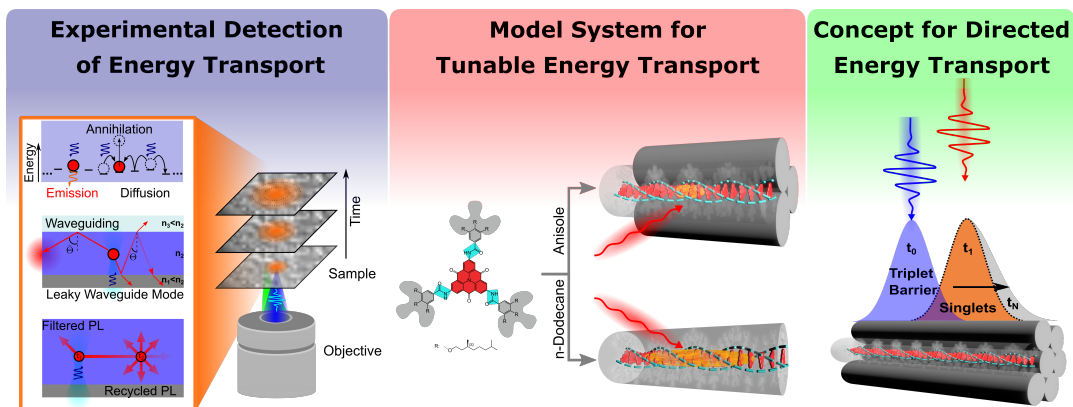


Figure 3.1: Key aspects of this thesis. Left: Fundamental experimental investigations of spatio-temporal dynamics, using detection-beam scanning of the transient photoluminescence. Center: Processing and characterization of a model system with tailored energy transport properties. Right: Concept for directed singlet exciton transport based on singlet-triplet annihilation. For details, see text and section 4.

2. The processing and characterization of a model system, allowing for robust and tunable energy transport properties.
3. The development of a new concept based on singlet-triplet annihilation, allowing directed energy transport.

Consequently, the approach of this thesis was to start at the experimental level and to develop a comprehensive picture of the photoluminescence signal obtained with recently introduced spatio-temporal techniques for resolving energy transport. We used PL microscopy combined with detection-beam scanning and time-correlated single-photon counting on individual supramolecular architectures. The spatio-temporal dynamics of long-range exciton transport ($> 100\text{nm}$) on pico- to nanosecond time scales can thus be tracked by detecting the spatio-temporal broadening of their PL signal after radiative decay. However, in addition to energy transport, exciton-exciton annihilation, waveguiding effects, and photon recycling have been reported to occur in organic functional assemblies. Because all these effects can occur simultaneously, resolving the exciton dynamics unambiguously is highly challenging. This issue is addressed in the first part of this thesis (section 4.1, Fig. 3.1, left part).

To shed light on the spatio-temporal dynamics of excitons in organic materials, we studied highly defined macroscopic single crystals of thiophene-based oligomers (Sajedeh Motamen and Günter Reiter, Freiburg), which should support all the mechanisms mentioned above. Using detection beam scanning in combination with numerical simulations, we addressed and resolved ambiguities in direct measurements of spatio-temporal exciton dynamics. In particular, we were able to distinguish and quantify exciton transport, exciton-exciton annihilation, photon recycling, and leakage radiation upon waveguiding. It is

shown that exciton-exciton annihilation and photon recycling lead to additional spatio-temporal transport dynamics and thus must be considered as possible spatio-temporal mechanisms. We showed that these additional dynamics can be reduced significantly by using low excitation fluences (reduces annihilation) and samples with sufficiently small PL quantum yields (reduces photon recycling). The latter can usually be found in H-aggregates. In summary, it was demonstrated how these various effects and mechanisms can be discriminated by a careful design of experiments, data evaluation, and numerical simulations. Thus, this publication provides important reference parameters for appropriate experimental conditions, a blueprint for data analysis of the spatio-temporal signal as well as insights regarding the selection of suitable model systems.

After characterizing the experimental conditions that grant statements about exciton energy transport, the second part of this thesis (section 4.2, Fig. 3.1, central part) is dedicated to the realization and characterization of a well-defined model system that allows for tuning morphology, electronic properties as well as the experimental observation of exciton transport. We utilized controlled self-assembly of a carbonyl-bridged triarylamine-based (CBT) building block (Hans-Werner Schmidt, Bayreuth) into H-type architectures to obtain either single supramolecular nanofibers or bundles of supramolecular nanofibers. The aggregates were studied by means of comprehensive steady-state investigations in solution in combination with numerical simulations. We found that exciton delocalization is influenced by bundling-induced electronic disorder. In particular, bundling leads to a loss of transition energy correlations between neighboring molecules. As a result, excitons in single nanofibers are delocalized over more molecules than in bundles. Using optical microscopy with detection beam scanning capability at low excitation fluences, we visualized long-range (μm) transport of singlet excitons in both architectures. We found significantly enhanced exciton diffusivities in single supramolecular nanofibers due to the increased exciton delocalization. Moreover, single nanofibers feature the largest exciton diffusivities of up to $1\text{ cm}^2/\text{s}$ that have been reported for H-aggregates so far. This finding provides the first direct experimental evidence that correlated transition energies of adjacent building blocks of supramolecular architectures improve the transport of electronic excitations. Therefore, the obtained results are relevant for the development of a theoretical understanding of energy transport as well as for the design of supramolecular architectures that are optimized for robust and highly efficient energy transport.

Based on these results, we developed and demonstrated an all-optical approach for tailoring the direction and magnitude of singlet exciton transport in bundles of CBT nanofibers, described in the third part of this thesis (section 4.3, Fig. 3.1, right part). For this purpose, we have extended the detection beam scanning setup introduced in section 4.1, using two temporally and spatially separated laser pulses. Intersystem crossing of the laser-generated singlet excitons creates a triplet population, which acts as a barrier for the mobile singlet population generated by the time-delayed following pulse since singlet excitons cannot pass

the triplet excitons due to singlet-triplet annihilation. Thus, by moving the laser excitation location, we can generate a freely positionable triplet-barrier for the mobile singlet excitons. Our new all-optical approach for tailored singlet exciton transport paves the way towards new design principles for functional photonic nanodevices and ultimately to a complete control over singlet exciton motion.

The key results of the publications are summarized in the following section and incorporated in the overall context. Details on the samples, the experiments, and analysis can be found in the respective sections.

3.1 KEY RESULTS

SECTION 4.1: ENERGY TRANSPORT AND LIGHT PROPAGATION MECHANISMS IN ORGANIC SINGLE CRYSTALS

Transport of excitation energy, exciton-exciton annihilation, and light propagation via waveguiding or photon recycling are key processes in nano- to micrometer-scale structures based on organic molecules, and are exploited in applications, such as excitonic and optoelectronic devices. However, the discrimination of these processes is challenging, since they can lead to similar spatio-temporal characteristics and can thus erroneously be attributed to exciton transport. Hence, to extract correct exciton diffusion lengths and to develop suitable design principles for novel structures, unambiguous identification of these processes is required.

The first section of this thesis aims at the differentiation and quantification of energy transport and light propagation mechanisms in organic functional materials. Therefore, we used the most direct tool available for imaging energy transport: Tracking the spatial and temporal evolution of photogenerated excitons. The goal was to identify ambiguities in direct measurements of spatio-temporal exciton dynamics, to find experimental methods to exclude mechanisms, and ultimately distinguish and quantify the influence of these various effects in such experiments. This would allow a better understanding of the individual mechanisms, their individual contributions to energy transport, and their mutual interplay.

As a model system, we investigated single crystals consisting of thiophene-benzene-thiophene (3TBT) oligomers. Due to their highly defined arrangement within the crystal and reasonable H-type coupling of the densely, cofacially stacked molecules, long-range exciton transport should be possible. These organic crystals show dimensions in the μm scale, sufficiently smooth surfaces, and a higher refractive index than their surrounding environment, allowing for waveguiding effects. Furthermore, 3TBT crystals feature strong spectral overlap between their absorption and PL spectra. Thus, photon recycling can take place, which refers to re-absorption and delayed re-emission of photons by other distant molecules within the crystal. These crystals are an ideal model system for the above mentioned goals since all relevant transport mechanisms should be supported.

The crystals were investigated using a home-built microscope with detection beam scanning capabilities in combination with single photon counting. We were able to exclude photon recycling via measuring the lifetimes of the directly out-coupled PL at the excitation position and the waveguided PL out-coupled at the distant crystal tip while keeping the excitation position fixed (see Fig. 3.2a,b). We found identical PL decay curves (see Fig. 3.2c) and thus re-absorption and delayed re-emission of distant molecules do not play a significant role in our system. This finding was confirmed by simulations of photon recycling using a kinetic Monte-Carlo ray-tracing algorithm. However, our simulations illustrate that photon recycling is manifested in the spatio-temporal data with identical

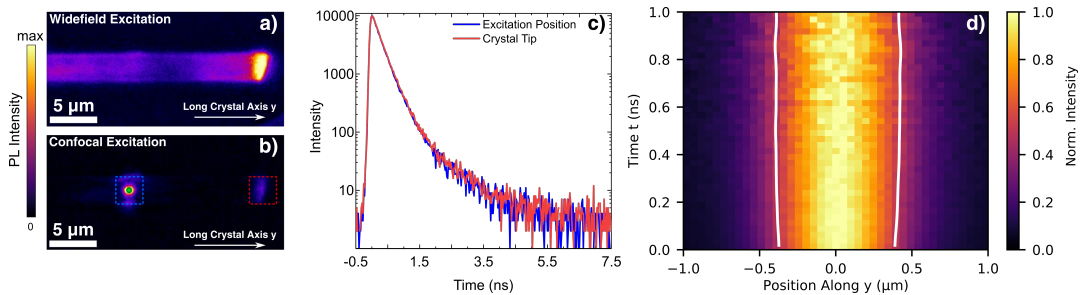


Figure 3.2: **a)** Widefield PL image of a 3TBT single crystal. **b)** PL image of the same crystal upon confocal excitation at the position marked with the green filled circle (within the blue dashed box). The blue and red dashed boxes indicate the detection area for PL decay measurements. **c)** PL decay curves measured for a spatially fixed excitation (green circle in **b)**) at the excitation position (blue) and at the tip of the crystal (red) after light propagation. **d)** Normalized PL intensity distribution $I(y,t)$ and its spatio-temporal evolution for the 3TBT crystal in **a)**, measured along the long crystal axis for a low excitation fluence. The white contour lines indicate the time evolution of the full width at half maximum. For details, see text and section 4.1.

characteristics as exciton diffusion and can be very pronounced in organic structures with high PL quantum yields and large overlap between the PL and absorption spectra. Since H-aggregates typically have small PL quantum yields, which reduces photon recycling, these systems seem ideal for spatio-temporal techniques.

To quantify the influence of leakage radiation upon waveguiding and energy transport on the PL signal, we performed detection beam scanning of the transient PL signal on individual crystals at low excitation fluences. The scans are performed along the long crystal axis, corresponding to the π -stacking direction of 3TBT molecules. Hence, Coulomb interactions along this direction are the strongest and exciton transport is most efficient. The resulting normalized intensity distribution, $I(y, t)$, as a function of distance y relative to the center of the excitation spot ($y = 0$) and time t after laser excitation reveals a broadening of the PL signal along the crystal's long axis within one nanosecond (see Fig. 3.2d).

Pure waveguiding effects only affect the smallest observable, "instantaneous" width of the PL profile at $t = 0$ and do not account for the further spatio-temporal dynamics. Using a Monte Carlo ray-tracing algorithm, we found that 20% of the instantaneous broadening of the non-Gaussian emission profile evaluated at time $t = 0$ of the spatio-temporal PL intensity distribution originates from radiative leaky mode waveguiding. If not taken into account, this effect would lead to an overestimation of transport distances determined via steady-state direct imaging methods.

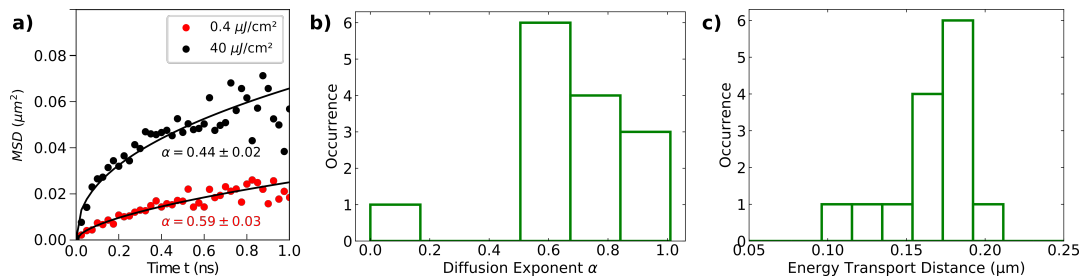


Figure 3.3: **a)** Temporal changes of the mean square displacements (MSD) for a low (red) and a high excitation fluence (black). The solid lines represent fits to a power law with a diffusion exponent α . **b)** Distribution of the diffusion exponent α . We found an average value of $\bar{\alpha} = 0.70 \pm 0.23$. **c)** Energy transport distances defined as $L_D = \sqrt{\max(MSD(t))}$. The average energy transport distance is $0.17 \pm 0.02 \mu\text{m}$. For details, see text and section 4.1.

The temporal broadening of the PL intensity distributions $I(y, t)$ were attributed to exciton diffusion. The analysis of in total 14 single crystals clearly showed a sublinear diffusion behavior, which is characteristic of exciton motion in a disordered energy landscape (see Fig. 3.3a, red dots). Moreover, we found a strong variation in the diffusion exponents from crystal to crystal, distributed around $\bar{\alpha} = 0.70 \pm 0.23$ (see Fig. 3.3b). This rather broad distribution is noteworthy since crystals are usually considered to be structurally highly defined. Therefore, disorder is likely of electronic nature due to, e.g., non-perfect side group arrangement. Thus, this finding underpins the intrinsic heterogeneous nature of organic self-assembled materials. Despite subdiffusion, we found remarkable exciton transport distance of up to $0.21 \mu\text{m}$ (see Fig. 3.3c) and high diffusivities of up to $0.2 \text{ cm}^2/\text{s}$.

To characterize the influence of exciton-exciton annihilation on the PL intensity distribution, we conducted an additional detection-beam scanning measurement at a high excitation fluence. In accordance with numerical simulations, we found a characteristic increase of exciton diffusivities and reduced diffusion exponents due to exciton-exciton annihilation (see Fig. 3.3a, black dots). Due to the Gaussian-shaped excitation profile, the generated exciton density is highest in the center and at short times after laser excitation. Consequently, the probability of exciton-exciton annihilation is highest in this center and at short times. This leads to a reduction of the peak PL-intensity, which artificially broadens the PL profiles in space. Importantly, these spatio-temporal effects of annihilation are not included in commonly used rate equation approaches, which assume normal diffusion.

In summary, we demonstrated the unambiguous assignment of the exciton transport properties in 3TBT crystals. We observed variation in the exciton diffusivity from crystal to crystal and found remarkable transport distances of up to 210 nm . We address and resolve ambiguities in direct measurements of spatio-temporal exciton dynamics and are able to quantify the influence of

exciton-exciton annihilation, photon recycling, and leaky mode waveguiding as possible sources of misinterpretation in such experiments. These insights pave the way for a precise characterization of exciton transport, enabling the development of design principles for enhanced exciton energy transport.

SECTION 4.2: ENHANCING LONG-RANGE ENERGY TRANSPORT IN SUPRAMOLECULAR ARCHITECTURES BY TAILORING COHERENCE PROPERTIES

Controlling long-range energy transport in supramolecular assemblies based on functional organic molecules is a hot topic and highly relevant for fundamental research as well as for future applications. In particular, the exploitation of quantum coherence effects for the development of novel nanophotonic and excitonic organic devices has been a long-standing goal. However, the realization of a well-defined system that allows for tuning morphology and electronic properties as well as for the direct detection of singlet exciton transport in space and time is challenging.

Having established an experimental design to resolve and quantify exciton transport in section 4.1, this section focuses on finding and characterizing a suitable model system that allows for tuning energy transport characteristics.

As a model system, we choose a carbonyl-bridged triarylamine-based (CBT) trisamide. The molecular design gives rise to the formation of H-aggregates, with the CBT-cores comprising an almost perfect cofacial stacking, enforced by three hydrogen-bonding amides. The H-type arrangement of the CBT-cores has recently been reported to support exciton transport up to several micrometers. However, all conclusions about the nature of this long-range energy transport were only indirect, because excitation energy was incoherently transferred to a fluorescent periphery. To go one step further, we have replaced the periphery with non-radiative side groups, which allows uncovering quantum coherent signatures of the H-aggregated cores and the underlying mechanisms enabling long-range exciton transport.

We utilize controlled self-assembly of a CBT-based building block into two well-defined supramolecular H-type architectures of different hierarchical levels. In this context, hierarchical self-assembly provides a means to control the local dielectric environment and can induce different types of energetic disorder along the supramolecular building blocks. Depending on the processing protocols, we are able to prepare either single supramolecular nanofibers or bundles of supramolecular nanofibers (see Fig. 3.4a,b), as confirmed by atomic force microscopy. Importantly, selected area electron diffraction revealed a characteristic cofacial stacking distance of 0.33 nm for both architectures and an intercolumnar spacing of 3.2 nm in the bundled system. Since the latter is substantially smaller than the building block's diameter (4.4 nm for extended side-chains), the peripheries of adjacent nanofibers are expected to interact strongly.

A comprehensive study of the steady state optical spectra in combination with numerical simulations based on the theory of Spano and co-workers leads to the conclusion that these aggregates with different hierarchical levels feature the same

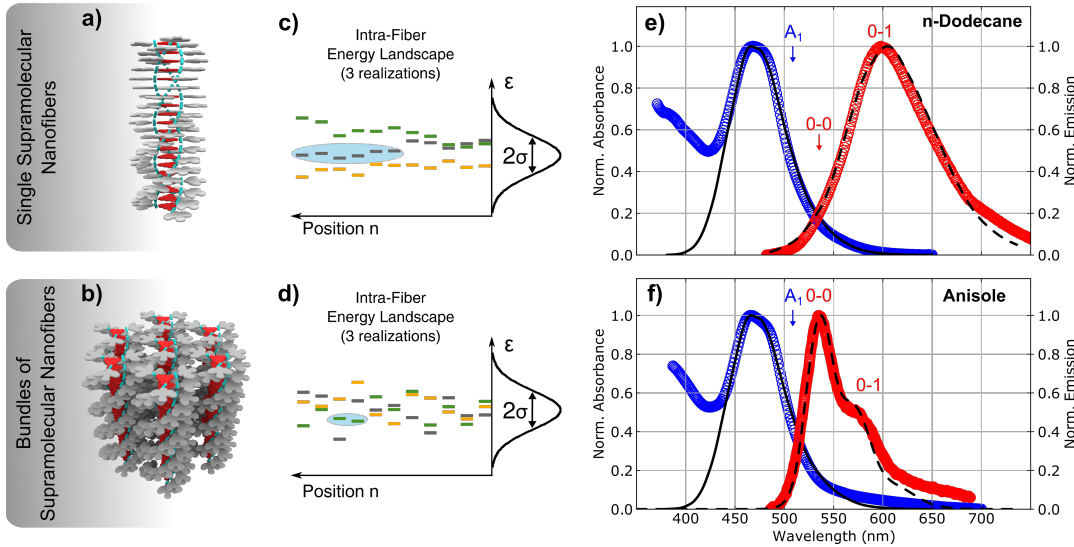


Figure 3.4: Self-assembly of a carbonyl-bridged triarylamine trisamide (CBT) building-block in *n*-dodecane results in single supramolecular nanofibers **a)** and in anisole in bundles of supramolecular nanofibers **b)**. **c,d)** Representation of three simulated realizations of transition energies of the building-blocks at position n within one single column for the simulated spectra in **e)** and **f)**. The spatial correlation length of transition energies for single nanofibers is $l_0 \geq 10$ **c)** and for bundles of nanofibers $l_0 = 0$ **d)** (left, intracolumn energy landscape), while the corresponding ensemble averages, with a Gaussian width of σ , over all columns (right), are almost identical. The ellipses indicate the delocalization of relaxed emitting states. **e,f)** Normalized absorption (blue) and photoluminescence spectra (red) of single supramolecular nanofibers in *n*-dodecane ($40 \mu\text{M}$) **e)** and bundles of supramolecular nanofibers in anisole ($200 \mu\text{M}$) **f)**, together with simulated spectra based on a Frenkel-Holstein Hamiltonian (black lines). For details, see text and section 4.2.

structural arrangement of the building blocks, i.e., the same electronic coupling and structural order within the columns of both architectures, with only subtle variations in the local electronic environment. This leads to different energetic disorder in individual fibers and bundles and hence the excited-state energy landscapes along one column (single nanofiber and within a bundle, respectively) show significant differences in their spatial transition energy correlations. We found that transition energies of adjacent CBT-cores in single supramolecular nanofibers are spatially correlated, resulting in smooth excited-state energy landscapes and a high degree of exciton delocalization (see Fig. 3.4c). In contrast, in bundles of nanofibers, spatial correlations of transition energies are absent. This leads to a disordered excited-state energy landscape with strongly localized exciton states (see Fig. 3.4d). Most likely, the uncorrelated transition energies in bundles of nanofibers are caused by very subtle local electronic perturbations

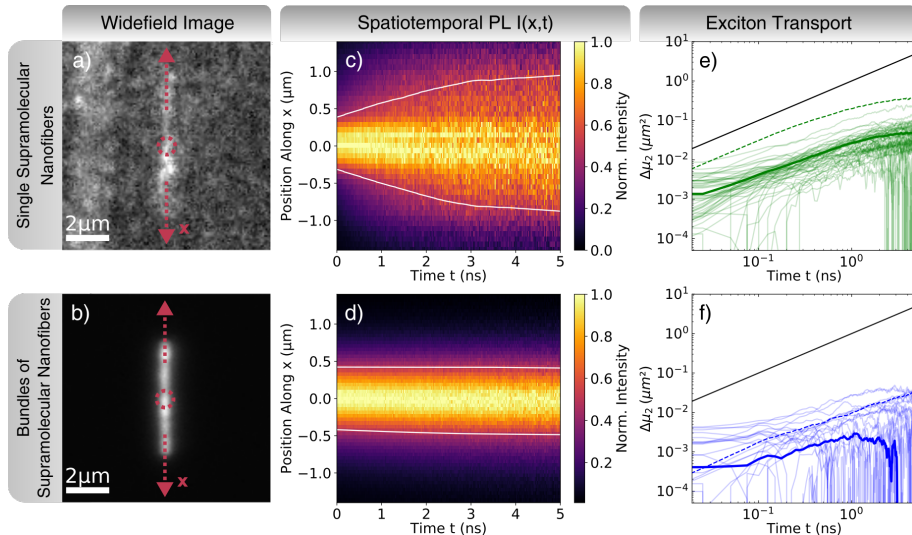


Figure 3.5: Direct visualization of long-range energy transport along supramolecular architectures. **a,b)** Widefield photoluminescence image of a single supramolecular nanofiber and a bundle of supramolecular nanofibers, respectively. Red dashed arrows indicate the scanning axis x ; dashed circles label the position $x = 0$ of the excitation spot. **c,d)** Normalized PL intensity distributions and their evolution in space and time for the single nanofiber in **a)** and the bundle in **b)**. The white contour lines indicate the time evolution of the full width at half maximum. **e,f)** Temporal changes of the second moments of the spatial intensity profiles for 56 nanofibers and 32 bundles of nanofibers (thin green and blue solid lines). The thick lines represent the average of all curves and the dashed lines the evolution of the second moment for the data in **c)** and **d)**. The black lines indicate a linear scaling in time, i.e., normal diffusion, as a guide for the eye. For details, see text and section 4.2.

due to interacting peripheries. These effects can be seen most clearly in the emission spectra. For supramolecular nanofibers, the 0-0 peak seems to be absent at room temperature (see Fig. 3.4e), suggesting a large degree of delocalization of the emitting excitons. In contrast, the PL spectrum of bundles shows a 0-0 peak that is only slightly suppressed compared to the non-aggregated system (see Fig. 3.4f), indicating strong localization of the excitons. Thus, these results demonstrate that our supramolecular architectures allow for tailoring coherence characteristics by altering the hierarchical level of the structures and hence are ideal to resolve the interplay between morphology, correlated electronic disorder, and delocalization in exciton transport.

Figure 3.5a and b show representative widefield photoluminescence images of spatially isolated nanostructures. We performed detection-beam scanning of the transient PL signal for in total 56 individual single nanofibers and 32 bundles. The normalized PL intensity distributions $I(x, t)$, as a function of the distance x relative to the center of the excitation spot and time t after laser excitation, revealed a clear broadening of the PL signal (see Fig. 3.5c,d),

which we have assigned to singlet exciton diffusion. We analyzed this temporal broadening quantitatively by changes of the second moments $\mu_2(t)$ of the spatial intensity profiles with respect to the second moment of the initial profile $\mu_2(0)$, i.e., $\Delta\mu_2(t) = \mu_2(t) - \mu_2(0)$. The obtained $\Delta\mu_2$ curves (see Fig. 3.5e,f) clearly demonstrate the faster and more pronounced broadening in single nanofibers due to enhanced energy transport properties. We attributed this difference to the distinct excited-state energy landscapes, i.e., the high degree of coherence (exciton delocalization) in single supramolecular nanofibers facilitates long-range energy transport. In particular, increasing the degree of coherence, i.e., exciton delocalization, via the supramolecular architectures enhances exciton diffusivities up to one order of magnitude. Moreover, we found that single supramolecular nanofibers exhibit diffusivities in the range of $D = 1\text{cm}^2/\text{s}$, which corresponds to the highest reported value for H-aggregates so far.

Our work provides new design principles for supramolecular architectures that are optimized for robust and highly efficient long-range energy transport. Specifically, our results suggest using isolated nanofibers rather than bundles of nanofibers for applications. Furthermore, our findings are relevant for the development of new theoretical approaches to describe long-range energy transport, in which the treatment of correlated transition energies of the supramolecular building blocks is a key aspect.

SECTION 4.3: ALL-OPTICAL CONTROL OF SINGLET EXCITON TRANSPORT IN INDIVIDUAL SUPRAMOLECULAR NANOSTRUCTURES BY TRIPLET GATING

Manipulating long-range energy transport along supramolecular architectures of functional organic molecules is a central goal of nanotechnology, as it opens up a new world of applications in fields as diverse as information technology and sustainable energy generation. However, progress is hampered by the lack of concept and model systems that operate at room temperature.

This part of the thesis demonstrates a method to block singlet exciton transport within supramolecular structures in a specific direction. The processing protocols, leading to the supramolecular architectures with long-range singlet exciton transport properties, and their spectroscopic characterization, elaborated in section 4.2, form the basis of this section.

As a model system, we choose bundles of CBT-based supramolecular nanofibers, because spatio-temporal measurements on bundles provide a high signal-to-noise ratio, enabling to detect small changes in the singlet exciton dynamics.

We have expanded our photophysical knowledge about singlet exciton properties of molecularly dissolved CBT and bundles to their triplet properties. Using time-correlated single-photon counting, we observed a weak delayed signal on microsecond time scales in addition to the rapid initial fluorescence decay that was already characterized in section 4.2. In combination with time-resolved electron paramagnetic resonance spectroscopy, we attributed the former to the phosphorescence signal from triplet states, which are populated by intersystem crossing from initially photoexcited singlet states. In particular, the triplet

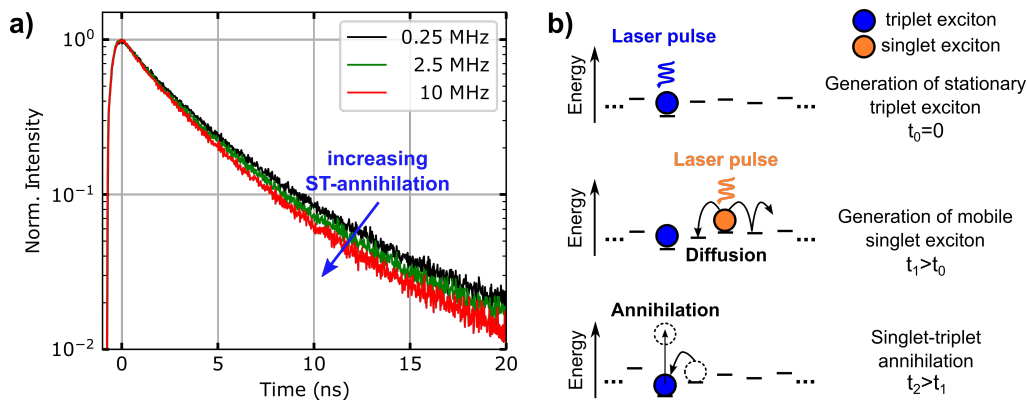


Figure 3.6: a) Fluorescence decay traces of bundles of supramolecular nanofibers in anisole ($400 \mu\text{M}$) at a fixed excitation fluence of $8.6 \times 10^{15} \text{ photons}/(\text{pulse cm}^2)$ for different laser repetition rates. The effect of singlet-triplet (ST) annihilation is visible as a reduction of the singlet exciton lifetimes. b) Schematic illustration of spatio-temporal tailoring of singlet exciton transport. At $t_0 = 0$ a laser pulse creates an initial singlet exciton that is converted into a triplet exciton (blue filled circle) via intersystem crossing. A second laser, arriving at $t_1 > t_0$, creates mobile singlet excitons (orange filled circle), spatially separated from the triplet population. At $t_2 > t_1$, the mobile singlet exciton encounters the triplet exciton and annihilation takes place, leaving behind a triplet exciton. For details, see text and section 4.3.

lifetime of molecularly dissolved CBT is 766 ns, while for bundles we found a lifetime of 1320 ns.

Moreover, we characterized the interaction of singlet and triplet excitons in bundles of supramolecular nanofibers, performing fluence and laser repetition rate dependent fluorescence lifetime measurements on a bulk dispersion in anisole. We found a decrease of the fluorescence lifetime upon increasing the laser repetition rate while keeping the excitation fluence per pulse constant, which is characteristic of singlet-triplet-annihilation (see Fig. 3.6a). The presence of long-lived triplet excitons in bundles of nanofibers can therefore strongly influence the dynamics of the singlet exciton population via singlet-triplet annihilation. Thus, our bundles of nanofibers are a suitable model system for an all-optical approach to manipulate singlet exciton transport via singlet-triplet annihilation. Since, after singlet-triplet annihilation, an excited triplet state survives due to spin conservation, appropriately positioned triplet excitons can serve as a barrier for the mobile singlet excitons. For this purpose, we have extended the detection scanning setup introduced in section 4.1, using two temporally and spatially separated laser pulses, i.e., a two-pulse experiment is conducted. The temporally preceding pulse (first pulse) effectively generates a triplet population via intersystem crossing of photo-generated singlet excitons. This triplet population acts as a barrier for the mobile singlet population

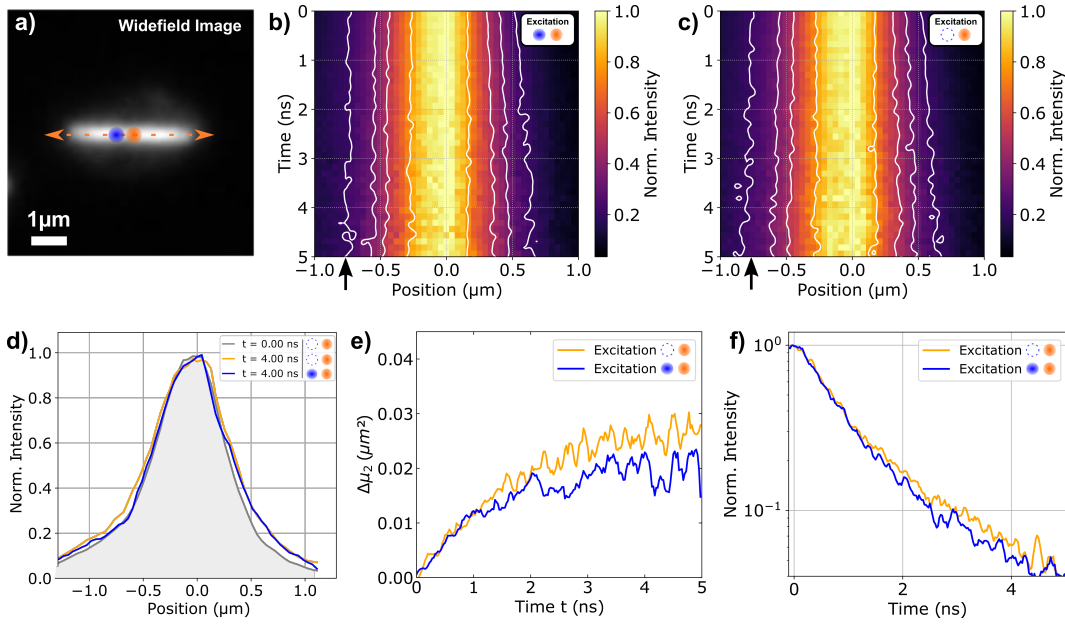


Figure 3.7: **a)** Widefield image of an individual bundle of nanofibers. Orange dashed arrows indicate the detection scanning axis x . The orange circle labels the center of the singlet population at position $x = 0$ nm. The blue circle indicates the center of the triplet exciton population at $x = -800$ nm. **b)** Normalized fluorescence intensity distribution and its evolution in space (x) and time (t) for the bundle in **a)** with the presence of the triplet exciton population (two-pulse experiment). **c)** Normalized fluorescence intensity distribution as in **b)**, but here without the presence of the triplet exciton population (reference experiment). The white contour lines in **b)** and **c)** indicate the widths of the intensity profiles. The solid arrows indicate the position at $x = -800$ nm from where fluorescence decay curves were extracted for **f)**. **d)** Fluorescence intensity profiles retrieved from the fluorescence intensity maps in **b)** (blue) and **c)** (orange) at different delay times t after singlet exciton generation. The grey line shows the initial intensity distribution at time $t = 0$ for the reference experiment. **e)** Temporal changes of the second moments $\Delta\mu_2$ of the spatial intensity profiles determined from the data in **b)** (blue) and **c)** (orange). **f)** Fluorescence decay curve, extracted at position $x = -800$ nm from the data in **b)** (blue) and **c)** (orange). For details, see text and section 4.3.

generated by the following pulse (second pulse), because singlet excitons cannot pass the triplet population due to singlet-triplet-annihilation (see Fig. 3.6b).

We resolved and quantified the control over singlet exciton transport within an individual bundle of nanofibers (see Fig. 3.7a). For this purpose, we followed the fluorescence signal of the singlet population generated by the second laser via detection-beam scanning of their transient fluorescence. The unambiguousness of our measurements was verified with an interleaved reference experiment on the same bundle, for which we have deactivated the first laser. Thus, the intrinsic,

unmanipulated singlet exciton dynamics were recorded, which can be compared to the two-pulse experiment.

Figure 3.7b shows the normalized spatio-temporal fluorescence distribution $I(x, t)$ as a function of the distance x relative to the center of the second pulse and time t after its arrival on the sample and Figure 3.7c shows the corresponding reference experiment. In contrast to the reference experiment, in which we observe singlet exciton transport in both directions along the bundle, for the two-pulse experiment exciton transport is asymmetrical and diminished towards the side where the triplet population is present (i.e., at $x = -800\text{nm}$, black arrow, Fig. 3.7b). This effect is clearly evident in the temporal evolution of the intensity profiles in Figure 3.7d: While for positions $x < 0\ \mu\text{m}$ the initial (grey line) and delayed (blue line) profiles overlap, i.e., no spatial broadening of the initial singlet exciton population occurs, to the right ($x > 0\ \mu\text{m}$) singlet exciton transport is entirely unperturbed since the profiles in the absence (orange line) and presence (blue line) of the triplet population overlap.

This observation is further supported by the temporal evolution of the second moments $\mu_2(t)$ of the spatial intensity profiles, with respect to the second moment of the initial profile $\mu_2(0)$, i.e., $\Delta\mu_2 = \mu_2(t) - \mu_2(0)$. We found systematically smaller $\Delta\mu_2$ values for the two-pulse experiment compared to the reference experiment, underpinning the diminished singlet exciton diffusion in the presence of a triplet population (see Fig. 3.7e). The lifetimes at the spatial position of the first laser pulse ($x = -800\ \text{nm}$) shows shorter lifetimes for the two-pulse experiment compared to the reference measurement (Figure 3.7f). This clearly proves the presence of singlet-triplet annihilation within a single bundle of nanofibers.

Thus, through a spatial and temporal separation of singlet and triplet populations, we prepared a reversible, position-dependent singlet-triplet-annihilation rate in the nanostructure. The presence of the triplet population acts as a barrier for the subsequently generated singlet exciton population because singlet-triplet annihilation reduces singlet exciton diffusion in the direction of the triplet exciton population. Moreover, this barrier can be created in any direction without restructuring the sample. These results demonstrate a scheme for all-optical control of singlet exciton transport and should prove useful for the design of functional photonic nanodevices.

3.2 INDIVIDUAL CONTRIBUTION

Publication 1: **Bernd Wittmann**, Stephan Wiesneth, Sajedeh Motamen, Laurent Simon, Françoise Serein-Spirau, Günter Reiter and Richard Hildner, *Energy transport and light propagation mechanisms in organic single crystals*

Contributions: I performed optical imaging and spectroscopy of individual single crystals, based on the preliminary work of Stephan Wiesneth. Together with Stephan Wiesneth, I wrote the Matlab-script for the kinetic Monte-Carlo ray-tracing simulations. I wrote the Matlab-script for the kinetic Monte Carlo simulations of exciton-exciton annihilation. I performed all numerical simulations. I analyzed and interpreted the experimental data. Furthermore, I wrote the paper together with Richard Hildner and input from all co-authors.

Publication 2: **Bernd Wittmann**, Felix A. Wenzel, Stephan Wiesneth, Andreas T. Haedler, Markus Drechsler, Klaus Kreger, Jürgen Köhler, E. W. Meijer, Hans-Werner Schmidt and Richard Hildner, *Enhancing Long-Range Energy Transport in Supramolecular Architectures by Tailoring Coherence Properties*, *J. Am. Chem. Soc.* 2020, 142, 18, 8323–8330

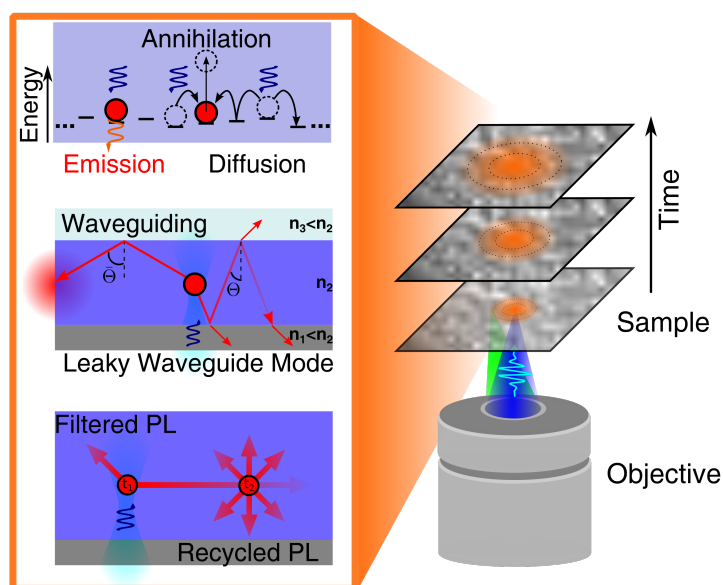
Contributions: I developed the processing protocols that enabled the preparation of single supramolecular nanofibers and bundles. I performed the majority of UV/vis, photoluminescence, and circular dichroism spectroscopy measurements in solution and was supported by Felix Wenzel. I performed atomic force microscopy on the self-assembled nanostructures. I performed most of the optical and spectroscopic measurements on single supramolecular nanofibers and bundles and was supported by Stefan Wiesneth. I performed the numerical simulations of the absorption and PL spectra. I prepared all figures, wrote a first draft of the manuscript and supplementary material, and led the scientific discussion.

Publication 3: **Bernd Wittmann**, Till Biskup, Klaus Kreger, Jürgen Köhler, Hans-Werner Schmidt and Richard Hildner, *All-optical control of singlet exciton transport in individual supramolecular nanostructures by triplet gating*

Contributions: I developed the concept of the all-optical approach for gated singlet exciton transport. I performed the optical imaging and spectroscopy measurements. I performed the numerical simulations of exciton diffusion. I analyzed and interpreted the experimental data. Furthermore, I wrote the paper together with Richard Hildner and input from all co-authors.

4 | PUBLICATIONS

4.1 ENERGY TRANSPORT AND LIGHT PROPAGATION MECHANISMS IN ORGANIC SINGLE CRYSTALS



Bernd Wittmann, Stephan Wiesneth, Sajedah Motamen, Laurent Simon, Françoise Serein-Spirau, Günter Reiter and Richard Hildner

Published in

The Journal of Chemical Physics

DOI: 10.1063/5.0019832

Reproduced from J. Chem. Phys. 2020, 153, 144202, with the permission of AIP Publishing

Copyright ©2020 AIP Publishing

Energy transport and light propagation mechanisms in organic single crystals

Bernd Wittmann¹, Stephan Wiesneth¹, Sajedeh Motamen², Laurent Simon³,
Françoise Serein-Spirau⁴, Günter Reiter², Richard Hildner^{*1,5}

¹Spectroscopy of Soft Matter, University of Bayreuth, Universitätsstraße 30,
95447 Bayreuth, Germany.

²Institute of Physics, University of Freiburg, Hermann-Herder-Straße 3,
79104 Freiburg, Germany.

³Institut de Sciences des Materiaux de Mulhouse IS2M, LRC 7228-CNRS-UHA,
4 rue des freres Lumiere, 68093 Mulhouse, France

⁴Institut Charles Gerhardt de Montpellier, UMR 5353-CNRS Equipe Architectures
Moléculaires et Matériaux Nanostructures (AM2N), Ecole Nationale Supérieure de Chimie de
Montpellier, 8 Rue de l'École Normale, 34296 Montpellier cedex 05, France

⁵Zernike Institute for Advanced Materials, University of Groningen, Nijenborgh 4, 9747 AG
Groningen, The Netherlands.

*Correspondence to: r.m.hildner@rug.nl.

Abstract:

Unambiguous information about spatio-temporal exciton dynamics in three-dimensional, nano- to micrometre-sized organic structures is difficult to obtain experimentally. Exciton dynamics can be modified by annihilation processes, and different light propagation mechanisms can take place, such as active waveguiding and photon recycling. Since these various processes and mechanisms can lead to similar spectroscopic and microscopic signatures on comparable time scales, their discrimination is highly demanding. Here, we study individual organic single crystals grown from thiophene-based oligomers. We use time-resolved detection-beam scanning microscopy to excite a local exciton population and monitor the subsequent broadening of the photoluminescence (PL) signal in space and on pico- to nanosecond time scales. Combined with Monte Carlo simulations we were able to exclude photon recycling for our system, whereas leakage radiation upon active waveguiding leads to an apparent PL broadening of about 20% compared to the initial exciton profile. Exciton-exciton annihilation becomes important at high excitation fluence and apparently accelerates the exciton dynamics and increases diffusion lengths. At low excitation fluences the spatio-temporal PL broadening results from exciton diffusion with diffusion lengths of up to 210 nm. Surprisingly, even in structurally highly ordered single crystals, the transport dynamics is subdiffusive and shows variations between different crystals.

Introduction:

Transport of excitation energy in assemblies of functional organic molecules is a key process in e.g. organic solar cells and organic light-emitting diodes ¹⁻⁴. In particular, the exciton diffusion length, i.e., the distance over which energy can be transported, is of great importance for device efficiency ²⁻⁴: While in solar cells a long transport distance is desired to reach an interface for generation of free charge carriers, in light-emitting diodes long transport distances can lead to unwanted non-radiative quenching at defect sites. Hence, precise measurements of transport distances and dynamics are required to be able to understand energy transport properties and to ultimately optimize molecular assemblies for the desired functionality.

Currently, organic single crystals attract substantial attention as suitable building blocks for new devices and applications ^{1,5-13}. In structurally highly ordered crystals molecules are densely packed and thus feature reasonably strong electronic Coulomb interactions. Hence, delocalised singlet excitons form that can propagate by incoherent hopping ¹⁴. However, direct measurements of transport distances in single crystals are scarce. For too high excitation densities such measurements can easily be misleading, since several excitons within the exciton diffusion length can be created. Excitons can then interact and annihilate (**Fig. 1a**), which yields an apparent increase in diffusion lengths and prevents a precise characterisation of energy transport distances ¹⁵⁻¹⁷. A further complication arises, because organic crystals are three-dimensional systems with spatial dimensions of some tens of nanometres up to millimetres, and they possess usually a higher refractive index than their surrounding media. Hence, different light propagation mechanisms can occur upon photoexcitation: First, active waveguiding can take place (**Fig. 1b**).

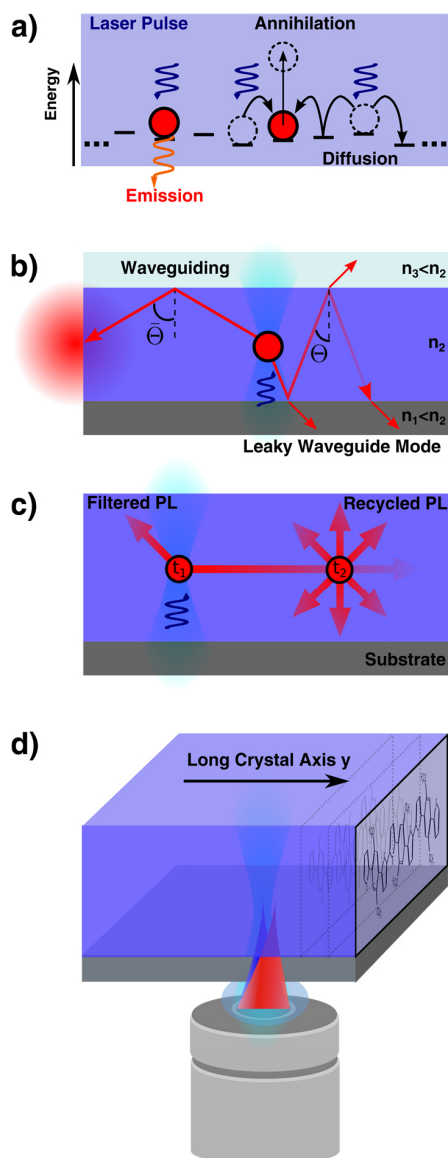


Figure 1. Energy transport and light propagation mechanisms in organic single crystals. **(a)** Exciton diffusion in a disordered energy landscape. Photogenerated excitons (red circles) can diffuse, annihilate or (radiatively) decay. **(b)** Active waveguiding of photoluminescence created within the crystal: The crystal, with anisotropic refractive index n_2 , is surrounded by media with lower refractive indices (glass substrate: n_1 , air: n_3). If emitted light is reflected at an angle $\bar{\theta}$ larger than the critical angle for total internal reflection, it is guided towards the crystal tip and then out-coupled. For angles θ smaller than the critical angle the emitted light can escape into the surrounding media (radiative leaky waveguide modes). **(c)** Photon recycling: PL generated at time $t=t_1$ is re-absorbed during its propagation through the crystal, which can generate delayed emission at $t_2 > t_1$. **(d)** Schematic illustration of the detection-beam scanning PL measurements on a 3TBT crystal: The crystal is confocally excited at a fixed position (light blue), while the detection position (red) is independently moved along the crystal's long (y -) axis.

Photoluminescence (PL) emitted within a crystal is reflected at interfaces of the crystal with e.g. a substrate or air. A fraction of light remains confined within the structure and propagates over long (μm to mm) distances^{5,6,18}. Notably, we have recently demonstrated that an organic layer with a sub-wavelength thickness of ca. 50 nm supports already active waveguiding¹⁹. In addition to such propagating waveguide modes, so-called radiative leaky waveguide modes (**Fig. 1b**) leave the structure into the substrate in close proximity to the excitation position²⁰, which can erroneously be attributed to energy transport. Second, photon recycling can take place, which refers to re-absorption and re-emission of photons by other (distant) molecules within a crystal (**Fig. 1c**). This effect can be significant if the PL quantum yield is high and/or the absorption and PL spectra strongly overlap^{21,22}. Since all these processes (except waveguiding) often occur on similar time scales, their discrimination and quantification become very challenging. The unambiguous identification of these processes, however, is of key importance to extract correct exciton diffusion lengths and to develop suitable design principles for novel structures.

To study energy transport in molecular assemblies, various indirect methods have been applied to date²³, such as time-resolved exciton-exciton annihilation²⁴, and PL quenching at sensitizers or surfaces^{2,25-27}. However, these methods have several shortcomings: They are usually applied to large ensembles (films and solutions) and thus average over disorder. Annihilation measurements on bulk samples lack *direct* spatial information, i.e., we do not know where the annihilation process takes place. Finally, quencher molecules or nearby surfaces perturb the system by deliberately introducing defects. Only recently, a few direct measurements of transport distances have been reported. These techniques exploit that an initial, spatially confined

exciton population broadens in space due to energy transport. A simple approach uses static microscopy to create an initial exciton population with a diffraction-limited excitation spot. The spatial broadening is detected by PL imaging and a comparison between this PL image and the excitation spot ^{28,29}. Using confocal microscopy with time-resolved detection-beam scanning ^{30,31}, the spatial broadening of the PL signal can be followed on pico- to nanosecond time scales. The time resolution can be extended to the femtosecond range with transient absorption microscopy ^{15,32,33}. The temporal information of these direct methods allows to rule out waveguiding via leaky modes as broadening effect, since waveguiding occurs quasi instantaneously with the speed of light. But the distinction between exciton transport, annihilation and photon recycling requires a more careful design of experiments and data evaluation. Here, we report on the quantification of the spatio-temporal dynamics of energy transport, annihilation and light propagation mechanisms in organic single crystals based on thiophene-benzene-thiophene (3TBT) oligomers ^{18,34}. These crystals are grown as previously described and possess a well-defined elongated geometry with the 3TBT oligomers being stacked cofacially along the long axis (*y* direction, **Fig. 1d**) ¹⁸. This H-type assembly of 3TBT molecules should favour long-range transport of excitation energy (singlet excitons) along the crystals' long axis ²⁹, which, however, has not been detected so far. The crystals' μm -scale dimensions and high refractive index allow for efficient active waveguiding ^{18,20}. Moreover, the spectral overlap between the absorption and PL spectra enables photon recycling. To distinguish the different transport regimes and propagation mechanisms, we use confocal PL microscopy combined with detection-beam scanning and time-correlated single-photon counting, see Supporting Information (Materials and Methods). In combination with Monte-Carlo simulations, we are able to distinguish and quantify all transport/propagation mechanisms. We find that exciton diffusion represents the

dominant contribution to the broadening of the diffraction-limited excitation spot in 3TBT crystals on a pico- to nanosecond timescale, while waveguiding via radiative leaky modes and photon recycling play only a minor role. Despite subdiffusive exciton transport in our highly ordered crystals, we observe long energy transport lengths up to 210 nm.

Results:

A widefield PL image of a representative 3TBT crystal with a width of 2.7 μm and a length exceeding 30 μm is shown in **Fig. 2a**. The crystal shows a weak and relatively homogeneous PL from its body and bright emission from its tip. This behaviour is characteristic of active waveguiding of PL that is emitted within the crystal into propagating waveguide modes and out-coupled at the crystal tip ^{18,20}.

Upon confocal excitation of the crystal at the position labelled with the green filled circle in **Fig. 2b**, we observe two distinct emission spots: First, there is relatively weak emission from the crystal tip (red dashed box), which results from active waveguiding of PL created at the excitation spot. Second, we observe direct emission from the excitation position (blue dashed box), which is clearly broadened along the crystal's long (y-) axis compared to the excitation profile (**Fig. 2c** and **Fig. S1**). We recently attributed this broadening to result predominantly from short-distance (μm) leaky-mode active waveguiding into the substrate ²⁰. However, based on the highly ordered H-type arrangement of the 3TBT molecules with reasonable electronic Coulomb coupling of about 320 cm^{-1} ¹³, substantial exciton diffusion lengths are to be expected as well. Moreover, 3TBT crystals feature strong spectral overlap between the absorption and PL spectra with a substantial extinction coefficient of $\sim 0.2\ \mu\text{m}^{-1}$ (**Fig. S2** and Ref. ²⁰), which, in principle, enables photon recycling. Hence, there is a clear need to discriminate between these transport/propagation mechanisms.

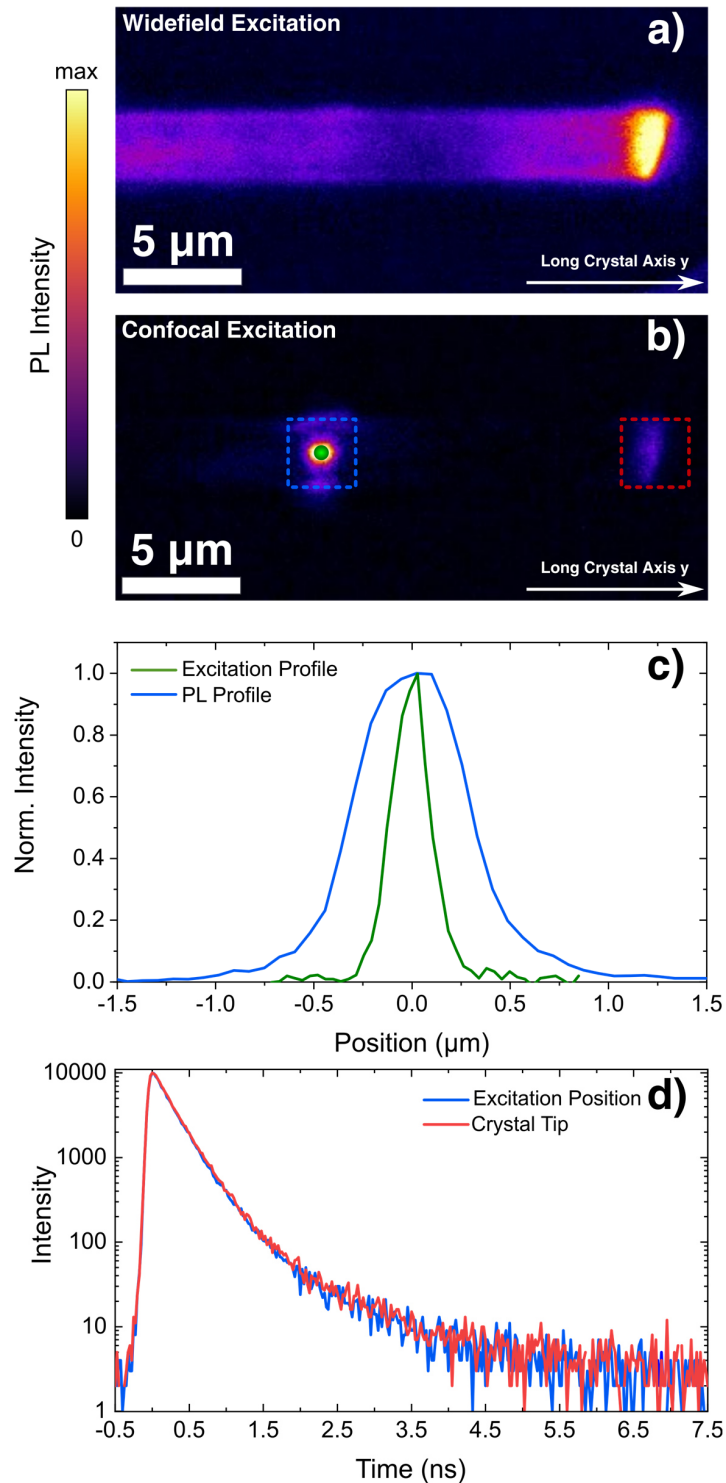


Figure 2. (a) Widefield PL image of a 3TBT single crystal. (b) PL image of the same crystal upon confocal excitation at the position marked with the green filled circle (within the blue dashed box). The blue and red dashed boxes indicate the detection area for PL decay measurements. (c) Excitation (green) and PL emission profile (blue) retrieved at the excitation position within the blue square in (b) along the long crystal axis. (d) PL decay curves measured for a spatially fixed excitation (green circle in (b)) at the excitation position (blue) and at the tip of the crystal (red) after light propagation.

Photon recycling. We first address photon recycling by measuring PL lifetimes at different positions, while the excitation remains fixed at the position labelled with the green filled circle in **Fig. 2b**. We recorded the PL lifetimes from this excitation position (blue dashed box) as well as from the crystal tip (red dashed box), which is 14 μm away from the excitation. The PL decay curves from both positions are identical and show a lifetime of $\tau = 0.35\text{ns}$ (**Fig. 2d**, see also **Fig. S3** for a second example). Photon recycling would lead to increasingly longer PL lifetimes with increasing distance to the excitation spot^{21,22} due to delayed emission of (re-)absorbed and re-emitted photons. Thus, we can rule out photon recycling as a significant propagation mechanism over 14 μm towards the crystal tip. Consequently, photon recycling can also not dominate the PL broadening on a smaller length scale below 1 μm directly around the excitation spot (**Fig. 2c**). To further corroborate this finding, we simulated photon recycling using a kinetic Monte-Carlo ray tracing algorithm (**Fig. S4**). We indeed found only a very small fraction of photons (< 3.4%) that is recycled over a distance of 14 μm (**Figs. S5-S7, Tab. S1**). We can thus exclude photon recycling for our system.

Leaky-mode waveguiding. To quantify the contribution of leakage radiation into the substrate in the vicinity of the excitation spot upon short-distance (μm) waveguiding, we performed a detection beam scanning experiment on the crystal shown in **Fig. 2**. We kept the excitation position fixed and measured PL decay curves, while scanning the detection position across the excitation position by some μm along the long crystal axis. To avoid exciton-exciton annihilation, we used a low excitation fluence of 0.4 $\mu\text{J}/\text{cm}^2$ and thus created only about 2.4 excitations/ μm along one π -stack of 3TBT molecules. **Fig. 3a** shows the resulting normalised PL intensity distribution, $I(y, t)$, as a function of distance y relative to the centre of the excitation spot ($y=0$)

and time t after laser excitation. This distribution reveals a slight broadening of the PL signal along the crystal's long axis within one nanosecond.

Considering the timescale of this broadening, this cannot result from leakage radiation. The latter propagates with the speed of light and can thus only be visible as an instantaneous ($t=0$), non-Gaussian broadening in the PL profile compared to the width of the excitation profile. Indeed, the instantaneous PL profile $I(y, t = 0)$ has a rather broad full width at half maximum (FWHM) of about 760 nm (**Fig. S8**). Measuring the influence of leakage radiation on this instantaneous PL profile requires two reference samples: A very thin sample and one with the same dimensions as the crystal in **Fig. 2a** with identical refractive index, surface roughness, etc., but without the ability of exciton diffusion. Such reference samples, however, are very difficult to realise. Thus, we demonstrate the instantaneous broadening due to radiative leaky-mode waveguiding using a Monte-Carlo ray trace algorithm that simulates PL profiles at the excitation position for two crystals with different heights (**Fig. S9**): One has a height of 2 μm , which is similar to that in the experiment and features waveguiding; the second crystal has a height of only 5 nm, and thus waveguiding and radiative leaky modes are suppressed. Note that photon recycling was 'deactivated' in these simulations by setting the PL quantum yield to zero (see SI). We find that the FWHM of the PL profile at $t = 0$ is 20% broader for the thick crystal compared to the thin one (**Fig. S9**). This effect is exclusively caused by the μm dimensions of the thick crystal with accompanying leakage radiation upon waveguiding.

Exciton Diffusion. The pico- to nanosecond broadening of the PL intensity distribution $I(y, t)$ in **Fig. 3a** is attributed to exciton diffusion over many tens of nanometres^{16,30,31}. That is, the initial exciton population, created by the excitation pulse, is transported away from the excitation spot prior to (radiative) decay.

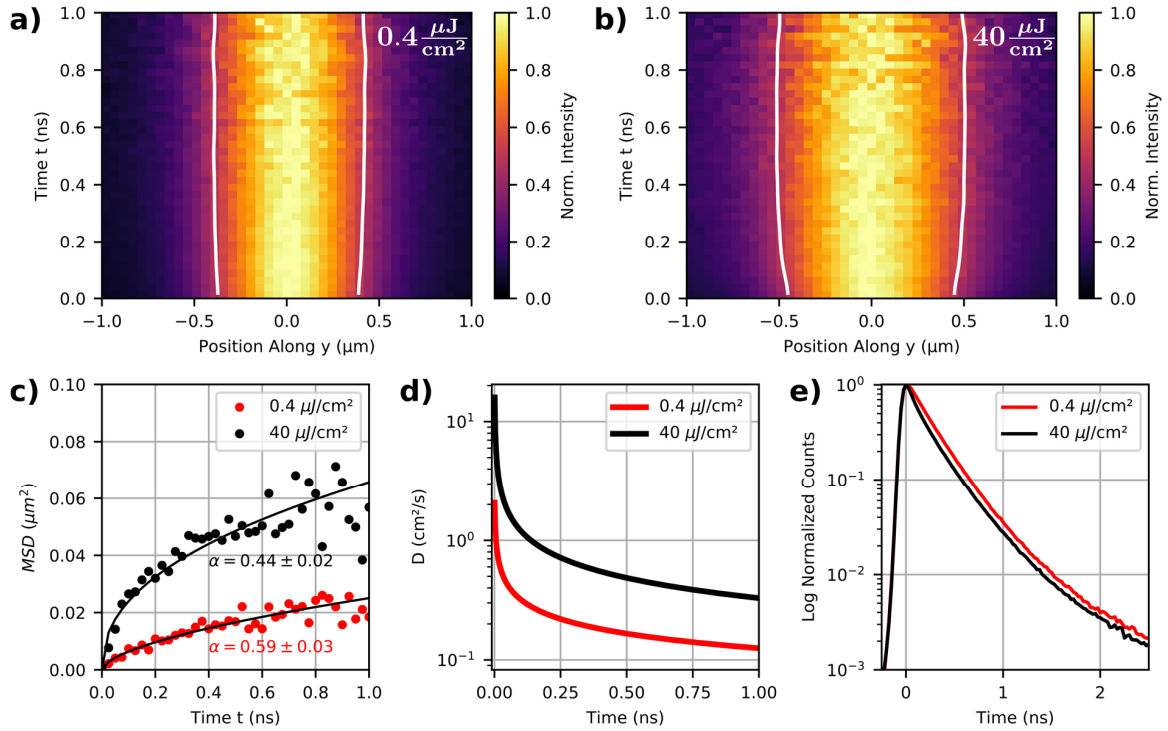


Figure 3. (a, b) Normalized PL intensity distributions $I(y,t)$ and their spatio-temporal evolution for the 3TBT crystal in Fig. 2, measured along the long crystal axis for an excitation fluence of $0.4 \mu\text{J}/\text{cm}^2$ (a) and $40 \mu\text{J}/\text{cm}^2$ (b). The white contour lines indicate the time evolution of the full width at half maximum. (c) Temporal changes of the mean square displacements (MSD) calculated from a (red) and b (black). The solid lines represent fits to a power law with a diffusion exponent α . (d) Time-dependent diffusivities $D(t)$, as determined from the fits to the MDS curves in c. (e) PL lifetime curves determined from the distributions in a (red) and b (black) by spatial integration.

We analysed the time-dependent broadening of this $I(y,t)$ distribution by calculating the mean-square displacement (MSD) as a function of time. We used a reconvolution approach to account for all instantaneous non-Gaussian broadening effects due to e.g. leaky-mode waveguiding (see SI for details). The measured spatio-temporal PL distribution $I(y,t)$ is fitted by a convolution of the initial (non-Gaussian) profile $I(y,t=0)$ and the Gaussian probability density function for exciton diffusion $G(y,t)$:

$$I(y,t) = I(y,0) * G(y,t). \quad (1)$$

The variance of $G(y,t)$ corresponds to the MSD reflecting the PL broadening due to transport as a function of time. The evolution of the MSD for the data in **Fig. 3a** is

shown in **Fig. 3c** (red points). We observe a clear sub-linear behaviour, which is characteristic of subdiffusive exciton motion. This indicates the presence of disorder that increasingly slows down diffusion for longer times^{10,14,35}. We found the same qualitative behaviour for 14 other single crystals (**Fig. S10**).

Subdiffusive motion can be modelled by fitting the MSD with a 1-dimensional model^{14,35–37}:

$$MSD(t) = At^\alpha. \quad (2)$$

Here α is the diffusion exponent and A is the exciton hopping coefficient, which is related to a time-dependent diffusivity via $D(t) = \frac{1}{2}A_\alpha t^{\alpha-1}$. For normal diffusion, $\alpha=1$, the diffusivity becomes time independent. In contrast, for subdiffusive motion, $\alpha<1$, a time-dependent diffusivity $D(t)$ arises, which results from a disordered energy landscape with asymmetric hopping rates (see Fig. 1a). Both the exponent and time-dependent diffusivity are determined by a fit to the data (**Fig. 3c**, red points, solid line).

The exponent is $\alpha = 0.59 \pm 0.03$, which indicates subdiffusion. The analysis of in total 14 different crystals yields a distribution of diffusion exponents with a mean value of $\bar{\alpha} = 0.70 \pm 0.23$ (**Fig. S10**). This variability of the exponent for different crystals is remarkable, since these are usually considered to be highly defined. Our observation thus underpins the intrinsic heterogeneous nature of organic self-assembled materials^{30,31}. The time-dependent diffusivity determined from the fit (**Fig. 3d**, red line) exhibits a rapid decrease by more than one order of magnitude within the first nanosecond. The initial high diffusivity is probably caused by fast energetic downhill migration to lower energy exciton states^{35,38–40}, and a subsequent equilibration into a quasi-static diffusion within the inhomogeneously broadened excited-state energy landscape of the crystal. Using the excited-state lifetime $\tau = 0.35 \text{ ns}$ (**Fig. 3e**, red),

measured for this low-fluence excitation, we find here $D(\tau) = 0.19 \text{ cm}^2/\text{s}$ (see also **Fig. S10**).

The analysis of the MSD as a function of time also allows us to retrieve the exciton diffusion length in this system using the square root of the maximum MSD, $L_D = \sqrt{\max(\text{MSD}(t))}$. From the measurement shown in **Fig. 3a** we find a diffusion length of $0.19 \mu\text{m}$. For the measurements on 14 crystals, we find that the diffusion lengths are distributed around an average value of $\bar{L}_D = 0.17 \pm 0.02 \mu\text{m}$, and a maximum diffusion length of $0.21 \mu\text{m}$ (**Fig. S10**). These exciton diffusion lengths are among the largest reported for H-aggregated crystalline structures^{25,26,33}.

Exciton-exciton annihilation. To characterize the influence of increasing excitation fluence, and thus of exciton-exciton annihilation on the PL intensity distributions, we conducted an additional detection-beam scanning measurement at a high fluence of $40 \mu\text{J}/\text{cm}^2$, corresponding to $240 \text{ excitations}/\mu\text{m}$ (**Fig. 3b**). Notably, this measurement was performed on the same crystal and at the same excitation position as that shown in **Fig. 3a**. The presence of annihilation in our data is verified by the reduction of the excited-state lifetime from $\tau = 0.35 \text{ ns}$ at low fluence to $\tau = 0.28 \text{ ns}$ at high fluence (**Fig. 3e**). Laser excitation generates an initial density of excitons within the excitation spot, which can diffuse as well as decay radiatively and non-radiatively. Interaction between excitons leads to annihilation, and thus to an additional decay channel with a concomitant decrease in the PL-lifetime. **Fig. 3b** shows the normalized spatial PL intensity distribution from the detection-beam scanning experiment at high fluence. Compared to the low-fluence measurement, the intensity distribution broadens faster and in a more pronounced way over the entire time range.

Following the same approach for the analysis of the PL broadening as above, we find that the MSDs are systematically larger for each point in time as compared to the low

fluence experiment (**Fig. 3c**, black dots vs. red dots). At high fluence the subdiffusive behaviour is still clearly visible. Based on the 1-dimensional diffusion model, we find a smaller diffusion exponent of $\alpha = 0.44 \pm 0.02$, and a larger diffusivity, which steeply decreases as function of time (**Fig. 3d**, black line). At the excited state lifetime $\tau = 0.28\text{ns}$ under high fluence excitation (**Fig. 3e**, black), we find $D(\tau) = 0.67\text{ cm}^2/\text{s}$. Moreover, the exciton diffusion length increases to $L_D = 270\text{ nm}$, which, however, is only an apparent increase. At higher fluence the mobility seems to be enhanced (larger $D(\tau)$), but diffusion is increasingly hindered by annihilation (smaller α). Importantly, this behaviour is not included in standard rate equation approaches for normal diffusion commonly applied to model such data^{41,42}, see also **Fig. S11**.

To gain insight into the relationship between energetic disorder, annihilation as well as the spatio-temporal dynamics of exciton diffusion, we performed kinetic Monte-Carlo simulations (see SI for details). For these simulations we averaged over 2000 energy landscapes with random Gaussian energy disorder. The same realisations of energy landscapes were used for both excitation densities of 2.4 excitations/ μm and 240 excitations/ μm as in the experiment. Our simulations in **Fig. 4a-d** reproduce all experimental trends, i.e., a time-dependent broadening of the exciton distribution as well as an apparently enhanced exciton mobility (and decreased diffusion exponent) for high excitation densities.

The apparent enhancement of the diffusivity at high excitation fluence can be traced back to the spatio-temporal behaviour of the annihilation probability: The Gaussian excitation profile creates an initial Gaussian-shaped exciton population. The loss of excitations due to annihilation is therefore highest in the centre of this distribution¹⁵ and at short times after laser excitation (**Fig. S12**). As illustrated in **Fig. 4e**, at early times we find an annihilation probability of 96% for high fluence (while for low fluence it is only 22 %).

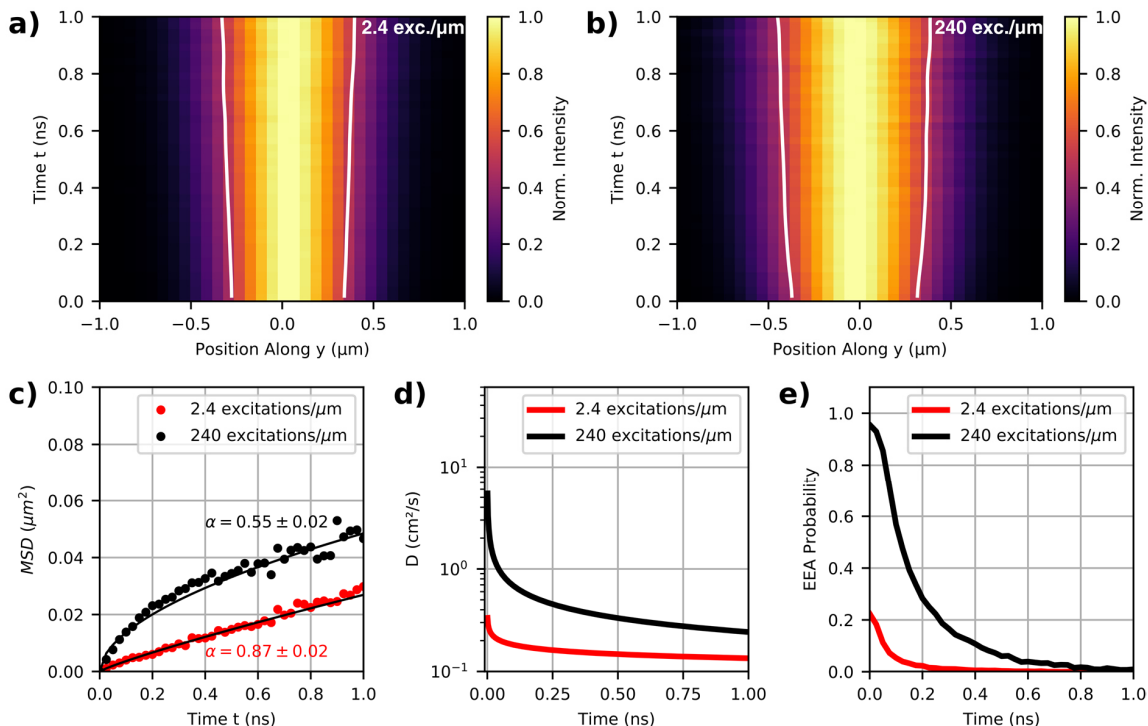


Figure 4. Kinetic Monte Carlo simulations of exciton diffusion and exciton-exciton annihilation. **(a, b)** Simulated normalized PL intensity distributions and their spatio-temporal evolution for an average over 2000 realizations of energetic disorder. The initial excitation densities were 2.4 excitations/μm (a) and 240 excitations/μm (b). The white contour lines indicate the time evolution of the full width at half maximum. **(c)** Temporal changes of the simulated MSD (dots) from a and b, with power law fits (solid lines). **(d)** Time-dependent diffusivities $D(t)$. **(e)** Calculated probabilities for exciton-exciton annihilation as a function of time.

Consequently, in the high fluence regime annihilation rapidly thins out the exciton population in the centre of the initial distribution. In other words, the peak exciton population is rapidly reduced, which ‘cuts off’ the peak of the PL-intensity profile at short times and artificially broadens this initial PL profile in space. The annihilation probability then decreases with time (**Fig. 4e**) due to annihilation, exciton diffusion and (non-)radiative decay. Exciton diffusion spatially broadens the annihilation probability with time (**Fig. S12**), which causes the PL intensity distribution to broaden further. This spatio-temporal behaviour of the annihilation probability highlights the

efficiency of energy transport in our 3TBT crystals. Our simulations along with our experiments thus reveal the origin of the apparently changed singlet exciton dynamics for increasing excitation fluences.

Conclusion:

We studied the spatio-temporal dynamics of energy transport and light propagation mechanisms in micrometre-scale 3TBT-based organic single crystals as a model system. We focussed here specifically on transport/propagation processes along the long axis of the crystals, which corresponds to the π -stacking direction of the 3TBT molecules. Along this direction the Coulomb interaction between molecules is strongest and thus (long-range) exciton transport is most efficient. We used detection-beam scanning methods in combination with kinetic Monte-Carlo simulations to distinguish between photon recycling, radiative leaky-mode waveguiding, energy transport and exciton-exciton annihilation. We excluded photon recycling as the main effect of the broadened emission in 3TBT crystals, because it only accounts for 3.4% of all detected photons. However, our study illustrates that photon recycling can be significant in organic structures with a high PL quantum yield and large overlap between the PL and absorption spectra, which is typical for J-aggregates. Moreover, our simulations show that photon recycling is manifested in spatio-temporal data with very similar characteristics as exciton diffusion. Leaky-mode waveguiding leads to about 20% instantaneous broadening of the non-Gaussian emission profile at time $t=0$ of the spatio-temporal PL-intensity distributions. If not taken into account, this mechanism therefore leads to a substantial overestimation of the total exciton diffusion lengths determined by steady-state direct imaging methods. Only the pico- to nanosecond temporal broadening of the spatial PL intensity distribution in the 3TBT crystals can be unambiguously attributed to

exciton diffusion, if low excitation fluences are used to avoid annihilation. Under those conditions, we found surprisingly large exciton diffusion lengths up to 210 nm. Exciton-exciton annihilation results in an apparent broadening of the spatial PL-intensity distribution with increasing excitation fluence, and thus leads to an overestimation of exciton diffusion lengths. Independent of the excitation fluence, the temporal PL-broadening exhibits a clear subdiffusive behaviour during the entire time-range. This observation is in contrast to standard rate equation approaches^{15,41} that assume normal diffusion for the short-time dynamics and a transition to subdiffusive transport at later times. In general, subdiffusive behaviour results from intrinsic disorder in organic structures. Since the structural arrangement of molecules, especially in single crystals, is very well-defined, this disorder is very likely purely electronic in nature, i.e., it results from disorder in the excited-state energy levels for instance due to non-perfect side group arrangements. Our results highlight that quantification of spatio-temporal exciton dynamics in nano- to micrometre scale organic structures requires careful evaluation of different energy transport regimes and light propagation mechanisms.

Supplementary Material:

See Supplementary Material for a description of materials and methods, of control experiments, of kinetic Monte Carlo ray tracing simulations of photon recycling and leaky mode waveguiding, and of kinetic Monte Carlo simulations of exciton transport and annihilation.

Acknowledgements:

We acknowledge financial support from the German Research Foundation (DFG) through project GRK1640 (BW and RH) and IRTG1642 (GR), stimulating discussions with Christian Schörner, and the continued support of this work by Jürgen Köhler.

Data Availability Statement:

The data that support the findings of this study are available from the corresponding author upon reasonable request.

References and Notes:

- ¹ C. Zhang, Y. Yan, Y.S. Zhao, and J. Yao, *Acc. Chem. Res.* **47**, 3448 (2014).
- ² S.M. Menke and R.J. Holmes, *Energy Environ. Sci.* **7**, 499 (2014).
- ³ O. V. Mikhnenko, P.W.M. Blom, and T.Q. Nguyen, *Energy Environ. Sci.* **8**, 1867 (2015).
- ⁴ H. Paul, C. David, and B.P. Rand, *Acc. Chem. Res.* **42**, 1740 (2009).
- ⁵ Q.H. Cui, Q. Peng, Y. Luo, Y. Jiang, Y. Yan, C. Wei, Z. Shuai, C. Sun, J. Yao, and Y.S. Zhao, *Sci. Adv.* **4**, eaap9861 (2018).
- ⁶ M.P. Zhuo, J.J. Wu, X.D. Wang, Y.C. Tao, Y. Yuan, and L.S. Liao, *Nat. Commun.* **10**, 3839 (2019).
- ⁷ L. Zang, *Acc. Chem. Res.* **48**, 2705 (2015).
- ⁸ M.J. Sun, Y. Liu, Y. Yan, R. Li, Q. Shi, Y.S. Zhao, Y.W. Zhong, and J. Yao, *J. Am. Chem. Soc.* **140**, 4269 (2018).
- ⁹ G.B. Piland and C.J. Bardeen, *J. Phys. Chem. Lett.* **6**, 1841 (2015).
- ¹⁰ C.J. Bardeen, *Annu. Rev. Phys. Chem.* **65**, 127 (2014).
- ¹¹ J. Gierschner and S.Y. Park, *J. Mater. Chem. C* **1**, 5818 (2013).
- ¹² J. Gierschner, L. Lüer, B. Milián-Medina, D. Oelkrug, and H.J. Egelhaaf, *J. Phys. Chem. Lett.* **4**, 2686 (2013).
- ¹³ S. Motamen, D. Raithel, R. Hildner, K. Rahimi, T. Jarrosson, F. Serein-Spirau, L. Simon, and G. Reiter, *ACS Photonics* **3**, 2315 (2016).
- ¹⁴ S.M. Vlaming, V.A. Malyshev, A. Eisfeld, and J. Knoester, *J. Chem. Phys.* **138**, 214316 (2013).
- ¹⁵ T. Zhu, Y. Wan, and L. Huang, *Acc. Chem. Res.* **50**, 1725 (2017).
- ¹⁶ N.S. Ginsberg and W.A. Tisdale, *Annu. Rev. Phys. Chem.* **71**, 1 (2020).
- ¹⁷ E.M. Grumstrup, *Opt. Express* **27**, 31385 (2019).
- ¹⁸ S. Motamen, C. Schörner, D. Raithel, J.P. Malval, T. Jarrosson, F. Serein-Spirau, L. Simon, R. Hildner, and G. Reiter, *Phys. Chem. Chem. Phys.* **19**, 15980 (2017).
- ¹⁹ C. Schörner, C. Neuber, and R. Hildner, *APL Photonics* **4**, 016104 (2019).
- ²⁰ C. Schörner, S. Motamen, L. Simon, G. Reiter, and R. Hildner, *ACS Omega* **3**, 6728 (2018).
- ²¹ Y. Fang, H. Wei, Q. Dong, and J. Huang, *Nat. Commun.* **8**, 14417 (2017).

- ²² I. Dursun, Y. Zheng, T. Guo, M. De Bastiani, B. Turedi, L. Sinatra, M.A. Haque, B. Sun, A.A. Zhumekenov, M.I. Saidaminov, F.P. García De Arquer, E.H. Sargent, T. Wu, Y.N. Gartstein, O.M. Bakr, O.F. Mohammed, and A. V. Malko, *ACS Energy Lett.* **3**, 1492 (2018).
- ²³ J.D.A. Lin, O. V. Mikhnenko, J. Chen, Z. Masri, A. Ruseckas, A. Mikhailovsky, R.P. Raab, J. Liu, P.W.M. Blom, M.A. Loi, C.J. García-Cervera, I.D.W. Samuel, and T.Q. Nguyen, *Mater. Horizons* **1**, 280 (2014).
- ²⁴ J.R. Caram, S. Doria, D.M. Eisele, F.S. Freyria, T.S. Sinclair, P. Reberstrost, S. Lloyd, and M.G. Bawendi, *Nano Lett.* **16**, 6808 (2016).
- ²⁵ A.K. Topczak, T. Roller, B. Engels, W. Brütting, and J. Pflaum, *Phys. Rev. B* **89**, 201203 (2014).
- ²⁶ X.H.H. Jin, M.B.B. Price, J.R.R. Finnegan, C.E.E. Boott, J.M.M. Richter, A. Rao, S. Matthew Menke, R.H.H. Friend, G.R.R. Whittell, and I. Manners, *Science*. **360**, 897 (2018).
- ²⁷ A.A. Mannanov, M.S. Kazantsev, A.D. Kuimov, V.G. Konstantinov, D.I. Dominskiy, V.A. Trukhanov, D.S. Anisimov, N. V Gultikov, V. V Bruevich, I.P. Koskin, A.A. Sonina, T. V Rybalova, I.K. Shundrina, E.A. Mostovich, D.Y. Paraschuk, and M.S. Pshenichnikov, *J. Mater. Chem. C* **7**, 60 (2019).
- ²⁸ K.A. Clark, E.L. Krueger, and D.A. Vanden Bout, *J. Phys. Chem. Lett.* **5**, 2274 (2014).
- ²⁹ A.T. Haedler, K. Kreger, A. Issac, B. Wittmann, M. Kivala, N. Hammer, J. Köhler, H.W. Schmidt, and R. Hildner, *Nature* **523**, 196 (2015).
- ³⁰ G.M. Akselrod, P.B. Deotare, N.J. Thompson, J. Lee, W.A. Tisdale, M.A. Baldo, V.M. Menon, and V. Bulovic, *Nat. Commun.* **5**, 3646 (2014).
- ³¹ B. Wittmann, F.A. Wenzel, S. Wiesneth, A.T. Haedler, M. Drechsler, K. Kreger, J. Köhler, E.W. Meijer, H.-W. Schmidt, and R. Hildner, *J. Am. Chem. Soc.* **142**, 8323 (2020).
- ³² C. Schnedermann, J. Sung, R. Pandya, S.D. Verma, R.Y.S. Chen, N. Gauriot, H.M. Bretscher, P. Kukura, and A. Rao, *J. Phys. Chem. Lett.* **10**, 6727 (2019).
- ³³ R. Pandya, R.Y.S. Chen, Q. Gu, J. Gorman, F. Auras, J. Sung, R. Friend, P. Kukura, C. Schnedermann, and A. Rao, *J. Phys. Chem. A* **124**, 2721 (2020).
- ³⁴ R.A. Silva, F. Serein-Spirau, M. Bouachrine, J.P. Lère-Porte, and J.J.E. Moreau, *J. Mater. Chem.* **14**, 3043 (2004).
- ³⁵ G.M. Akselrod, F. Prins, L. V. Poulidakos, E.M.Y. Lee, M.C. Weidman, A.J. Mork, A.P. Willard, V. Bulović, and W.A. Tisdale, *Nano Lett.* **14**, 3556 (2014).
- ³⁶ J. Wu and K.M. Berland, *Biophys. J.* **95**, 2049 (2008).
- ³⁷ S. Havlin and D. Ben-Avraham, *Adv. Phys.* **51**, 187 (2002).

³⁸ R. Kersting, U. Lemmer, R.F. Mahrt, K. Leo, H. Kurz, H. Bässler, and E.O. Göbel, *Phys. Rev. Lett.* **70**, 3820 (1993).

³⁹ R. Hildner, U. Lemmer, U. Scherf, and J. Köhler, *Chem. Phys. Lett.* **429**, 103 (2006).

⁴⁰ G.R. Hayes, I.D.W. Samuel, and R.T. Phillips, *Phys. Rev. B* **52**, 569 (1995).

⁴¹ S. Deng, E. Shi, L. Yuan, L. Jin, L. Dou, and L. Huang, *Nat. Commun.* **11**, 664 (2020).

⁴² Y. Wan, Z. Guo, T. Zhu, S. Yan, J. Johnson, and L. Huang, *Nat. Chem.* **7**, 785 (2015).

Supporting Information

**Energy transport and light propagation mechanisms in
organic single crystals**

Bernd Wittmann¹, Stephan Wiesneth¹, Sajedah Motamen², Laurent Simon³
Françoise Serein-Spireau⁴, Günter Reiter², Richard Hildner^{*1,5}

¹Spectroscopy of Soft Matter, University of Bayreuth, Universitätsstraße 30, 95447 Bayreuth,
Germany.

²Institute of Physics, University of Freiburg, Hermann-Herder-Straße 3, 79104 Freiburg, Germany.

³Institut de Sciences des Materiaux de Mulhouse IS2M, LRC 7228-CNRS-UHA,
4 rue des freres Lumiere, 68093 Mulhouse, France

⁴Institut Charles Gerhardt de Montpellier, UMR 5353-CNRS Equipe Architectures Moleculaires et
Materiaux Nanostructures (AM2N), Ecole Nationale Supérieure de Chimie de Montpellier, 8 Rue de
l'Ecole Normale, 34296 Montpellier cedex 05, France

⁵Zernike Institute for Advanced Materials, University of Groningen, Nijenborgh 4,
9747 AG Groningen, The Netherlands.

*Correspondence to: r.m.hildner@rug.nl.

Table of Contents

Materials and Methods	3
Fig. S1: Comparison of excitation and PL profiles.	5
Fig. S2: Spatially resolved PL spectra	6
Fig. S3: PL lifetime measurement on a thin crystal	7
Photon Recycling: Kinetic Monte Carlo Ray-Tracing	8
Fig. S4: Flow chart of the kinetic Monte Carlo ray tracing simulation.	8
Fig. S5: Simulations of spatially resolved PL spectra based on the kinetic ray tracing simulation.	10
Fig. S6: Simulations of spatially resolved PL-decays based on the kinetic ray tracing simulations.	11
Tab. S1: Calculated contribution of re-emitted (recycled) photons to the total number of detected photons for increasing PL quantum yields (QY).	12
Fig. S7: Spatio-temporal broadening of the PL caused by photon recycling based on the kinetic ray tracing simulations.	13
Fig. S8: Comparison of the spatio-temporal broadening for a nanobead and a 3TBT crystal.	14
Fig. S9: Quantification of emission profiles due to leaky-mode waveguiding based on kinetic ray tracing simulations.	15
Fig. S10: Statistics of energy transport measurements for 14 different single crystals measured with low excitation fluence.	16
Fig S11: Fitting MSD(t) with two diffusion regimes	17
Kinetic Monte Carlo Simulation of Exciton-Exciton Annihilation.	18
Fig. S12: Dynamics of the annihilation probability for the simulations shown in Fig. 4 of the main text.	19
Incoherent Exciton Diffusion Model	20
Fig. S13: Control experiment on a reference sample without long-range energy transport.	21

Materials and Methods

Materials. 3TBT is 100% regioregular with a molecular weight of $M = 1492.32$ g/mol and a contour length of 3.6 nm. As reported recently¹, micrometer-sized 3TBT single crystals are grown in solution at a relatively high crystallization temperature (60 °C). Subsequently, 10 μ L of this solution is spin cast at 1000 rotations/min onto a cleaned glass substrate, so that spatially well-separated single crystals can be optically identified on the substrate. This preparation results in a three-layer geometry of the sample: glass substrate, single crystal, and air.

Optical imaging and spectroscopy. Optical imaging and spectroscopy was performed at room temperature under ambient conditions using a home-built microscope. The excitation source was a pulsed diode laser (LDH-P-C-450B, Picoquant; 2.5 MHz repetition rate, 70 ps pulse duration) that operates at a wavelength of 450 nm. The laser light was spatially filtered and directed to the microscope, which was equipped with an infinity-corrected high-numerical aperture oil-immersion objective (PlanApo, 60 \times , numerical aperture 1.45; Olympus). The sample was placed in the focal plane of the objective, and the sample position was controlled by a piezo-stage (Tritor 102 SG, piezosystem jena). Photoluminescence (PL) was collected by the same objective and passed a set of dielectric filters (dichroic beam splitter z460RDC, long-pass filter LP467; AHF Analysentechnik) to suppress scattered or reflected laser light. For the detection of the PL signal several detection paths were used and switching between these modes is achieved by flip mirrors. These detection paths comprise two telecentrically arranged lenses and a closed-loop piezo scan mirror (S-335.2.SH, PI):

First, in imaging mode the PL signal is imaged onto a sCMOS camera (Zyla 4.2 sCMOS, Andor) using two illumination methods. For confocal illumination the laser light is tightly focused by the high-NA objective to a spot with a full width at half maximum of ~ 235 nm in the sample plane (see Fig. S1). For widefield illumination we flipped an additional lens (widefield lens) into the excitation beam path to focus the laser light into the back-focal plane of the microscope objective. This allows for nearly uniform illumination of a large area with ~ 70 μ m diameter in the sample plane, to acquire overview PL images of our samples and to identify isolated crystals (see e.g. Fig. 2a).

Second, to position the detection spot independently from the confocal excitation spot within the objective's focal plane, the piezo scan mirror is used. As detectors we used a single-photon-counting avalanche photodiode (MPD, Picoquant), and fed its electrical signal into a time-correlated single-photon-counting module (TimeHarp 260 PICO, Picoquant). For PL-lifetime measurements at the excitation and crystal tip position (Fig. 2d) the magnification was chosen to be 16x, which corresponds to a detector's active area in the sample plane of 3 μ m x 3 μ m (see blue and red boxes in Fig. 2b). This low magnification allows taking into account spatially dependent effects at the excitation position that alter the PL-lifetime, such as exciton diffusion and exciton-exciton annihilation. Since the PL-decay curves do not behave mono-exponentially, all lifetimes reported correspond to the passed time until the curve has decayed to the 1/e value of the maximum. For the detection-beam scanning experiments in Fig. 3, the magnification was 83x to allow for a sufficient spatial resolution.

Finally, to record emission spectra, we focused the PL onto the entrance slit of a spectrograph (IsoPlane 160, Princeton Instruments, 150 grooves per millimetre, blaze wavelength 500 nm) equipped with a back-illuminated electron-multiplying CCD camera (iXon Ultra DU-897U-CS0-BVF, Andor Technology).

The excitation fluences were between 0.4 μ J cm⁻² and 40 μ J cm⁻² for confocal illumination and 0.01 μ J cm⁻² for widefield illumination. These confocal fluences correspond to a maximum excitation probability between 2.4 and 240 absorbed photons per pulse per 2700 π -

stacked 3TBT molecules (corresponding to 1 μm), calculated for a typical absorption cross section of $\sigma \approx 10^{-15}\text{cm}^2$. Hence, in the confocal excitation spot 0.6, respectively, 60 excitations were generated.

Numerical Simulations. For kinetic Monte-Carlo simulations of photon recycling and energy transport we used home-written Matlab-scripts. Further details are outlined in the sections of the Supporting Information below.

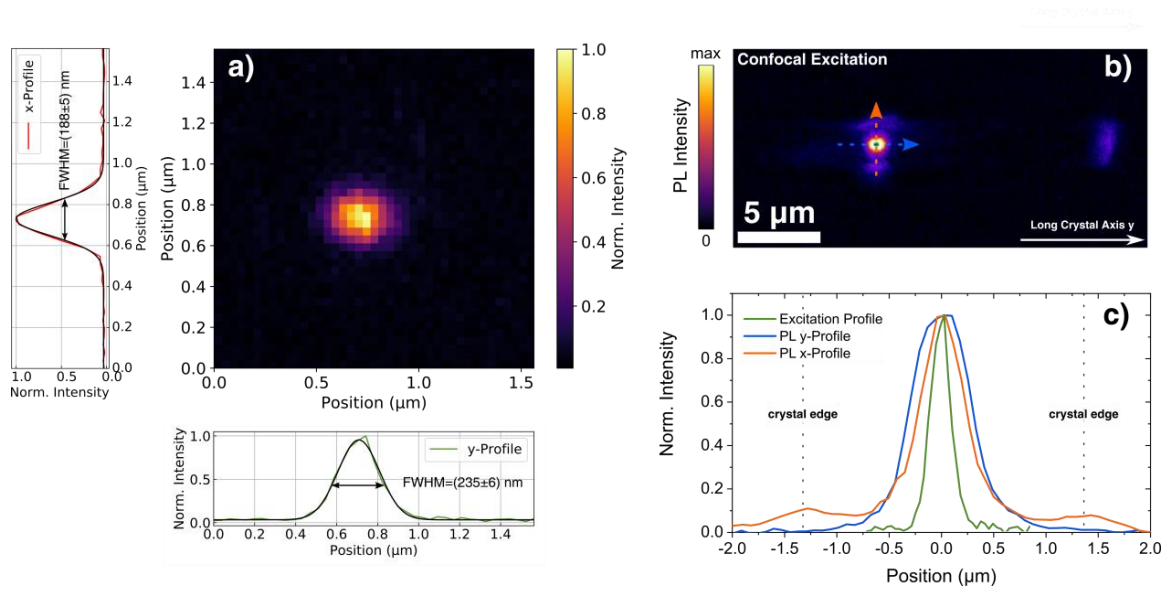


Fig. S1: Comparison of excitation and PL profiles. (a) Characterisation of the laser excitation profile. We raster scanned a single fluorescence microsphere (0.1 μm diameter, Red Fluorescence Carboxylated Ps Latex, Nanosphere) across the laser excitation spot to characterise its size. The confocal image is shown as a map with colour-coded intensity. The shown profiles are along the x- and y-scanning axis and were taken through the intensity maximum of the map. (b) PL image of the same crystal as in Fig. 2 upon confocal excitation at the position marked with the green circle. The arrows indicate the direction along which we extracted the PL profiles around the excitation position. (c) Excitation (green, see also (a)) and PL profiles along the corresponding axes in (b). The side peaks in the profile along the crystal's short (x-) axis result from active waveguiding of PL along the crystal's short axis and out-coupling at the crystal edges (indicated by the dotted vertical lines).

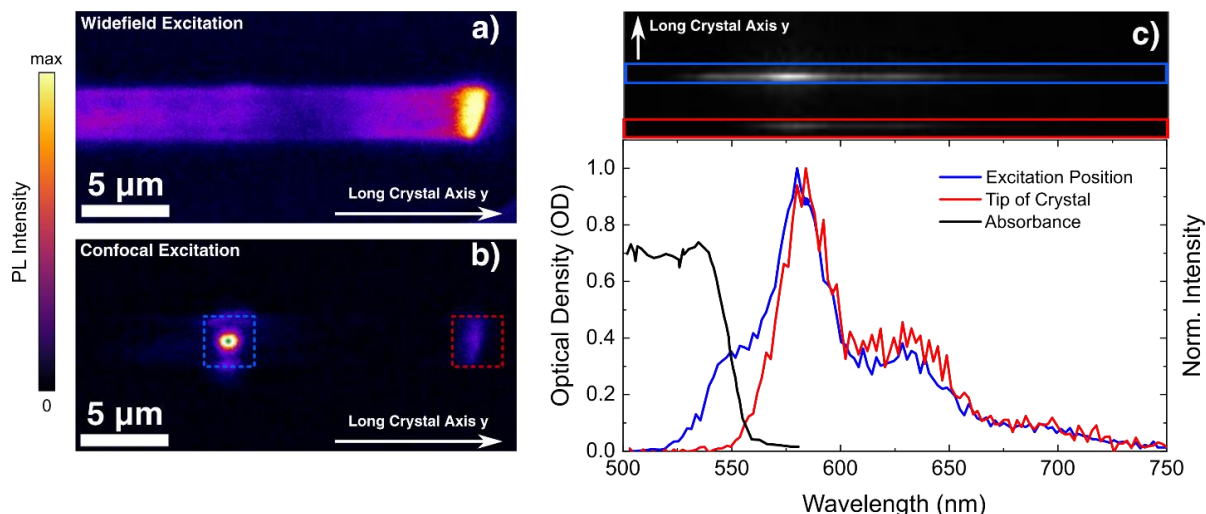


Fig. S2: Spatially resolved PL spectra. In order to obtain a more profound insight into propagation behaviour, we have aligned the long crystal axis along the slit of a spectrometer. This allows us to characterize the spectral changes spatially. **a)** Widefield PL image of a 3TBT crystal and **(b)** PL of the same crystal as in (a) upon confocal excitation at the position marked with the blue circle. The blue, respectively, red box highlight the position of the PL at the excitation position and at the tip of the crystal. **(c)** Spatially resolved PL spectra. The blue and the red boxes correspond to the PL spectra at the excitation position and at the crystal's tip. While the electronic 0-0 PL peak at around 550 nm is still present at the excitation position, it disappeared completely at the tip of the crystal¹. This distance- and energy-dependent behaviour of the PL-spectrum is characteristic for reabsorption of emitted photons in the overlap region of absorption (black line, taken from²) and PL spectra and hence can lead to partial photon recycling.

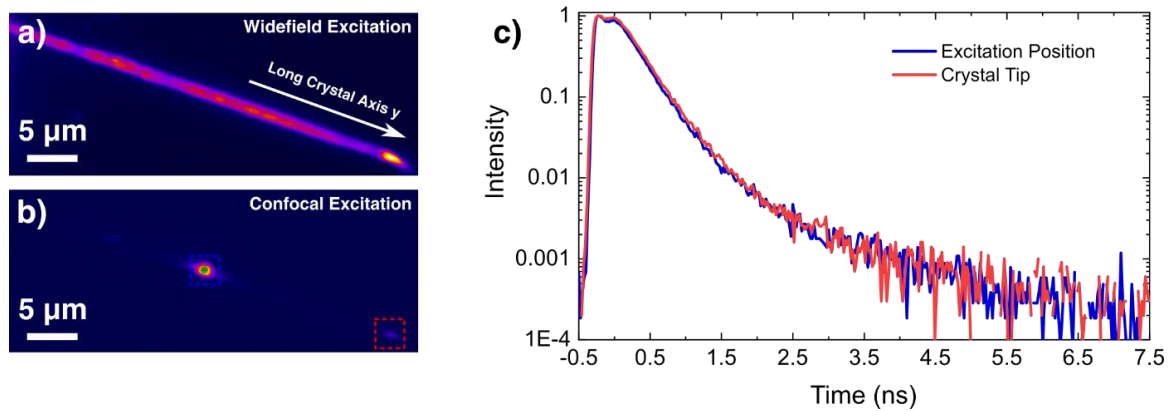


Fig. S3: PL lifetime measurement on a thin crystal. (a) Widefield PL image of a thin 3TBT crystal. (b) PL image of the same crystal as in (a) upon confocal excitation at the position marked with the green circle. The blue and red boxes indicate the detection area for PL-decay measurements at the excitation position and at the tip of the crystal, respectively. (c) PL-decay measured at the excitation position (blue) and at the tip of the crystal (red), as shown in (b). Also for thin crystals, the lifetime curves at the excitation spot and the crystal tip are essentially identical.

Photon Recycling: Kinetic Monte Carlo Ray-Tracing

For our simulation, we have extended the Monte Carlo ray tracing algorithm of Wang et al.³ to a kinetic Monte Carlo simulation that includes the temporal information of the processes. Schematically, the simulation runs as follows (Fig. S4): It starts by generating a photon and tracks it until it either is lost due to non-radiative decay or leaves the crystal or stays in a loop for more than 100 iterations. Photon generation is modelled as an isotropic emission process from a point source. A wavelength is randomly assigned using the normalized PL spectrum as distribution function. At each encounter of the photon trajectory with the boundary of the crystal, the probabilities of reflection and refraction are considered based on the Fresnel equations. Based on the distance travelled in the crystal and the wavelength, the probabilities of photon re-absorption and re-emission are evaluated. Detection of a photon occurs if the photon leaves the crystal in the direction of the glass substrate, where the objective is located (Fig. 1). All relevant information about the photon is then saved in a database, i.e., its position, arrival time, and wavelength.

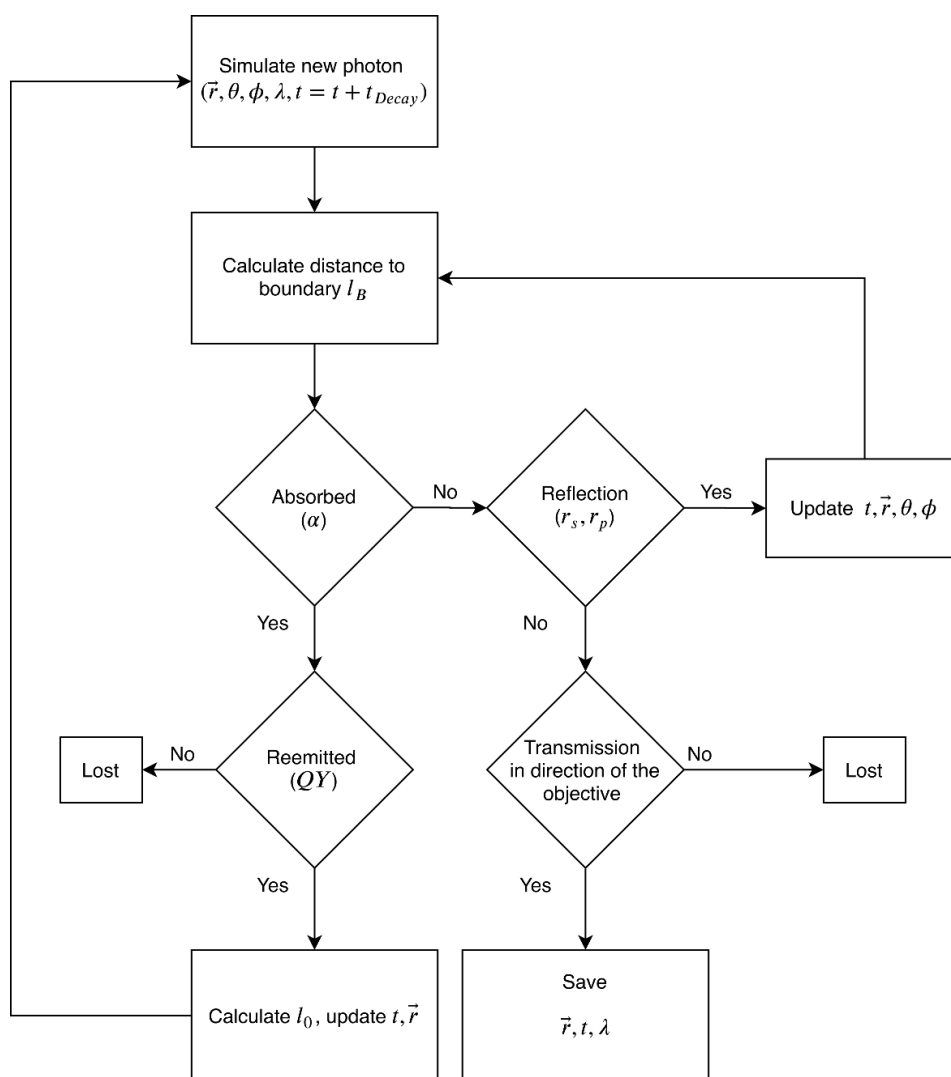


Fig. S4: Flow chart of the kinetic Monte Carlo ray tracing simulation.

The crystal is modelled as a rectangular cuboid, with a width of 2.7 μm , a height of 2 μm (calculated from the measured aspect ratio from Ref. ²) and a length of 28 μm . The crystal has a wavelength dependent refractive index $n_2(\lambda)$ ² and lies on a glass substrate with refractive index $n_1 = 1.5$. The remaining five faces of the cuboid are surrounded by air with the refractive index $n_3 = 1$.

Since the probability of absorbing a photon is proportional to the excitation intensity, the simulation starts by generating a photon within the confocal laser excitation profile modelled by a Gaussian function

$$I(\rho, z) = I_0 e^{-\alpha z} \left(\frac{\omega_0}{\omega(z)} \right)^2 e^{-\frac{2\rho^2}{\omega^2(z)}}. \quad (1)$$

Here, z is the direction of the optical axis (normal to the glass substrate) and $\rho = \sqrt{x^2 + y^2}$ corresponds to the radial distance with respect to the optical axis. I_0 is the incident intensity, which is attenuated along the optical axis with an absorption coefficient of $\alpha(\lambda = 450 \text{ nm}) = 0.3 \mu\text{m}^{-1}$. $\omega(z) = \omega_0 \sqrt{1 + \left(\frac{z}{z_R}\right)^2}$ is the lateral beam width with a minimum value of $\omega_0 = 200 \text{ nm}$ at $z = 0$. $z_R = \frac{\pi\omega_0^2 n_2(\lambda_{ex})}{\lambda_{ex}} \approx 560 \text{ nm}$ is the Rayleigh length and $\lambda_{ex} = 450 \text{ nm}$ is the wavelength of the laser excitation.

The time t_{Decay} of photon emission is determined by $t_{Decay} = -\tau \ln(\zeta_1)$, where $\tau = 0.35 \text{ ns}$ is the lifetime of the excited state (Fig. 2) and $\zeta_i \in (0,1]$ are uniform random numbers. The probability of the emission at some wavelength is equal to the normalized PL spectrum at the same wavelength.

The photons are emitted isotropically from a point source. The direction of emission is determined by the azimuthal angle ϕ and polar angle θ in spherical coordinates according to

$$\phi = 2\pi\zeta_2 \quad (2)$$

$$\theta = \text{acos}(1 - 2\zeta_3). \quad (3)$$

Based on the position of the emitter and the direction of emission, the point of impact on the cuboid faces, the distance travelled l_B , the angles of reflection and the angle to the normal of the face are determined.

The probability that a photon is reabsorbed while traversing the distance l_B is $p = 1 - e^{-\alpha(\lambda)l_B}$, where $\alpha(\lambda)$ is the wavelength dependent absorption coefficient. This probability is compared with another random number ζ_4 and if $p > \zeta_4$, the photon is re-absorbed, otherwise the photon reaches the face of the cuboid. If the photon is re-absorbed, the distance l_0 that the photon traversed before being absorbed is expressed as $l_0 = -\frac{\ln(1-p\zeta_5)}{\alpha(\lambda)}$. The required time for traversing this distance is given by $t_1 = \frac{l_0}{v_g(\lambda)}$, with $v_g(\lambda)$ being the group velocity of the photon.

The probability of re-emission is determined by the PL quantum yield QY , and occurs for $\zeta_6 < QY$. If re-emission takes place, the wavelength, the direction and the time of emission are updated as described above.

In case a photon reaches the boundary, the probability of reflection is derived from the Fresnel equations. Assuming the photon with a random polarization, the probability that it is reflected on the surface is

$$q = 0.5|r_s|^2 + 0.5|r_p|^2. \quad (4)$$

Here, r_s and r_p are the reflection coefficients for p and s polarized light, respectively. Another random number is used to decide whether reflection occurs, e.g. if $q < \zeta_7$ the photon is reflected. A schematic representation of the main decision steps with the relevant physical properties is presented in the flow chart Fig. S4.

Figs. S5 to S7 show simulated PL spectra, PL decay curved, and spatio-temporal PL intensity distributions based on the kinetic Monte Carlo ray tracing approach. Since for our 3TBT crystals only the PL quantum yield (QY) is unknown, we specifically simulate PL decay curves and PL intensity distributions as a function of the QY, that can then be compared to our experimental results shown in Fig. 2 and 3 of the main text.

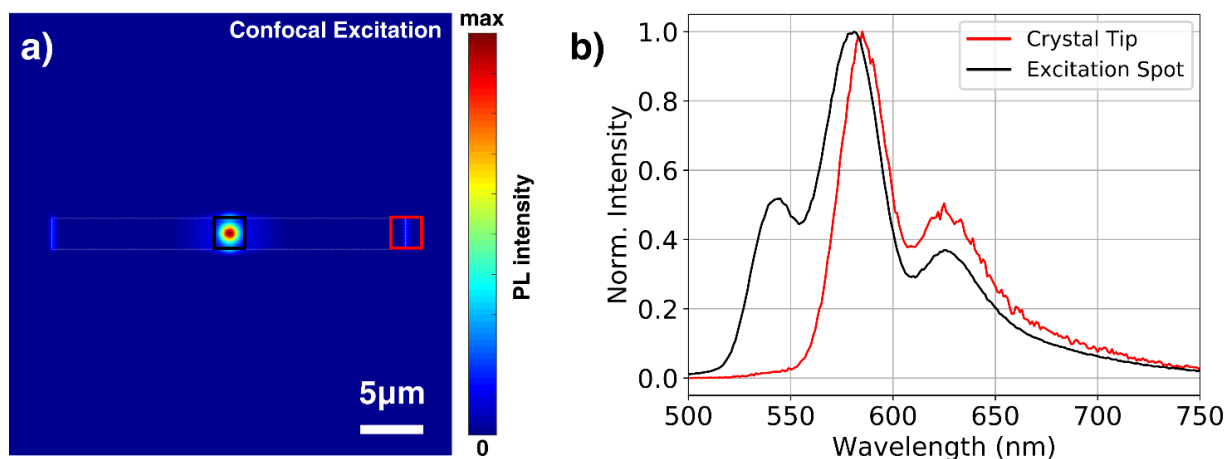


Fig. S5: Simulations of spatially resolved PL spectra based on the kinetic ray tracing simulation. (a) Simulated PL image of a 3TBT crystal upon confocal excitation at the position with the highest PL intensity (centre). The white dotted rectangle shows the edges of the simulated crystal. We used the same geometry as for the real crystal in Fig. 2. The black and red boxes highlight the position of the PL at the excitation position and at the tip of the crystal. These areas are used for the simulation of the PL-decay curves shown in Fig. S6. (b) Simulated PL spectra at the excitation position (black) and at the tip of the crystal after traversing the crystal (red). We find excellent agreement with experiment in Fig. S2.

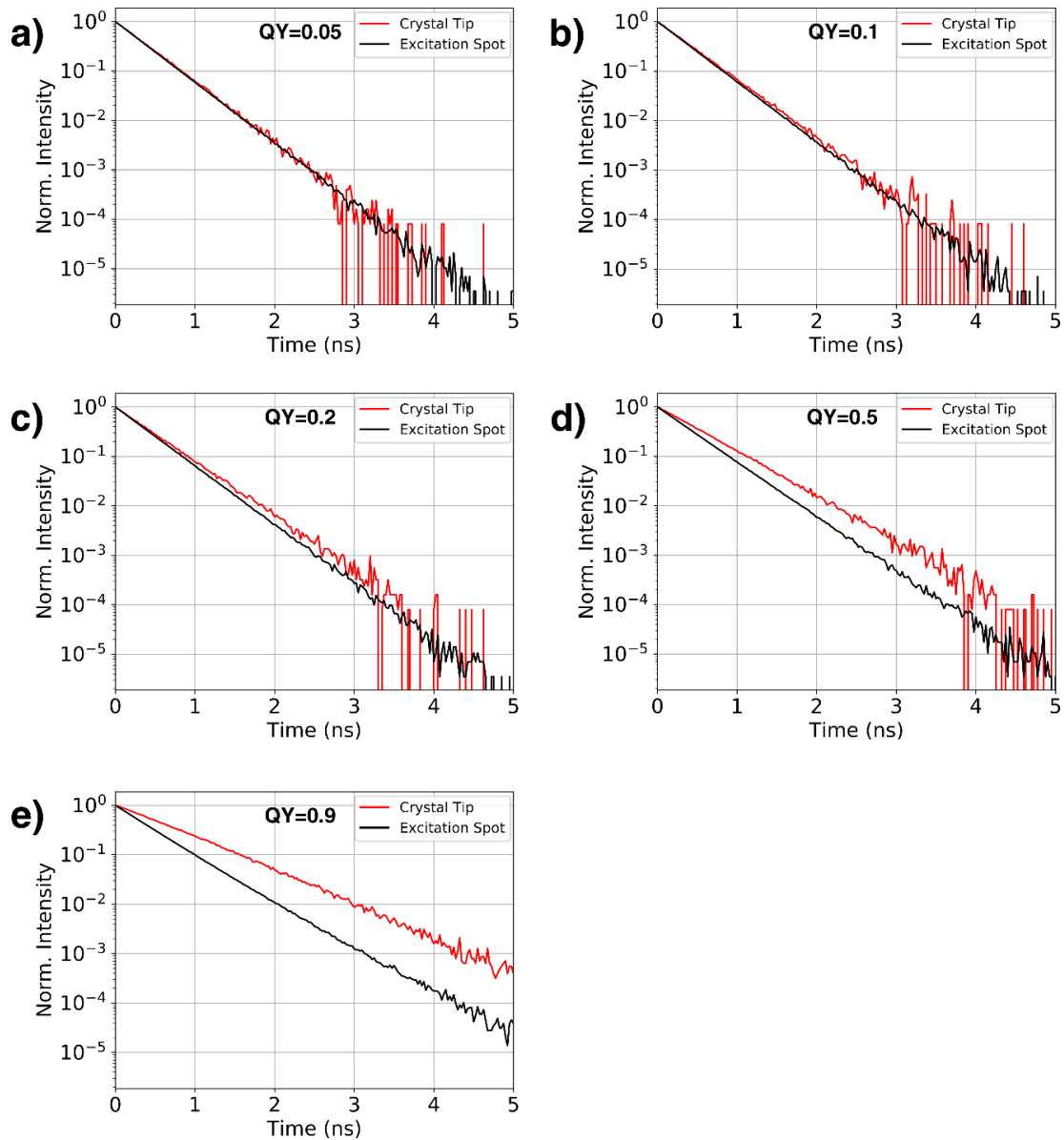


Fig. S6: Simulations of spatially resolved PL-decays based on the kinetic ray tracing simulations. Simulated PL-decay curves evaluated at the excitation position (black box, Fig. S5) and at the tip of the crystal (red box, Fig. S5) for increasing PL quantum yields (QY). Up to a quantum yield of $QY = 0.1$ the lifetime curves at the excitation spot and the crystal tip are essentially identical. From these simulations we are thus able to estimate an upper bound on the unknown QY of our 3TBT crystals of 0.1.

QY	0.05	0.1	0.2	0.5	0.9
Recycled Emission (%)	1.66	3.34	6.71	17.32	32.67

Tab. S1: Calculated contribution of re-emitted (recycled) photons to the total number of detected photons for increasing PL quantum yields (QY). The specified percentage is calculated as the ratio between re-emitted (at least once) and detected photons divided by the total number of detected photons. With increasing quantum yields the percentage of re-emitted photons increases linearly.

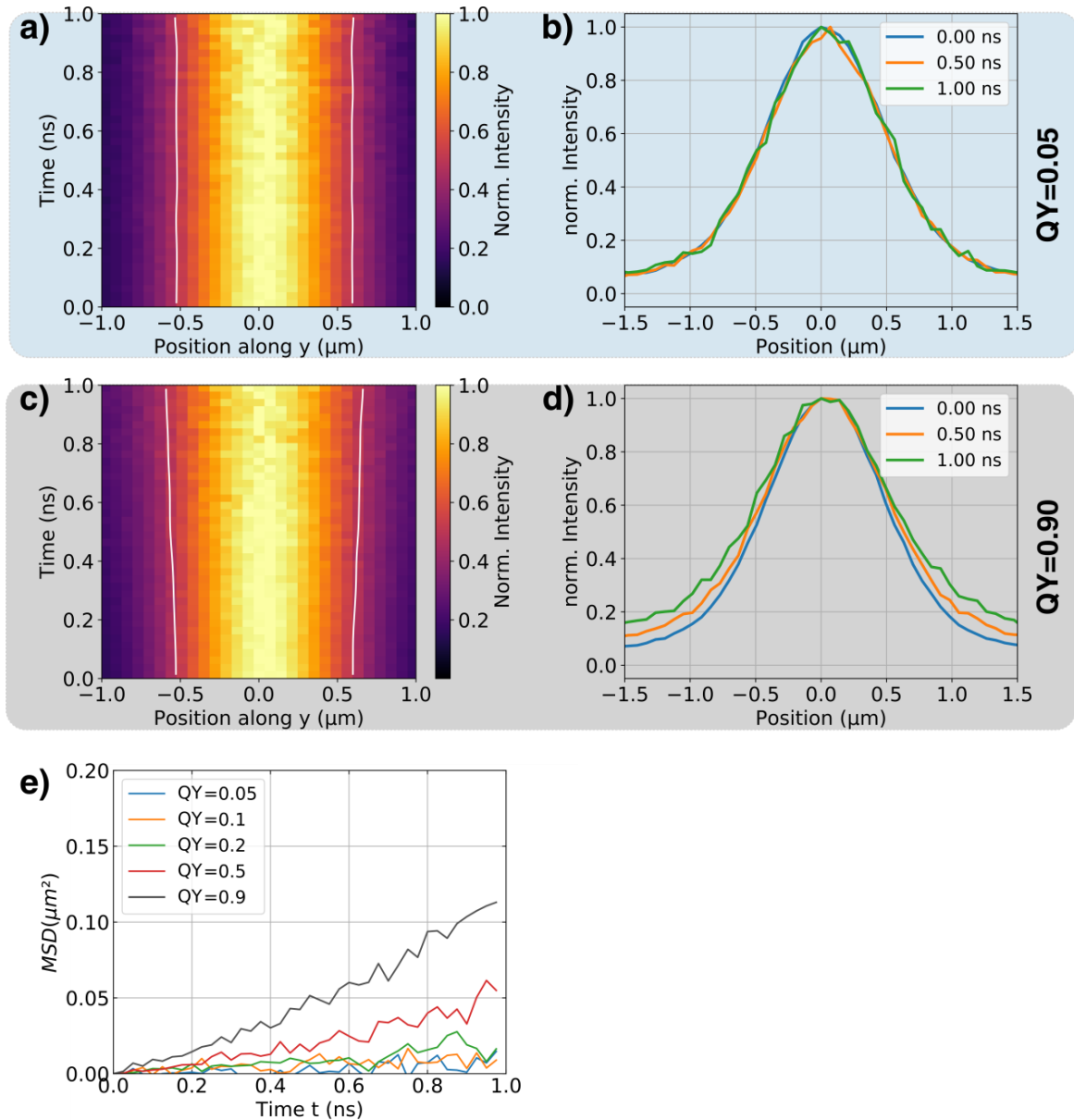


Fig. S7: Spatio-temporal broadening of the PL caused by photon recycling based on the kinetic ray tracing simulations. (a,c) Normalized spatio-temporal PL intensity distributions evaluated along the long crystal axis shown in Fig. S5 for PL quantum yields $QY=0.05$ (a) and $QY=0.9$ (c). The excitation position is $y=0$, and the arrival time of the excitation pulse is at $t=0$ ns. The contour lines indicate the time evolution of the full width at half maximum of the distribution. (b,d) Normalized spatial intensity distributions $I(y, t_i)$ extracted from (a) and (c) at three times. (e) Mean square displacements (MSD) as function of time, calculated from PL intensity distributions $I(y, t)$ for different QY. For $QY \leq 0.1$ we do not find a broadening of the MSDs due to photon recycling, which is related to e.g. the limited number of maximum detected photons, and the limited spatial and temporal resolution. For $QY > 0.1$ the MSD grows linearly in time, which is characteristic of normal diffusion. Importantly, a QY between 0.2 and 0.5 already leads to a broadening that can be resolved in our experiments. This illustrates that (i) photon recycling must be regarded as a broadening mechanism in 3D samples with already limited QY, and (ii) the QY of our crystals is very likely below 0.1.

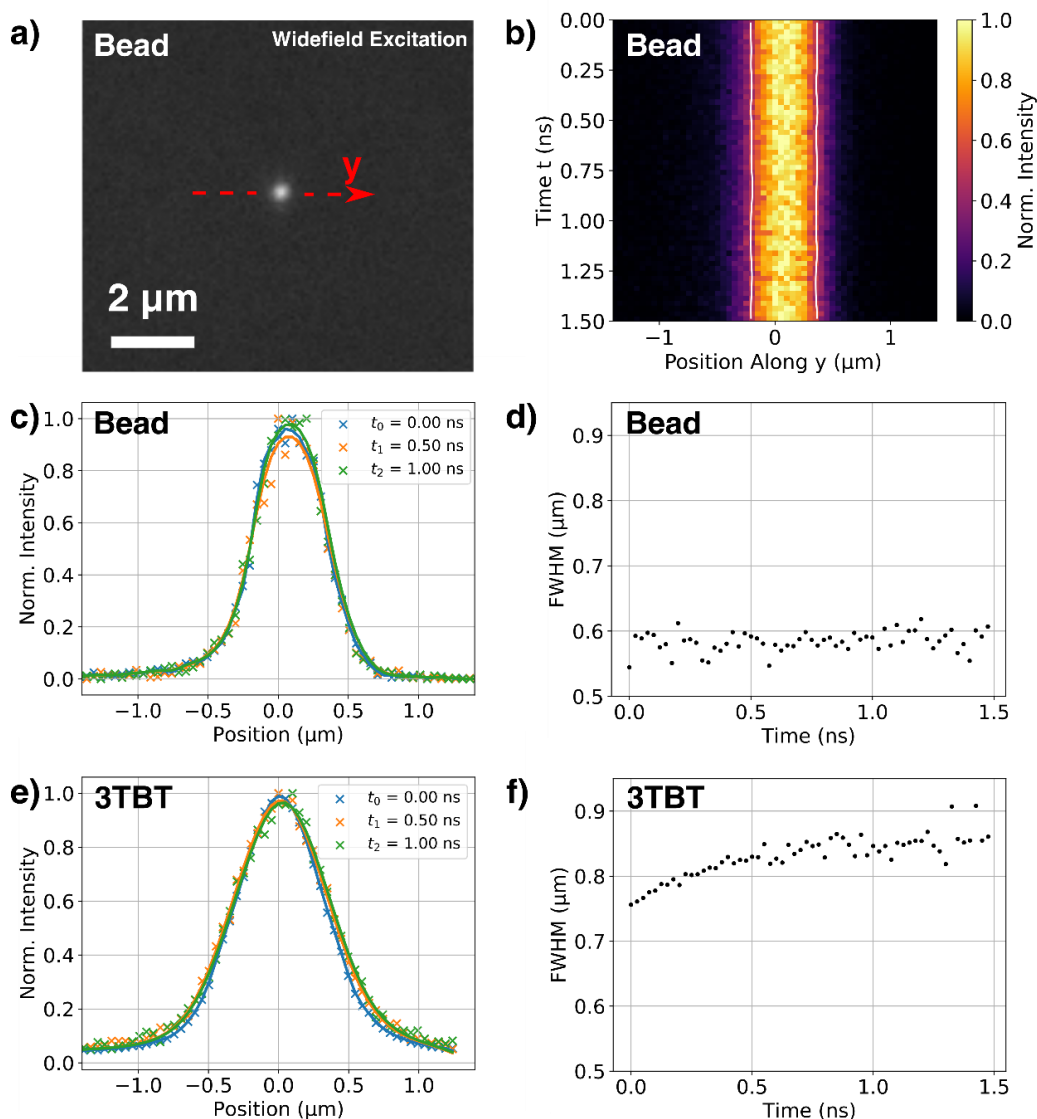


Fig. S8: Comparison of the spatio-temporal broadening for a nanobead and a 3TBT crystal. (a) Widefield PL image of an isolated SiO_x-nanobead with a diameter of 52 nm. The red arrow illustrates the direction of the detection scanning (y-axis). (b) Normalized spatio-temporal PL intensity distribution measured along the axis indicated in (a). The excitation position is at $y=0$, and $t=0$ is the arrival time of the excitation pulse. The contour lines indicate the time evolution of the full width at half maximum (FWHM). (c) Normalized profiles taken from the spatial intensity distribution $I(y, t_i)$ of the nanobead at three times. The solid lines are fits using a reconvolution approach (see below). (d) FWHM of the $I(x, t_i)$ profiles for the nanobead, revealing no temporal broadening. (e) Normalized profiles taken from the spatial intensity distribution $I(x, t_i)$ for the 3TBT crystal shown in Fig. 2 at three times with the corresponding fits. (f) FWHM of the $I(x, t_i)$ profiles for the 3TBT crystal, revealing a clear temporal broadening and an initial FWHM($t = 0$) of 760 nm. The FWHM at time $t = 0$ for the crystal is broader compared to the single nanobead due to the convolution of the 3D-sample area of the crystal with the excitation profile and leakage radiation modes from the 3D crystal (see also Fig. S9)².

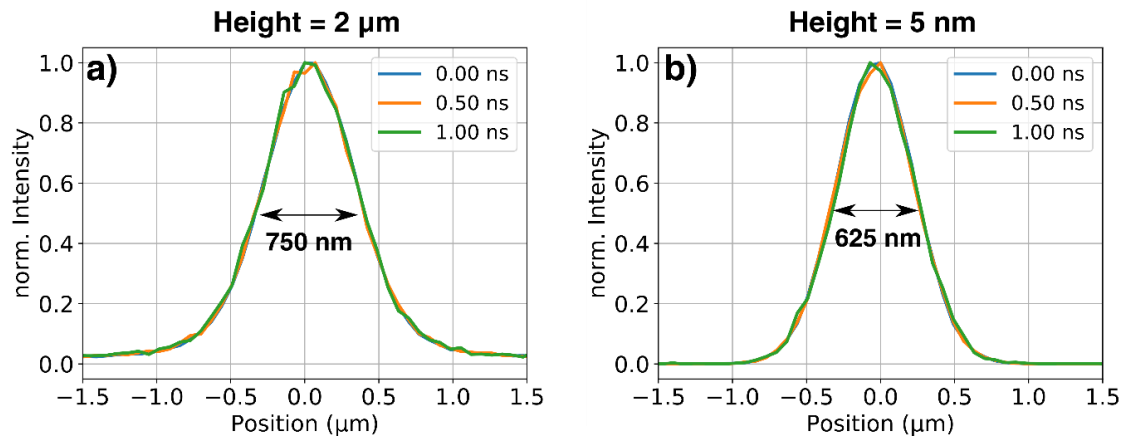


Fig. S9: Quantification of emission profiles due to leaky-mode waveguiding based on kinetic ray tracing simulations. Normalised profiles of full spatio-temporal PL intensity distributions as in Fig. S7 for a 3TBT crystal with a height of 2 μm (a) and 5 nm (b). In these simulations the PL quantum yield was set to $QY=0$ to suppress photon recycling (Note that the QY is only required to calculate photon recycling; the ‘first’ emitted photon after absorption of a laser photon always creates an emitted photon). We find that the FWHM at $t=0$ is 20% broader for the thick crystal due to leaky-mode waveguiding into the substrate (which cannot occur in the very thin crystal).

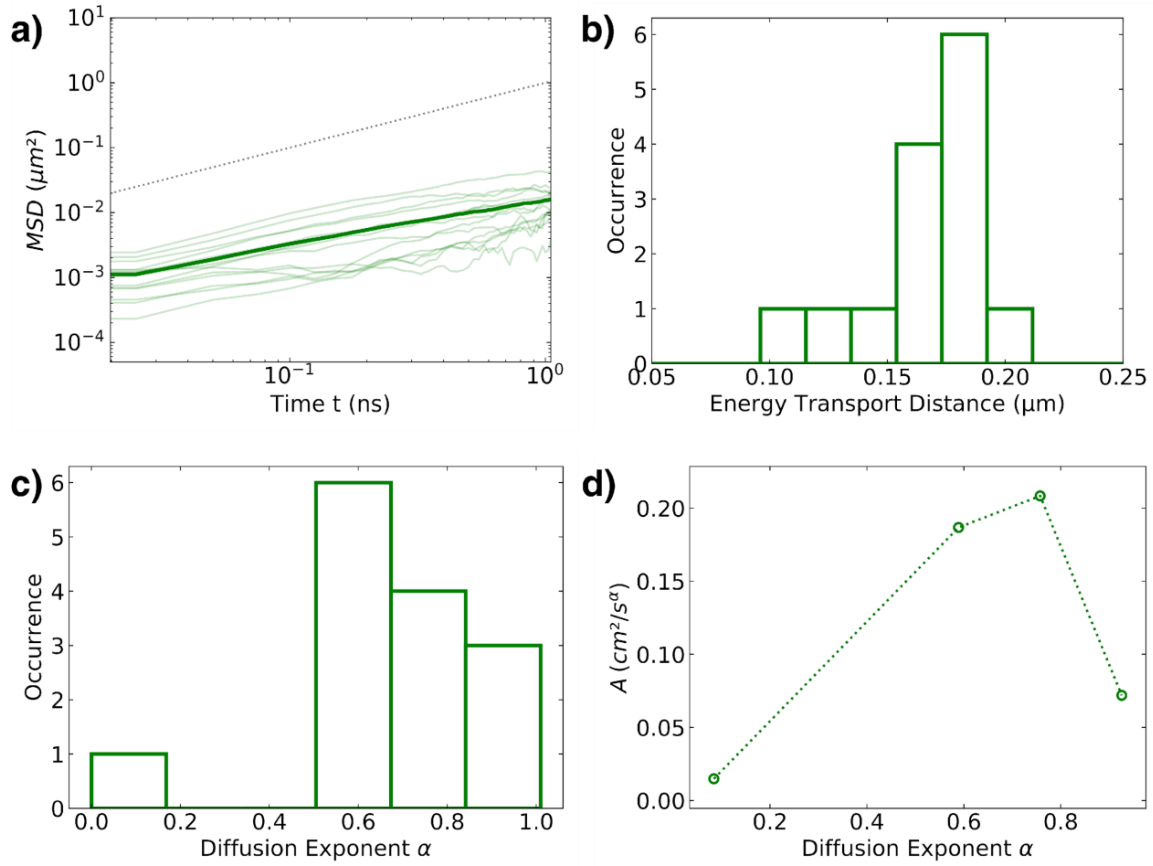


Fig. S10: Statistics of energy transport measurements for 14 different single crystals measured with low excitation fluence. (a) Temporal changes of the MSDs extracted from spatio-temporal PL intensity distributions as described in the main text. The thick line represents the average of all curves. The black dotted line indicates a linear scaling in time, i.e., normal diffusion, as a guide to the eye. (b) Energy transport distances defined as $L_D = \sqrt{\max(\text{MSD}(t))}$. The average energy transport distance is $0.17 \pm 0.02 \mu\text{m}$. (c) Distribution of the diffusion exponent α , evaluated for $t < 3\tau = 1.05\text{ns}$, where τ is the excited state lifetime. We found an average value of $\bar{\alpha} = 0.70 \pm 0.23$. (d) Averaged hopping coefficients A as a function of α .

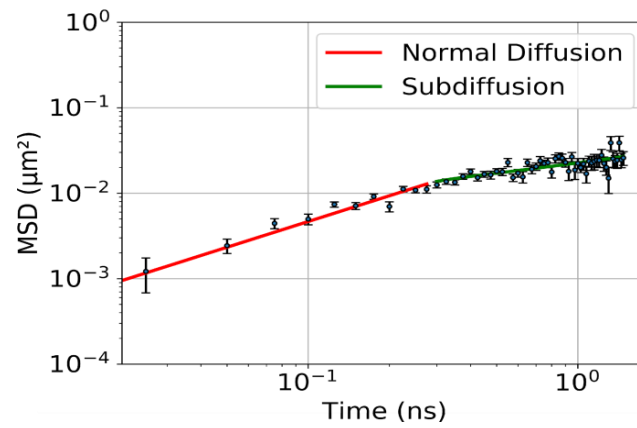


Fig S11: Fitting $\text{MSD}(t)$ with two diffusion regimes. The MSD retrieved from the crystal in Fig. 3a at low excitation fluence is shown here on a double-logarithmic scale and analysed with the standard approach of normal diffusion at small times and an apparent transition to subdiffusion for longer times. For $t < 0.27\text{ns}$ normal diffusion, $\alpha = 1$, yields a diffusion constant of $D = 0.23 \pm 0.01\text{ cm}^2/\text{s}$. For $t > 0.27\text{ns}$ a subdiffusive fit gives a diffusion exponent $\alpha = 0.70 \pm 0.39$.

Kinetic Monte Carlo Simulation of Exciton-Exciton Annihilation.

The dynamics of exciton transport along a one dimensional stack were simulated numerically using a kinetic Monte Carlo (KMC) algorithm, in which the excitons undergo a series of stochastic transport steps (incoherent hopping) in a disordered energy landscape. We assume a one-dimensional diffusion model because $\pi - \pi$ -stacking of the 3TBT results in the highest electronic couplings and exciton delocalization along the long crystal axis. Therefore diffusion mainly takes place in this direction, and diffusion along directions perpendicular to the π -stacking direction can be neglected here.

A one-dimensional stack is built from $N = 30000$ 3TBT molecules with a $\pi - \pi$ -spacing of 0.37 nm. To take exciton delocalization in the simulation into account, each stack is divided into domains comprising 10 molecules. This domain size $N'=10$ was determined from the best fit to our experimental data (Fig. 3a and b), and this number is in agreement with typical delocalization lengths of excitons in thiophene-based H-aggregated polymers⁴. The excited-state energy landscape is chosen from a Gaussian distribution with a standard deviation of $\sigma = 43$ meV determined from the inhomogeneous line width in Ref.². Since our crystal represents in fact an ensemble of 1D H-aggregated stacks, we average over 2000 realisations of energy landscapes. Excitations were generated in the middle of a stack within a Gaussian excitation profile according to the experimentally created exciton density. Furthermore, the generation time of the excitons is randomly chosen from a Gaussian-shaped temporal distribution with a FWHM of 70 ps, in accordance to the experimental pulse duration. The excitations can decay within their excited state lifetime or hop between adjacent domains. Excitons can also interact with each other, i.e., exciton-exciton annihilation (EEA) takes place. The annihilation radius is set to be one domain size. An EEA event causes immediate deletion of one of the excitons, and only the remaining one can be transported or decay.

For the excited-state decay we use the experimental decay rate $k_d = \frac{1}{0.35ns}$ (inverse lifetime). All decayed photons are “detected” by sorting them into the corresponding bin of the spatio-temporal PL distribution $I(y, t)$. For a hopping step, the exciton is either transferred to the right or left neighbouring domain with a transport rate k_{ET} . This transport rate depends on the specific energy landscape, i.e., on the energy difference ΔE between the adjacent domains:

$$k_{ET} = \begin{cases} k_0 & \text{if } \Delta E < 0 \\ k_0 \exp\left(-\frac{\Delta E}{k_B T}\right) & \text{if } \Delta E > 0. \end{cases} \quad (5)$$

Here, the rate constant $k_0 = 25000$ 1/ns is treated as a free parameter and determined from the best fit to the data. Hops to energetically higher levels are scaled with a Boltzmann factor with $k_B T \approx 25$ meV corresponding to the thermal energy at room temperature. This procedure is repeated until 4000 photons were detected in the maximum of the spatio-temporal map $I(y, t)$. To obtain an image comparable to the experiment, the simulated map is convoluted with a Gaussian point-spread function.

Finally, we note that the assumption of incoherent hops of delocalised excitons was necessary to describe the high diffusion lengths in the subdiffusive regime for our crystals. Without delocalization, we would not have been able to reproduce the experimental data (Fig. 3a and b) within this model.

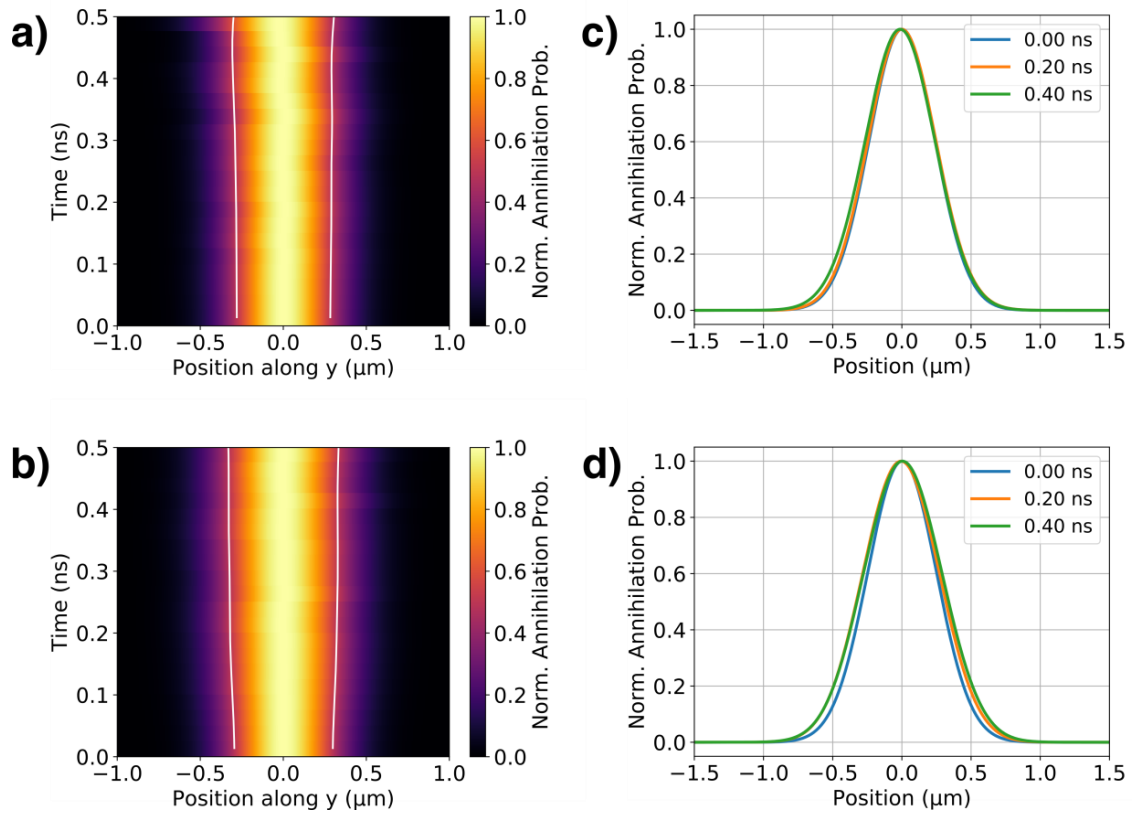


Fig. S12: Dynamics of the annihilation probability for the simulations shown in Fig. 4 of the main text. (a,b) Simulated normalized probability of annihilation and its evolution in space and time for an average of 2000 realizations of energetic disorder with 2.4 excitations/ μm (a) and 240 excitations/ μm (b). (c,d) Illustration of the normalized spatial annihilation probability $P_{annihilation}(y, t_i)$ for three times t_i . The annihilation probability is described by a broadening Gaussian that is broadening and features a decreasing amplitude with time (see also Fig. 4e of the main text).

Incoherent Exciton Diffusion Model

The extended diffusion equation for 1-dimensional incoherent transport with an exponential decay of the excitations reads⁵⁻⁷

$$\frac{\partial n(y,t)}{\partial t} = D(t) \frac{\partial^2 n(y,t)}{\partial y^2} - kn(y,t) + p \cdot Exc(y), \quad (6)$$

where $n(y,t)$ is the exciton distribution that depends on both space and time, p is the probability of absorption and $Exc(y)$ is the excitation profile. $D(t)$ is the time-dependent diffusivity that is related to an exciton hopping coefficient A by $D(t) = \frac{1}{2} A_\alpha t^{\alpha-1}$ with fractional time units for A ⁸. Finally, k is the constant exciton decay rate, i.e., the inverse exciton lifetime. Superdiffusive transport is characterized by $1 < \alpha \leq 2$. For normal diffusion, $\alpha = 1$, the diffusivity $D = \frac{1}{2} A$ is time independent with units of cm^2s^{-1} . Subdiffusion is characterized by $0 < \alpha < 1$ and occurs for exciton motion in a disordered excited-state energy landscape^{9,10}.

The solution to equation (6) using a delta-function shaped excitation profile $Exc(y)$ centred at $y = 0$, is given by^{5,6}

$$n(y,t) \propto \exp\left(-\frac{y^2}{2At^\alpha}\right) \exp(-kt) \equiv G(y,t). \quad (7)$$

Note that the exponential decay ($\exp(-kt)$) for the exciton population in equation (7) only changes the magnitude of this distribution at any point in time, but not its shape (width). Normalization of the distribution to its maximum value at each point in time removes this exponential decay. Equation (7), is the probability density function, or the propagator function for diffusion.

Equation (7) shows that the variance of the exciton distribution, the mean square displacement MSD $\langle n(t)^2 \rangle$, evolves in time as⁵⁻⁷

$$\langle n(t)^2 \rangle = MSD(t) = At^\alpha, \quad (8)$$

In a general situation with electronic disorder in the excited-state energy landscape the time-dependent diffusivity $D(t) = \frac{1}{2} A_\alpha t^{\alpha-1}$ decreases with time^{7,8}, see also Fig. 3d of the main text.

For normal diffusion ($\alpha = 1$), equation (8) transforms to

$$\langle n(t)^2 \rangle = MSD(t) = 2Dt. \quad (9)$$

For an arbitrary initial distribution $n(y,0)$, the time dependent exciton distribution at time t is given as a convolution of the initial condition with the time-dependent propagator function $n(y,t) = n(y,0) * G(y,t)$.

In general, the measured spatial intensity distribution (e.g. Fig. 3a,b) is a convolution of the initial exciton distribution $n(y)$, the Gaussian probability density function for exciton diffusion (diffusion propagator) $G(y,t)$, the detection point spread function $PSF(y)$ and the function of the APD detector size $C(y)$ ^{6,7}

$$I(y,t) = n(y) * G(y,t) * PSF(y) * C(y). \quad (10)$$

Here, we used a reconvolution approach to account for all non-Gaussian broadening effects due to e.g. reflections at interfaces, scattering at defects and radiative leaky waveguide modes. The measured spatio-temporal emission distribution $I(y,t)$ is fitted to a convolution of the initial profile $I(y, t = 0)$, which includes the initial exciton distribution, the PSF, the detector size, reflections and other time-independent effects, and $G(y, t)$:

$$I(y, t) \propto I(y, 0) * G(y, t). \quad (11)$$

Again, the variance of $G(y, t)$ corresponds to the MSD, reflecting the PL broadening as a function of time.

Characterisation of the setup

To characterise the setup, we used agglomerated SiO_x-nanobeads (Corpuscular, diameter 52 nm), because energy transport between the nanobeads is negligible and a time-dependent broadening of the PL profile is not expected. Fig. S13 displays the results of detection-beam scanning on these nanobeads.

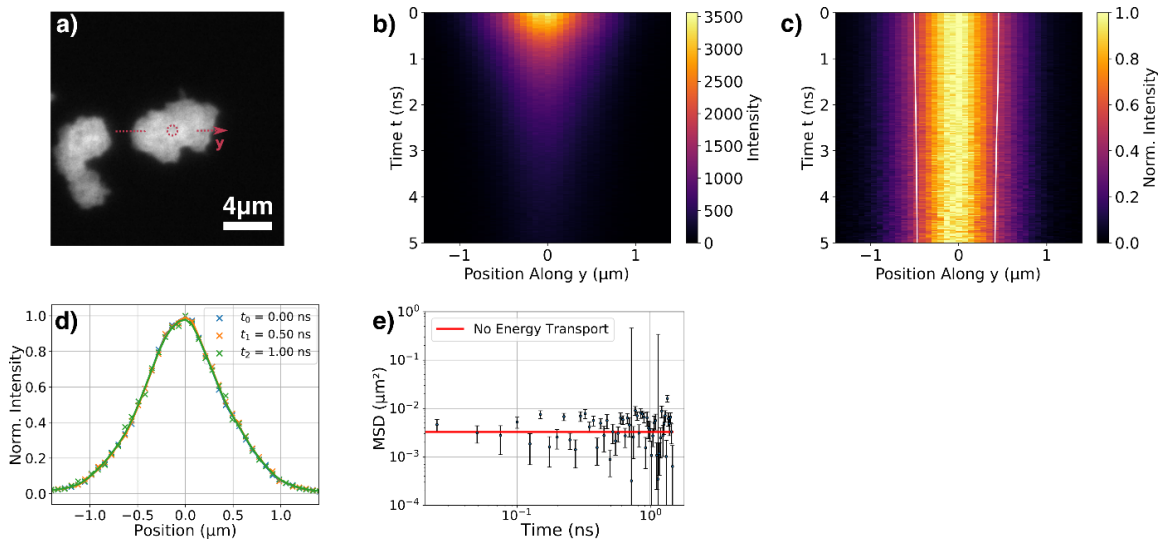


Fig. S13: Control experiment on a reference sample without long-range energy transport. (a) Widefield PL image of agglomerated SiO_x-nanobeads. The dashed red circle and arrow illustrate the position of confocal excitation and the direction of the detection scanning (y -axis), respectively. (b) Spatio-temporal PL intensity distribution $I(y, t)$. (c) Normalized PL intensity distribution. In (b) and (c) the position y denotes the distance relative to the excitation position ($y=0$) along the arrow in (a), and $t=0$ ns corresponds to the arrival time of the excitation pulse. To emphasize changes in the width of the distribution, it is normalized for the representation in (c) at each time step. The contour lines indicate the time evolution of the full width at half maximum. (d) Profiles taken from the normalized intensity distribution $I(y, t_i)$ in (c) for three times t_i and the fits, as explained above. (e) Temporal changes of the MSD of the profiles in (d), revealing no resolvable energy transport in agglomerated SiO_x-nanobeads. Taken from Ref. ¹¹.

References:

- ¹ S. Motamen, C. Schörner, D. Raithel, J.P. Malval, T. Jarrosson, F. Serein-Spirau, L. Simon, R. Hildner, and G. Reiter, *Phys. Chem. Chem. Phys.* **19**, 15980 (2017).
- ² C. Schörner, S. Motamen, L. Simon, G. Reiter, and R. Hildner, *ACS Omega* **3**, 6728 (2018).
- ³ X. Wang, S. Chang, J. Yang, M. Zhou, D. Cao, and J. Tan, *Appl. Opt.* **46**, 8446 (2007).
- ⁴ F.C. Spano, J. Clark, C. Silva, and R.H. Friend, *J. Chem. Phys.* **130**, 074904 (2009).
- ⁵ K.A. Clark, E.L. Krueger, and D.A. Vanden Bout, *J. Phys. Chem. Lett.* **5**, 2274 (2014).
- ⁶ G.M. Akselrod, P.B. Deotare, N.J. Thompson, J. Lee, W.A. Tisdale, M.A. Baldo, V.M. Menon, and V. Bulovic, *Nat. Commun.* **5**, 3646 (2014).
- ⁷ G.M. Akselrod, F. Prins, L. V. Poulikakos, E.M.Y. Lee, M.C. Weidman, A.J. Mork, A.P. Willard, V. Bulović, and W.A. Tisdale, *Nano Lett.* **14**, 3556 (2014).
- ⁸ J. Wu and K.M. Berland, *Biophys. J.* **95**, 2049 (2008).
- ⁹ S. Havlin and D. Ben-Avraham, *Adv. Phys.* **51**, 187 (2002).
- ¹⁰ S.M. Vlaming, V.A. Malyshev, A. Eisfeld, and J. Knoester, *J. Chem. Phys.* **138**, 214316 (2013).
- ¹¹ B. Wittmann, F.A. Wenzel, S. Wiesneth, A.T. Haedler, M. Drechsler, K. Kreger, J. Köhler, E.W. Meijer, H.-W. Schmidt, and R. Hildner, *J. Am. Chem. Soc.* **142**, 8323 (2020).



Enhancing Long-Range Energy Transport in Supramolecular Architectures by Tailoring Coherence Properties

Bernd Wittmann, Felix A. Wenzel, Stephan Wiesneth, Andreas T. Haedler, Markus Drechsler, Klaus Kreger, Jürgen Köhler, E. W. Meijer, Hans-Werner Schmidt,* and Richard Hildner*

Cite This: *J. Am. Chem. Soc.* 2020, 142, 8323–8330

Read Online

ACCESS |



Metrics & More

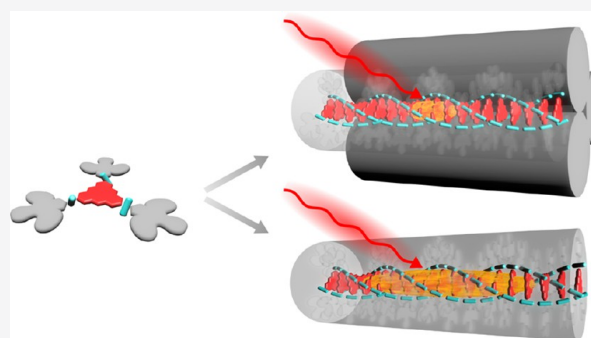


Article Recommendations



Supporting Information

ABSTRACT: Efficient long-range energy transport along supramolecular architectures of functional organic molecules is a key step in nature for converting sunlight into a useful form of energy. Understanding and manipulating these transport processes on a molecular and supramolecular scale is a long-standing goal. However, the realization of a well-defined system that allows for tuning morphology and electronic properties as well as for resolution of transport in space and time is challenging. Here we show how the excited-state energy landscape and thus the coherence characteristics of electronic excitations can be modified by the hierarchical level of H-type supramolecular architectures. We visualize, at room temperature, long-range incoherent transport of delocalized singlet excitons on pico- to nanosecond time scales in single supramolecular nanofibers and bundles of nanofibers. Increasing the degree of coherence, i.e., exciton delocalization, via supramolecular architectures enhances exciton diffusivities up to 1 order of magnitude. In particular, we find that single supramolecular nanofibers exhibit the highest diffusivities reported for H-aggregates so far.



INTRODUCTION

Supramolecular chemistry provides intriguing opportunities to create nano- to mesoscale assemblies with unprecedented optical and electronic functionalities owing to cooperative interactions between the constituent building blocks.^{1–7} A key functionality for potential applications is, for example, efficient long-range excitation energy transport.^{4,8–14} In general, energy transport in organic materials is governed by the delicate interplay between electronic Coulomb coupling between densely packed molecules and electronic and structural disorder. On the one hand, electronic coupling leads to the formation of delocalized exciton states; that is, electronic excitations are coherently shared by many molecules, which we refer to as (quantum) coherent transport. On the other hand, electronic and structural disorder leads to a localization of excitons on small domains of supramolecular assemblies.^{15,16} If disorder dominates, long-range transport cannot be realized, because incoherent Förster-type hopping of strongly localized excitons limits transport to some tens of nanometers.¹⁷ In contrast, reducing disorder increases exciton delocalization, and thus the degree of coherence.^{15,18–20} Such combined incoherent–coherent transport, i.e., incoherent hops of delocalized excitons,^{12,21–24} with a strong contribution of coherence, indeed allowed achieving distances beyond 1 μm .^{12,23} However, a full understanding and control of long-range energy transport is still highly complex, because in

supramolecular nanostructures the electronic coupling and disorder are typically of the same order of magnitude. This so-called intermediate regime renders disentangling the different contributions to energy transport difficult, on both the theoretical and experimental side.¹⁶ Since transport efficiencies and distances are predicted to be largest in this regime,^{21,25,26} a unique picture is desirable for the design of novel excitonic materials and devices.^{2,4,5,7–9}

A straightforward approach to modify electronic coupling and disorder makes use of the self-assembly of defined nanostructures based on the same building blocks. In this context, so-called pathway complexity can be exploited to form thermodynamically and kinetically stable supramolecular aggregates with different structural order^{6,27,28} and thus with significantly altered photophysical and energy transport properties. In contrast, supramolecular aggregates with different hierarchical levels^{11,29–31} feature the same structural arrangement of the building blocks, i.e., the same electronic coupling, with only subtle variations in the local electronic

Received: February 7, 2020

Published: April 11, 2020



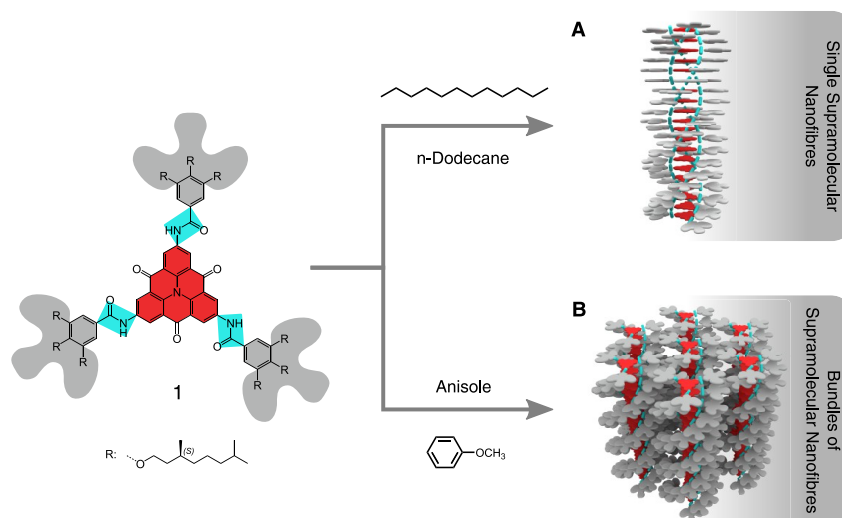


Figure 1. Supramolecular architectures of compound **1** with different hierarchical levels. Left: Compound **1** comprising a carbonyl-bridged triarylamine core (red), three amide moieties (blue), and chiral bulky peripheries (gray). Self-assembly in *n*-dodecane results in single supramolecular nanofibers (A) and in anisole in bundles of supramolecular nanofibers (B).

environment. Such structures are therefore ideal candidates to reveal the interplay between the electronic coupling and disorder.

Here we present stable and robust supramolecular architectures based on a carbonyl-bridged triarylamine trisamide (CBT, compound **1**, see ref ³²) with different hierarchical levels depending on the solvent, i.e., single supramolecular nanofibers and bundles of supramolecular nanofibers (Figure 1). The molecular design of compound **1** results in columnar structures with a well-defined, cofacial H-type arrangement of the CBT cores that is driven by directed hydrogen bonding between amide groups. Excitons in these supramolecular architectures possess different degrees of coherence (delocalization), tuned by bundling-induced electronic disorder. We are thus able to resolve the competition between coherence and disorder and to demonstrate its impact on long-range, pico- to nanosecond, incoherent transport of singlet excitons in supramolecular architectures on the level of single nanostructures at room temperature. In contrast to previous work on nanotubular assemblies,^{11,30} we find a higher degree of coherence and thus enhanced exciton diffusivities in single supramolecular nanofibers.

RESULTS AND DISCUSSION

Controlled Self-Assembly of Single Nanofibers and Bundles of Nanofibers. Using two selected solvents, we are able to self-assemble compound **1** into distinct supramolecular morphologies (see Supporting Information section 1). In *n*-dodecane, compound **1** forms single supramolecular nanofibers of several micrometers in length (Figures 2A and S1) and uniform heights of about 2 nm (Figure 2B), as shown by atomic force microscopy (AFM), which is consistent with our previous work on single CBT-nanofibers.^{23,32} Transmission electron microscopy (TEM, Figure 2C) reveals single supramolecular nanofibers and nanofibers partially located next to each other due to sample preparation. The selected area electron diffraction (SAED) pattern features a signal corresponding to a distance of 0.33 nm (Figure 2D) caused

by cofacial stacking of CBT cores along the supramolecular nanofibers.^{23,32}

Self-assembly of compound **1** in anisole results in bundles of supramolecular nanofibers with widths and heights on the order of 100 nm, as shown by AFM and TEM measurements (Figure 2E,F,G and Figure S1). The SAED pattern yields the characteristic cofacial stacking distance of 0.33 nm between CBT cores (Figure 2H). Additionally, SAED at smaller angles (Figure S2) reveals defined signals corresponding to a distance of 2.8 nm. Assuming a columnar hexagonal packing of the nanofibers,³² we obtain an intercolumnar spacing of 3.2 nm. This distance is substantially smaller than the calculated diameter of about 4.4 nm for the extended compound **1**.³² In bundles the peripheries of adjacent nanofibers therefore strongly interact. Based on these data, we estimate that one bundle consists of approximately 2000 nanofibers.

Optical Properties of Nanofibers and Bundles. UV-vis and photoluminescence (PL) spectra of dissolved compound **1** in THF (Figure 3A) exhibit the characteristic vibronic progression of an aromatic molecule (see Supporting Information section 4, Table S1). The maxima at 460 nm and 490 nm, respectively, are attributed to the electronic (0–0) π – π^* transition of the CBT core.^{33,34}

The absorption spectra of supramolecular nanofibers and bundles of nanofibers are shown in Figure 3B and C, respectively (see also Figure S3). Both feature a substantially reduced intensity of the highest-wavelength (lowest-energy) peak around 520 nm (labeled A₁) compared to the spectrum of dissolved compound **1**. This spectral change is characteristic for delocalized absorbing excitons in H-aggregates, formed by substantial electronic Coulomb coupling between adjacent CBT cores.³⁵ Circular-dichroism spectra of dispersions of both supramolecular morphologies feature nearly identical signatures (Figure S4) indicating no significant difference in the structural arrangement of the CBT cores in supramolecular nanofibers and bundles of nanofibers.

After absorption rapid, subpicosecond relaxation within the exciton bands takes place toward lower-energy, relaxed exciton states,²² from where emission occurs (see Supporting

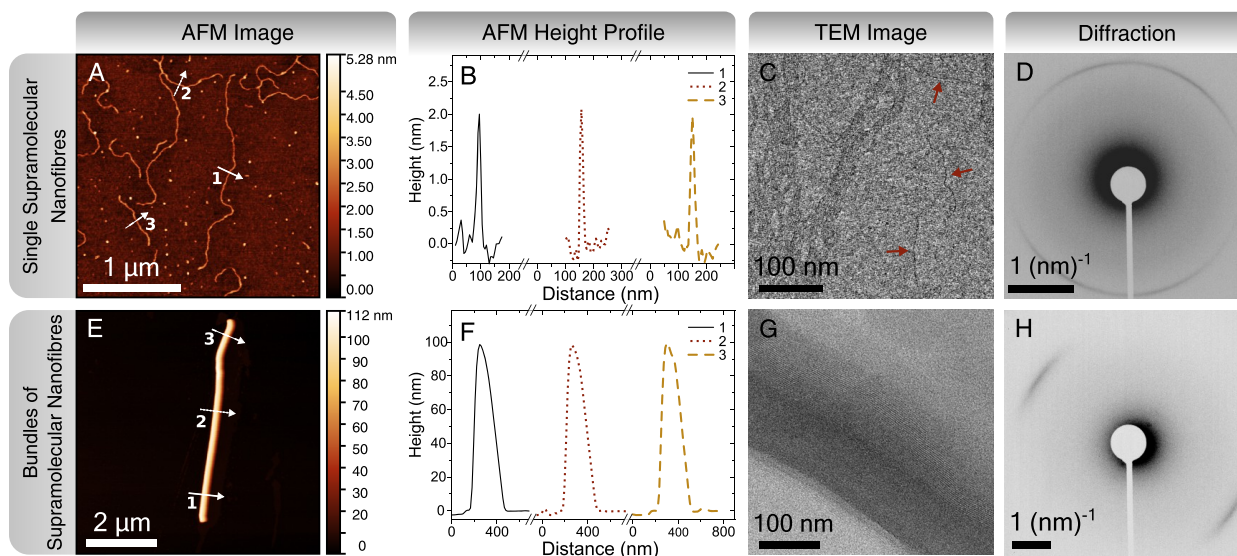


Figure 2. Morphological and structural characterization of the supramolecular architectures. (A) AFM image (topographical scan) of single supramolecular nanofibers prepared from a dispersion of compound **1** in *n*-dodecane ($4 \mu\text{M}$, $\sim 10 \text{ ppm}$). (B) Height profiles along the arrows labeled in A. (C) TEM image of single nanofibers partially located next to each other ($40 \mu\text{M}$, $\sim 100 \text{ ppm}$). Arrows indicate isolated single nanofibers. (D) SAED pattern corresponds to a stacking distance of 0.33 nm between CBT cores. (E) AFM image of a bundle of supramolecular nanofibers prepared from a dispersion of compound **1** in anisole ($40 \mu\text{M}$, $\sim 100 \text{ ppm}$). (F) Height profiles along the arrows labeled in E. (G) TEM image of a bundle of nanofibers. (H) SAED pattern corresponds to a stacking distance of 0.33 nm.

Information section 4, Figure S5). In the PL spectrum of supramolecular nanofibers the 0–0 peak seems to be absent at room temperature (Figure 3B, see also Supporting Information section 4, Figure S6). These data suggest a large degree of electronic order and thus of coherence with a pronounced delocalization of relaxed emitting excitons³⁵ along nanofibers. In contrast, the corrected PL spectrum of bundles of nanofibers (Figures 3C and S7) features a 0–0 peak that is only slightly suppressed compared to that of dissolved compound **1**. This observation indicates strong localization of the relaxed emitting exciton over only a few CBT cores and thus a small degree of coherence. The localization must result predominantly from electronic disorder, because the structural order within the columns of both architectures appears to be comparable (Figure S4). Our data for bundles of nanofibers thus demonstrate a rapid disorder-induced localization of initially delocalized absorbing excitons prior to emission.²¹

The influence of electronic disorder on the relaxed emitting excitons in our supramolecular architectures is further confirmed by the trend in the excited-state lifetimes (PL quantum yields), which increase (decrease) from 2.7 ns (13.8%) for the dissolved compound **1** to 3.5 ns (2.6%) for bundles and 5.4 ns (1.3%) for single nanofibers (see Table S2 and Figure S8). This enhancement in lifetimes is highly beneficial for long-range energy transport,¹⁵ as we previously reported.²³

To quantify the electronic Coulomb coupling and the electronic disorder between CBT cores from the spectra in Figure 3B,C, we performed numerical simulations based on the theory of Spano and co-workers using a disordered Holstein Hamiltonian (ref 35 and Supporting Information section 5). The intercolumnar distance of 3.2 nm within bundles prevents delocalization of electronic excitations between columns. A bundle is thus modeled as an arrangement of independent nanofibers. Electronic (energy) disorder is included by taking

the CBT cores' transition energy offsets from a Gaussian distribution with a width σ . Moreover, we include a correlation length l_0 that accounts for differences in the spatial distribution of disorder in the transition energies (Figure S5).

The simulations (Figure 3B,C, black lines) agree very well with the experimental data in the relevant spectral region. The absorption spectra of both architectures are well described by a common set of parameters, i.e., by an electronic coupling of $J_0 = 735 \text{ cm}^{-1}$ (91 meV) and an electronic disorder of $\sigma = 1036 \text{ cm}^{-1}$ (130 meV, see Figure S9 and Supporting Information section 5), which places both morphologies in the intermediate coupling regime.

The differences between the PL spectra of nanofibers and bundles can only be modeled using different correlation lengths. The absence of the 0–0 PL peak in the spectrum of nanofibers requires a correlation length of $l_0 \geq 10$ CBT cores with a disorder of $\sigma = 1076 \text{ cm}^{-1}$ (134 meV, see Supporting Information section 5). Due to this spatial correlation in the transition energies, a nanofiber is segmented into domains that possess a rather uniform excited-state energy landscape (Figure 3E). The delocalization of the relaxed, emitting singlet excitons can then be quantified by the coherence number of $N_{\text{coh}} \geq 5.4$ CBT cores. In contrast, the strong 0–0 PL peak intensity in the PL spectrum of bundles of nanofibers requires a vanishing correlation length ($l_0 = 0$). The relaxed emitting exciton in bundles is thus localized on approximately 2.9 CBT cores due to the rough excited-state energy landscape along nanofibers in bundles (Figure 3F). The different excited-state energy landscapes along one column (single nanofiber and within a bundle, respectively) due to the distinct spatial transition energy correlations is visualized in Figure 3E,F. We note that these realizations are directly taken from the numerical simulations.

Direct Visualization of Exciton Transport. Our optical spectroscopy data demonstrate that we are able to tune the

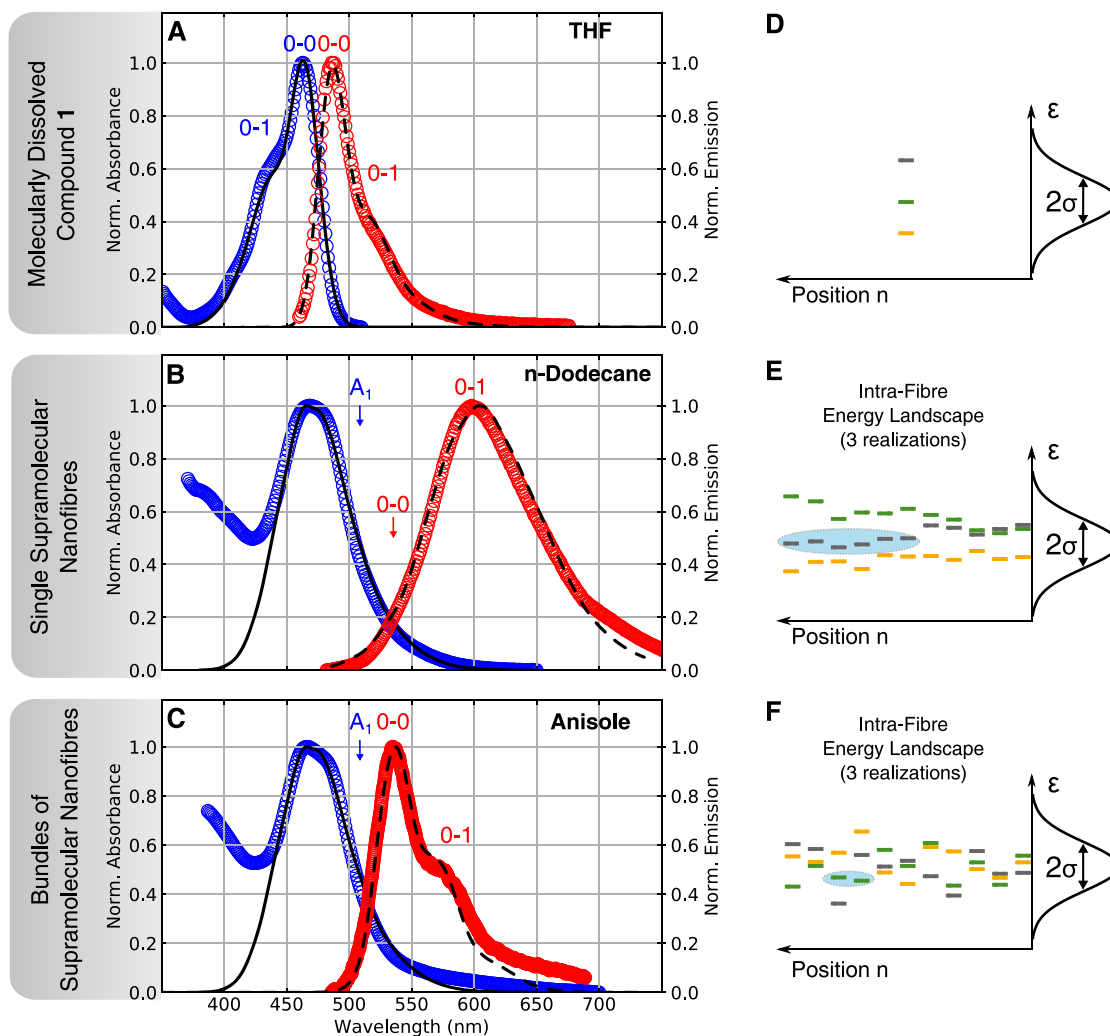


Figure 3. Optical properties of compound **1** and supramolecular architectures. (A) Normalized absorption (blue) and photoluminescence spectra (red) of dissolved compound **1** in THF ($40 \mu\text{M}$) with the corresponding Franck–Condon analysis (black lines). (B, C) Normalized absorption (blue) and photoluminescence spectra (red) of single supramolecular nanofibers in *n*-dodecane ($40 \mu\text{M}$) (B) and bundles of supramolecular nanofibers in anisole ($200 \mu\text{M}$) (C), together with simulated spectra based on a Frenkel–Holstein Hamiltonian (black lines). (D) Illustration of the inhomogeneous distribution of transition energies of the building block at position n within one single column for three realizations. (E, F) Representation of three simulated realizations of transition energies of the building block at position n within one single column for the simulated spectra in B and C. The spatial correlation length of transition energies for single nanofibers is $l_0 \geq 10$ and for bundles of nanofibers $l_0 = 0$ (left, intracolumn energy landscape), while the corresponding ensemble averages, with a Gaussian width σ , over all columns (right) are almost identical. The ellipses indicate the delocalization of relaxed emitting states.

coherence characteristics of the relaxed excitons along the H-type columns by altering the hierarchical level of our architectures. These relaxed excitons are responsible for incoherent long-range transport, since they perform many hopping steps within their substantial excited-state lifetime in our H-aggregates. Importantly, the hopping rates of delocalized excitons have to be described by a generalized Förster theory, in which optically dark exciton states contribute to the hopping rates.^{36–38} These systems are thus ideal to resolve the interplay between morphology, correlated electronic disorder, and coherence (delocalization) in the long-range incoherent transport of excitons along individual, spatially isolated nanostructures on pico- to nanosecond time scales. Figure 4A and B display representative wide-field PL images of isolated nanostructures, both with lengths of several micro-

meters, in agreement with the AFM data (Figure 2A,E). The single nanofiber shows a small PL signal (Figure 4A), which demonstrates the weakly optically allowed nature of the emitting excitons and thus the high degree of coherence within the nanofiber. The signal from the bundle of nanofibers is significantly stronger mainly owing to the large number of columns within the bundle (Figure 4B) and to a lesser extent due to the higher PL quantum efficiency of one column in a bundle (see Table S2).

Having located isolated nanostructures, we switched the microscope to confocal illumination and centered each nanostructure in the diffraction-limited focus of a pulsed laser (red dashed circles, Figure 4A,B). Combining detection-beam scanning with time-correlated single-photon counting³⁹ (see Supporting Information sections 1 and 6), we measured

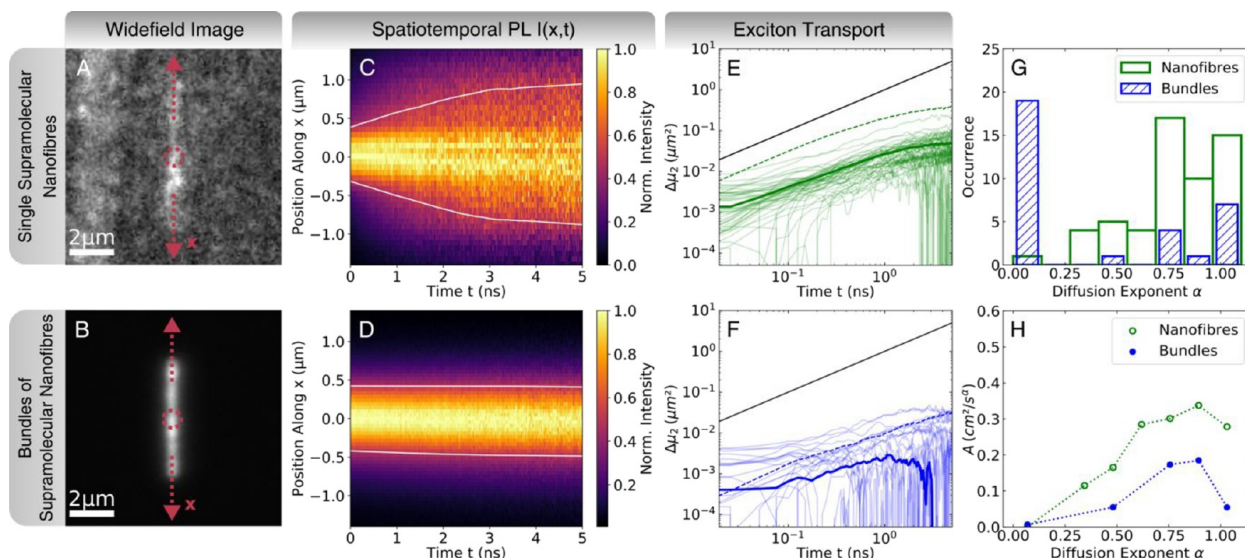


Figure 4. Direct visualization of long-range energy transport along supramolecular architectures. (A, B) Wide-field photoluminescence image of a single supramolecular nanofiber and a bundle of supramolecular nanofibers, respectively. Red dashed arrows indicate the scanning axis x ; dashed circles label the position $x = 0$ of the excitation spot. (C, D) Normalized PL intensity distributions and their evolution in space and time for the single nanofiber in A and the bundle in B. The white contour lines indicate the time evolution of the full width at half-maximum. (E, F) Temporal changes of the second moments of the spatial intensity profiles for 56 nanofibers and 32 bundles of nanofibers (thin green and blue solid lines). The thick lines represent the average of all curves, and the dashed lines indicate a linear scaling in time, i.e., normal diffusion, as a guide for the eye. (G) Distribution of the diffusion exponent α for all nanofibers (green) and bundles (blue) in E and F, evaluated for $t < 1$ ns. (H) Averaged hopping coefficients A as a function of α for nanofibers (green) and bundles (blue).

PL decay curves while scanning the detection position along the long axis of the nanostructures (dashed arrows in Figure 4A,B). Figure 4C and D show the resulting PL intensity distributions, $I(x, t)$, as a function of the distance x relative to the center of the excitation spot and time t after laser excitation. Normalization of the spatial intensity distributions at each point in time (Figure S13) reveals the broadening of the PL signal along the nanostructures' long axes on (sub-)nanosecond time scales. Hence, the initial singlet exciton population, created by the diffraction-limited excitation pulse, is transported away from the excitation spot prior to (radiative) decay. This energy transport is significantly more pronounced for the single nanofiber compared to the bundle of nanofibers (Figure 4C,D, white contour lines). We attribute this difference to the distinct excited-state energy landscapes (Figure 3E,F). We rule out artifacts due to saturation and technical issues, since we operate under very low excitation fluences, and we have performed an independent control experiment on a system that does not show long-range energy transport (see Supporting Information, Materials and Methods, and Figure S12).

To quantitatively describe the time-dependent broadening of the spatial intensity distributions, we calculated the second moments $\mu_2(t)$ ²² at time t as a measure for their widths (Figure S13). We evaluated changes of $\mu_2(t)$ with respect to the second moment (width) of the initial distribution $\mu_2(0)$:

$$\Delta\mu_2(t) = \mu_2(t) - \mu_2(0) \quad (1)$$

The $\Delta\mu_2(t)$ curves retrieved from the data in Figure 4C,D are shown as thick dashed lines in Figure 4E,F. At short times ($t \leq 1$ ns), we find similar slopes for both curves. However, the $\Delta\mu_2(t)$ values for the single nanofiber are larger by more than 1

order of magnitude compared to those for the bundle. This observation reflects the faster and more pronounced broadening of the initial exciton population in the single nanofiber due to more efficient energy transport. For longer times ($t \geq 2.5$ ns) the broadening slows down and a plateau is reached for both architectures. We confirmed the same trend for in total 56 single nanofibers and 32 bundles, illustrated with thin solid green and blue lines in Figure 4E,F.

The second moments $\Delta\mu_2(t)$ follow to a good approximation a power law for $t < 1$ ns. We can thus fit the transport dynamics with a diffusion model^{11,17,22,39–41} (see Supporting Information section 7):

$$\Delta\mu_2(t) = At^\alpha \quad (2)$$

Here α is the diffusion exponent and A is the exciton hopping coefficient, which is related to the time-dependent diffusivity $D(t) = \frac{1}{2}At^{\alpha-1}$. Figure 4G shows the exponents for nanofibers (green bars) and bundles (blue hatched bars) for all curves in Figure 4E,F. We find a broad distribution with $0 \leq \alpha \leq 1$ (for $t < 1$ ns) due to the intrinsic electronic disorder in deposited supramolecular nanostructures. For single nanofibers the mean exponent is $\alpha_{\text{Fiber}} = 0.78 \pm 0.24$, and a significant fraction exhibits $\alpha \approx 1$, which indicates normal diffusion visualized in Figure 4E,F with black solid lines. In contrast, the mean exponent for bundles is smaller with $\alpha_{\text{Fiber}} = 0.37 \pm 0.47$, which is characteristic for strongly subdiffusive transport due to the disordered energy landscape.²² Notably, for bundles the highest occurrence of exponents is at $\alpha \approx 0$. This behavior is expected for a system with strong local electronic perturbations (Figure 3F), in which trapping hinders exciton transport.²² For the single nanofibers the average exciton hopping coefficients A as a function of the exponent α are larger (Figure 4H). This

translates into higher diffusivities $D(t)$ for single nanofibers: For example, for the nanofiber shown in Figure 4C we find $D_{\text{Fiber}}(t = 1 \text{ ns}) = 1.03 \text{ cm}^2/\text{s}$, which is the largest value reported for an H-aggregate and is more than 1 order of magnitude larger than the diffusivity for the bundle shown in Figure 4D with $D_{\text{Bundle}}(t = 1 \text{ ns}) = 0.05 \text{ cm}^2/\text{s}$ (see also Figure S14).

CONCLUSION

Our H-type supramolecular architectures with different hierarchical levels represent a versatile system to understand the subtle interplay between electronic coupling, disorder, and coherence for efficient long-range, incoherent transport of delocalized singlet excitons. We have demonstrated remarkable differences in the spectroscopic properties as well as in the energy transport characteristics of single supramolecular nanofibers and bundles of nanofibers. The transition energies of adjacent CBT cores in single supramolecular nanofibers are spatially correlated, resulting in smooth excited-state energy landscapes. The concomitant high degree of coherence (exciton delocalization) facilitates long-range incoherent energy transport. In contrast, in bundles of nanofibers spatial correlations in the transition energies are found to be absent. This gives rise to a disordered excited-state energy landscape with strongly localized excitons. Hence, exciton transport is hindered by trapping in local energy minima.²² The uncorrelated transition energies in bundles of nanofibers can be explained by very subtle local electronic perturbations due to interacting peripheries.³⁰ Alternatively, disorder on a local scale between columns may arise from a geometric frustration in a hexagonal packing due to compensation of macrodipoles.⁴² Both effects can destroy shared electronic environments. Our observations are a manifestation of coherence-enhanced diffusivities of excitons^{15,18,43} and highlight the critical role of spatially correlated transition energies of the supramolecular building blocks for long-range energy transport.⁴⁴ The present data therefore add a new dimension to the development of a detailed theoretical understanding of energy transport in columnar H-type supramolecular nanostructures⁴⁵ as well as for the design of novel, optimized nanophotonic applications.

ASSOCIATED CONTENT

Supporting Information

The Supporting Information is available free of charge at <https://pubs.acs.org/doi/10.1021/jacs.0c01392>.

Materials and methods; additional characterization of supramolecular architectures by AFM, electron diffraction, and optical spectroscopy; numerical simulations of optical spectra and exciton diffusion model (PDF)

AUTHOR INFORMATION

Corresponding Authors

Hans-Werner Schmidt – Macromolecular Chemistry and Bavarian Polymer Institute, University of Bayreuth, 95447 Bayreuth, Germany; orcid.org/0000-0002-1761-1153; Email: hans-werner.schmidt@uni-bayreuth.de

Richard Hildner – Spectroscopy of Soft Matter, University of Bayreuth, 95447 Bayreuth, Germany; Zernike Institute for Advanced Materials, University of Groningen, 9747 AG Groningen, The Netherlands; orcid.org/0000-0002-7282-3730; Email: r.m.hildner@rug.nl

Authors

Bernd Wittmann – Spectroscopy of Soft Matter, University of Bayreuth, 95447 Bayreuth, Germany

Felix A. Wenzel – Macromolecular Chemistry and Bavarian Polymer Institute, University of Bayreuth, 95447 Bayreuth, Germany; Institute for Complex Molecular Systems, Laboratory of Macromolecular and Organic Chemistry, Eindhoven University of Technology, 5612, AZ, Eindhoven, The Netherlands

Stephan Wiesneth – Spectroscopy of Soft Matter, University of Bayreuth, 95447 Bayreuth, Germany

Andreas T. Haedler – Macromolecular Chemistry and Bavarian Polymer Institute, University of Bayreuth, 95447 Bayreuth, Germany; Institute for Complex Molecular Systems, Laboratory of Macromolecular and Organic Chemistry, Eindhoven University of Technology, 5612, AZ, Eindhoven, The Netherlands

Markus Drechsler – Bavarian Polymer Institute, University of Bayreuth, 95447 Bayreuth, Germany

Klaus Kreger – Macromolecular Chemistry and Bavarian Polymer Institute, University of Bayreuth, 95447 Bayreuth, Germany; orcid.org/0000-0003-3021-1311

Jürgen Köhler – Spectroscopy of Soft Matter, University of Bayreuth, 95447 Bayreuth, Germany; orcid.org/0000-0002-4214-4008

E. W. Meijer – Institute for Complex Molecular Systems, Laboratory of Macromolecular and Organic Chemistry, Eindhoven University of Technology, 5612, AZ, Eindhoven, The Netherlands; orcid.org/0000-0003-4126-7492

Complete contact information is available at:

<https://pubs.acs.org/doi/10.1021/jacs.0c01392>

Notes

The authors declare no competing financial interest.

ACKNOWLEDGMENTS

We acknowledge financial support from the German Research Foundation (DFG) through the research training group GRK1640 and from the Bavarian State Ministry of Science and the Arts through the Collaborative Research Network “Solar Technologies go Hybrid”. We acknowledge support by the Elite Network of Bavaria (ENB) through the study programs “Macromolecular Science” (F.A.W.) and “Biological Physics” (R.H.) as well as the Max-Weber program (F.A.W.). We are grateful to Doris Hanft and Sandra Ganzleben (Macromolecular Chemistry, University of Bayreuth) for their help with syntheses. We thank Markus Hund (KeyLab Surface and Interface Characterization) of the Bavarian Polymer Institute for support with AFM measurements and Sooruban Shanmugaratnam (Biochemistry, University of Bayreuth) for help with CD spectroscopy.

REFERENCES

- (1) Sengupta, S.; Würthner, F. Chlorophyll J-Aggregates: From Bioinspired Dye Stacks to Nanotubes, Liquid Crystals, and Biosupramolecular Electronics. *Acc. Chem. Res.* **2013**, *46* (11), 2498–2512.
- (2) Liess, A.; Arjona-Esteban, A.; Kudzus, A.; Albert, J.; Krause, A. M.; Lv, A.; Stolte, M.; Meerholz, K.; Würthner, F. Ultranarrow Bandwidth Organic Photodiodes by Exchange Narrowing in Merocyanine H- and J-Aggregate Excitonic Systems. *Adv. Funct. Mater.* **2019**, *29* (21), 1–9.

- (3) Aida, T.; Meijer, E. W.; Stupp, S. I. Functional Supramolecular Polymers. *Science* **2012**, *335* (6070), 813–817.
- (4) Boulais, E.; Sawaya, N. P. D.; Veneziano, R.; Andreoni, A.; Banal, J. L.; Kondo, T.; Mandal, S.; Lin, S.; Schlau-Cohen, G. S.; Woodbury, N. W.; Yan, H.; Aspuru-Guzik, A.; Bathe, M. Programmed Coherent Coupling in a Synthetic DNA-Based Excitonic Circuit. *Nat. Mater.* **2018**, *17* (2), 159–166.
- (5) Moulin, E.; Armao, J. J.; Giuseppone, N. Triarylamine-Based Supramolecular Polymers: Structures, Dynamics, and Functions. *Acc. Chem. Res.* **2019**, *52* (4), 975–983.
- (6) Korevaar, P. A.; George, S. J.; Markvoort, A. J.; Smulders, M. M. J.; Hilbers, P. A. J.; Schenning, A. P. H. J.; De Greef, T. F. A.; Meijer, E. W. Pathway Complexity in Supramolecular Polymerization. *Nature* **2012**, *481* (7382), 492–496.
- (7) Ciesielski, A.; Palma, C.-A.; Bonini, M.; Samori, P. Towards Supramolecular Engineering of Functional Nanomaterials: Pre-Programming Multi-Component 2D Self-Assembly at Solid-Liquid Interfaces. *Adv. Mater.* **2010**, *22*, 3506–3520.
- (8) Scholes, G. D.; Fleming, G. R.; Chen, L. X.; Aspuru-Guzik, A.; Buchleitner, A.; Coker, D. F.; Engel, G. S.; Van Grondelle, R.; Ishizaki, A.; Jonas, D. M.; Lundeen, J. S.; McCusker, J. K.; Mukamel, S.; Ogilvie, J. P.; Olaya-Castro, A.; Ratner, M. A.; Spano, F. C.; Whaley, K. B.; Zhu, X. Using Coherence to Enhance Function in Chemical and Biophysical Systems. *Nature* **2017**, *543* (7647), 647–656.
- (9) Jin, X. H.; Price, M. B.; Finnegan, J. R.; Boott, C. E.; Richter, J. M.; Rao, A.; Matthew Menke, S.; Friend, R. H.; Whittell, G. R.; Manners, I. Long-Range Exciton Transport in Conjugated Polymer Nanofibers Prepared by Seeded Growth. *Science* **2018**, *360* (6391), 897–900.
- (10) Winiger, C. B.; Li, S.; Kumar, G. R.; Langenegger, S. M.; Häner, R. Long-Distance Electronic Energy Transfer in Light-Harvesting Supramolecular Polymers. *Angew. Chem., Int. Ed.* **2014**, *53* (49), 13609–13613.
- (11) Clark, K. A.; Krueger, E. L.; Vanden Bout, D. A. Direct Measurement of Energy Migration in Supramolecular Carbocyanine Dye Nanotubes. *J. Phys. Chem. Lett.* **2014**, *5* (13), 2274–2282.
- (12) Caram, J. R.; Doria, S.; Eisele, D. M.; Freyria, F. S.; Sinclair, T. S.; Rebertrost, P.; Lloyd, S.; Bawendi, M. G. Room-Temperature Micron-Scale Exciton Migration in a Stabilized Emissive Molecular Aggregate. *Nano Lett.* **2016**, *16* (11), 6808–6815.
- (13) Lin, H.; Camacho, R.; Tian, Y.; Kaiser, T. E.; Würthner, F.; Scheblykin, I. G. Collective Fluorescence Blinking in Linear J-Aggregates Assisted by Long-Distance Exciton Migration. *Nano Lett.* **2010**, *10* (2), 620–626.
- (14) Wan, Y.; Stradomska, A.; Knoester, J.; Huang, L. Direct Imaging of Exciton Transport in Tubular Porphyrin Aggregates by Ultrafast Microscopy. *J. Am. Chem. Soc.* **2017**, *139* (21), 7287–7293.
- (15) Brédas, J. L.; Sargent, E. H.; Scholes, G. D. Photovoltaic Concepts Inspired by Coherence Effects in Photosynthetic Systems. *Nat. Mater.* **2017**, *16* (1), 35–44.
- (16) Fassioli, F.; Dinshaw, R.; Arpin, P. C.; Scholes, G. D. Photosynthetic Light Harvesting: Excitons and Coherence. *J. R. Soc., Interface* **2014**, *11* (92), 20130901.
- (17) Menke, S. M.; Holmes, R. J. Exciton Diffusion in Organic Photovoltaic Cells. *Energy Environ. Sci.* **2014**, *7* (2), 499–512.
- (18) Scholes, G. D. Designing Light-Harvesting Antenna Systems Based on Superradiant Molecular Aggregates. *Chem. Phys.* **2002**, *275* (1–3), 373–386.
- (19) Topczak, A. K.; Roller, T.; Engels, B.; Brüitting, W.; Pflaum, J. Nonthermally Activated Exciton Transport in Crystalline Organic Semiconductor Thin Films. *Phys. Rev. B: Condens. Matter Mater. Phys.* **2014**, *89* (20), 201203.
- (20) Sung, J.; Kim, P.; Fimmel, B.; Würthner, F.; Kim, D. Direct Observation of Ultrafast Coherent Exciton Dynamics in Helical π -Stacks of Self-Assembled Perylene Bisimides. *Nat. Commun.* **2015**, *6* (1), 8646.
- (21) Moix, J. M.; Khasin, M.; Cao, J. Coherent Quantum Transport in Disordered Systems: I. the Influence of Dephasing on the Transport Properties and Absorption Spectra on One-Dimensional Systems. *New J. Phys.* **2013**, *15* (8), 085010.
- (22) Vlaming, S. M.; Malyshev, V. A.; Einfeld, A.; Knoester, J. Subdiffusive Exciton Motion in Systems with Heavy-Tailed Disorder. *J. Chem. Phys.* **2013**, *138* (21), 214316.
- (23) Haedler, A. T.; Kreger, K.; Issac, A.; Wittmann, B.; Kivala, M.; Hammer, N.; Köhler, J.; Schmidt, H. W.; Hildner, R. Long-Range Energy Transport in Single Supramolecular Nanofibres at Room Temperature. *Nature* **2015**, *523* (7559), 196–199.
- (24) Spano, F. C.; Clark, J.; Silva, C.; Friend, R. H. Determining Exciton Coherence from the Photoluminescence Spectral Line Shape in Poly(3-Hexylthiophene) Thin Films. *J. Chem. Phys.* **2009**, *130* (7), 074904.
- (25) Mohseni, M.; Aspuru-Guzik, A.; Rebertrost, P.; Shabani, A.; Lloyd, S.; Huelga, S. F.; Plenio, M. B. Environment-Assisted Quantum Transport. In *Quantum Effects in Biology*; Cambridge University Press, 2014; pp 159–176.
- (26) Novo, L.; Mohseni, M.; Omar, Y. Disorder-Assisted Quantum Transport in Suboptimal Decoherence Regimes. *Sci. Rep.* **2016**, *6* (1), 18142.
- (27) Fukui, T.; Kawai, S.; Fujinuma, S.; Matsushita, Y.; Yasuda, T.; Sakurai, T.; Seki, S.; Takeuchi, M.; Sugiyasu, K. Control over Differentiation of a Metastable Supramolecular Assembly in One and Two Dimensions. *Nat. Chem.* **2017**, *9* (5), 493–499.
- (28) Wagner, W.; Wehner, M.; Stepanenko, V.; Würthner, F. Supramolecular Block Copolymers by Seeded Living Polymerization of Perylene Bisimides. *J. Am. Chem. Soc.* **2019**, *141* (30), 12044–12054.
- (29) Eisele, D. M.; Arias, D. H.; Fu, X.; Bloemsmas, E. A.; Steiner, C. P.; Jensen, R. A.; Rebertrost, P.; Eisele, H.; Tokmakoff, A.; Lloyd, S.; Nelson, K. A.; Nicastro, D.; Knoester, J.; Bawendi, M. G. Robust Excitons Inhabit Soft Supramolecular Nanotubes. *Proc. Natl. Acad. Sci. U. S. A.* **2014**, *111* (33), E3367–E3375.
- (30) Kim, T.; Ham, S.; Lee, S. H.; Hong, Y.; Kim, D. Enhancement of Exciton Transport in Porphyrin Aggregate Nanostructures by Controlling the Hierarchical Self-Assembly. *Nanoscale* **2018**, *10* (35), 16438–16446.
- (31) Marty, R.; Szilluweit, R.; Sánchez-Ferrer, A.; Bolissety, S.; Adamcik, J.; Mezzenga, R.; Spitzner, E.-C.; Feifer, M.; Steinmann, S. N.; Corminboeuf, C.; Frauenrath, H. Hierarchically Structured Microfibers of “Single Stack” Perylene Bisimide and Quaterthiophene Nanowires. *ACS Nano* **2013**, *7* (10), 8498–8508.
- (32) Haedler, A. T.; Meskers, S. C. J.; Zha, R. H.; Kivala, M.; Schmidt, H. W.; Meijer, E. W. Pathway Complexity in the Enantioselective Self-Assembly of Functional Carbonyl-Bridged Triarylamine Trisamides. *J. Am. Chem. Soc.* **2016**, *138* (33), 10539–10545.
- (33) Valera, J. S.; Gómez, R.; Sánchez, L. Tunable Energy Landscapes to Control Pathway Complexity in Self-Assembled N-Heterotriangulenes: Living and Seeded Supramolecular Polymerization. *Small* **2018**, *14* (3), 1702437.
- (34) Haedler, A. T.; Beyer, S. R.; Hammer, N.; Hildner, R.; Kivala, M.; Köhler, J.; Schmidt, H. W. Synthesis and Photophysical Properties of Multichromophoric Carbonyl-Bridged Triarylamines. *Chem. - Eur. J.* **2014**, *20* (37), 11708–11718.
- (35) Hestand, N. J.; Spano, F. C. Expanded Theory of H- and J-Molecular Aggregates: The Effects of Vibronic Coupling and Intermolecular Charge Transfer. *Chem. Rev.* **2018**, *118* (15), 7069–7163.
- (36) Sumi, H. Bacterial Photosynthesis Begins with Quantum-Mechanical Coherence. *Chem. Rec.* **2001**, *1* (6), 480–493.
- (37) Scholes, G. D.; Jordanides, X. J.; Fleming, G. R. Adapting the Förster Theory of Energy Transfer for Modeling Dynamics in Aggregated Molecular Assemblies. *J. Phys. Chem. B* **2001**, *105* (8), 1640–1651.
- (38) Beljonne, D.; Curutchet, C.; Scholes, G. D.; Silbey, R. J. Beyond Förster Resonance Energy Transfer in Biological and Nanoscale Systems. *J. Phys. Chem. B* **2009**, *113* (19), 6583–6599.

(39) Akselrod, G. M.; Deotare, P. B.; Thompson, N. J.; Lee, J.; Tisdale, W. A.; Baldo, M. A.; Menon, V. M.; Bulovic, V. Visualization of Exciton Transport in Ordered and Disordered Molecular Solids. *Nat. Commun.* **2014**, *5* (1), 3646.

(40) Havlin, S.; Ben-Avraham, D. Diffusion in Disordered Media. *Adv. Phys.* **2002**, *51* (1), 187–292.

(41) Wu, J.; Berland, K. M. Propagators and Time-Dependent Diffusion Coefficients for Anomalous Diffusion. *Biophys. J.* **2008**, *95* (4), 2049–2052.

(42) Zehe, C. S.; Hill, J. A.; Funnell, N. P.; Kreger, K.; van der Zwan, K. P.; Goodwin, A. L.; Schmidt, H.-W.; Senker, J. Mesoscale Polarization by Geometric Frustration in Columnar Supramolecular Crystals. *Angew. Chem., Int. Ed.* **2017**, *56* (16), 4432–4437.

(43) Lloyd, S.; Mohseni, M. Symmetry-Enhanced Supertransfer of Delocalized Quantum States. *New J. Phys.* **2010**, *12* (7), 075020.

(44) Lee, C. K.; Shi, L.; Willard, A. P. Modeling the Influence of Correlated Molecular Disorder on the Dynamics of Excitons in Organic Molecular Semiconductors. *J. Phys. Chem. C* **2019**, *123* (1), 306–314.

(45) Saikin, S. K.; Shakirov, M. A.; Kreisbeck, C.; Peskin, U.; Proshin, Y. N.; Aspuru-Guzik, A. On the Long-Range Exciton Transport in Molecular Systems: The Application to H-Aggregated Heterotriangulene Chains. *J. Phys. Chem. C* **2017**, *121* (45), 24994–25002.

Supporting Information

for

Enhancing Long-Range Energy Transport in Supramolecular Architectures by Tailoring Coherence Properties

Bernd Wittmann¹, Felix A. Wenzel^{2,3}, Stephan Wiesneth¹, Andreas T. Haedler^{2,3},
Markus Drechsler⁴, Klaus Kreger², Jürgen Köhler¹, E. W. Meijer³, Hans-Werner Schmidt^{*2},
Richard Hildner^{*1,5}

Affiliations:

¹Spectroscopy of Soft Matter, University of Bayreuth, Universitätsstraße 30, 95447 Bayreuth, Germany.

²Macromolecular Chemistry and Bavarian Polymer Institute, University of Bayreuth, Universitätsstraße 30, 95447 Bayreuth, Germany.

³Institute for Complex Molecular Systems, Laboratory of Macromolecular and Organic Chemistry, Eindhoven University of Technology, 5612 AZ Eindhoven, The Netherlands.

⁴Bavarian Polymer Institute, University of Bayreuth, Universitätsstraße 30, 95447 Bayreuth, Germany.

⁵Zernike Institute for Advanced Materials, University of Groningen, Nijenborgh 4, 9747 AG Groningen, The Netherlands.

*Correspondence to: r.m.hildner@rug.nl and hans-werner.schmidt@uni-bayreuth.de.

Table of Content

1. Materials and Methods	2
2. Characterisation of Supramolecular Architectures of Compound 1	4
3. Selected Area Electron Diffraction of Bundles of Supramolecular Nanofibres	5
4. Optical Spectroscopy and Spectroscopic Characteristics of H-Aggregates	6
5. Numerical Simulations of Experimental Spectra	15
6. Experimental Setup	18
7. Incoherent Exciton Diffusion Model	20
8. References	23

1. Materials and Methods

Materials. The synthesis, purification and characterization of compound **1** is described in detail elsewhere ¹. All solvents were of HPLC grade and used as received.

Molecularly dissolved solution of compound 1. A 40 μM solution of compound **1** in THF (boiling point: 66 $^{\circ}\text{C}$) was refluxed for 20 minutes under stirring and allowed to cool to room temperature.

Self-assembly of compound 1. Compound **1** was added at a concentration of 40 μM (~100 p.p.m., 0.01 wt%) in n-dodecane (bp.: 216 $^{\circ}\text{C}$) or anisole (bp.: 154 $^{\circ}\text{C}$), respectively. A homogeneous dispersion was ensured by ultrasonication for 15 minutes. The dispersions were refluxed for 30 minutes under stirring and then allowed to cool to room temperature. The self-assembly process was monitored via UV/vis and PL spectroscopy until no spectral changes were detected. Subsequently, all samples were stored for 24 hours prior investigation.

AFM. For AFM measurements, we used silicon wafers as substrate. The self-assembled 40 μM dispersions were either spin-coated directly or spin-coated after dilution to a concentration of 4 μM . All samples were dried under vacuum. AFM images were recorded on a Dimension 3100 NanoScope V (Veeco Metrology Group). Scanning was performed in tapping mode using silicon nitride (Si_3N_4) cantilevers (OTESPA-R3, Bruker) with a typical spring constant of 26 N m^{-1} and a typical resonance frequency of 300 kHz. Image processing and analysis was conducted with the Gwyddion 2.52 software.

TEM and SAED. The self-assembled 40 μM dispersions were drop-cast on a carbon-coated copper grid and the solvent was removed with a filter paper. Finally, all samples were dried under vacuum. TEM images were recorded with a Zeiss / LEO EM922 Omega and a JEOL JEM-2200FS energy filtering transmission electron microscope (EFTEM) both operated at 200 kV in bright-field and diffraction mode. Zero-loss filtered micrographs ($\Delta E \sim 0$ eV) were recorded with bottom mounted camera systems. The Zeiss microscope was equipped with a CCD camera system (Ultrascan 1000, Gatan) and the JEOL microscope with a CMOS camera system (OneView, Gatan). Both camera systems were operated with an image acquisition and processing software (Digital Micrograph GMS 1.9 resp. 3.3).

UV/vis, photoluminescence and circular dichroism spectroscopy in solution. UV/vis absorption spectra were recorded on a Perkin Elmer Lambda750 spectrophotometer. Photoluminescence (PL) spectra were measured on a Varian Cary Eclipse at excitation wavelengths of 430 nm for n-dodecane dispersions and THF solutions and 380 nm for anisole dispersions. All PL spectra were corrected for reabsorption with the factor $k_{abs} = 10^{0.5 OD(\lambda)}$, where $OD(\lambda)$ is the wavelength dependent absorbance. The PL quantum efficiency was measured on a JASCO FP-8600 spectrofluorometer equipped with an integrating sphere (ILF-835). Circular dichroism spectra were recorded on a Jasco J-715 spectrophotometer. All measurements were conducted with Hellma QS quartz-glass cuvettes.

Optical imaging and spectroscopy of single supramolecular nanofibres and bundles. The 40 μM -dispersions were either diluted to 4 μM before spin-coating, or spin-coated undiluted on microscopy cover slips (borosilicate glass; thickness 0.17 μm ; Carl Roth). All samples were dried under vacuum. Optical imaging and spectroscopy was performed using a home-built microscope (Fig. S11). The excitation source was a pulsed diode laser (LDH-P-C-450B, Picoquant; 2.5 MHz repetition rate, 70 ps pulse duration) that operates at a wavelength of 450 nm. The laser light was spatially filtered and directed to the microscope, which was equipped

with an infinity-corrected high-numerical aperture oil-immersion objective (PlanApo, 60 \times , numerical aperture 1.45; Olympus). The sample was placed in the focal plane of the objective, and the sample position was controlled by a piezo-stage (Tritor 102 SG, from piezosystem jena). Photoluminescence was collected by the same objective and passed a set of dielectric filters (dichroic beam splitter z460RDC, long-pass filter LP467; AHF Analysentechnik) to suppress scattered or reflected laser light.

The detection beam path is equipped with a closed-loop piezo scan mirror (S-335.2.SH, PI) and a single-photon-counting avalanche photodiode (MPD, Picoquant) to position the detection spot independently from the confocal excitation spot (Fig. S11). The electrical signal of the photodiode was fed into a time-correlated single-photon-counting module (TimeHarp 260 PICO, Picoquant).

In imaging mode, the photoluminescence signal was imaged onto a CMOS camera (Zyla 4.2 sCMOS, Andor). In this mode, we used two illumination methods. First, for widefield illumination we flipped an additional lens (widefield lens) into the excitation beam path to focus the laser light into the back-focal plane of the microscope objective. This allows for nearly uniform illumination of a large area with ~ 70 μm diameter in the sample plane, to acquire overview PL images of our samples and to identify elongated nanostructures (Fig. 4A and 4B). Second, for confocal illumination the widefield lens was removed and the laser light was tightly focused to a spot with a half width at half maximum of ~ 170 nm in the sample plane. A flip-mirror allows to switch between imaging and single-photon counting mode of the setup.

For measurements on single supramolecular nanofibres and bundles, the excitation intensities were below 140 W cm^{-2} for confocal illumination and 1.3 W cm^{-2} for widefield illumination. These intensities correspond to a maximum excitation probability of 0.1 absorbed photon per pulse per 3000 CBT-cores along a column and confirm that our experiments are conducted in a regime where annihilation does not play a role. All experiments were carried out at room temperature under ambient conditions.

Numerical Simulations. For the numerical simulation of the absorption and PL spectra shown in Fig. 3B,C we used home-written Matlab-scripts. The electronic Coulomb coupling between CBT-cores along a column was treated in nearest-neighbour approximation. The transition energies of the CBT-cores were taken from a Gaussian distribution with width σ . To account for different degrees of intra-column electronic disorder, a correlation length l_0 was introduced, i.e., with increasing l_0 , the distribution of transition energies within a column becomes smoother (see Fig. 3D). To model the experimental spectra we averaged over 10^4 realisations of electronic disorder and performed a residual analysis. Further details are outlined in the Supplementary Materials, Fig. S9 and S10 and section 5.

2. Characterisation of Supramolecular Architectures of Compound 1

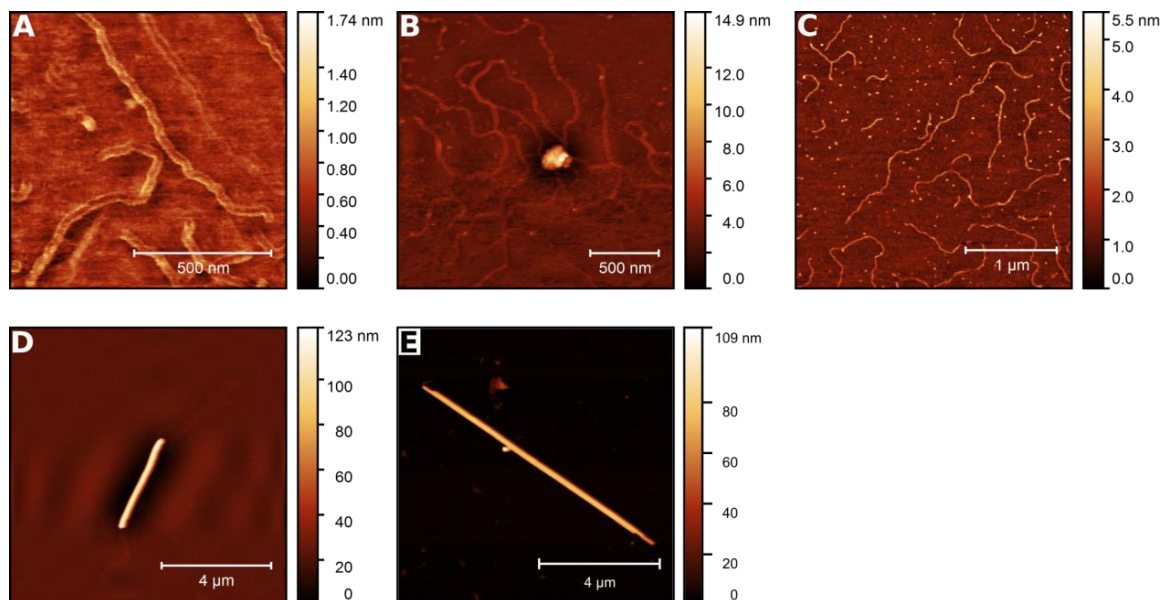


Fig. S1: AFM images of single supramolecular nanofibres and bundles of nanofibres. A-C) AFM images (topographical scan) of single nanofibres spin-coated from a dispersion of compound **1** in n-dodecane (A,B: 40 μM ; C: 4 μM) demonstrating the presence of single nanofibres at concentrations of 4 μM as well as of 40 μM . The discrepancy between the heights and the diameters of the nanofibres, as determined by AFM (2–2.5 nm) and molecular modelling (4.4 nm)², respectively, is a known phenomenon^{3,4}. D,E) AFM images (topographical scan) of bundles of nanofibres spin-coated from a dispersion of compound **1** in anisole at a concentration of 40 μM .

3. Selected Area Electron Diffraction of Bundles of Supramolecular Nanofibres

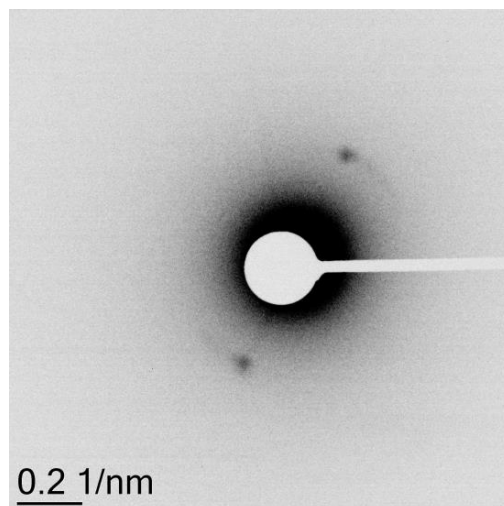


Fig. S2: Selected Area Electron Diffraction (SAED) at smaller angles. SAED pattern from a sample as in Fig. 2G (prepared from a dispersion of self-assembled compound **1** in anisole, concentration 40 μM), which reveals sharp signals corresponding to a distance of 2.8 nm. Assuming a columnar hexagonal packing of nanofibres within bundles¹, this plane-plane distance corresponds to an intercolumnar spacing of 3.23 nm.

4. Optical Spectroscopy and Spectroscopic Characteristics of H-Aggregates

Franck-Condon Analysis of Absorption and PL Spectra

For the Franck-Condon analysis of the PL and absorption spectra of molecularly dissolved compound **1** in THF (Fig. 3A) we assume coupling of the electronic transition to a single effective vibrational mode (carbon-bond stretch). In this situation, the normalized spectra for PL $I_{PL}(\omega)$ and for absorption $I_{Abs}(\omega)$ can be described by ⁵

$$\frac{I_{PL}(\omega)}{n^2\omega^3} \propto \sum_m \frac{S^m}{m!} e^{-S} \Gamma[\omega - (\omega_{0-0} - m\omega_0)] \quad (1)$$

$$\frac{I_{Abs}(\omega)}{n\omega} \propto \sum_m \frac{S^m}{m!} e^{-S} \Gamma[\omega - (\omega_{0-0} + m\omega_0)] \quad (2)$$

Here S is the Huang–Rhys factor for the effective vibrational mode with energy ω_0 , ω_{0-0} is the energy of the purely electronic 0–0 transition, $m = (1, 2, \dots)$ denotes the vibrational quantum number and n is the refractive index. Γ is the Gaussian (inhomogeneous) line width function with a standard deviation σ , which we allow to be different for the electronic and vibronic transitions (the effective mode is typically a superposition of several modes that are closely spaced and that give rise to a larger “effective” inhomogeneous line width for the ensemble vibronic transition).

To describe both the absorption and the PL with the same Huang-Rhys factor S and vibrational energy ω_0 , we fit absorption and PL simultaneously. The parameters for the best fit are shown in Tab. S1.

Tab. S1: Franck-Condon analysis of the absorption and PL spectra of molecularly dissolved compound 1 in THF.

	S	ω_{0-0}/eV	ω_0/eV	σ_{0-0}/eV	$\sigma_{0-1,2..}/eV$
Abs.	0.54 ± 0.02	2.664 ± 0.003	0.157 ± 0.005	0.090 ± 0.002	0.133 ± 0.008
PL	0.54 ± 0.02	2.544 ± 0.003	0.157 ± 0.005	0.082 ± 0.003	0.105 ± 0.008

Concentration-Dependent Absorption Spectra of Compound **1** in Anisole

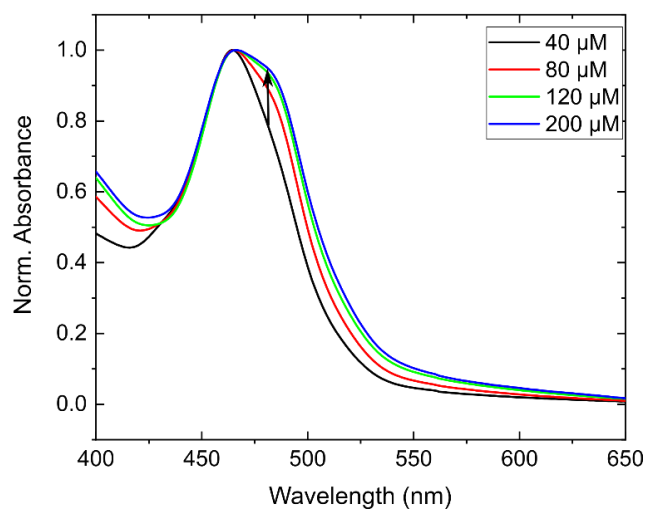


Fig. S3: Concentration-dependent absorption spectra of compound **1 in anisole.** Due to the remaining solubility of compound **1** at low concentrations (40 μM , black) in anisole, the absorption is a superposition of the absorption of molecularly dissolved compound **1** and of bundles of nanofibres. We therefore increased the concentration until no further spectral changes occurred (at 200 μM , blue), i.e., mainly bundles of nanofibres exist in the anisole dispersion.

Circular-Dichroism Spectroscopy

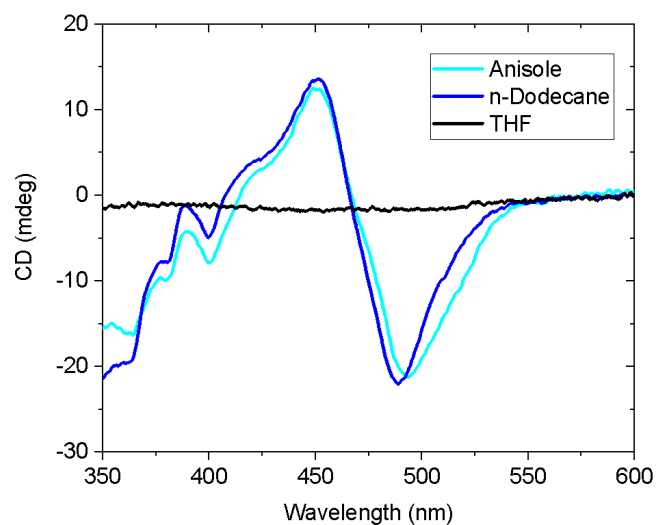


Fig. S4: Circular dichroism spectroscopy of compound 1. Circular dichroism spectra of compound **1** in THF (molecularly dissolved, black), n-dodecane (single supramolecular nanofibres, blue) and anisole (bundles of supramolecular nanofibres, cyan), each recorded at a concentration of about 40 μM (~ 100 ppm) at room temperature. While there is no circular-dichroism signal for the molecularly dissolved building block in THF, aggregates formed in n-dodecane and anisole exhibit a nearly identical circular-dichroism activity, which suggests a comparable structural arrangement within the columns of the supramolecular aggregates ⁶.

Optical Absorption and PL Spectra of Molecular Aggregates

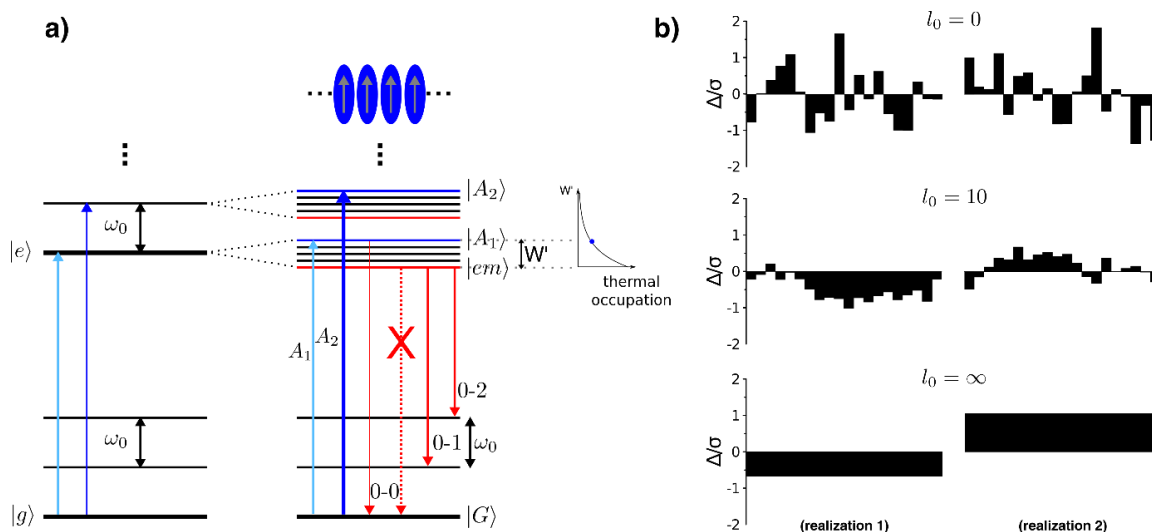


Fig. S5: Spano model of H-type assemblies. **a)** Left: Energy level scheme for a molecule with an intra-molecular vibrational mode of energy w_0 , coupling to the electronic transition between electronic ground $|g\rangle$ and excited electronic state $|e\rangle$. Right: Upon electronic Coulomb coupling between molecules a progression of vibronic exciton bands is formed, separated in energy by the vibrational energy w_0 and with an exciton bandwidth W' . The optically accessible exciton states, labelled $|A_1\rangle, |A_2\rangle, \dots$, are located at the top of each band (blue solid lines), while emission occurs only from the lowest-energy exciton state $|em\rangle$ (red solid line). In a perfect H-aggregate the 0-0 transition from $|em\rangle$ into the ground state $|G\rangle$ is optically forbidden, while the 0-1, 0-2, ... transitions are still allowed. Thermal energy populates (optically allowed) higher-energy exciton states in the lowest-energy exciton band. Hence, with increasing temperature an increasing intensity of the 0-0 PL intensity is observed. Solid coloured arrows indicate the allowed optical transitions^{7,8}. **b)** Six realisations of correlated site-energy disorder along an aggregate. Left and right column depict two different realisations of transition energy offsets Δ_n of an aggregate consisting of $N=20$ monomers for three correlation lengths l_0 (increasing from the top to the bottom)^{7,9}.

The optical spectra of organic molecules show a pronounced vibronic progression (Fig. 3A). This electron-phonon coupling of intra-molecular vibrations (typically carbon-bond stretch modes with energies $\omega_0 \approx 1400 - 1600 \text{ cm}^{-1}$) to electronic transitions is characterised by the Huang-Rhys parameter S . In the simplest picture, each molecule is described as a two level system, which couples to one (effective) intra-molecular vibration with the vibrational energy ω_0 (Fig. S5a, left).

If organic molecules are densely assembled in an aggregate, their transition dipole moments interact via electronic Coulomb coupling J_0 (in nearest-neighbour approximation). To include the influence of electron-phonon coupling on the aggregate spectra, Spano *et al.*⁶⁻⁹ introduced one- and two-particle states. A one-particle state $|n, \tilde{\nu}\rangle$ consist of one vibronically excited molecule n , i.e., molecule n is in its electronically excited state with $\tilde{\nu} \geq 0$ vibrational quanta, and all other molecules of the aggregate are in their vibrationless electronic ground state. For two-particle states $|n, \tilde{\nu}, n', \nu'\rangle$, in addition to the vibronic excitation of molecule n , molecule $n' (\neq n)$ is in a vibrational excited state $\nu' \geq 1$ of its electronic ground state. The a th eigenstate of the aggregate can then be written as a superposition of one- and two-particle states,

$$|\Psi^\alpha\rangle = \sum_{n,\tilde{\nu}} c_{n,\tilde{\nu}}^\alpha |n, \tilde{\nu}\rangle + \sum_{n,\tilde{\nu}} \sum_{n',\nu'} c_{n,\tilde{\nu},n',\nu'}^\alpha |n, \tilde{\nu}, n', \nu'\rangle, \quad (3)$$

where the wave function coefficients c_j^i are obtained via diagonalization of the Hamiltonian of the system.

Now a series of vibronic exciton bands form (Fig. S5a, right) that feature a reduced bandwidth W' compared to the free exciton bandwidth $W = 4|J_0|$ due to electron-phonon coupling. In perfect, disorder-free systems, vibronic excitons are delocalised over the entire aggregate. For H-aggregates only transitions from the ground state to the highest-energy exciton of each band are allowed. These optically accessible states are labelled $|A_{i+1}\rangle$ ($i = 0, 1, \dots$) and correlate to the $0 - i$ transitions of the isolated molecule (Fig. S5 a). Consequently, the optically accessible vibronic exciton states show up as a progression of peaks with an energy difference of ω_0 in the absorption spectrum. Furthermore, as the coupling J_0 rises, the oscillator strength is increasingly redistributed towards higher energy bands (e.g. from $|A_1\rangle$ to $|A_2\rangle, \dots$), leading to a decreased $|A_1\rangle$ intensity compared to the monomer 0-0-intensity in absorption. Hence, the relative intensity of the $|A_1\rangle$ absorption is a direct measure for the magnitude of the electronic Coulomb coupling.

PL takes place from the lowest-energy exciton state $|em\rangle$ of the lowest-energy vibronic exciton band. Absence of disorder leads to a highly symmetric exciton wave function for this state with alternating sign of wavefunction coefficients between consecutive monomers, leading to destructive interference of the 0-0-intensity compared to the monomer PL spectrum. Hence, in ideal H-aggregates the 0-0-peak in emission is completely suppressed, while the remaining progression (0-1, 0-2, etc.) is still visible, because momentum conservation is satisfied by simultaneously exciting a vibration in the electronic ground state.

If PL spectra are recorded at temperatures $T \neq 0\text{K}$, states above the lowest-energy exciton state become thermally accessible (thermally activated emission), i.e., PL stems no longer exclusively from the lowest-energy exciton state $|em\rangle$. For ideal H-aggregates, increasing temperature thus leads to an enhanced 0-0 PL intensity. As the bandwidth W' of the lowest-energy exciton band rises, thermal occupation of higher-energy exciton states becomes less likely (for a given temperature, see Fig. S5a, right, thermal occupation of states), i.e., the 0-0 PL intensity is determined by the ratio between the thermal energy and the exciton bandwidth W .

Until now we considered disorder-free aggregates with excitons being delocalised over the entire aggregate ($N_{coh} = N$, N_{coh} is the number of coherently coupled molecules). In real aggregates, structural and electronic disorder is present, which localises excitons ($N_{coh} < N$).

Because of electronic disorder, the transition energies of the individual molecules of the aggregate are distributed around an average transition energy ϵ_0 . For a description of this distribution, the individual transition energy offsets Δ_n are chosen from a joint Gaussian distribution⁹

$$P(\Delta_1, \dots, \Delta_N) = \left[\frac{1}{\sqrt{2\pi}} \right]^N \frac{1}{\sqrt{\det A}} \exp[-0.5 \sum_{n,m=1}^N (A^{-1})_{nm} \Delta_n \Delta_m] \quad (4)$$

where $(A^{-1})_{nm}$ are the elements of the inverse of the covariance matrix A . The matrix elements are given by

$$A_{nm} = \sigma^2 e^{-\frac{|n-m|}{l_0}}, \quad (5)$$

where σ is a measure for the disorder strength, defined as $\sigma \equiv \sqrt{\langle \Delta_n^2 \rangle}$ ($\langle \dots \rangle$ denotes the mean over all realizations). l_0 describes the spatial correlation of transition energies in units of monomers. For $l_0 = 0$ each transition energy offset Δ_n is chosen independently from a Gaussian distribution. In the opposite limit of infinite spatial correlation ($l_0 = \infty$) each monomer within one aggregate exhibits the same energy and disorder is entirely inter-aggregate, see Fig. S5b. By means of correlated energy disorder, inter-aggregate (disorder between aggregates, parameter σ) as well as intra-aggregate electronic disorder (within one aggregate, parameter l_0) is taken into account.

Qualitatively, at $T = 0K$ and for increasing disorder (increasing σ and/or decreasing l_0) the 0-0 PL intensity increases, due to the broken symmetry in the exciton wave function. Moreover, the 0-0 PL intensity is a strong function of N_{coh} , in contrast to the sideband PL 0-1, 0-2, etc.⁹. Therefore, the 0-0 PL-intensity reports on the degree of coherence of the emitting exciton, in particular, the number of coherently coupled molecules N_{coh} can be determined from

$$N_{coh} \equiv \frac{1}{\langle C^{em}(0) \rangle} \sum_{s=-(N-1)}^{N-1} |\langle C^{em}(s) \rangle|. \quad (6)$$

Here, the coherence function for the emitting exciton $|em\rangle$, i.e., the delocalisation of the vibronically excited centre of mass of the exciton, is defined as⁹

$$C^{em}(s) = \sum_n \sum_{\tilde{\nu}, \tilde{\nu}'} f_{\tilde{\nu},0} f_{\tilde{\nu}',0} c_{n,\tilde{\nu}}^{em} c_{n+s,\tilde{\nu}'}^{em}, \quad (7)$$

where $f_{\tilde{\nu},\nu}$ are the vibrational overlap factors, $c_{n,\tilde{\nu}}^{em}$ are the one-particle coefficients and s counts the monomers along the aggregate.

For example, for aggregates without disorder ($\sigma = 0$ and/or $l_0 = \infty$) and periodic boundary conditions $N_{coh} = N$.

Note that motional narrowing should be in principle observable in our data. However, motional narrowing affects mainly the 0-0 PL peak line width, which is largely suppressed in our supramolecular nanofibres. Also the probability of the presence of energetically low-lying states in an aggregate decreases with increasing correlation length l_0 ⁹. Consequently, the linewidths in emission decrease only slightly with increasing size of the aggregates.

Temperature-Dependent PL Spectroscopy of Compound 1 in n-Dodecane

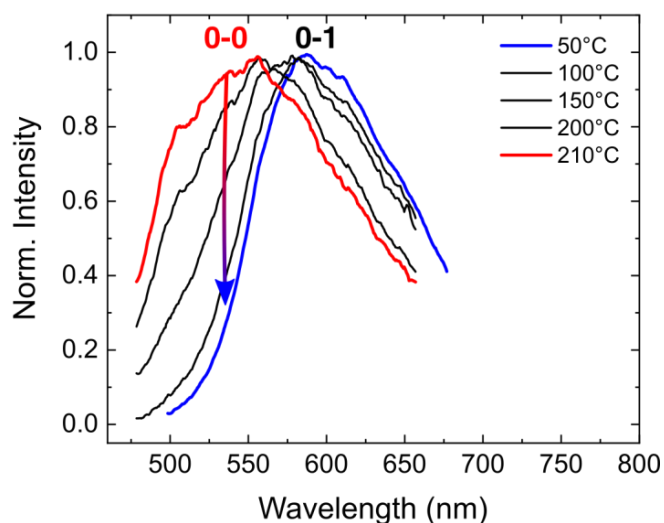


Fig. S6: Temperature-dependent PL spectra of compound 1 in n-dodecane. To support our assignment of the 0-0 and 0-1-peak in the PL spectrum taken from a dispersion of compound 1 in n-dodecane at room temperature (Fig. 3B), we performed temperature dependent PL-spectroscopy on this dispersion. Upon cooling from 210 °C to room temperature, the 0-0 peak decreases continuously. For these measurements, the dispersions are filled in Hellma QS quartz-glass cuvettes at a concentration of 40 μM (100 ppm). The cuvettes were placed inside an aluminium block on a heating plate. The excitation source was a continuous-wave laser that operates at a wavelength of 405 nm. The PL passed a dielectric filter (long-pass filter LP467; AHF Analysentechnik) and was focussed onto the entrance slit of a spectrograph (SpectraPro 2150, Princeton, 300 grooves per millimetre, blaze wavelength 500 nm) equipped with a CCD camera (pco.pixelfly usb, PCO).

Correction of Bundle PL Spectra

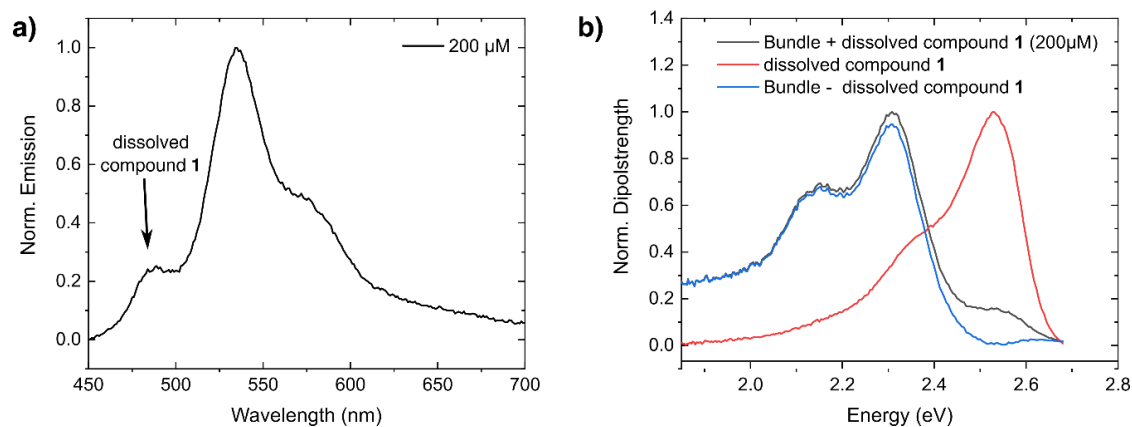


Fig. S7: Correction of the PL spectrum of compound 1 in anisole. **a)** Raw PL-spectrum of compound 1 in anisole at a concentration of 200 μM at room temperature. The peak at 490 nm stems from molecularly dissolved compound 1 in the dispersion due to some degree of remaining solubility. The stronger signal at longer wavelengths (> 510 nm) corresponds to PL from bundles of nanofibres. **b)** To obtain exclusively the PL spectrum of bundles (without monomer contribution), we converted the PL spectrum to an energy scale $I_{PL}(E)$ and to dipole strength via $I_{DP}(E) \propto I_{PL}(E)/E^3$, black curve. We then subtracted a converted, scaled and slightly shifted (0.01 eV) molecularly dissolved spectrum of compound 1 (red curve) from the measured and converted PL. The blue curve shows the resulting dipole strength of bundles of nanofibres.

Excited-State Lifetimes, Radiative Rates and PL Quantum Yields (PL-QY)

The PL decay was recorded by time-correlated single-photon counting (Fig. S8). For bundles an additional long-pass filter LP545 (AHF Analysentechnik) was used to suppress the monomer emission. The PL decay of dissolved compound **1** (THF) shows an exponential behaviour, see table S2.

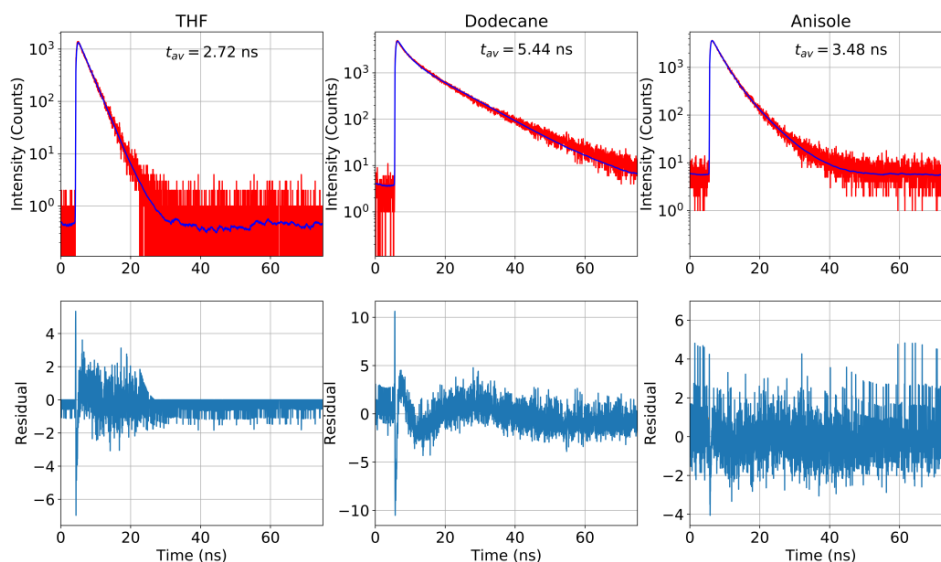


Fig. S8: PL-lifetime measurements. Left: Molecularly dissolved compound **1** in THF, middle: Single nanofibres in n-dodecane, right: Bundles of nanofibres in anisole. Top row: Time-correlated single-photon counting data (red) with fit function (blue). Bottom row: Weighted residuals. For all measurements, the concentration was 40 μM .

For both single supramolecular nanofibres (in n-dodecane) and for bundles of nanofibres (anisole) we found a bi-exponential PL decay with time constants t_i (relative amplitudes F_i) of $t_1 = 2.26 \text{ ns}$ ($F_1 = 3705.7$) and $t_2 = 10.45 \text{ ns}$ ($F_2 = 2353.59$), respectively $t_1 = 2.65 \text{ ns}$ ($F_1 = 3470.49$) and $t_2 = 5.97 \text{ ns}$ ($F_2 = 1144.86$). From these numbers we calculated the amplitude-averaged lifetime

$$t_{av} = \frac{\sum F_i t_i}{\sum F_i}. \quad (8)$$

Tab. S2: PL-QY, excited-state lifetime and radiative lifetimes of (self-assembled) compound **1 in THF, n-dodecane and anisole (concentration: 40 μM).**

	PL-QY	Excited state lifetime t_{av}	Radiative lifetime τ_r
THF	13.79 %	2.72 ns	19.72 ns
n-Dodecane	1.30 %	5.44 ns	418.46 ns
Anisole	2.58 %	3.48 ns	134.88 ns

5. Numerical Simulations of Experimental Spectra

To determine the electronic Coulomb coupling J_0 between the CBT-cores, the electronic disorder σ and the correlation length l_0 along the columns (single nanofibres as well as in bundles), we simulated the optical spectra of self-assembled compound **1** based on the numerical solution of a disordered Holstein Hamiltonian⁶⁻⁹ and a residual analysis between simulation and data (Fig. 3B,C). The size of each nanofibre was limited for most of the cases to $N = 20$ CBT-cores for two reasons: First, this reduces the computational effort if combined with a truncation of the two-particle basis set (i.e., the position of the vibrationally excited molecule with respect to the vibronically excited molecule, see Fig. S5a; e.g. CutOff = 3: the vibrationally excited molecule sits at most three units away). Second, the 0-0 PL intensity is almost independent of N ⁹ and for $N > 20$ the absorption spectra remain unchanged⁶. Finally, we shifted the calculated spectra in energy to fit the measurements, which accounts for the (unknown) change of non-resonant dispersive interactions⁸ when going from molecularly dissolved compound **1** to self-assembled compound **1**.

Usually, absorption spectra are used to determine the exciton bandwidth $W = 4J_0$. Unfortunately, our broad absorption spectra (Fig. 3B,C) made an unambiguous retrieval of all parameters (σ, J_0, l_0) impossible. We started therefore with the PL spectrum of isolated supramolecular nanofibres with its unique feature - the largely suppressed 0-0 peak intensity (Fig. 3B), which is approximately a function of $(l_0, \frac{\sigma}{W})$ ⁹. We obtained then a *lower bound* for W for a maximised correlation length, i.e., $l_0 = \infty$ (see below for details). Based on these values for W the parameters W , σ and l_0 were further refined to reproduce all measured spectra of the different supramolecular morphologies. We exploited that the electronic Coulomb coupling J_0 (and thus the exciton bandwidth W) must be very similar in both isolated nanofibres and bundles of nanofibres, because the $\pi - \pi$ -distance between CBT-cores (Fig. 2), the absorption spectra (Fig. 3B,C) as well as the circular dichroism spectra (Fig. S4) are almost identical for both morphologies.

Overall, we were able to reproduce the experimental spectra in Fig. 3 with good agreement using the following set of parameters:

$$\begin{aligned} W &\approx 4.3 S\omega_0, \\ \sigma &\approx 0.85 \omega_0, \\ l_0 &\approx 10 && \text{for single nanofibres in n-dodecane,} \\ l_0 &\approx 0 && \text{for bundles of nanofibres in anisole.} \end{aligned}$$

The parameters $S = 0.54$ and $\omega_0 = 0.157$ were determined by a Franck-Condon analysis of the PL and absorption spectra of molecularly dissolved compound **1** in THF (see Tab. S1).

Simulation of the PL of isolated nanofibres:

We varied W within the interval $W = S\omega_0 [2, 2.5, \dots, 6]$ to reproduce the suppressed 0-0 PL peak of the isolated nanofibres, and the energy disorder σ within the interval $\sigma = \omega_0 [0.75, 0.8, \dots, 1.05]$ to reproduce the linewidth. Smaller values of W did not describe the suppressed 0-0 PL intensity of isolated nanofibres at room temperature. For a correlation length of $l_0 = \infty$ the smallest residual for a truncation CutOff = 3 was obtained for $W = 5.5 \omega_0 S$ and $\sigma = 0.85 \omega_0$ (Fig. S9a and black dashed curve in Fig. 3B). Also a more accurate calculation with a truncation of CutOff = 6 (Fig. S9b) led to nearly identical results, and the residuals ran

into a minimum for $W \geq 4.0 \omega_0 S$ and $0.80 \omega_0 \leq \sigma \leq 0.90 \omega_0$. Note that *the values for W represent lower bounds*, because the correlation length was maximised.

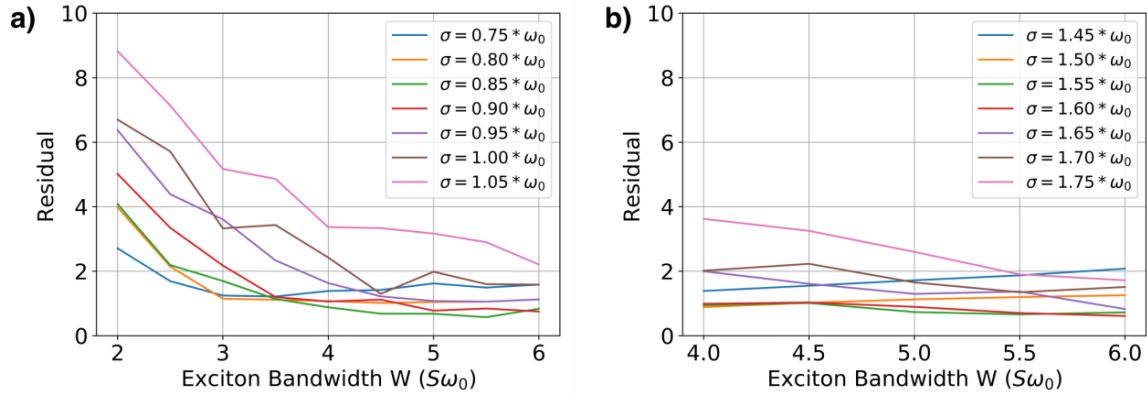


Figure S9: Residual analysis for the PL-spectrum of isolated nanofibres. a) Residuals for a calculation with truncation of $\text{CutOff} = 3$. b) Residuals for a calculation with a truncation of $\text{CutOff} = 6$.

Simulation of the absorption of isolated nanofibres and bundles of nanofibres:

Since the absorption depends only weakly on l_0 (because σ is of the order of W^{10}), we also set $l_0 = \infty$ for the simulation of the absorption spectra and performed a residual analysis for W and σ . To be consistent with the simulation of the PL we limit the intervals to $W = S\omega_0 [4, 4.1, \dots, 5.5]$ and $\sigma = \omega_0 [0.75, 0.76, \dots, 0.85]$. For both single nanofibres and bundles the smallest residual was obtained for $W = 4.3 \omega_0 S$ and $\sigma = 0.84 \omega_0$, see Fig. 3B,C (black lines).

Simulation of the PL of bundles of nanofibres:

Here, the challenge was to reproduce a “monomer-like” PL spectrum with a relatively large value of $W = 4.3 \omega_0 S$ for the exciton bandwidth. We took two steps: (i) We increased the disorder within the nanofibres in bundles by setting $l_0 = 0$, and (ii) we increased the number of monomers to $N = 60$ to increase the probability of finding monomers with site energies in the bottom tail of the Gaussian inhomogeneous distribution. For computational reasons, we chose a truncation of $\text{CutOff} = 1$. The PL spectrum in anisole, in particular the pronounced 0-0 PL intensity, can then be reproduced with the parameters $W = 4.3 \omega_0 S$ and $\sigma = 0.8$. Note, in order to get a good fit for higher values of σ , i.e. $\sigma = 0.85 \omega_0$, the size of the nanofibres N have to be increased further. Importantly, a heavy-tailed Levy-type disorder¹¹ is not required to produce “monomer-type” PL spectra from molecular aggregates.

Coherence length N_{coh} for nanofibres and bundles of nanofibres:

Finally, we refined the value of l_0 to obtain an estimate for the coherence length N_{coh} in isolated nanofibres in n-dodecane. We chose the values determined above for $W = 4.3 \omega_0 S$ and $\sigma = 0.85 \omega_0$ and performed a residual analysis for the PL spectrum with respect to l_0 . To describe the suppressed 0-0 PL peak we restricted the spectral region to 486 nm - 600 nm (Fig. S10a). Furthermore, we used $N = 40$ monomers per nanofibre to minimize boundary effects and a truncation of $CutOff = 3$ to minimize computational efforts. From the best fit we found that $l_0 \approx 10$ CBT-cores, which leads to the coherence number $N_{coh} = 5.44$ CBT-cores (Fig. S10 b). Note, that as a consequence of our underestimated value for the coupling, this correlation length and coherence number itself is *a lower limit only*.

We obtained a coherence number for the bundles of $N_{coh} = 2.94$ CBT-cores, using $W = 4.3 \omega_0 S$; $\sigma = 0.85 \omega_0$; $l_0 = 0$ and $N = 60$ CBT-cores from the simulation of the bundle PL (see above). Note, that this coherence number decreases with increasing N .

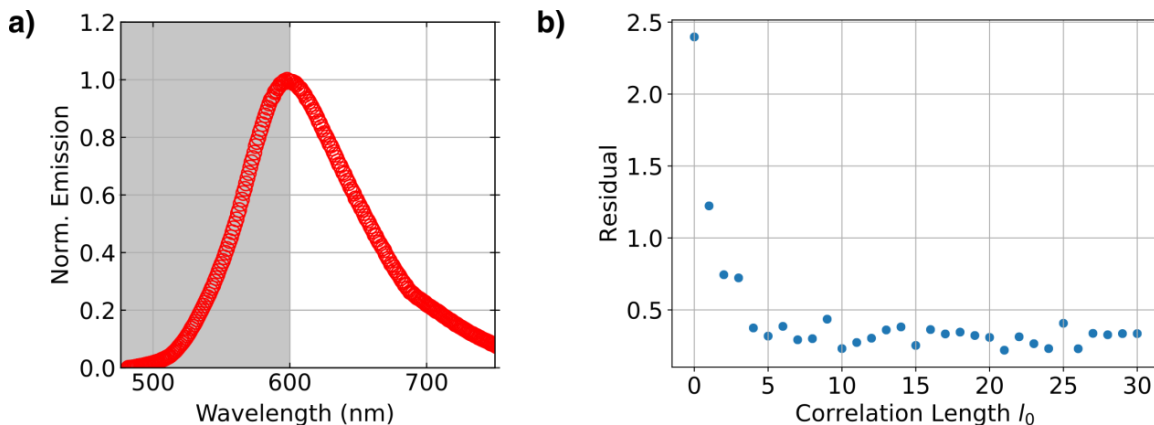


Figure S10: Coherence length in isolated nanofibres. a) PL spectrum of single supramolecular nanofibres in n-dodecane. The area highlighted in grey indicates the spectral region used for the residual analysis. b) Results of the residual analysis for the area highlighted in grey in a). The correlation length is given in units of CBT-cores along a nanofibre.

6. Experimental Setup

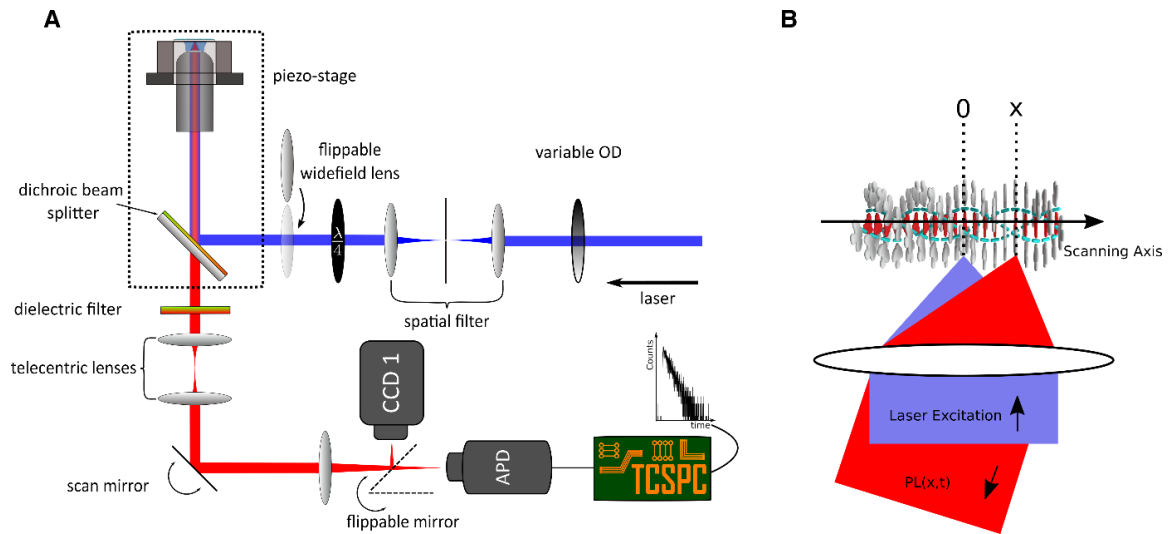


Fig S11: Experimental Setup. **A)** Optical setup with detection-beam scanning capabilities. For details, see 1. Materials and Methods. **B)** Schematic illustration of detection-beam scanning [modified, ¹²]. During the entire detection-beam scan, the confocal excitation spot remains at the same position of the nanostructure, while the detection position imaged onto the APD is independently moved with the scan mirror.

To characterise the setup in Fig. S11, we used agglomerated SiO_x-nanobeads (Corpuscular, diameter 52 nm), because energy transport between the nanobeads is negligible and a time-dependent broadening of the PL profile is not expected. Fig. S12 displays the results of detection-beam scanning on these nanobeads.

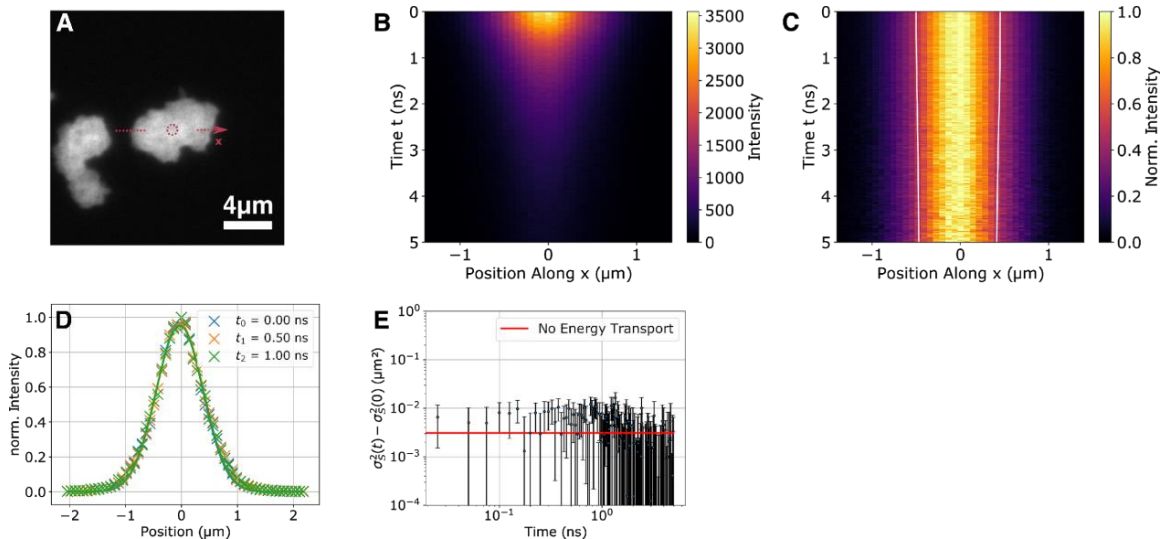


Fig. S12: Control experiment. **A)** Widefield PL image of agglomerated SiO_x-nanobeads. The dashed red circle and arrow illustrate the position of confocal excitation and the direction of the detection scanning (x -axis), respectively. **B)** Spatio-temporal PL intensity distribution $I(x, t)$. **C)** Normalized PL intensity distribution as it evolves in space and time, measured along the axis illustrated by the red dashed arrow in A). The position x denotes the distance relative to the excitation position ($x=0$) along the arrow in A), and $t = 0$ ns corresponds to the arrival time of the excitation pulse. To emphasize changes in the width of the distribution, it is normalized at each time step. The contour lines indicate the time evolution of the full width at half maximum. **D)** Illustration of the normalized spatial intensity distribution $I(x, t_i)$ for three times t_i and the corresponding Gaussian fits, yielding e.g. a standard deviation of $\sigma_I(t = 0) = 411$ nm. Note that this number is determined by the convolution of the Gaussian excitation profile, the detection point-spread function and the detector chip size. **E)** Temporal changes of the second moments of the singlet excitons, revealing no resolvable energy transport in agglomerated SiO_x-nanobeads.

7. Incoherent Exciton Diffusion Model

The extended diffusion equation for 1-dimensional incoherent transport with an exponential decay of the excitations reads ¹³⁻¹⁵

$$\frac{\partial n(x,t)}{\partial t} = D(t) \frac{\partial^2 n(x,t)}{\partial x^2} - kn(x,t), \quad (9)$$

where $n(x,t)$ is the exciton distribution that depends on both space and time. $D(t)$ is the time-dependent diffusivity that is related to an exciton hopping coefficient A by $D(t) = \frac{1}{2} A_\alpha t^{\alpha-1}$ with fractional time units for A ¹⁶. Finally, k is the constant exciton decay rate.

Superdiffusive transport is characterized by $\alpha > 1$. For normal diffusion, $\alpha = 1$, the diffusivity $D = \frac{1}{2} A$ is time independent with units of cm^2s^{-1} . Subdiffusion is characterized by $\alpha < 1$ and occurs for exciton motion in a disordered excited-state energy landscape ^{17,18}.

In our experiments the diffraction-limited confocal excitation spot creates to a good approximation an exciton population with a Gaussian profile and a standard deviation of σ . The solution to equation (9) is given then

$$n(x,t) \propto \exp\left(-\frac{x^2}{2\sigma^2 + 2At^\alpha}\right) \exp(-kt). \quad (10)$$

Note that the exponential decay ($\exp(-kt)$) for the exciton population in equation (10) only changes the magnitude of this distribution at any point in time (and not its shape) and vanishes upon normalization to its maximum value at a given time, see Fig. 4C,D.

Equation (10) shows that the variance of the exciton distribution, which is also called the mean square displacement MSD $\langle x(t)^2 \rangle$, evolves in time as ^{13,14}

$$\langle x(t)^2 \rangle = \sigma_n^2(t) = \sigma^2 + At^\alpha, \quad (11)$$

In a general situation with electronic disorder in the excited-state energy landscape the time-dependent diffusivity $D(t) = \frac{1}{2} A_\alpha t^{\alpha-1}$ decreases with time ^{15,16} (Fig. S14).

For normal diffusion ($\alpha = 1$), equation (12) transforms to

$$\langle x(t)^2 \rangle = \sigma_n^2(t) = \sigma^2 + 2Dt. \quad (12)$$

In general, the measured spatial intensity distribution (e.g. Fig. 4C,D) is a convolution of the exciton distribution $n(x,t)$, the detection point spread function $PSF(x)$ and the function of the APD detector size $C(x)$

$$I(x,t) = n(x,t) * PSF(x) * C(x). \quad (13)$$

The PSF can be well approximated by a Gaussian function. The APD detector size is $50 \mu\text{m}$ and if the magnification of the setup of 83.9 is considered, the convolution of the PSF and the APD function can be well approximated with a Gaussian function with a time-independent variance σ_{setup} (see above Fig. S12). Therefore, the variance of the resulting Gaussian function is

$$\sigma_I^2(t) = \sigma_n^2(t) + \sigma_{setup}^2. \quad (14)$$

The temporal changes in the variance of the spatial intensity distributions, i.e., the changes in the MSD, are calculated using the difference of the Gaussian variance (Eq. (14)) at a time t and the Gaussian variance at a fixed reference time $t = 0$. Using Eq. (11), the changes in the MSD due to diffusion with a Gaussian initial condition is then given by^{13,14}

$$\Delta MSD = \sigma_I^2(t) - \sigma_I^2(0) = At^\alpha. \quad (15)$$

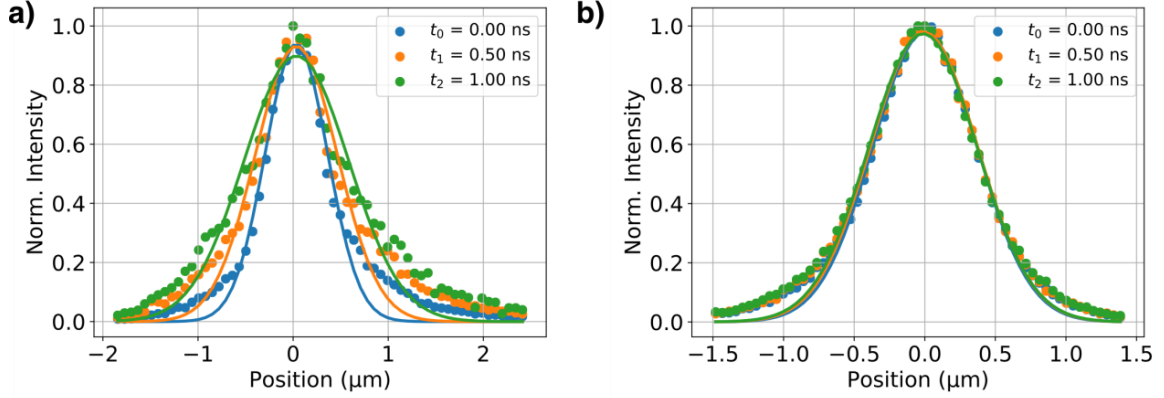


Fig. S13: Normalized spatial intensity distributions. **a,b)** Profiles from the normalized spatial intensity distributions $I(x, t_i)$ for the single nanofibre and the bundle of nanofibres, respectively, shown in Fig. 4C,D. The profiles were extracted at three times t_i and the solid lines show fits with Gaussian functions.

Fig. S13a,b show three profiles from the normalised spatial intensity distributions in Fig. 4C,D at different times. While Gaussian fits can roughly reproduce the intensity distribution of bundles, the profiles for the single nanofibre are very clearly non-Gaussian. This observation is related to the fact that each single nanofibre possesses its own unique excited-state energy landscape, which we directly probe in our single nanofibre experiment. In other words, we do not perform an ensemble average, and thus do not average out the specifics of each individual system. Thus, $n(x, t)$ does not evolve in time according to a Gaussian function.

To account for the non-Gaussian profiles, we evaluated the changes of the second moments (a measure for the widths) of our spatial intensity distributions, i.e.,

$$\Delta\mu_2(t) = \mu_2(t=0) - \mu_2(t) = At^\alpha. \quad (16)$$

For our spatial intensity distribution $I(x, t)$ the second moment at each point in time is defined as

$$\mu_2 = \frac{1}{N} \int (x - \mu_1)^2 I(x, t) dx \quad (17)$$

where $N = \int I(x, t) dx$ is the integrated PL intensity and $\mu_1(t) = \frac{1}{N} \int x I(x, t) dx$ is the corresponding first moment (i.e., a measure for the centre of mass of the profile).

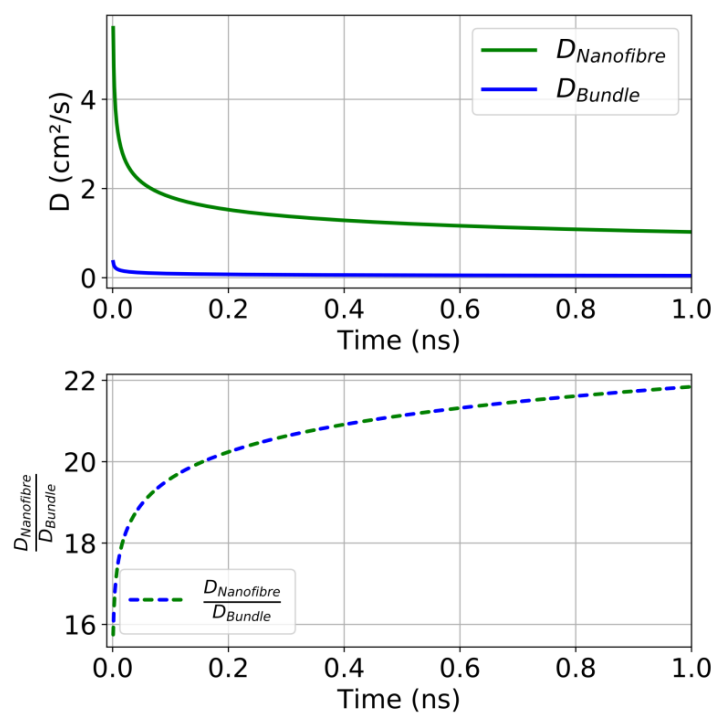


Fig. S14: Time-dependent diffusivities. Time-dependent diffusivity D of the single supramolecular nanofibre (green) and bundle (blue) shown in Fig. 4A,B.

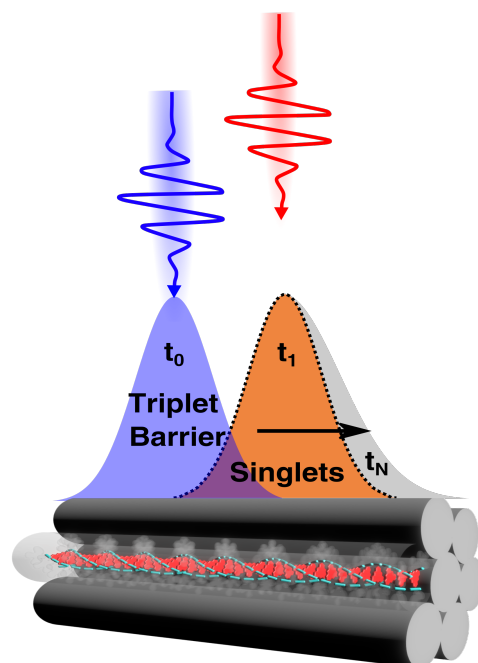
8. References

- (1) Haedler, A. T.; Meskers, S. C. J.; Zha, R. H.; Kivala, M.; Schmidt, H. W.; Meijer, E. W. Pathway Complexity in the Enantioselective Self-Assembly of Functional Carbonyl-Bridged Triarylamine Trisamides. *J. Am. Chem. Soc.* **2016**, *138* (33), 10539–10545. <https://doi.org/10.1021/jacs.6b05184>.
- (2) Haedler, A. T.; Kreger, K.; Issac, A.; Wittmann, B.; Kivala, M.; Hammer, N.; Köhler, J.; Schmidt, H. W.; Hildner, R. Long-Range Energy Transport in Single Supramolecular Nanofibres at Room Temperature. *Nature* **2015**, *523* (7559), 196–199. <https://doi.org/10.1038/nature14570>.
- (3) Eisele, D. M.; Knoester, J.; Kirstein, S.; Rabe, J. P.; Vanden Bout, D. A. Uniform Exciton Fluorescence from Individual Molecular Nanotubes Immobilized on Solid Substrates. *Nat. Nanotechnol.* **2009**, *4* (10), 658–663. <https://doi.org/10.1038/nnano.2009.227>.
- (4) Zhang, W.; Jin, W.; Fukushima, T.; Saeki, A.; Seki, S.; Aida, T. Supramolecular Linear Heterojunction Composed of Graphite-like Semiconducting Nanotubular Segments. *Science* **2011**, *334* (6054), 340–343. <https://doi.org/10.1126/science.1210369>.
- (5) Köhler, A.; Bässler, H. *Electronic Processes in Organic Semiconductors: An Introduction*. Wiley-VCH; 2015.
- (6) Spano, F. C.; Meskers, S. C. J.; Hennebicq, E.; Beljonne, D. Probing Excitation Delocalization in Supramolecular Chiral Stacks by Means of Circularly Polarized Light: Experiment and Modeling. *J. Am. Chem. Soc.* **2007**, *129* (22), 7044–7054. <https://doi.org/10.1021/ja067321g>.
- (7) Hestand, N. J.; Spano, F. C. Expanded Theory of H- and J-Molecular Aggregates: The Effects of Vibronic Coupling and Intermolecular Charge Transfer. *Chem. Rev.* **2018**, *118* (15), 7069–7163. <https://doi.org/10.1021/acs.chemrev.7b00581>.
- (8) Spano, F. C. The Spectral Signatures of Frenkel Polarons in H- and J-Aggregates. *Acc. Chem. Res.* **2010**, *43* (3), 429–439. <https://doi.org/10.1021/ar900233v>.
- (9) Spano, F. C.; Clark, J.; Silva, C.; Friend, R. H. Determining Exciton Coherence from the Photoluminescence Spectral Line Shape in Poly(3-Hexylthiophene) Thin Films. *J. Chem. Phys.* **2009**, *130* (7), 074904. <https://doi.org/10.1063/1.3076079>.
- (10) Clark, J.; Silva, C.; Friend, R. H.; Spano, F. C. Role of Intermolecular Coupling in the Photophysics of Disordered Organic Semiconductors: Aggregate Emission in Regioregular Polythiophene. *Phys. Rev. Lett.* **2007**, *98* (20), 206406. <https://doi.org/10.1103/PhysRevLett.98.206406>.
- (11) Merdasa, A.; Jiménez, Á. J.; Camacho, R.; Meyer, M.; Würthner, F.; Scheblykin, I. G. Single Lévy States-Disorder Induced Energy Funnels in Molecular Aggregates. *Nano Lett.* **2014**, *14* (12), 6774–6781. <https://doi.org/10.1021/nl5021188>.
- (12) Ciesielski, R.; Schäfer, F.; Hartmann, N. F.; Giesbrecht, N.; Bein, T.; Docampo, P.; Hartschuh, A. Grain Boundaries Act as Solid Walls for Charge Carrier Diffusion in Large Crystal MAPI Thin Films. *ACS Appl. Mater. Interfaces* **2018**, *10* (9), 7974–7981. <https://doi.org/10.1021/acsami.7b17938>.
- (13) Clark, K. A.; Krueger, E. L.; Vanden Bout, D. A. Direct Measurement of Energy Migration in Supramolecular Carbocyanine Dye Nanotubes. *J. Phys. Chem. Lett.* **2014**, *5* (13), 2274–2282. <https://doi.org/10.1021/jz500634f>.
- (14) Akselrod, G. M.; Deotare, P. B.; Thompson, N. J.; Lee, J.; Tisdale, W. A.; Baldo, M. A.; Menon, V. M.; Bulovic, V. Visualization of Exciton Transport in Ordered and Disordered Molecular

Solids. *Nat. Commun.* **2014**, *5* (1), 3646. <https://doi.org/10.1038/ncomms4646>.

- (15) Akselrod, G. M.; Prins, F.; Poulikakos, L. V.; Lee, E. M. Y.; Weidman, M. C.; Mork, A. J.; Willard, A. P.; Bulović, V.; Tisdale, W. A. Subdiffusive Exciton Transport in Quantum Dot Solids. *Nano Lett.* **2014**, *14* (6), 3556–3562. <https://doi.org/10.1021/nl501190s>.
- (16) Wu, J.; Berland, K. M. Propagators and Time-Dependent Diffusion Coefficients for Anomalous Diffusion. *Biophys. J.* **2008**, *95* (4), 2049–2052. <https://doi.org/10.1529/biophysj.107.121608>.
- (17) Havlin, S.; Ben-Avraham, D. Diffusion in Disordered Media. *Adv. Phys.* **2002**, *51* (1), 187–292. <https://doi.org/10.1080/00018730110116353>.
- (18) Vlaming, S. M.; Malyshev, V. A.; Einfeld, A.; Knoester, J. Subdiffusive Exciton Motion in Systems with Heavy-Tailed Disorder. *J. Chem. Phys.* **2013**, *138* (21), 214316. <https://doi.org/10.1063/1.4808155>.

4.3 ALL-OPTICAL CONTROL OF SINGLET EXCITON TRANSPORT IN INDIVIDUAL SUPRAMOLECULAR NANOSTRUCTURES BY TRIPLET GATING



Bernd Wittmann, Till Biskup, Klaus Kreger, Jürgen Köhler, Hans-Werner Schmidt and Richard Hildner

All-optical control of singlet exciton transport in individual supramolecular nanostructures by triplet gating

Bernd Wittmann¹, Till Biskup², Klaus Kreger³, Jürgen Köhler¹, Hans-Werner Schmidt³,
Richard Hildner*^{1,4}

Affiliations:

¹Spectroscopy of Soft Matter, University of Bayreuth, Universitätsstraße 30, 95447 Bayreuth, Germany.

²Chair of Physical Chemistry and Chemical Education, University of Saarland, Campus B2 2, 66123 Saarbrücken, Germany.

³Macromolecular Chemistry and Bavarian Polymer Institute, University of Bayreuth, Universitätsstraße 30, 95447 Bayreuth, Germany.

⁴Zernike Institute for Advanced Materials, University of Groningen, Nijenborgh 4, 9747 AG Groningen, The Netherlands.

*Correspondence to: r.m.hildner@rug.nl.

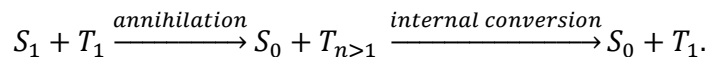
Abstract:

Directed transport of singlet excitation energy is a key process in natural light harvesting and a desired feature in assemblies of functional organic molecules for organic electronics and nanotechnology applications. However, progress in this direction is hampered by the lack of concepts and model systems. Here we demonstrate an all-optical approach to control singlet exciton transport pathways via singlet-triplet annihilation within individual 1-dimensional H-type supramolecular nanostructures. We use two temporally and spatially separated laser pulses to generate a local triplet exciton population and a subsequent local singlet exciton population. The local triplet exciton population operates as a gate for the singlet exciton transport, since singlet-triplet annihilation hinders singlet exciton motion across the triplet exciton population. We visualize and quantify the control over singlet exciton transport via the fluorescence signal of the supramolecular nanostructure using a detection-beam scanning approach combined with time-correlated single-photon counting. Our new approach paves the way towards complete, all-optical control over singlet exciton transport and ultimately towards new design principles for functional photonic nanodevices.

Introduction:

Controlling the flow of excitation energy (excitons) within supramolecular assemblies of functional organic materials is a key feature to expand their applicability in various fields, from sustainable energy generation to (quantum) information technology. While important design principles for long-range energy transport are emerging¹⁻⁷, there is a lack of approaches to manipulate transport of excitation energy within supramolecular structures in a reliable and reversible manner. In this direction, an intriguing example is provided by the photosynthetic apparatus in nature⁸⁻¹⁰: Sophisticated pigment-protein complexes direct excitation energy towards a reaction centre via a built-in energy funnel using only a single species of pigment molecules. This funnel is created by a precise spatial organisation of the pigments as well as by carefully tuned interactions between the pigments and the protein scaffold. Although this energy funnel is not reversible, it inspired several synthetic approaches. For instance, appending chemically distinct chromophores to a DNA scaffold^{11,12} or doping 1-dimensional supramolecular nanostructures with acceptor molecules^{13,14} predefines the direction for energy transfer using one or more transfer steps. Control of energy transport by external stimuli was shown in organic single crystals by applying an electric field¹⁵ or a local strain gradient with an atomic force microscope tip that creates local topological quenchers¹⁶. However, all these approaches are based on structuring samples / substrates in advance, i.e., the direction of transport cannot be reversed, or they can induce irreversible changes to the system, which inhibits full control over exciton transport. Hence, there is a lack of suitable model systems and concepts to enable room-temperature manipulation of exciton transport and to promote the development of flexible and reconfigurable organic excitonic devices.

A highly flexible, reversible and non-invasive approach to control exciton transport in supramolecular nanostructures is an all-optical method based on independently photo-



An appropriately positioned local triplet exciton population can therefore serve as a barrier for the transport of singlet excitons and form a controllable gate. This gate is self-sustaining within the long triplet lifetime, due to the survival of an excited triplet exciton after the annihilation process.

Here, we demonstrate this all-optical approach and control singlet exciton transport pathways via singlet-triplet annihilation in individual 1-dimensional supramolecular nanostructures. Using a two-pulse excitation scheme we effectively generate an initial triplet exciton population via inter-system crossing of initially generated singlet excitons, and subsequently with a spatial offset, we generate mobile singlet excitons (**Fig. 1**). The presence of a local triplet exciton population effectively steers singlet excitons away from the triplet population. This controlled singlet exciton transport within a single nanostructure is then monitored with time-resolved detection-beam scanning.

We exploit supramolecular nanostructures based on a carbonyl-bridged triarylamine trisamide (CBT, **Fig. 1**, see Ref. ^{6,19,20}). The molecular design of CBT gives rise to a cofacial arrangement of the CBT-cores, which is driven by directed hydrogen bonding between the amide groups. This H-type arrangement of the CBT cores supports singlet exciton transport up to several micrometres ^{6,7}. Moreover, long-lived triplet states in carbonyl-bridged triarylaminines have been observed ²¹. We specifically study individual bundles of supramolecular nanofibres that we reported recently ⁶. Since each bundle comprises more than 1000 H-type nanofibres, the fluorescence signal from singlet excitons features a high signal-to-noise ratio to detect small changes in time- and spatially resolved measurements. CBT-based bundles of supramolecular nanofibres are therefore a prototypical test bed for studying and controlling singlet exciton transport via a triplet exciton gate.

Results and Discussion:

The presence of a long-lived excited triplet state in our supramolecular CBT building block, molecularly dissolved in THF, was verified by time-resolved detection of the electron paramagnetic resonance (TREPR) signal following pulsed laser excitation ²² (**Fig. S1a**, see also Materials and Methods in the Supporting Information, SI). In supramolecular assemblies based on triarylamine triplet excitons have recently been shown to exist as well ²¹. We determined singlet and triplet excited-state lifetimes on bulk dispersions both of molecularly dissolved CBT and of bundles of nanofibres (in anisole) using time-correlated single-photon counting after pulsed excitation of singlet states (**Fig. 2a** and **Fig. S1b**). For both samples, we find a rapid initial decay on nanosecond time scales, associated with the prompt fluorescence from the singlet excited states. Moreover, a much weaker delayed signal on microsecond time scales is present. We attribute this long-lived signal to phosphorescence from triplet states that are populated via intersystem crossing from initially excited singlet states. For molecularly dissolved CBT the singlet lifetime is 2.7 ns, while for bundles of nanofibres we find a longer singlet exciton lifetime of 4.1 ns due to the H-type aggregation of CBT cores ⁶. This trend is also found for the phosphorescence lifetimes: For molecularly dissolved CBT the triplet lifetime is 766 ns (**Fig S1**), while for the bundles we find 1320 ns (**Fig. 2a**).

To characterize the influence of singlet-triplet annihilation on the singlet exciton dynamics, we performed fluence and laser repetition rate dependent fluorescence lifetime measurements on bundles of nanofibres in anisole dispersion. **Fig. 2b** shows an example for which the excitation fluence per pulse was kept constant at $8.6 \cdot 10^{15}$ photons/(pulse \cdot cm²), while the laser repetition rate was increased from 0.25 MHz to 10 MHz. We find that the fluorescence lifetime decreases from 4 ns to 3.3 ns. This characteristic trend indicates efficient annihilation between mobile singlet excitons and triplet excitons ^{17,23} within bundles of nanofibres. This effect is particularly pronounced at high fluences and at laser repetition rates higher than the

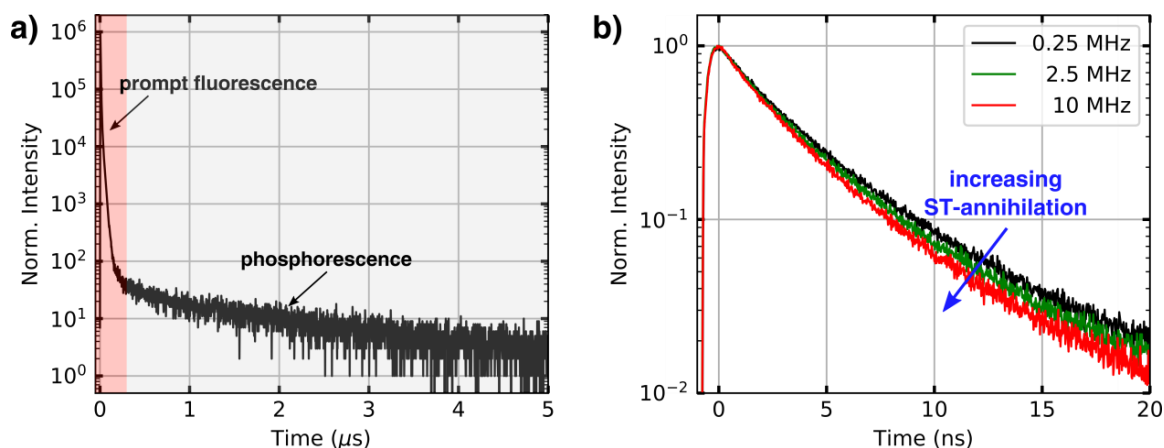


Figure 2. Photoluminescence kinetics of bundles of supramolecular nanofibres in anisole dispersion. **a)** Time-resolved photoluminescence decay with a prompt fluorescence signal within nanoseconds, originating from singlet excitons (red boxed area), and a weaker phosphorescence signal on microsecond time scales, stemming from triplet excitons (grey boxed area). **b)** Fluorescence decays of singlet excitons at a fixed excitation fluence of 8.6×10^{15} photons/(pulse \cdot cm 2) for increasing laser repetition rates. The effect of singlet-triplet (ST) annihilation is clearly visible as a reduction of the singlet exciton lifetimes. For both measurements the concentration of the dispersion was 400 μ M.

inverse triplet lifetime (**Fig. S2**). In this situation, the triplet population accumulates and does not fully decay between subsequent laser pulses. Mobile singlet excitons thus encounter an increasing number of triplet excitons for annihilation, which creates an additional decay channel for singlet excitons and reduces their excited-state lifetime (**Fig. S3**).

These data demonstrate that the presence of long-lived triplet excitons in bundles of nanofibres strongly influences the dynamics of singlet excitons via singlet-triplet annihilation. The combination of long-range singlet exciton transport, the presence of long-lived triplet states that enable singlet-triplet annihilation and the 1-dimensional nature of our bundles of nanofibres make this system perfectly suited to manipulate singlet exciton transport by spatio-temporal control of local triplet exciton populations.

To demonstrate such control of singlet exciton motion in individual bundles of nanofibres, we spin-coated bundles from a 40 μ M anisole dispersion onto microscopy cover slips. **Fig. 3a**

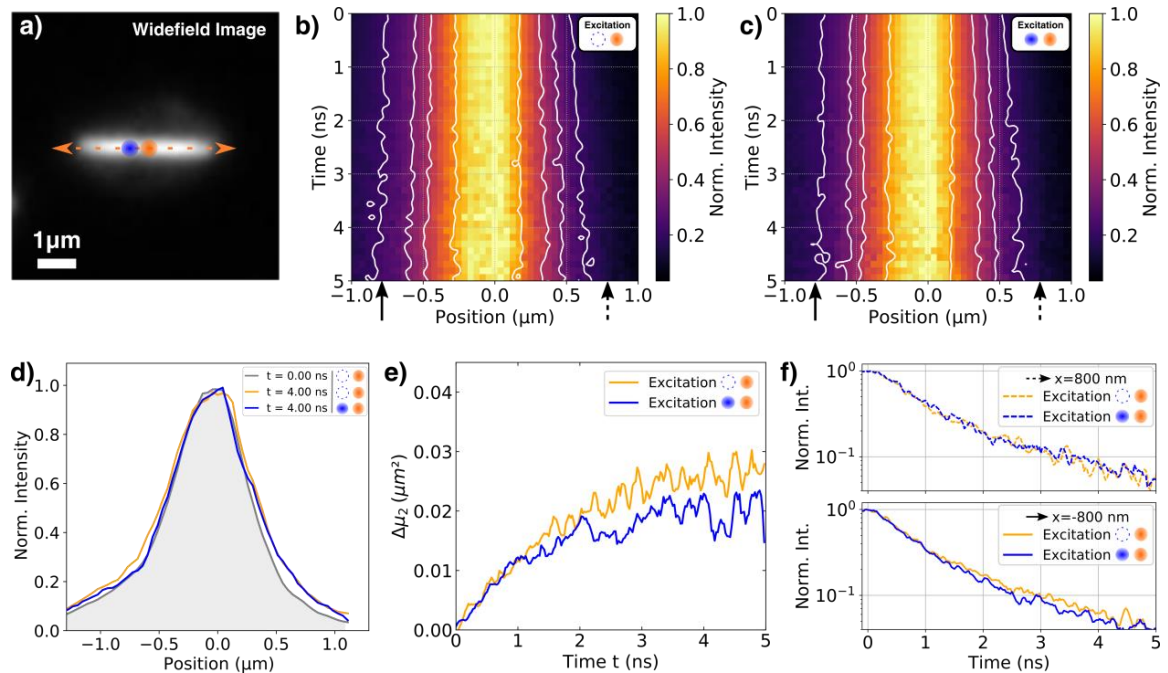


Figure 3. Controlled singlet exciton transport in a single bundle of supramolecular nanofibres. **a)** Widefield photoluminescence image of an individual bundle. The orange dashed arrow indicates the detection scanning axis x . The orange circle labels the centre of the singlet population at position $x = 0$ nm. The blue circle indicates the centre of the triplet exciton population at $x = -800$ nm. **b)** Normalized fluorescence intensity distribution and its evolution in space (x) and time (t) for the bundle in (a) without the presence of the triplet exciton population. **c)** Normalised fluorescence intensity distribution as in (b), but here with the presence of the triplet exciton population. The white contour lines in (b) and (c) indicate the widths of the intensity profiles. The solid and dashed arrows indicate the positions at $x = -800$ nm and $x = 800$ nm from where fluorescence decay curves were extracted for (f). **d)** Fluorescence intensity profiles retrieved from the fluorescence intensity maps in (b) (orange) and (c) (blue) at a delay time of $t = 4$ ns after singlet exciton generation. The grey line shows the initial fluorescence intensity distribution at time $t = 0$ ns. **e)** Temporal changes of the second moments $\Delta\mu_2$ (widths) of the spatial intensity profiles determined from the data in (b) (orange) and (c) (blue). **f)** Fluorescence decay curves extracted from the data in (b) (orange) and (c) (blue) at position $x = 800$ nm (top, dashed lines) and $x = -800$ nm (bottom, solid lines).

displays a representative widefield image of an isolated bundle (note that this image represents predominantly the prompt fluorescence from singlet excitons, see Fig. 2a). For this bundle we find a length of several micrometres, in agreement with our recent work⁶. We excite this bundle confocally by two distinct pulsed lasers: First, a 420 nm laser (‘triplet laser’) is used to create a singlet exciton population 800 nm to the left of the centre of the

bundle (i.e., at $x = -800 \text{ nm}$, blue circle, **Fig. 3a**). Second, a 450 nm laser ('singlet laser') is used to create a singlet exciton population in the centre of the bundle (i.e., at $x = 0 \text{ nm}$, orange circle, **Fig. 3a**). This 'singlet laser' hits the sample 120 ns after arrival of the 'triplet laser'. The naming of the two lasers reflects that 120 ns after the arrival of the 'triplet laser' all (short-lived) singlet excitons already decayed and only triplet excitons generated by intersystem crossing survived. The 'singlet laser' excitation thus creates a spatially separated and temporally delayed singlet exciton population. If those singlet excitons diffuse to the left, they can interact with triplet excitons via singlet-triplet annihilation, whereas singlet excitons migrating to the right along the bundle will not encounter this triplet population and transport is unperturbed.

We visualise the spatio-temporal dynamics of singlet excitons along the bundle, created by the 'singlet laser', using a detection-beam scanning approach combined with time-correlated single-photon counting of the prompt fluorescence signal^{6,24}. We measure fluorescence decay curves at fixed positions of the laser foci, while scanning the detection position along the long (x -) axis of the bundle. We thus create a time-dependent distribution of the prompt fluorescence of singlet excitons, $I(x, t)$, as a function of the distance x relative to the centre of the 'singlet laser' and time t after its arrival on the sample (see Materials and Methods, SI). To exclude artefacts (defocusing, bleaching etc.) we record two fluorescence decay curves for each detection position before moving to the next. The first fluorescence decay is measured only with the 'singlet laser' as the excitation source, while for the second decay curve both the 'triplet laser' and the 'singlet laser' hit the sample with time ordering as explained above. This interleaved experiment allows to unambiguously assign changes in the singlet exciton dynamics to the presence or absence of the triplet population, since the measurement with only the 'singlet laser' serves as a reference for the unperturbed singlet exciton dynamics along the bundle. Finally, we normalize the spatial intensity distributions at each point in time to emphasize the fluorescence broadening along the bundle's long axis.

Fig. 3b shows the resulting spatio-temporal fluorescence distribution $I(x, t)$ of our reference experiment, generated only by ‘singlet laser’ excitation. In analogy to our previous work⁶, the fluorescence intensity distribution reveals a broadening in both directions of the bundle’s long axis on a (sub-)nanosecond time scale. The symmetric nature of this broadening is evident from intensity profiles at different times t_i after singlet exciton generation (**Fig. 3d**, grey and orange lines). This temporal change of the fluorescence profiles reflects the unperturbed, long-range nature of singlet exciton diffusion in both directions.

For the measurement with both lasers active the resulting temporal broadening of the fluorescence distribution $I(x, t)$ is shown in **Fig. 3c**. This broadening now appears to be asymmetrical and hindered towards the left side ($x < 0 \mu\text{m}$), where the triplet exciton population is present on the bundle. This effect is also visible in the temporal evolution of the intensity profiles in **Fig. 3d**: While for positions $x < 0 \mu\text{m}$ the initial and delayed profiles overlap (grey and blue lines), i.e., no spatial broadening of the initial singlet exciton population occurs, to the right ($x > 0 \mu\text{m}$) singlet exciton diffusion is unperturbed, since the profiles in absence and presence of the triplet population overlap (orange and blue lines).

We analysed this temporal broadening quantitatively by changes of the second moments $\mu_2(t)$ of the spatial intensity profiles⁶, with respect to the second moment of the initial profile $\mu_2(0)$, i.e.,

$$\Delta\mu_2(t) = \mu_2(t) - \mu_2(0).$$

The $\Delta\mu_2(t)$ curves retrieved from the data in **Figs. 3b** and **3c** are shown in **Fig. 3e**. For both curves we clearly observe a sub-linear behaviour, which is characteristic of subdiffusive exciton motion due to a disordered excited-state energy landscape²⁵, as we recently reported⁶. However, for times $t > 1 \text{ ns}$ and both lasers active, the $\Delta\mu_2(t)$ values (**Fig. 3e**, blue line) are systematically smaller compared to those with only the ‘singlet laser’ active, i.e., without

the initial triplet population on the bundle (**Fig. 3e**, orange line). This behaviour underpins the restricted singlet exciton diffusion in the presence of the triplet exciton population.

To confirm that this hindered singlet exciton diffusion towards the left of the bundle is caused by singlet-triplet annihilation, we extracted the fluorescence lifetimes as a function of the position relative to the centre ($x = 0 \mu\text{m}$) of the ‘singlet laser’ from the fluorescence intensity distributions in **Fig. 3b** and **3c**. While the fluorescence lifetimes retrieved at $x = 800 \text{ nm}$ to the right of the ‘singlet laser’ do not differ (**Fig. 3f**, top), the lifetimes at $x = -800 \text{ nm}$ to the left side are shorter for the measurement where both lasers excite the bundle (**Fig. 3f**, bottom). This clearly proves that singlet-triplet annihilation processes take place in our system, and that this process only occurs locally at the position of the initial triplet exciton population.

The presence of a triplet exciton population thus creates a barrier, which is responsible for the hindered singlet exciton dynamics within the bundle of nanofibres towards the position of the ‘triplet laser’ excitation. Thus, we designed a controllable gate for singlet excitons with their motion being regulated by a local triplet exciton population (**Fig. S4**). Notably, this gate can be written at any suitable position (**Fig. S5**). The ‘triplet laser’ serves as the user input for our gate, i.e., if this input is active, diffusion in one direction is suppressed via singlet-triplet annihilation: If a singlet exciton approaches the triplet barrier, singlet-triplet annihilation occurs, leaving behind a triplet exciton to create a self-sustaining barrier. Numerical simulations using a simple diffusion equation reproduce this behaviour with an effective position-dependent annihilation rate (see SI, 2. Numerical Simulations and **Fig. S4**). This rate is approximately constant over time for the (short) singlet exciton lifetime. The gate remains closed until the user input is deactivated, i.e., the ‘triplet laser’ is turned off, the triplet excitons return to the ground state, and the annihilation rate becomes zero.

Conclusion:

In conclusion, we visualized tailored singlet exciton transport in bundles of supramolecular H-type nanofibres based on organic functional molecules. Using two spatio-temporally separated laser pulses we photo-excite two independent exciton populations within a bundle. The first pulse effectively generates a triplet exciton population via inter-system crossing of initially generated singlet excitons. This triplet population acts as a barrier for the subsequently generated singlet exciton population, because singlet-triplet annihilation hinders singlet exciton diffusion across the triplet exciton population within the bundle of nanofibres. The singlet-triplet annihilation rate is position-dependent and can be controlled by the spatial separation of the singlet and triplet exciton populations. In this way, a fully reversible, optically switchable triplet exciton gate for the control of singlet exciton migration is created that does not require restructuring the sample. This result opens new opportunities for design principles for new photonic nanodevices and paves the way towards tailored, all-optical control of singlet exciton energy transport.

Acknowledgements:

We acknowledge financial support from the German Research Foundation (DFG) through the research training group GRK1640 and from the Bavarian State Ministry of Science and the Arts through the Collaborative Research Network 'Solar Technologies go Hybrid'. We acknowledge support by the Elite Network of Bavaria (ENB) through the study program "Biological Physics" (JK, RH). We are grateful to Felix Wenzel, Doris Hanft and Sandra Ganzleben (Macromolecular Chemistry, University of Bayreuth) for their help with synthesis and self-assembly.

References and Notes:

- (1) Brédas, J. L.; Sargent, E. H.; Scholes, G. D. Photovoltaic Concepts Inspired by Coherence Effects in Photosynthetic Systems. *Nat. Mater.* **2016**, *16* (1), 35–44. DOI: 10.1038/nmat4767.
- (2) Zhu, T.; Wan, Y.; Huang, L. Direct Imaging of Frenkel Exciton Transport by Ultrafast Microscopy. *Acc. Chem. Res.* **2017**, *50* (7), 1725–1733. DOI: 10.1021/acs.accounts.7b00155.
- (3) Scholes, G. D. Designing Light-Harvesting Antenna Systems Based on Superradiant Molecular Aggregates. *Chem. Phys.* **2002**, *275* (1–3), 373–386. DOI: 10.1016/S0301-0104(01)00533-X.
- (4) Caram, J. R.; Doria, S.; Eisele, D. M.; Freyria, F. S.; Sinclair, T. S.; Rebentrost, P.; Lloyd, S.; Bawendi, M. G. Room-Temperature Micron-Scale Exciton Migration in a Stabilized Emissive Molecular Aggregate. *Nano Lett.* **2016**, *16* (11), 6808–6815. DOI: 10.1021/acs.nanolett.6b02529.
- (5) Topczak, A. K.; Roller, T.; Engels, B.; Brütting, W.; Pflaum, J. Nonthermally Activated Exciton Transport in Crystalline Organic Semiconductor Thin Films. *Phys. Rev. B* **2014**, *89* (20), 201203. DOI: 10.1103/PhysRevB.89.201203.
- (6) Wittmann, B.; Wenzel, F. A.; Wiesneth, S.; Haedler, A. T.; Drechsler, M.; Kreger, K.; Köhler, J.; Meijer, E. W.; Schmidt, H.-W.; Hildner, R. Enhancing Long-Range Energy Transport in Supramolecular Architectures by Tailoring Coherence Properties. *J. Am. Chem. Soc.* **2020**, *142* (18), 8323–8330. DOI: 10.1021/jacs.0c01392.
- (7) Haedler, A. T.; Kreger, K.; Issac, A.; Wittmann, B.; Kivala, M.; Hammer, N.; Köhler, J.; Schmidt, H. W.; Hildner, R. Long-Range Energy Transport in Single Supramolecular Nanofibres at Room Temperature. *Nature* **2015**, *523* (7559), 196–199. DOI: 10.1038/nature14570.
- (8) Scholes, G. D.; Fleming, G. R.; Olaya-Castro, A.; van Grondelle, R. Lessons from Nature about Solar Light Harvesting. *Nat. Chem.* **2011**, *3* (10), 763–774. DOI: 10.1038/nchem.1145.
- (9) Cogdell, R. J.; Gall, A.; Köhler, J. The Architecture and Function of the Light-Harvesting Apparatus of Purple Bacteria: From Single Molecules to in Vivo Membranes. *Q. Rev. Biophys.* **2006**, *39* (3), 227–324. DOI: 10.1017/S0033583506004434.
- (10) Mirkovic, T.; Ostroumov, E. E.; Anna, J. M.; van Grondelle, R.; Govindjee; Scholes, G. D. Light Absorption and Energy Transfer in the Antenna Complexes of Photosynthetic Organisms. *Chem. Rev.* **2017**, *117* (2), 249–293. DOI: 10.1021/acs.chemrev.6b00002.
- (11) Boulais, E.; Sawaya, N. P. D.; Veneziano, R.; Andreoni, A.; Banal, J. L.; Kondo, T.; Mandal, S.; Lin, S.; Schlau-Cohen, G. S.; Woodbury, N. W.; Yan, H.; Aspuru-Guzik, A.; Bathe, M. Programmed Coherent Coupling in a Synthetic DNA-Based Excitonic Circuit. *Nat. Mater.* **2018**, *17* (2), 159–166. DOI: 10.1038/NMAT5033.
- (12) Heilemann, M.; Tinnefeld, P.; Sanchez Mosteiro, G.; Garcia Parajo, M.; Van Hulst, N. F.; Sauer, M. Multistep Energy Transfer in Single Molecular Photonic Wires. *J. Am. Chem. Soc.* **2004**, *126* (21), 6514–6515. DOI: 10.1021/ja049351u.
- (13) Jevric, J.; Langenegger, S. M.; Häner, R. Light-Harvesting Supramolecular Polymers: Energy Transfer to Various Polyaromatic Acceptors. *European J. Org. Chem.* **2020**, 4677–4680. DOI: 10.1002/ejoc.202000441.
- (14) Gierschner, J. Directional Exciton Transport in Supramolecular Nanostructured Assemblies. *Phys. Chem. Chem. Phys.* **2012**, *14* (38), 13146–13153. DOI: 10.1039/C2CP42057K.
- (15) Cui, Q. H.; Peng, Q.; Luo, Y.; Jiang, Y.; Yan, Y.; Wei, C.; Shuai, Z.; Sun, C.; Yao, J.; Zhao, Y. S. Asymmetric Photon Transport in Organic Semiconductor Nanowires through Electrically Controlled Exciton Diffusion. *Sci. Adv.* **2018**, *4* (3), 1–8. DOI: 10.1126/sciadv.aap9861.

- (16) Chaudhuri, D.; Li, D.; Che, Y.; Shafran, E.; Gerton, J. M.; Zang, L.; Lupton, J. M. Enhancing Long-Range Exciton Guiding in Molecular Nanowires by H-Aggregation Lifetime Engineering. *Nano Lett.* **2011**, *11* (2), 488–492. DOI: 10.1021/nl1033039.
- (17) Amerongen, H. van; Grondelle, R. van; Valkunas, L. *Photosynthetic Excitons*; World Scientific, 2000. DOI: <https://doi.org/10.1142/3609>.
- (18) Köhler, A.; Bässler, H. *Electronic Processes in Organic Semiconductors: An Introduction*; Wiley-VCH Verlag GmbH & Co. KGaA: Weinheim, Germany, 2015. DOI: 10.1002/9783527685172.
- (19) Haedler, A. T.; Meskers, S. C. J.; Zha, R. H.; Kivala, M.; Schmidt, H. W.; Meijer, E. W. Pathway Complexity in the Enantioselective Self-Assembly of Functional Carbonyl-Bridged Triarylamine Trisamides. *J. Am. Chem. Soc.* **2016**, *138* (33), 10539–10545. DOI: 10.1021/jacs.6b05184.
- (20) Valera, J. S.; Gómez, R.; Sánchez, L. Tunable Energy Landscapes to Control Pathway Complexity in Self-Assembled N-Heterotriangulenes: Living and Seeded Supramolecular Polymerization. *Small* **2018**, *14* (3), 1702437. DOI: 10.1002/sml.201702437.
- (21) Hamzehpoor, E.; Perepichka, D. F. Crystal Engineering of Room Temperature Phosphorescence in Organic Solids. *Angew. Chemie Int. Ed.* **2020**, *59* (25), 9977–9981. DOI: 10.1002/anie.201913393.
- (22) Biskup, T. Structure-Function Relationship of Organic Semiconductors: Detailed Insights From Time-Resolved EPR Spectroscopy. *Front. Chem.* **2019**, *7*, 10. DOI: 10.3389/fchem.2019.00010.
- (23) Pflock, T. J.; Oellerich, S.; Southall, J.; Cogdell, R. J.; Ullmann, G. M.; Köhler, J. The Electronically Excited States of LH2 Complexes from *Rhodospseudomonas Acidophila* Strain 10050 Studied by Time-Resolved Spectroscopy and Dynamic Monte Carlo Simulations. I. Isolated, Non-Interacting LH2 Complexes. *J. Phys. Chem. B* **2011**, *115* (28), 8813–8820. DOI: 10.1021/jp202353c.
- (24) Akselrod, G. M.; Deotare, P. B.; Thompson, N. J.; Lee, J.; Tisdale, W. A.; Baldo, M. A.; Menon, V. M.; Bulovic, V. Visualization of Exciton Transport in Ordered and Disordered Molecular Solids. *Nat. Commun.* **2014**, *5* (1), 3646. DOI: 10.1038/ncomms4646.
- (25) Vlaming, S. M.; Malyshev, V. A.; Eisfeld, A.; Knoester, J. Subdiffusive Exciton Motion in Systems with Heavy-Tailed Disorder. *J. Chem. Phys.* **2013**, *138* (21), 214316. DOI: 10.1063/1.4808155.

Supporting Information

for

All-optical control of singlet exciton transport in individual supramolecular nanostructures by triplet gating

Bernd Wittmann¹, Till Biskup², Klaus Kreger³, Jürgen Köhler¹, Hans-Werner
Schmidt³, Richard Hildner^{*1,4}

Affiliations:

¹Spectroscopy of Soft Matter, University of Bayreuth, Universitätsstraße 30, 95447 Bayreuth, Germany.

²Chair of Physical Chemistry and Chemical Education, University of Saarland, Campus B2 2, 66123 Saarbrücken, Germany.

³Macromolecular Chemistry and Bavarian Polymer Institute, University of Bayreuth, Universitätsstraße 30, 95447 Bayreuth, Germany.

⁴Zernike Institute for Advanced Materials, University of Groningen, Nijenborgh 4, 9747 AG Groningen, The Netherlands.

*Correspondence to: r.m.hildner@rug.nl.

Inhalt

1. Materials and Methods	2
Table S1. Simulation parameters for the TREPR spectrum	5
Fig. S1: TrEPR spectrum and photoluminescence decays	6
Fig. S2: Fluorescence decay traces of bundles of nanofibres dispersed in anisole (400 μ M) at different excitation fluences.	7
Fig. S3: Determination of the singlet-triplet annihilation rate in bundles of nanofibres in a 400 μ M anisole dispersion.....	8
2. Numerical Simulations.....	10
Fig. S4: Schematic illustration and numeric simulation of tailored spatio-temporal singlet-triplet annihilation.....	12
Fig. S5: Direct visualization of controlled singlet exciton transport in another single bundle of supramolecular nanofibres.	13
Fig S6: Characterisation of the laser foci.....	15
3. References.....	16

1. Materials and Methods:

Materials.

The synthesis, purification and characterization of the supramolecular CBT building block is described in detail elsewhere ¹.

Molecularly dissolved solution of CBT. A 40 μM solution in THF (boiling point: 66 °C) was refluxed for 20 minutes under stirring and allowed to cool to room temperature.

Self-assembly of CBT. CBT was added at a concentration of 40 μM (~100 p.p.m., 0.01 wt%) or 400 μM (~1000 p.p.m., 0.1 wt%) in anisole (boiling point: 154 °C). A homogeneous dispersion was ensured by ultrasonication for 15 minutes. The dispersions were refluxed for 30 minutes under stirring and then allowed to cool to room temperature. All solvents were of HPLC grade and used as received ².

Methods.

Time-resolved detection of the electron paramagnetic resonance (TREPR). TREPR spectroscopy with a time resolution of down to 10 ns allows for real-time observation, e.g., of short-lived radical-pair and triplet states generated by pulsed laser excitation ³. In contrast to conventional continuous-wave EPR spectroscopy, which usually involves magnetic-field modulation to improve the signal-to-noise ratio, TREPR is recorded in a high-bandwidth direct-detection mode, so as not to constrain the time resolution of the experiment. Consequently, positive and negative signal amplitudes in TREPR correspond to enhanced absorptive (A) and emissive (E) electron-spin polarisations of the EPR transitions, respectively.

All TREPR experiments were performed at 80 K using a commercial EPR spectrometer (Bruker ESP380E) in conjunction with a Bruker microwave bridge (ER 046 MRT) equipped with a low-noise high-bandwidth video amplifier. The sample was placed in a synthetic-quartz (Suprasil) sample tube (3 mm inner diameter) and irradiated in a dielectric-ring resonator (Bruker ER 4118X-MD5), which was immersed in a helium gas-flow cryostat (Oxford CF-935) cooled with liquid nitrogen. The temperature was regulated to ± 0.1 K by a temperature controller (Oxford ITC-503). The time resolution of the experimental setup was in the 10 ns range. A microwave frequency counter (Hewlett-Packard HP 5352B) was used to monitor the microwave frequency. Optical excitation at the respective wavelengths was carried out with an optical parametric oscillator (OPO) system (Opta BBO-355-vis/IR) pumped by an Nd:YAG laser (Spectra Physics, Quanta Ray GCR 190-10) with a pulse width of approximately 6 ns, and a pulse energy of 1 mJ. The repetition rate of the laser was set to 10 Hz. A transient recorder (LeCroy 9354A) with a digitizing rate of 2 ns/11 bit was used to acquire the time-dependent EPR signal. To eliminate the background signal induced by the laser entering the EPR cavity, TREPR signals were accumulated at off-resonance magnetic-field positions (background) and subtracted from those recorded on-resonance. This background signal is completely independent in its shape from both, laser wavelength and magnetic field, and normally long-lived compared to the detected spin-polarised EPR signal. Background subtraction was performed directly in the transient recorder and a background signal repeatedly recorded after each tenth time trace of the experimental data.

Further experimental parameters: Microwave frequency, 9.69010 GHz, microwave power: 2 mW (20 dB attenuation, source power 200 mW), frequency-mixer detection, video amplifier set to 42 dB amplification and 25 MHz bandwidth, 1000 averages per point, laser excitation at 464 nm with 1 mJ per pulse and a shot repetition rate of 10 Hz.

Optical experiments. Time-resolved photoluminescence decays of dispersions were recorded with a time-resolved confocal fluorescence microscope (MicroTime 200, Picoquant), equipped with a 405 nm pulsed diode laser (LDH-D-C-405, Picoquant) at a repetition rate of 0.2 MHz with an air objective (NA=0.4). The excitation fluence was $4.3 \cdot 10^{16}$ photons/(pulse·cm²). In detection, we used a long-pass filter LP561 (AHF Analysentechnik).

Fluence- and repetition rate dependent time-resolved fluorescence decays of dispersions were recorded with a home-built microscope (see below), equipped with a 450 nm pulsed laser diode (LDH-P-C-450B, Picoquant) an air objective (NA=0.5). An additional long-pass filter LP545 (AHF Analysentechnik) was used to suppress the CBT monomer emission in the dispersion. All measurements of dispersions were conducted using Hellma QS quartz-glass cuvettes.

Optical imaging and spectroscopy of single bundles of supramolecular nanofibres. The 40 µM-dispersion was spin-coated on microscopy cover slips (borosilicate glass; thickness 0.17 µm; Carl Roth). All samples were dried under vacuum. Optical imaging and spectroscopy was performed using a home-built microscope (see Ref. 2). The excitation sources were pulsed diode lasers (LDH-P-C-450B, LDH-D-C-420, Picoquant; 70 ps pulse duration) that operate at a wavelength of 450 nm and 420 nm, respectively. The temporal separation between the pulses from both lasers is controlled by two laser drivers (PDL-800-D, PDL800-B, Picoquant), which are connected via their respective Sync-output and Sync-input and thus both lasers use the same internal clock. Due to the cable length and the internal-delay of the external trigger input of the laser driver, the 450 nm laser is delayed by 120 ns with respect to the 420 nm laser. A shutter in front of the lasers allows a separate activation of the lasers. The spatial separation of the lasers in the sample plane is achieved by two excitation paths, in which the 420 nm laser is scanned via tilting a mirror. The lasers were combined via a 50/50 beam splitter and directed to the microscope, which was equipped with an infinity-corrected high-numerical aperture oil-immersion objective (PlanApo, 60x, numerical aperture 1.45; Olympus). The sample was placed in the focal plane of the objective, and the sample position was controlled by a piezo-stage (Tritor 102 SG, from piezosystem jena). Photoluminescence was collected by the same objective and passed a set of dielectric filters (dichroic beam splitter z460RDC, long-pass filter LP467; AHF Analysentechnik) to suppress scattered or reflected laser light.

The detection beam path is equipped with a closed-loop piezo scan mirror (S-335.2.SH, PI) and a single-photon-counting avalanche photodiode (MPD, Picoquant) to position the detection spot independently from the confocal excitation spot. The electrical signal of the photodiode was fed into a time-correlated single-photon-counting module (TimeHarp 260 PICO, Picoquant).

In imaging mode, the photoluminescence signal was imaged onto a CMOS camera (Zyla 4.2 sCMOS, Andor). In this mode, we used two illumination methods. First, for widefield illumination we flipped an additional lens (widefield lens) into the excitation beam path to focus the laser light into the back-focal plane of the microscope objective. This allows for nearly uniform illumination of a large area with $\sim 70 \mu\text{m}$ diameter in the sample plane, to acquire overview PL images of our samples and to identify elongated nanostructures (Fig. 3A). Second, for confocal illumination the widefield lens was removed and the laser light was tightly focused to a spot with a full width at half maximum (FWHM) of $\sim 211 \text{ nm}$ for the 450 nm laser in the sample plane and 265 nm for the 420 nm laser, respectively (see Fig. S6). A flip-mirror allows to switch between imaging and single-photon counting mode of the setup.

For measurements on isolated bundles of supramolecular nanofibres, we used a repetition rate of 5 MHz and an excitation intensity of 115 W cm^{-2} for confocal illumination of the 450nm laser, respectively, 540 W cm^{-2} for the 420nm laser. For widefield illumination we used a excitation intensity of 1 W cm^{-2} . All experiments were carried out at room temperature under ambient conditions.

Simulations. All simulations of triplet spectra have been performed using the fitting framework TSim⁴ based on the EasySpin software package⁵ available for MATLAB® (MathWorks), and here the routine “pepper”. Parameters included were the g and D tensor and the triplet sublevel populations (in zero field). Line broadening (Γ) was included using a combination of Lorentzian (Γ_L) and Gaussian (Γ_G) lines.

For all simulations, the g tensor was assumed to be isotropic, with $g_{iso} = 2.002$. This left the parameters D and E of the zero-field splitting tensor D , the populations p_1 , p_2 , and p_3 , and the two line widths Γ_L and Γ_G as the only free parameters that were adjusted. For a more detailed explanation of these parameters and their meanings, see Ref.³.

Fitting the spectral simulations to the experimental data was done with the routine “lsqcurvefit” from the MATLAB® Optimization Toolbox™ using the trust-region-reflective least squares algorithm. For the final simulation parameters obtained from fitting, cf. Table S1.

For the numerical simulation of the spatio-temporal singlet-triplet annihilation shown in Fig. S4b, we used home-written Python-scripts. Further details are outlined below in section 2.

Table S1. Simulation parameters for the TREPR spectrum shown in Fig. S1. The simulation parameters are the complete set of parameters used for simulating the spectrum shown in Fig. S1. Γ is the line width the simulation has been convoluted with.

g_{iso}	p_1	p_2	p_3	D / MHz	E / MHz	Γ_G / mT	Γ_L / mT
2.002	0.289	0.339	0.372	1008 \pm 2	187 \pm 2	4.9 \pm 0.6	4.6 \pm 0.4

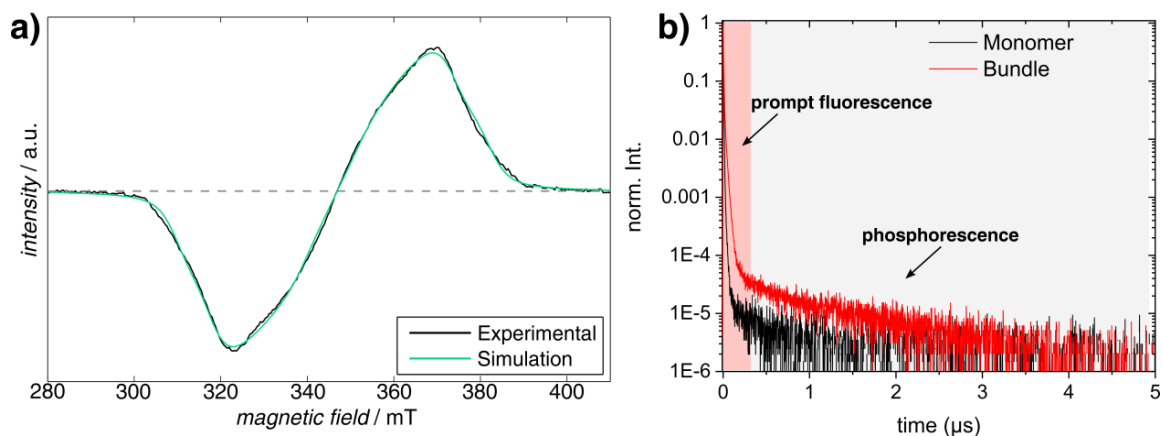


Fig. S1: TrEPR spectrum and photoluminescence decays. **a)** TrEPR spectrum of a 40 μM dispersion of molecularly dissolved CBT (black) in THF measured at $t = 900 \text{ ns}$ after laser excitation of CBT, together with the simulated curve (green). The parameters used for the simulations are shown in Tab. S1. **b)** Time-resolved photoluminescence decay of a 40 μM dispersion of molecularly dissolved CBT in THF (black), respectively of a 400 μM dispersion of bundles of nanofibres in anisole (red). Both show a prompt fluorescence signal within nanoseconds and a weaker phosphorescence signal on microsecond time scales. For molecularly dissolved CBT the triplet lifetime is 700 ns (black line), while for the bundles we find a longer lifetime of 1320 ns (red line).

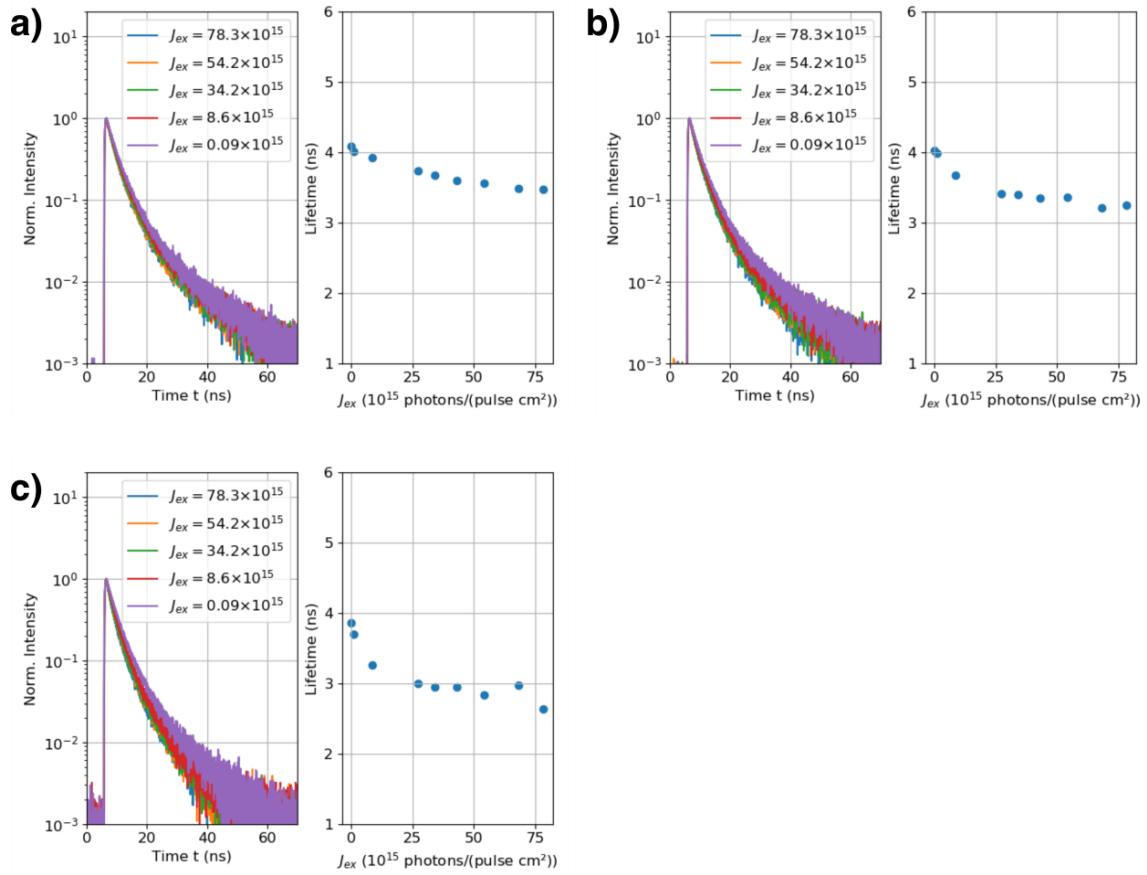


Fig. S2: Fluorescence decay traces of bundles of nanofibres dispersed in anisole (400 μM) at different excitation fluences. The laser repetition rates were 0.25 MHz (a), 2.5 MHz (b) and 10 MHz (c). Left parts: Representative fluorescence decay traces for the fluences indicated in the legend in units of photons/(pulse \cdot cm 2). Right parts: Amplitude-averaged lifetimes of the fluorescence decays as a function of the corresponding fluence. We fitted the data to a convolution of the instrument response function and a bi-exponential fluorescence decay with time constants t_i and relative amplitudes F_i . The shown amplitude-averaged lifetimes are calculated according to $t_{av} = \frac{\sum F_i t_i}{\sum F_i}$. Examples of fits are shown in Fig. S3.

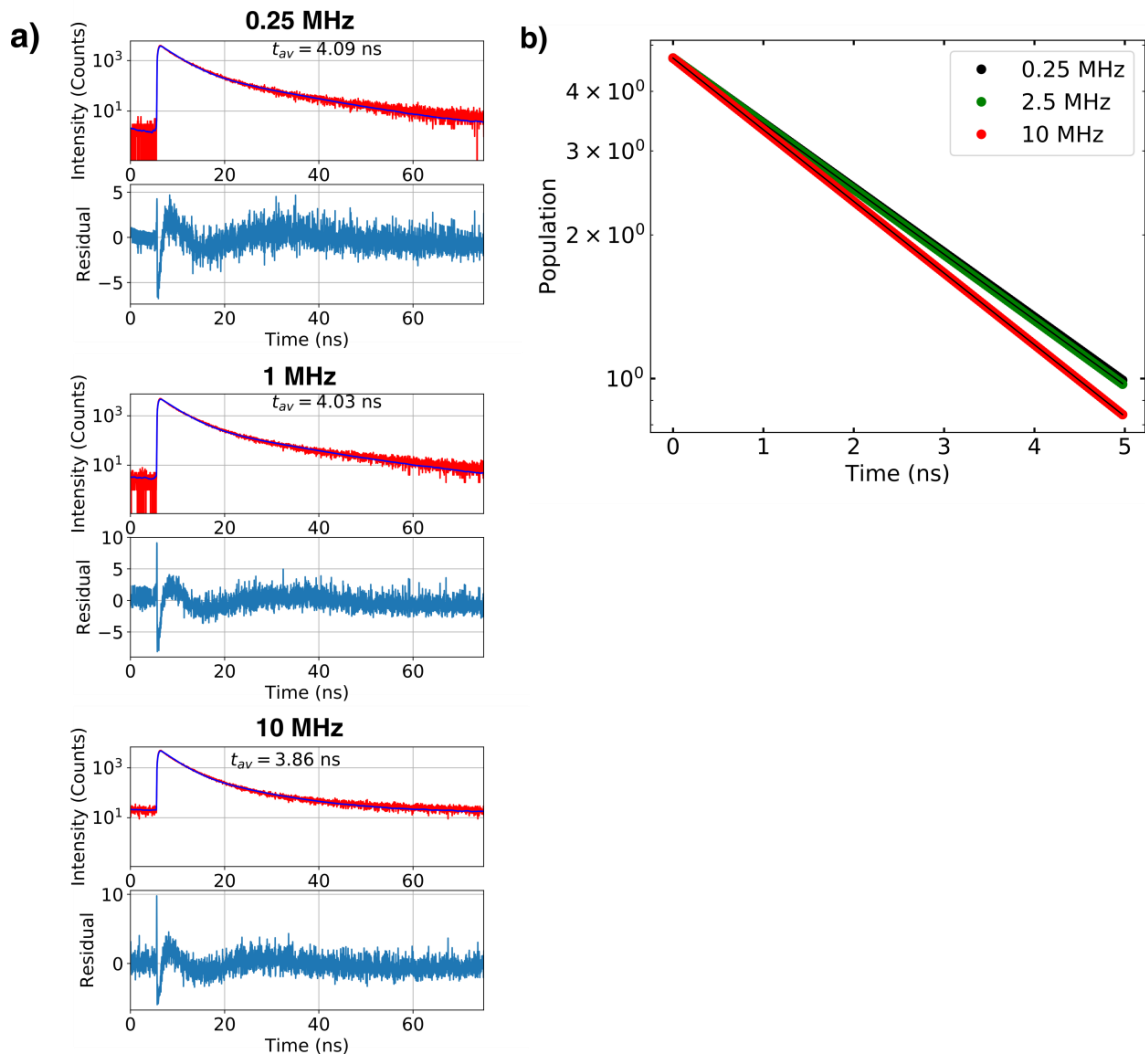


Fig. S3: Determination of the singlet-triplet annihilation rate in bundles of nanofibres in a 400 μ M anisole dispersion. a) Each panel shows, for a fixed excitation fluence of 0.09×10^{15} photons/(pulse cm^2) but different laser repetition rate, a fluorescence decay trace (top, red line) with the corresponding bi-exponential fit function (top, blue line) and the weighted residuals (bottom). For 0.25 MHz we found time constants t_i (relative amplitudes F_i) of $t_1 = 3.19$ ns ($F_1 = 4174.1$) and $t_2 = 12.55$ ns ($F_2 = 442.92$). For 2.5 MHz we found $t_1 = 3.18$ ns ($F_1 = 5310.06$) and $t_2 = 12.73$ ns ($F_2 = 519.36$). For 10 MHz we found $t_1 = 3.00$ ns ($F_1 = 5188.49$) and $t_2 = 10.8998$ ns ($F_2 = 632.041$). b) To extract the singlet-triplet annihilation rate, we use a simple exponential fit $S_{450}(t) = S_{450}(t=0)e^{-(k+\gamma T_{450})t}$ ⁶. Here, $S_{450}(t=0)$ is the total concentration of the generated singlet excitons at time $t=0$ after ‘singlet laser’ excitation at 450 nm, k is the total decay rate for the singlet excitons, γ is the rate constant of singlet-triplet annihilation and T_{450} is the stationary triplet exciton concentration formed after intersystem crossing. The singlet population along one nanofibre in a bundle is estimated according to⁷

$$S_{450}(t=0) = \left(\frac{\chi \lambda_{ex} (1 - 10^{-OD_{ex}})}{hc} \right) \left(\frac{OD_{max} \pi R_b^2}{\epsilon_{max}} \right)^{-1} * \left(\frac{2R_b}{a_0} \right),$$

where $\chi = 6 \times 10^{-14} J$ is the pulse energy, $R_b = 225 nm$ is the radius of excitation, $OD_{exc} = 1.48$ is the optical density of the dispersion at the laser excitation, respectively $OD_{max} = 1.8$ at the absorption maximum, $\lambda_{ex} = 450 nm$ is the wavelength of excitation, hc is Planck's constant times the speed of light, $\epsilon_{max} = 4500 (M^{-1}cm^{-1})$ the molar absorptivity at the absorption maximum, and $a_0 = 0.33 nm$ is the distance between the monomers along a nanofibre ². The product of the first term (number of excitations) and the second term (focal concentration) is a measure for the excitation probability of one monomer within the excitation spot ⁷. The last term corresponds to the number of monomers along one fibre within the excitation spot. T_{450} is given by

$$T_{450} = \frac{-k + \sqrt{k^2 + 4\gamma k_{ISC} S_{450}(t=0) / k_T \tau_{rep}}}{2\gamma}.$$

Here, $k_{ISC} = \frac{1}{4.19 ns}$ is the intersystem crossing rate, τ_{rep} is the repetition time of the laser excitation and $k_T = \frac{1}{1320 ns}$ is the decay rate for triplet excitons. k_{ISC} is an upper limit, since we assumed that the entire non-radiative channel for singlet exciton decay contributes to intersystem crossing. The fluorescence quantum yield of bundles is $QY = 2.58\%$ ².

The data shown in (a) are, for simplicity, approximated mono-exponentially, where the decay time corresponds to the amplitude-averaged lifetimes $t_{av} = \frac{\sum F_i t_i}{\sum F_i}$ of our bi-exponential fits. We used a global fit of $S_{450}(t) = S_{450}(t=0)e^{(-k + \gamma T_{450})t}$ to this approximated data set (see b), i.e., this equation is fitted simultaneously to all three traces to obtain the best overall fit. This best fit yields an annihilation rate of $\gamma = \frac{1}{(4133 \pm 30) ns} = (2.4 \pm 0.02) \times 10^{-4} ns^{-1}$.

Since the real intersystem crossing rate is unknown, we also fitted the data to the intersystem crossing rates of $k_{ISC} = 0.0238 \frac{1}{ns}$ ($k_{ISC} = 0.00238 \frac{1}{ns}$), yielding $\gamma = 0.002 ns^{-1}$ ($\gamma = 0.02 ns^{-1}$). These additional numbers were then also used for the simulations of the singlet exciton dynamics (see 2. Numerical Simulations).

2. Numerical Simulations:

For the simulation of the singlet exciton dynamics in the presence of a triplet barrier, we assume 3 coupled equations. We distinguish between the singlet S_i and triplet population T_i generated by two lasers, indicated by the index $i = 450, 420$ for the 'singlet' 450 nm laser and for the 'triplet' 420 nm laser, respectively.

1. $\frac{\partial S_{450}(x,t)}{\partial t} = D_S(t) \frac{\partial^2}{\partial x^2} S_{450}(x,t) - \gamma S_{450}(x,t) T_{450}(x) - k S_{450}(x,t) - \gamma S_{450}(x,t) T_{420}(x)$
2. $\frac{\partial T_{450}(x,t)}{\partial t} \approx 0$
3. $\frac{\partial T_{420}(x,t)}{\partial t} \approx 0$

Here, D_S is the diffusivity of the singlet excitons, γ is the singlet-triplet annihilation rate along a fibre in the bundle (Fig. S3) and k is the total decay rate of the bundle's singlet exciton population. The singlet exciton population generated by the 'triplet' 420 nm laser is not considered here because our experimental conditions ensure that it has already decayed when the 'singlet' laser arrives on the sample. The term $k S_{450}(x,t)$ reflects the (non-)radiative decay of the singlet excitons and does not play a role after normalizing the signal at each point in time for the spatio-temporal maps, analogous to the experiment (Fig. 3b,c). Therefore, this term is no longer considered. During the singlet exciton lifetime, we assume a constant triplet exciton population

given by $T_{450,420} = \frac{-k + \sqrt{k^2 + 4\gamma k_{ISC} S_{450,420}(t=0) / k_T \tau_{rep}}}{2\gamma}$, where $S_{450,420}(t=0)$ is the initially generated singlet exciton population generated by the 'singlet' and the 'triplet' laser, respectively (see Fig. S3). Equation (1.) indicates that singlet-triplet annihilation already occurs for the 'singlet laser' alone. In general, annihilation leads to an additional broadening of the spatio-temporal intensity map. However, this term is not relevant for the changed singlet exciton dynamics in Fig. 3c, since both reference experiment (only 'singlet laser' activated, Fig. 3b) and the experiment with both lasers activated (Fig. 3c) are equally affected by this term. Thus equation (1.) can be simplified to:

4. $\frac{\partial S_{450}(x,t)}{\partial t} \approx D_S(t) \frac{\partial^2}{\partial x^2} S_{450}(x,t) - \gamma T_{420}(x) S_{450}(x,t).$

Hence, the changed singlet exciton dynamics in the presence of triplet excitons can be understood by a simple diffusion equation with an effective singlet-triplet annihilation rate defined as $\gamma_{eff}(x) = \gamma T_{420}(x)$. Equation (4.) is numerically solved using a home written python script to calculate the spatio-temporal fluorescence intensity distributions in Fig. S4 below.

Note that we normalize all populations to that of the singlet population generated by the 'singlet laser', i.e., $S_{450}(t=0)$. Due to the different absorption cross section of $\sigma_{450nm} = 1.4 \times 10^{-17} \text{ cm}^2$ ($\sigma_{420nm} = 1.03 \times 10^{-17} \text{ cm}^2$) and the excitation intensities of 115 W cm^{-2} (540 W cm^{-2}) for the 'singlet' laser ('triplet' laser), the initial singlet population generated by the 'triplet laser' is 3.45 times larger compared to the singlet population generated by 'singlet' laser, i.e. $S_{420}(t=0) = 3.45 S_{450}(t=0)$. This singlet

population is converted via intersystem crossing into a triplet population corresponding to

$T_{420} = \frac{-k + \sqrt{k^2 + 4\gamma k_{ISC} S_{420}(t=0) / k_T \tau_{rep}}}{2\gamma}$. For the spatial distribution of both the singlet and the triplet exciton population we assume Gaussian initial distributions with standard deviations according to the experimental conditions (see Fig. S6). Furthermore, we used the estimated annihilation rate of $\gamma = 8.04 \times 10^{-4} \text{ ns}^{-1}$ (see Fig. S3). Without loss of generality, we choose $D_S = 0.05 \frac{\text{cm}^2}{\text{s}}$ in accordance with our previous work ². The simulated and, analogously to the experiment, normalized spatio-temporal singlet exciton dynamics are shown in Fig. S4b.

Note that also for the above mentioned pairs for intersystem crossing rate and annihilation constant ($k_{ISC} = 0.0238 \frac{1}{\text{ns}}$ and $\gamma = 0.008 \text{ ns}^{-1}$) and ($k_{ISC} = 0.00238 \frac{1}{\text{ns}}$ and $\gamma = 0.08 \text{ ns}^{-1}$), see Fig. S3, we obtain similar results. Finally, we note that also the simulation of the full equation (1.) leads to similar results.

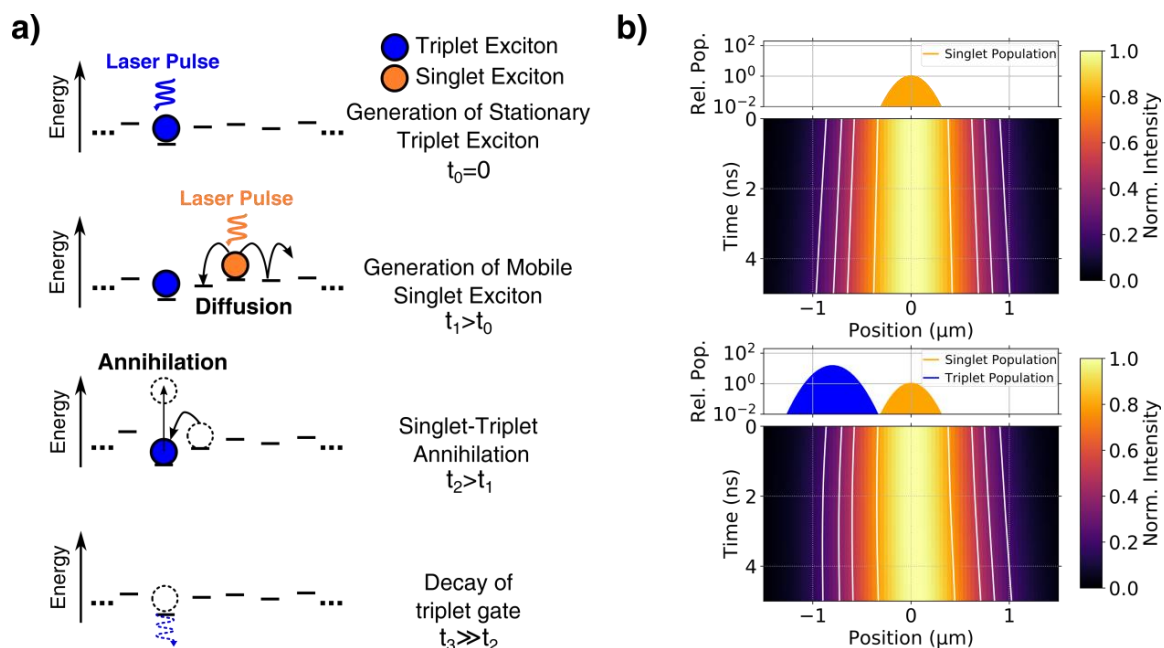


Fig. S4: Schematic illustration and numeric simulation of tailored spatio-temporal singlet-triplet annihilation. (a) Schematic illustration of gated singlet exciton diffusion: At $t_0 = 0$ a laser pulse creates an initial singlet exciton that is converted into a triplet exciton (blue filled circle) via intersystem crossing. A second laser arriving at $t_1 > t_0$ creates mobile singlet excitons (orange filled circle), spatially separated from the triplet population. At $t_2 > t_1$, the mobile singlet exciton encounters the triplet exciton and annihilation takes place, leaving behind only a triplet exciton (self-sustaining barrier, see main text). Finally, at time $t_3 \gg t_2$ the triplet exciton decays (by phosphorescence or non-radiatively) and the gate is deactivated. (b) Simulated singlet exciton diffusion in the absence (top) and in the presence of a triplet population (below). For details see section 2. Numerical Simulations.

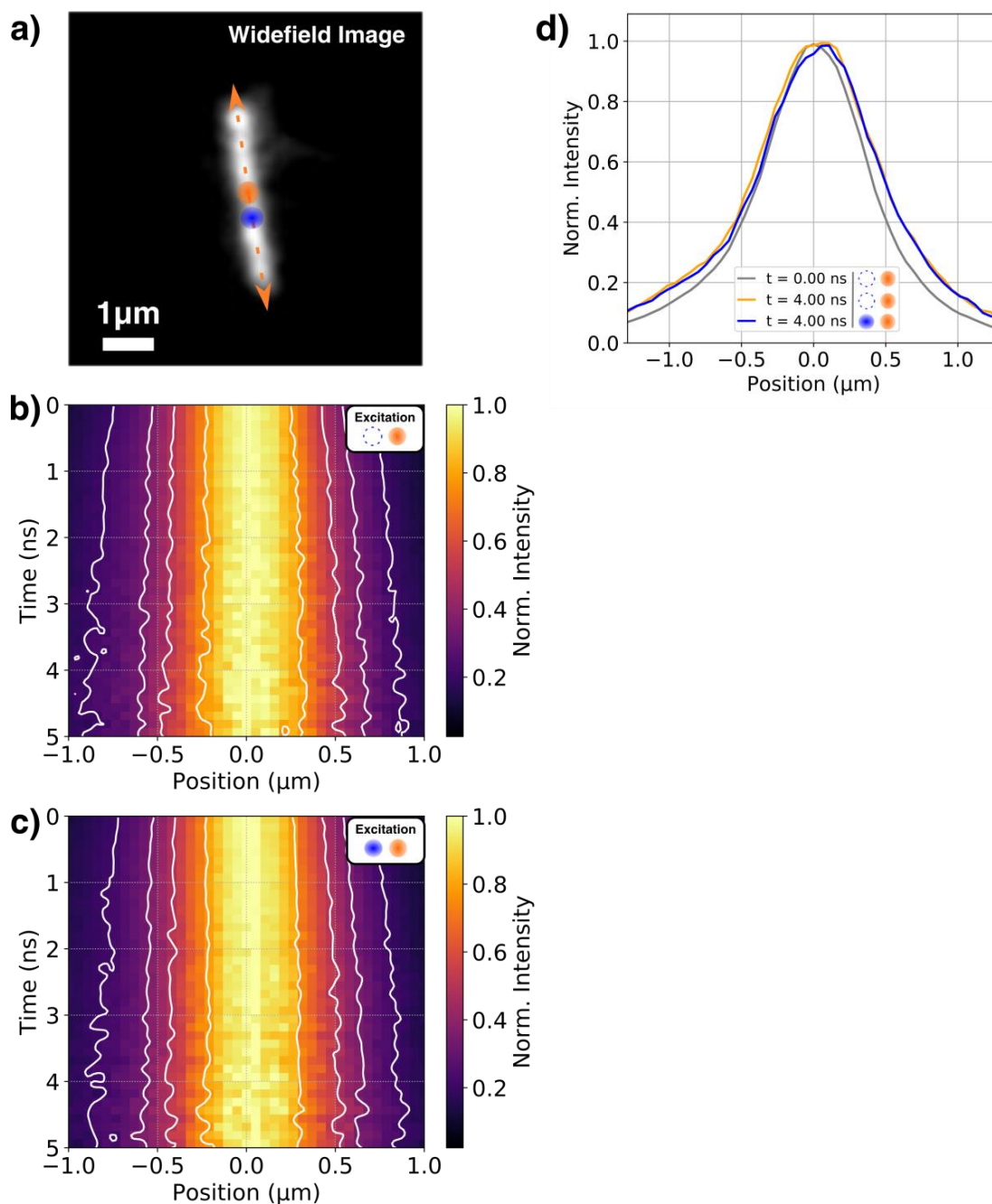


Fig. S5: Direct visualization of controlled singlet exciton transport in another single bundle of supramolecular nanofibres. **a)** Widefield image of an individual bundle. Orange dashed arrows indicate the detection scanning axis x . The orange circle labels the position $x = 0$ of the singlet population. The blue circle indicates the position of the triplet population. **b)** Normalized fluorescence intensity distribution and its evolution in space and time for the bundle in (a) for the measurement with only the 'singlet laser' activated. **c)** Normalized fluorescence intensity distribution as in (b), but here both the 'singlet' and 'triplet laser' are activated. The triplet population is generated on the left side of the map. The white contour lines in (b,c) indicate the widths of the intensity profiles. **d)** Intensity profiles retrieved from the fluorescence intensity maps in b) (orange) and c) (blue) at different delay times t after singlet

exciton generation. The grey line shows the initial intensity distribution at time $t = 0$ generated by the 'singlet laser'. While for positions $x < 0 \mu\text{m}$ the initial (grey line) and delayed (blue line) profiles partly overlap, i.e., spatial broadening of the initial singlet exciton population is hindered, to the right ($x > 0 \mu\text{m}$) singlet exciton diffusion is entirely unperturbed, since the profiles in absence (orange line) and presence (blue line) of the triplet population overlap.

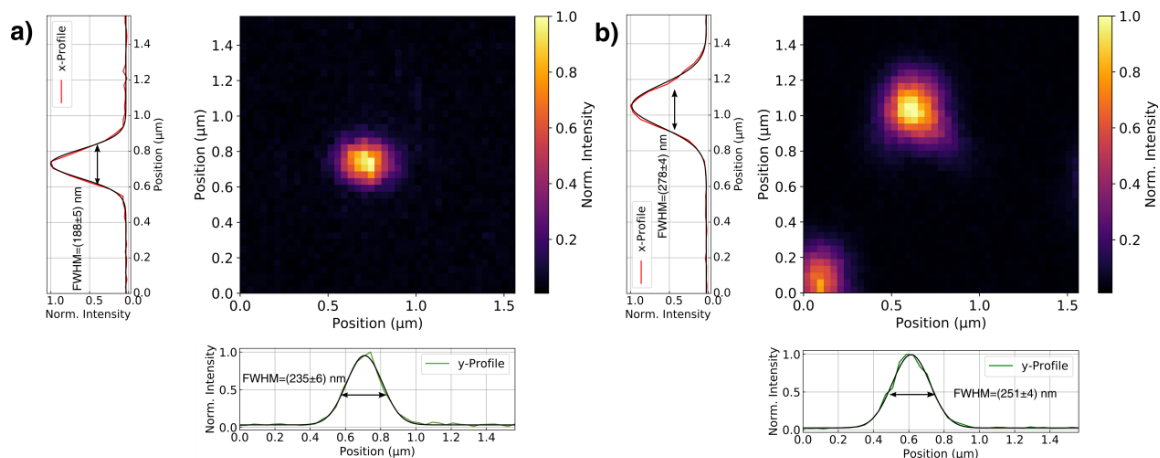


Fig S6: Characterisation of the laser foci. a) 450 nm 'singlet' laser. b) 420 nm 'triplet' laser. We raster scanned single fluorescence microspheres (0.1 μ m diameter, Red Fluorescence Carboxylated Ps Latex, Nanosphere) along the laser excitation spot to characterise their sizes. The confocal image is shown as map with colour-coded intensity. The shown profiles are along the x- and y-scanning axis and were placed through the intensity maximum of the map.

3. References

- (1) Haedler, A. T.; Meskers, S. C. J.; Zha, R. H.; Kivala, M.; Schmidt, H. W.; Meijer, E. W. Pathway Complexity in the Enantioselective Self-Assembly of Functional Carbonyl-Bridged Triarylamine Trisamides. *J. Am. Chem. Soc.* **2016**, *138* (33), 10539–10545. DOI: 10.1021/jacs.6b05184.
- (2) Wittmann, B.; Wenzel, F. A.; Wiesneth, S.; Haedler, A. T.; Drechsler, M.; Kreger, K.; Köhler, J.; Meijer, E. W.; Schmidt, H.-W.; Hildner, R. Enhancing Long-Range Energy Transport in Supramolecular Architectures by Tailoring Coherence Properties. *J. Am. Chem. Soc.* **2020**, *142* (18), 8323–8330. DOI: 10.1021/jacs.0c01392.
- (3) Biskup, T. Structure-Function Relationship of Organic Semiconductors: Detailed Insights From Time-Resolved EPR Spectroscopy. *Front. Chem.* **2019**, *7*, 10. DOI: 10.3389/fchem.2019.00010.
- (4) Meyer, D. L.; Lombeck, F.; Huettner, S.; Sommer, M.; Biskup, T. Direct S₀→T Excitation of a Conjugated Polymer Repeat Unit: Unusual Spin-Forbidden Transitions Probed by Time-Resolved Electron Paramagnetic Resonance Spectroscopy. *J. Phys. Chem. Lett.* **2017**, *8* (7), 1677–1682. DOI: 10.1021/acs.jpcllett.7b00644.
- (5) Stoll, S.; Schweiger, A. EasySpin, a Comprehensive Software Package for Spectral Simulation and Analysis in EPR. *J. Magn. Reson.* **2006**, *178* (1), 42–55. DOI: 10.1016/j.jmr.2005.08.013.
- (6) Zaushitsyn, Y.; Jespersen, K. G.; Valkunas, L.; Sundström, V.; Yartsev, A. Ultrafast Dynamics of Singlet-Singlet and Singlet-Triplet Exciton Annihilation in Poly(3-2'-Methoxy-5' Octylphenyl)Thiophene Films. *Phys. Rev. B* **2007**, *75* (19), 195201. DOI: 10.1103/PhysRevB.75.195201.
- (7) Caram, J. R.; Doria, S.; Eisele, D. M.; Freyria, F. S.; Sinclair, T. S.; Rebentrost, P.; Lloyd, S.; Bawendi, M. G. Room-Temperature Micron-Scale Exciton Migration in a Stabilized Emissive Molecular Aggregate. *Nano Lett.* **2016**, *16* (11), 6808–6815. DOI: 10.1021/acs.nanolett.6b02529.

4.3 ALL-OPTICAL CONTROL OF SINGLET EXCITON TRANSPORT IN INDIVIDUAL SUPRAMOLECULAR NANOSTRUCTURES BY TRIPLET GATING

EIDESSTATTLICHE VERSICHERUNG

Hiermit versichere ich an Eides statt, dass ich die vorliegende Arbeit selbstständig verfasst und keine anderen als die von mir angegebenen Quellen und Hilfsmittel verwendet habe.

Weiterhin erkläre ich, dass ich keine Hilfe von gewerblichen Promotionsberatern bzw. -vermittlern oder ähnlichen Dienstleistern weder bisher in Anspruch genommen habe, noch künftig in Anspruch nehmen werde.

Zusätzlich erkläre ich hiermit, dass ich keinerlei frühere Promotionsversuche unternommen habe.

Außerdem erkläre ich mich einverstanden, dass die elektronische Fassung meiner Dissertation unter Wahrung meiner Urheberrechte und des Datenschutzes einer gesonderten Prüfung unterzogen werden kann.

Des Weiteren erkläre ich mich einverstanden, dass bei Verdacht wissenschaftlichen Fehlverhaltens Ermittlungen durch universitätsinterne Organe der wissenschaftlichen Selbstkontrolle stattfinden können.

Ort, Datum

Bernd Wittmann